Numerical Modeling and Dynamic Analysis of Two-Rotor Floating Offshore Wind Turbines

Omar El Beshbichi

Thesis submitted in fulfilment of
the requirements for the degree of
PHILOSOPHIAE DOCTOR
(PhD)

University of
Stavanger

Faculty of Science and Technology
Department of Mechanical and Structural Engineering and Materials Science
2023

Preface

This thesis is submitted in partial fulfillment of the requirements for the degree of Doctor of Philosophy (PhD) at the University of Stavanger (UiS), Norway. The research work has been carried out at the Faculty of Science and Technology, Department of Mechanical and Structural Engineering and Material Science, in the period from December 2019 to February 2023. The main supervisor was Prof. Muk Chen Ong, and the co-supervisor was Prof. Yihan Xing. The PhD project was funded by the Equinor Akademia program at the University of Stavanger.

I confirm that this thesis is my own work and I have documented all sources and material used.

Stavanger, Norway
January 10, 2023

Omar El Beshbichi

Acknowledgements

First and foremost, I would like to express my gratitude for my supervisors, whose support, passion, and friendship have been the pillars of my doctoral pursuit. Thank you to my main supervisor Prof. Muk Chen Ong for the guidance, care for quality, and for giving me the opportunity to pursue this PhD degree from which I have learned and grown so much. I am also grateful to my co-supervisor Prof. Yihan Xing for sharing his vast technical knowledge and for the indispensable and fascinating discussions which made this work possible.

I am also grateful to all my fellow colleagues and friends at UiS which made these years memorable. I would like to mention my colleague and flatmate Chern Fong Lee for all the experiences, good dialogues, and micro-projects we shared especially during COVID lockdown, and the best officemate Yucong Ma for good and productive times shared in the same working space and for showing me glimpses into a remote culture.

A special and heartfelt thank you goes to my family: my parents and my sister, which have always provided unconditional love and support.

Abstract

The exploitation of offshore wind in deep waters by means of floating wind turbines is steadily gaining traction as a suitable option to produce renewable energy. Among the innovative technologies recently proposed, two-rotor floating wind turbines offer significant advantages in terms of smaller blades deployed offshore, cheaper operations, fewer installations, and sharing of the floating platform. Although examples of commercial prototypes currently under development are many, the scientific literature lacks thorough studies on the dynamic performance of such systems. As a consequence, a better understanding of the major design drivers of such systems leading toward the definition of a baseline design is required.

Floating wind turbines are highly dynamic systems subjected to environmental loads from waves, currents, and wind. Moreover, the dynamic response of wind turbines is heavily influenced by the nonlinear behavior of the servo systems, such as cut-in, cut-out, and failure conditions. As such, dynamic analysis is often carried out by means of fully-coupled tools able to consider all factors in an integrated environment. To date, there is a lack of an open-source fully-coupled tool able to easily analyze the dynamics of two-rotor floating wind turbines. This PhD thesis presents the development of such a tool. Development work was mostly carried out in Modelica through the open-source environment OpenModelica and the freely-available Modelica Standard Library. The dynamics of the system and structural dynamics of tower and blades were implemented by means of a multibody approach. Linear hydrodynamics was solved in DNV Wadam and the associated hydrodynamic loads were imported into the tool as time realizations. Moreover, the well-known aerodynamic module AeroDyn within the NREL package FAST was integrated into the environment for the

computation of aerodynamic loads based on the blade-element momentum approach. Benchmark studies showed good performance and accuracy compared with standard single-rotor packages.

The tool was also employed to examine various dynamic aspects of two-rotor floating wind turbine concepts. Global dynamic analysis of a two-rotor wind turbine mounted on a spar-type floating platform showed significant platform yaw response due to wind turbulence intensity and the distribution of thrust loads on the structure. Modification of the blade-pitch control system was found to be beneficial to reduce platform yaw response. As a consequence, the design of an optimal control strategy based on a linear quadratic regulator was carried out, showing better performance than reference control strategies without the need for large usage of the actuation systems. Furthermore, the analysis of the long-term extreme response of the same two-rotor floating system was carried out by means of a variety of methods. A modification of the 50-year environmental contour method considering the cut-off condition of the system was assessed, showing a small underestimation of wind-induced responses as compared with a full long-term analysis. This method may thus be considered a fast alternative for the long-term extreme assessment of two-rotor floating wind turbines. The global response of the two-rotor wind turbine system mounted on different platform types was also assessed. Results showed the largest platform yaw response for the spar type, while the greatest structural loads were obtained for the tension-leg type. The semi-submersible type showed the greatest response in extreme conditions, but the most balanced response in operational conditions. The analysis of blade-pitch actuation faults on the dynamics and loads of a two-rotor system was also carried out. Results showed significant dynamic loads on the tower structure which can be detrimental in terms of fatigue life. Shutdown delay between rotors implies greater torsional loads on the structure, while loads on the faulty blades are not affected by the choice of platform employed or two-rotor application.

List of Appended Publications

Paper 1

El Beshbichi, O., Xing, Y., Ong, M. C. (2021). An object-oriented method for fully coupled analysis of floating offshore wind turbines through mapping of aerodynamic coefficients. *Marine Structures*, 78:102979.

Paper 2

El Beshbichi, O., Xing, Y., Ong, M. C. (2021). Dynamic analysis of two-rotor wind turbine on spar-type floating platform. *Ocean Engineering*, 236:109441.

Paper 3

El Beshbichi, O., Rødstøl, H., Xing, Y., Ong, M. C. (2022). Prediction of long-term extreme response of two-rotor floating wind turbine concept using the modified environmental contour method. *Renewable Energy*, 189:1133-1144.

Paper 4

El Beshbichi, O., Xing, Y., Ong, M. C. (2022). LQR optimal control of two-rotor wind turbine mounted on spar-type floating platform. *Journal of Offshore Mechanics and Arctic Engineering*, 145(2):022001.

Paper 5

El Beshbichi, O., Xing, Y., Ong, M. C. (2022). Modelica-AeroDyn. Development, benchmark, and application of a comprehensive object-oriented tool for dynamic analysis of non-conventional horizontal-axis floating wind turbines. *Wind Energy*. (Under review)

Paper 6

El Beshbichi, O., Xing, Y., Ong, M. C. (2022). Comparative dynamic analysis of two-rotor wind turbine on spar-type, semi-submersible, and tension-leg floating platforms. *Ocean Engineering*, 266(3):112926.

Paper 7

El Beshbichi, O., Xing, Y., Ong, M. C. (2022). Load response of a two-rotor floating wind turbine undergoing blade-pitch system faults. *Wind Energy*. (Under review)

Contents

Chapter 1

Introduction

1.1   Background and Motivation

In the last few years, offshore wind has been an exceptionally fast-growing industry. Estimates of the global cumulative offshore capacity in 2021 is about 35 GW, while the offshore wind capacity installed in 2020 is about 6.1 GW (GWEC, 2019). Offshore wind is appealing since wind tends to be faster and steadier offshore than inland, and since it is less intrusive to densely populated areas (Cruz and Atcheson, 2016). The installation of offshore wind turbines currently relies on fixed foundations, of which three major classes are monopile, jacket, and tripod (Cruz and Atcheson, 2016). The major limitation of these designs is the maximum water depth at which they are economically feasible to deploy. The maximum water depth at which they can be used is set to approximately 50 m (shallow water sites), while the average water depth of currently deployed wind farms is 27.2 m (Cruz and Atcheson, 2016). However, most of the ideal offshore wind energy sites across the globe are characterized by much deeper water depths (Jonkman, 2007).

Floating offshore wind turbines (FOWTs) have been proposed as a technological solution for the exploitation of deepwater locations (Jonkman, 2007; Cruz and Atcheson, 2016). These concepts have been extensively studied in the last decades, and several examples of full-scale deployment are present. Classification of floating foundations considers the manner in which the structure achieves hydrostatic stability. The spar-type platform uses ballast to achieve

stability, the TLP-type uses tensioned station-keeping lines, while the barge-type platform uses the platform waterplane static stability (Jonkman, 2009b). Early examples are Hywind Demo, a 2.3 MW FOWT developed by Equinor ASA and deployed in Karmøy, Norway in 2009 (Equinor, 2020a), and WindFloat®, a 2 MW FOWT prototype developed by Principle Power, Inc. and deployed in Aguçadoura, Portugal in 2011 (Principle Power, 2016). Hywind Scotland is the first FOWT farm composed of five 6 MW wind turbines mounted on spar-type platforms, commissioned by Equinor ASA off the coast of Peterhead, Scotland in 2017 (Equinor, 2020b). Principle Power has also recently commissioned two FOWT farms, WindFloat Atlantic in 2017 and Kincardine Offshore Windfarm in 2021. They are composed, respectively, of three V164-8.4 MW and five V164-9.5 MW wind turbines mounted on semi-submersible platforms, and deployed off the coasts of Viana do Castelo, Portugal and Aberdeenshire, Scotland (Principle Power, 2016).

Reduction of the overall cost of energy may in principle be achieved also by downscaling wind turbines into equivalent multi-rotor systems (two or more wind turbines installed on the same structure, as illustrated in Figure 1.1). The development of multi-rotor wind turbines is an old idea, first developed early in the 20th century when the lack of advanced glass fiber composite materials made the manufacturing of large rotors unfeasible (Jamieson and Branney, 2012). The nominal wind turbine power scales with the square of the rotor radius. On the other hand, blade mass scales with the cube of the rotor radius (Jamieson and Branney, 2012). Employing an array of rotors in place of an equivalent single-rotor configuration is thus advantageous in terms of power-to-weight ratio. Multi-rotor wind turbine concepts are also interesting to reduce the costs associated with the manufacturing, transportation, and operation and maintenance of big wind turbine components. Vestas Wind Systems A/S and the Technical University of Denmark, for instance, studied a multi-rotor wind turbine concept composed of four 225 kW turbines (4R-V29), showing good performance in terms of faster wake recovery and marginally higher power production compared to an equivalent single-rotor configuration (van der Laan et al., 2019). In addition to the potential advantages already mentioned, multi-rotor wind turbines mounted on floating platforms entail major advantages in
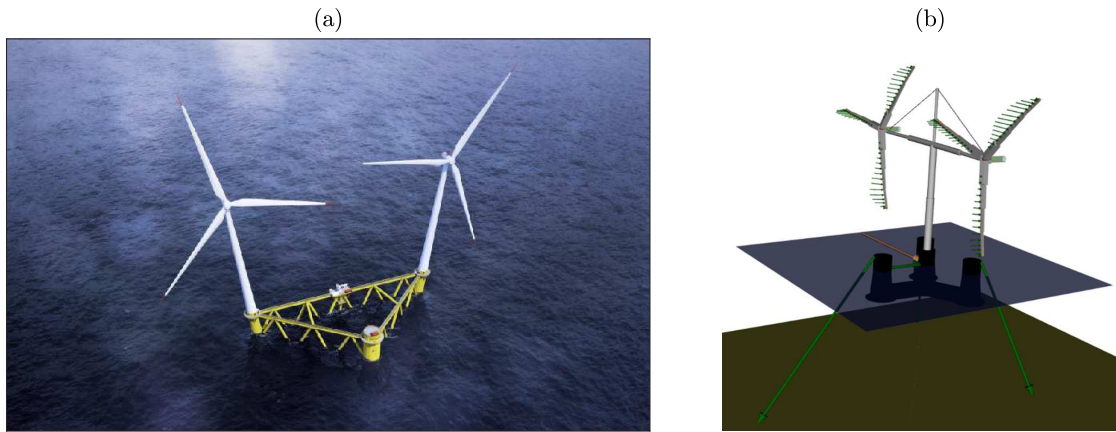
Figure 1.1: a) Hexicon TwinWind$^{\text{TM}}$ (Hexicon, 2021a). b) One of the two-rotor floating wind turbine concepts considered in this work.

terms of station-keeping and platform sharing, cheaper offshore operations associated with the handling of smaller components, and fewer net installations.

Despite the rapid development of multi-rotor FOWT systems, the literature lacks information about their dynamic response. Although some multi-rotor FOWT structures have been developed, design standards lack information leading toward a baseline design. A better understanding of the major dynamic features of these systems in operational and extreme environmental conditions is thus needed. Moreover, standard control algorithms for blade-pitch control may not be suitable for multi-rotor employment. As such, suitable control strategies should be investigated in more detail. The features of an optimal floating platform design for multi-rotor applications have also not been formally investigated, as well as major structural design considerations given normal operational conditions, extreme conditions, and fault conditions.

New FOWT designs are normally analyzed and validated by means of fully-coupled dynamic tools. Such codes are able to predict the coupled system response due to aerodynamic and hydrodynamic loads, station-keeping, structural dynamics, and control systems. This method is also called the aero-hydro-elastic-servo fully-coupled approach (Cruz and Atcheson, 2016). Major design tools are, for instance, FAST by NREL, Bladed by DNV, HAWC2 by DTU, and SIMO/RIFLEX by Marintek (Cordle and Jonkman, 2011; Robertson et al.,

Table 1.1: Overview of major offshore wind modeling tools capabilities (Jonkman et al., 2010; Cordle and Jonkman, 2011; Robertson et al., 2014b; DNV, 2021). (T: Turbine. P: Platform. Mod: Modal dynamics. MBS: Multi-Body System. FE: Finite-Element. SS: Steady-State. BEM: Blade Element/Momentum. GDW: Generalized dynamic wake. DS: dynamic stall. PF: Potential Flow. ME: Morison's Equation. QS: Quasi-Static. Dyn: Dynamic. MRC: Multi Rotor Capability.)

	Developer	Structural Dynamics	Aero Dynamics	Hydro Dynamics	Mooring Loads	MRC
Present Tool (OM+AeroDyn)	-	T: MBS P: Rigid	(BEM or GDW) + DS	PF + ME	QS	✓
FAST v8	NREL	T: Mod/MBS P: Rigid	(BEM or GDW) + DS	PF + ME	QS	–
Bladed	DNV	T: Mod/MBS P: MBS	(BEM or GDW) + DS	ME	QS	–
HAWC2	DTU	T: MBS/FE P: MBS/FE	(BEM or GDW) + DS	ME	FE/Dyn	–
Simo-Riflex+ AeroDyn	MARINTEK + NREL	T: FE P: FE	(BEM or GDW) + DS	PF + ME	FE/Dyn	–

2014b). Table 1.1 lists their modeling capabilities. These tools offer the necessary fidelity needed for prototypal analysis. However, they offer very low flexibility concerning the accommodation of non-conventional wind turbine configurations. To date, none of these tools is able to consider multi-rotor FOWT systems. On the other hand, a few experimental codes have been recently presented that employ more sophisticated aerodynamic formulations coupled with standard multi-body dynamics modules. These architectures may, in principle, be able to accommodate multi-rotor applications. See, for instance, the work by Ramos-García et al. (2022) in which a vortex code is coupled with HAWC2. Moreover, the work by Manolas et al. (2020) presents a fully-coupled architecture in which a free-wake aerodynamic model is included. However, experimental codes are typically optimized for a fixed configuration and are hard to employ in a flexible way for different cases. It would require huge code development efforts each time a new multi-rotor FWT concept with a different turbine configuration is to be studied. The low flexibility in handling arbitrary turbine configurations makes these codes impractical to study innovative multi-rotor FWTs with a vast range of concepts and configurations proposed. To close the current gap existing in numerical tool flexibility, two major objectives of this work can be stated as 1) the development and benchmark of a comprehensive fully-coupled tool able to easily accommodate arbitrary platform and tower geometries and the number of wind turbines used, and 2) the employment of the tool to gather insights on the dynamics of two-rotor FOWT systems aiming at the definition of a baseline design. The tool must also be flexible enough to allow for further development and modification of existing code.

The development work has been carried out in Modelica, which is a non-proprietary, object-oriented, equation-based language developed by the non-profit Modelica Association and used to conveniently model complex physical systems (The Modelica Association, 2020). The development of numerical tools for the analysis of FOWTs written in Modelica is relatively new, albeit some modeling experience exists (Strobel et al., 2011; Brommundt et al., 2012; Leimeister and Thomas, 2017). The open-source platform OpenModelica has been used as development environment. OpenModelica is the major open-source platform based on the Modelica language, mainly used in academic re-

search and supported by the Open Source Modelica Consortium (OSMC, 2021). Modelica offers a freely available Modelica Standard Library (MSL), suitable to model dynamic systems of various physical domains, such as mechanical, thermal, control, and electrical. The object-oriented nature of Modelica allows for a flexible way of generating complex multi-domain models and facilitates the reuse of common classes throughout the model. Object-oriented modeling is then convenient when a fully-coupled approach is needed. Modelica language is also advantageous for the establishment of analysis platforms suitable to be further extended in time by different developers, it greatly aids debugging stages, and it is well suitable for code sharing. Front-end platforms include commercial and open-source options. Dymola is a common commercial platform, developed by the European company Dassault Systèmes and available within CATIA (Elmqvist, 2014).

The tool developed in this work implements industry-standard fidelity levels of the system dynamics, structural dynamics, and formulation of the external loads acting on the system. Aerodynamic loads are implemented by integrating into Modelica the well-established open-source aerodynamic module AeroDyn v15 from the NREL package FAST v8. AeroDyn implements blade-element momentum (BEM) aerodynamics with the inclusion of Prandtl tip and hub losses, as well as Pitt-Peters skewed flow and Gaulert corrections (Moriarty and Hansen, 2005). The proximity between rotors is assumed to have no influence on the wind velocity profile, i.e., the aerodynamic loads on blades are computed by considering the undisturbed turbulent wind profile and the blade local velocity induction factors only. The current modeling assumption resulted adequate to extract useful information about the global dynamics of two-rotor FOWT systems. Nonetheless, the effect of the aerodynamic interaction between rotors on the system response should be later investigated in detail by means of high-fidelity methods and findings should be integrated into the code.

1.2 Multi-Rotor Wind Turbine Systems

To date, the literature lacks a thorough depiction of the dynamic performance of multi-rotor FOWTs. However, commercial development of multi-rotor floating wind turbines is advancing rapidly. Figure 1.2 shows examples of multi-rotor wind turbine systems either developed in the past or currently under development. In the following, information about a selection of multi-rotor wind turbine systems is given.

Early examples of multi-rotor FOWT research are InnWind and MUFOW. InnWind (INNWIND, 2015) was an EU-funded project proposing a 20 MW wind turbine configuration employing 45 turbines 444 KW each. Conclusions claimed a reduction of the LCoE against an equivalent single-rotor configuration of about 15%. Kirchner-Bossi and Porté-Agel (2020) showed that the optimization of the layout of multi-rotor wind farms may lead to significant benefits also in terms of overall power density compared to a baseline single-rotor wind farm layout. On the other hand, the Multiple Unit Floating Offshore Windfarm project (MUFOW) (Barltrop, 1993), initiated in 1993 by a UK-based consortium, investigated of the feasibility of arrays of wind turbines mounted on a single floating platform. The study highlighted potential advantages of the system in terms of cheaper installations per machine, greater hydrostatic stability, better platform motion characteristics given by the larger floater, and easier maintenance procedures. However, the concept has not been further analyzed in detail. Vestas Wind Systems A/S installed a multi-rotor demonstrator at the Technical University of Denmark, named 4R-V29, composed of four 225kW wind turbines mounted on a single structure and in operation between 2016 and 2019. van der Laan et al. (2019) recently compared numerical results obtained from several Reynolds-Averaged Navier-Stokes equations (RANS) tools against field measurements of power performance and wake deficit, showing faster wake recovery and marginally higher power output at below-rated environmental conditions given by the rotors aerodynamic interaction. Bastankhah and Abkar (2019) also performed a large-eddy simulation to study the wake flow properties of a similar four-rotor concept. They found out that the wake recovery is faster at short downwind distances with respect to a single-rotor

Figure 1.2: Examples of selected multi rotor wind turbine designs under development. a) Hexicon TwinWind™ (Hexicon, 2021a). b) EnBW Nezzy² (EnBW, 2021b). c) Rosenberg Worley Flex2Power (Flex2Power, 2022). d) WCS Wind Catching (Wind Catching Systems, 2022). e) DTU 4R-V29 prototype (decommissioned).

system. TwinWind$^{\text{TM}}$ by Hexicon, for instance, is a two-rotor wind turbine system mounted on a semi-submersible platform (Hexicon, 2021a). Claimed design advantages are the increased power density and associated reduction of the levelized cost of energy compared with an equivalent single-rotor design. Hexicon is planning to deploy a full-scale demonstrator at the Metcentre's deep water area in Norway by the end of 2022 (Hexicon, 2021b). Another example is Flex2Power by Rosenberg Worley AS (Flex2Power, 2022), a slim, modularized, and elastic platform for combined wind, wave, and solar energy production. Major advantages of this concept are the significantly low construction and service cost, the low material usage, and the lightweight and flexible design. Ocean basin tests were carried out in June 2021 with successful results. Design certification is currently in process by DNV. A scaled prototype is planned to be deployed off the coast of Norway in the next years. Wind Catching by Wind Catching Systems (WCS) (Wind Catching Systems, 2022) is also a good example of multi-rotor FOWT development. The system is composed of a steel grid of 117 small turbines mounted on a semi-submersible floating platform. Major claimed advantages are an increased power density, significant scalability, and easier operation and maintenance compared to an equivalent set of single-rotor FOWTs. A final example is Nezzy[2], currently under development by EnBW and Aerodyn Engineering (EnBW, 2021b; Aerodyn Engineering, 2021). The system is composed of a two-rotor wind turbine supported by a light Y-shaped semi-submersible platform (EnBW, 2021a). A scaled prototype has been installed in the Bay of Greifswald in the Baltic Sea in 2020, showing good dynamic behavior under operational and storm conditions. A full-scale prototype is expected to be tested in China in the next years.

1.3   Objectives and Methodology

In view of the issues raised above, this thesis is intended to set a starting point for the dynamic analysis of two-rotor FOWTs. The aim is to give designers and standards organizations elements directed towards the definition of a baseline two-rotor FOWT design. The document is structured into two main parts. The first part of the thesis deals with the development and benchmark of a fully-coupled environment for the dynamic analysis of two-rotor FOWTs. The first associated section presents the general structure of the tool and the implementation of the external loads and servo systems by assuming rigid body dynamics and concentrated aerodynamic loads at the rotor hubs. This simplified method results in an efficient approach for the fast assessment of two-rotor FOWT prototypes. The second associated section presented the implementation of the complete system dynamics, the structural dynamics of tower and blades, and the aerodynamic loads acting on blades based on the BEM approach in an integrated environment. In the second part of the thesis, the tool is employed to perform design work and assess the dynamic response of two-rotor FOWT systems. In particular, the following sub-objectives have been defined and achieved:

1. To establish and benchmark a comprehensive fully-coupled tool for the dynamic analysis of two-rotor FOWTs. The tool should enable industry-standard fidelity and should be able to easily accommodate arbitrary platform and tower geometries and number of wind turbines used.

2. To analyze the global dynamic response of a two-rotor FOWT concept undergoing operational environmental conditions. The major dynamic aspects of the system should be highlighted.

3. To design and test a blade-pitch control algorithm suitable for two-rotor applications.

4. To investigate the long-term extreme response of a two-rotor FOWT concept. Simplified methods, such as the environmental contour method (ECM) and the modified environmental contour method (MECM), should be assessed to test their feasibility in two-rotor applications.

5. To compare the dynamic response of a two-rotor wind turbine mounted on different floating platform types. Elements aimed at the definition of an optimal platform type for two-rotor applications should be highlighted.

6. To analyze the dynamic response and loads of a two-rotor FOWT concept undergoing blade-pitch actuation faults.

1.4 Thesis Structure and Declaration of Authorship

The organization of the thesis structure is presented in Figure 1.3 and follows the order of the research objectives previously outlined. All the journal papers presented as the content of this thesis are co-authored. The contents of each chapter and authorship contribution for each publication are described in the following.

Chapter 2: The third chapter presents the first part of the development work of a tool for the fully-coupled analysis of innovative horizontal-axis floating wind turbine systems. This part of the development work deals with the definition of the general tool structure, the external loads acting on the system, and the servo systems. Major assumptions employed at this stage are 1) single rigid body dynamics, 2) simplified rotor dynamics to define the aerodynamic state of the system, and 3) concentrated aerodynamic loads computed by means of steady-state thrust and torque coefficients.

This chapter is partly published as:

El Beshbichi, O., Xing, Y., Ong, M.C. (2021). An Object-Oriented Method for Fully Coupled Analysis of Floating Offshore Wind Turbines through Mapping of Aerodynamic Coefficients. *Marine Structures*, 78:102979.

The PhD candidate is the first author of the paper and contributed to the work conceptualization, conducted the development work and the numerical simulations, post-processed the results, and wrote the main manuscript. Prof.

Yihan Xing, who is the second author, contributed to the work conceptualization, provided comments on the manuscript draft, supervision, and discussion of the results. Prof. Muk Chen Ong contributed to the work conceptualization, provided comments on the manuscript draft, supervision, and discussion of the results.

Chapter 3: The fourth chapter presents the second part of the development work of a tool for the fully-coupled analysis of innovative horizontal-axis floating wind turbine systems. This part of the development work deals with the inclusion of the full-system multi-body dynamics, the structural dynamics of tower and blades, and the distributed aerodynamic loads based on the blade-element momentum approach.

This chapter is under review as:

El Beshbichi, O., Xing, Y., Ong, M.C. (2021). Modelica-AeroDyn: Development, benchmark, and application of a comprehensive object-oriented tool for dynamic analysis of non-conventional horizontal-axis floating wind turbines. *Wind Energy.*

The PhD candidate is the first author of the paper and contributed to the work conceptualization, conducted the development work and the numerical simulations, post-processed the results, and wrote the main manuscript. Prof. Yihan Xing, who is the second author, contributed to the work conceptualization, provided comments to the manuscript draft, supervision, and discussion of the results. Prof. Muk Chen Ong contributed to the work conceptualization, provided comments on the manuscript draft, supervision, and discussion of the results.

Chapter 4: The fifth chapter presents the dynamic analysis of a two-rotor floating wind turbine concept.

This chapter is partly published as:

El Beshbichi, O., Xing, Y., Ong, M.C. (2021). Dynamic analysis of two-rotor wind turbine on spar-type floating platform. *Ocean Engineering,*

236:109441.

El Beshbichi, O., Xing, Y., Ong, M.C. (2021). Modelica-AeroDyn: Development, benchmark, and application of a comprehensive object-oriented tool for dynamic analysis of non-conventional horizontal-axis floating wind turbines. *Wind Energy*.

The PhD candidate is the first author of the paper and contributed to the work conceptualization, conducted the numerical simulations, post-processed the results, and wrote the main manuscript. Prof. Yihan Xing, who is the second author, contributed to the work conceptualization, provided comments to the manuscript draft, supervision, and discussion of the results. Prof. Muk Chen Ong provided comments on the manuscript draft, supervision, and discussion of the results.

Chapter 5: The sixth chapter presents the optimal control design of a two-rotor floating wind turbine concept.

This chapter is published as:

El Beshbichi, O., Xing, Y., Ong, M.C. (2022). Linear Quadratic Regulator Optimal Control of Two-Rotor Wind Turbine Mounted on Spar-Type Floating Platform. *Journal of Offshore Mechanics and Arctic Engineering*, 145(2):022001.

The PhD candidate is the first author of the paper and contributed to the work conceptualization, conducted the numerical simulations, post-processed the results, and wrote the main manuscript. Prof. Yihan Xing, who is the second author, contributed to the work conceptualization, provided comments to the manuscript draft, supervision, and discussion of the results. Prof. Muk Chen Ong provided comments on the manuscript draft, supervision, and discussion of the results.

Chapter 6: The seventh chapter presents the evaluation of the long-term extreme response of a two-rotor floating wind turbine concept by means of full long-term analysis and contour methods.

This chapter is published as:

El Beshbichi, O., Rødstøl, H., Xing, Y., Ong, M.C. (2022). Prediction of long-term extreme response of two-rotor floating wind turbine concept using the modified environmental contour method. *Renewable Energy*, 189:1133-1144.

The PhD candidate is the first author of the paper and contributed to the work conceptualization, provided supervision, and wrote the main manuscript. Henrik Rødstøl, who is the second author, conducted the numerical simulations and post-processed the results. Prof. Yihan Xing, who is the third author, contributed to the work conceptualization, provided comments to the manuscript draft, supervision, and discussion of the results. Prof. Muk Chen Ong provided comments on the manuscript draft, supervision, and discussion of the results.

Chapter 7: The eighth chapter presents a comparative dynamic analysis of a two-rotor floating wind turbine concept mounted on spar-type, semi-submersible, and TLP floating platforms.

This chapter is published as:

El Beshbichi, O., Xing, Y., Ong, M.C. (2022). Comparative dynamic analysis of two-rotor wind turbine on spar-type, semi-submersible, and tension-leg floating platforms. *Ocean Engineering*.

The PhD candidate is the first author of the paper and contributed to the work conceptualization, conducted the numerical simulations, post-processed the results, and wrote the main manuscript. Prof. Yihan Xing, who is the second author, contributed to the work conceptualization, provided comments to the manuscript draft, supervision, and discussion of the results. Prof. Muk Chen Ong provided comments on the manuscript draft, supervision, and discussion of the results.

Chapter 8: The ninth chapter presents the loads analysis of a two-rotor floating wind turbine concept undergoing blade-pitch faults.

This chapter is under review as:

El Beshbichi, O., Xing, Y., Ong, M.C. (2022). Load response of a two-rotor floating wind turbine undergoing blade-pitch system faults. *Wind Energy*.

The PhD candidate is the first author of the paper and contributed to the work conceptualization, conducted the numerical simulations, post-processed the results, and wrote the main manuscript. Prof. Yihan Xing, who is the second author, contributed to the work conceptualization, provided comments to the manuscript draft, supervision, and discussion of the results. Prof. Muk Chen Ong provided comments on the manuscript draft, supervision, and discussion of the results.

Chapter 10: The conclusions, original contributions to the PhD project, and the recommended future research are given in the last chapter.
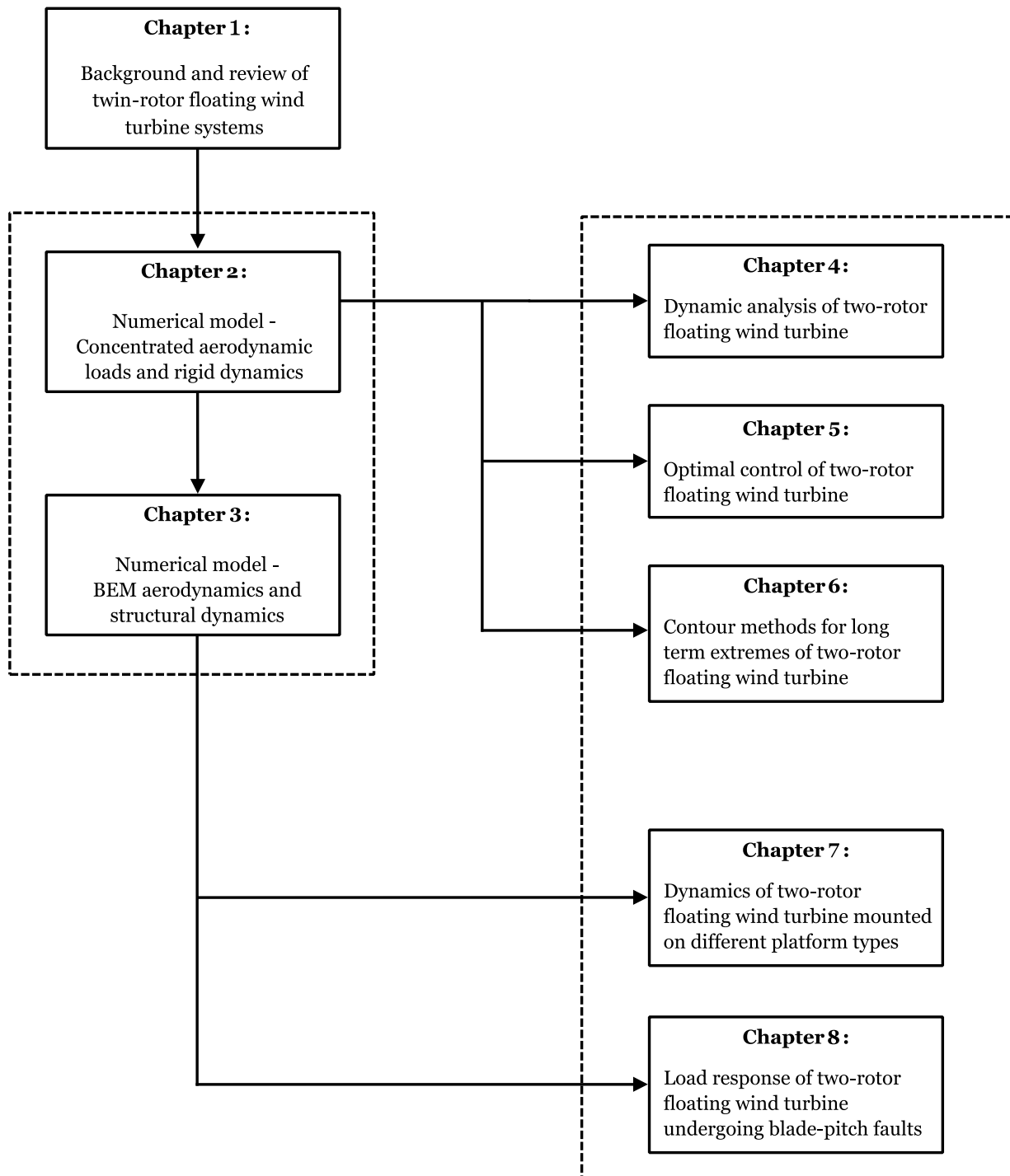
Figure 1.3: Structure of the present thesis.

Chapter 2

Numerical Model – Concentrated Aerodynamic Loads and Rigid Dynamics

Omar El Beshbichi [a], Yihan Xing [a], Muk Chen Ong [a]

[a] Department of Mechanical and Structural Engineering and Materials Science, University of Stavanger, Stavanger, Norway.

This content is partly published as:

2.1   Introduction

This chapter presents the first development stage of the thesis. This stage defined the general structure of the tool and implemented the hydrodynamic loads, the aerodynamic loads, the station-keeping loads, and the wind turbine servo systems. Major assumptions considered at this stage are 1) single rigid body dynamics, 2) simplified rotor dynamics used to determine the aerodynamic state of the system, and 3) concentrated aerodynamic loads computed by mapping the steady-state aerodynamic coefficients of the baseline NREL 5 MW wind turbine. This aerodynamic modeling approach presents itself as a viable alternative to more complex beam-element momentum (BEM) models or overly simplified approaches.

2.2   Methodology

2.2.1   Hydrodynamics

The following method is based on work by Jonkman (2009b), where validation and benchmark work can be found. Several assumptions are generally considered to simplify the hydrodynamic problem. The body displacements are assumed to be small, which is a valid assumption in most practical cases (Jonkman, 2007). Assuming small body displacements is necessary to linearize the hydrodynamic problem, take advantage of the superimposition principle, and employ incident wave models such as Airy wave theory (Newman, 1977; Faltinsen, 1993). The fluid is assumed inviscid and irrotational. The hydrodynamic problem can be split into hydrostatics, radiation, and diffraction. Added mass and added damping compose the radiative contribution, while external wave loads are associated with diffraction and Froude-Krylov loads (Faltinsen, 1993). The equations of motion of a rigid floater can be described as (Jonkman

et al., 2009):

$$[M]\ddot{\underline{q}} + [C]\underline{q} + C_{0,3} = -[A]_{inf}\ddot{\underline{q}} - \int_0^t [K(t-\tau)]\dot{\underline{q}}d\tau$$
$$+\underline{F}_{waves} + \underline{F}_{mooring} + \underline{F}_{drag} - [B]_{added}\dot{\underline{q}} + \underline{F}_g \tag{1}$$

where $\underline{q}$ denotes the floater rigid degrees of freedom (DoFs), $[M]$ and $[C]$ are, respectively, the inertia and hydrostatic matrices, $C_{0,3}$ is the buoyancy load from Archimedes' principle, $[A]_{inf}$ is the added mass matrix at infinite incident wave frequency, $[K]$ is the wave-radiation-retardation kernel matrix, $\underline{F}_{waves}$ are the loads from incident waves, $\underline{F}_{mooring}$ are the mooring system loads, $\underline{F}_{drag}$ are viscous drag loads, $[B]_{added}$ is the linear added damping matrix, and $\underline{F}_g$ are the gravitational loads.

Incident wave loads

The irregular wave elevation, ξ, can be defined as (Jonkman, 2007):

$$\xi(t) = \frac{1}{2\pi} \int_{-\infty}^{+\infty} W(\omega)\sqrt{2\pi S^{2-Sided}(\omega)}e^{j\omega t}d\omega \tag{2}$$

Equation (2) is an Inverse Fourier Transform (IFT) of the 2-Sided Wave PSD, $S^{2-Sided}(\omega)$, and results in a time realization. $W(\omega)$ is the Fourier Transform of a White Gaussian Noise (WGN) time realization, and can be defined in several ways. In this work, it is defined through the piecewise Box-Muller formulation (Box and Muller, 1958):

$$\begin{cases} W(\omega) = 0, & \text{if } \omega = 0 \\ W(\omega) = r(cos\phi + jsin\phi), & \text{if } \omega > 0 \\ W(\omega) = r(cos\phi - jsin\phi), & \text{if } \omega < 0 \end{cases} \tag{3}$$

where:

$$r = \sqrt{-2ln[U_1(|\omega|)]}$$
$$\phi = 2\,U_2(|\omega|)$$

(4)

where $U_1(\omega)$ and $U_2(\omega)$ are independent random samples defined on the unit interval (0,1). The 2-Sided Wave PSD is commonly defined by means of the JOint North Sea WAve Project (JONSWAP) spectra, based on the Pierson-Moskowitz spectra. They are defined in the design standard IEC 61400-3 (International Electrotechincal Commission, 2009).

The incident wave loads time realization, $\underline{F}_{waves}(t)$, is related to the wave elevation and defined as (Jonkman, 2007):

$$\underline{F}_{waves}(t) = \frac{1}{2\pi}\int_{-\infty}^{+\infty} W(\omega)\sqrt{2\pi S^{2-Sided}(\omega)}\underline{X}(\omega,\psi)e^{j\omega t}d\omega$$

(5)

where ψ is the heading angle, and $\underline{X}(\omega,\psi)$ is the vector of wave-excitation loads on the platform per unit wave amplitude. Figure 2.1 shows a wave amplitude time realization (in this case relative to H_s = 6 m and T_p = 10 s), and the comparison between the target JONSWAP power spectral density with the one associated with the time realization. The white gaussian noise contribution is clearly visible.

Regular waves can be implemented by defining the PSD of a sinusoidal wave of amplitude A and frequency ω^*:

$$\begin{cases} S_r^{1-Sided}(\omega) = 0, & \text{if } \omega \neq \omega^* \\ S_r^{1-Sided}(\omega) = \frac{(A/\sqrt{2})^2}{d\omega}, & \text{if } \omega = \omega^* \end{cases}$$

(6)

where $d\omega$ is the frequency resolution of the PSD.

Wave-Radiation Damping

The wave-radiation damping term, $\int_0^t [K(t-\tau)]\dot{\underline{q}}d\tau$, also called potential damping, is a convolution integral implementing memory effects of the platform in-
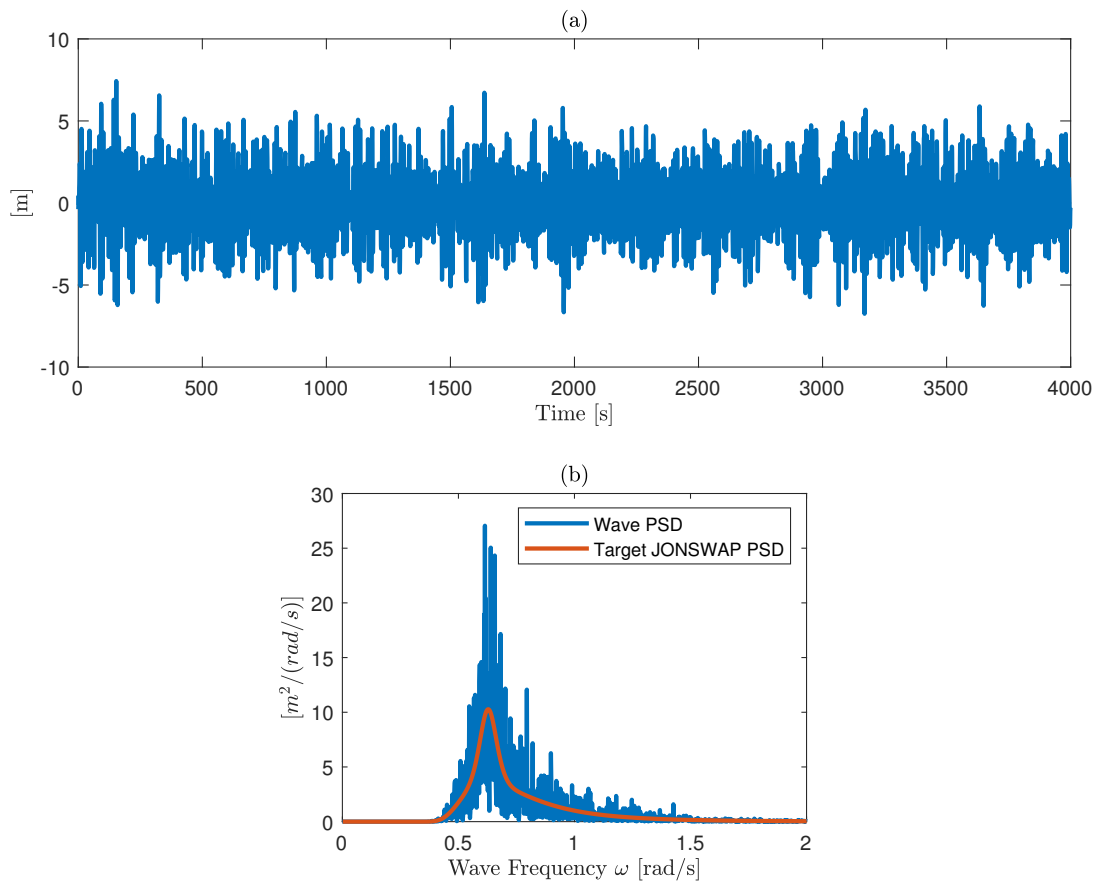
Figure 2.1: a) Wave elevation time realization. b) Wave power spectral density computed from time realization versus target JONSWAP power spectral density (H_s = 6 m and T_p = 10 s).

teracting with the fluid (Jonkman, 2007). The convolution representation was first proposed by Cummins (1962). If i and j are DOFs indices, the wave-radiation-retardation kernel $K_{ij}(t)$ represents the hydrodynamic load acting upon the platform in the direction i due to a unit platform velocity impulse in the direction j. The wave-radiation-retardation kernel matrix is commonly computed by an Inverse Cosine Transform (ICT) time realization of the frequency-domain damping matrix, $[B(\omega)]$:

$$[K(t)] = \frac{2}{\pi} \int_0^\infty [B(\omega)]cos(\omega t)d\omega \tag{7}$$

FAST-HydroDyn implements directly the convolution integral in the time-domain (Jonkman, 2007). However, the convolution term is inconvenient for simulation and for the analysis and design of motion control systems (Perez and Fossen, 2008). Because the convolution is a dynamic linear operator, it can be approximated by linear ordinary differential equations or state-space model. Kristiansen and Egeland (2003) have first proposed this approach for the approximation of convolution integrals in hydrodynamic modeling. Duarte et al. (2013) expanded HydroDyn with a state-space realization of the convolution term, SS-Fitting. An approximation of the ij convolution term, μ_{ij}:

$$\mu_{ij} \simeq \int_0^t K_{ij}(t - \tau)\dot{q}_{ij}d\tau \tag{8}$$

can be defined in the state-space form as:

$$
\begin{aligned}
\dot{\xi}_{ij} &= [\alpha]_{ij}\xi_{ij} + [\lambda]_{ij}\dot{q}_{ij} \\
\mu_{ij} &= [\theta]_{ij}\xi_{ij} + [\gamma]_{ij}\dot{q}_{ij}
\end{aligned} \tag{9}
$$

where $[\alpha]_{ij}, [\lambda]_{ij}, [\theta]_{ij}, [\gamma]_{ij}$ are the ij state-space matrices, and ξ_{ij} is the ij state vector. The matrices dimensions are, respectively, (mxm), $(mx1)$, $(1xm)$, and $(1x1)$, where m is the state-space approximation order. After proper matrix

assembly, the total state-space approximation can be defined as:

$$\dot{\underline{\xi}} = [\alpha]\underline{\xi} + [\lambda]\underline{\dot{q}}$$
$$\underline{\mu} = [\theta]\underline{\xi} + [\gamma]\underline{\dot{q}} \tag{10}$$

The final matrices dimensions are, respectively, $(36mx36m)$, $(36mx6)$, $(6x36m)$, and $(6x6)$. The state-space approximation implementation is based on the system identification scheme employing the Hankel SVD method, first proposed by Kung (1978). This scheme is implemented in MATLAB in the function IMP2SS (impulse to state-space) within the Robust Control Toolbox. If the input unit impulse-response is discrete, the output must be scaled with the time step, dt:

$$[\alpha]_{ij} = [\alpha]_{ij}$$
$$[\lambda]_{ij} = [\lambda]_{ij}$$
$$[\theta]_{ij} = [\theta]_{ij}dt \tag{11}$$
$$[\gamma]_{ij} = 0$$

where $[\gamma]_{ij}$ is forced to be zero in order to keep the causality of the system (Duarte et al., 2013).

This method allows for high accuracy but generally entails a high approximation order ($m > 200$). Consequently, the computational efficiency is reduced (Duarte et al., 2013). Hankel Singular Values (HSVs) are a measure of the "energy" associated with each state variable of a dynamic system (Machowski et al., 2012). The HSV distribution of the state-space approximation of the wave-radiation-retardation kernel follows a Pareto distribution. That is, a small number of states account for most of the total state energy. Figure 2.2 shows the HSV distribution for the state-space approximation of the surge-surge wave-radiation-retardation kernel, $K_{11}(t)$. Only a small set of states accounts for most of the impulse energy. For instance, the first two states account for 77.5 % of the total impulse energy. It is then possible to consider a limited subset of states for
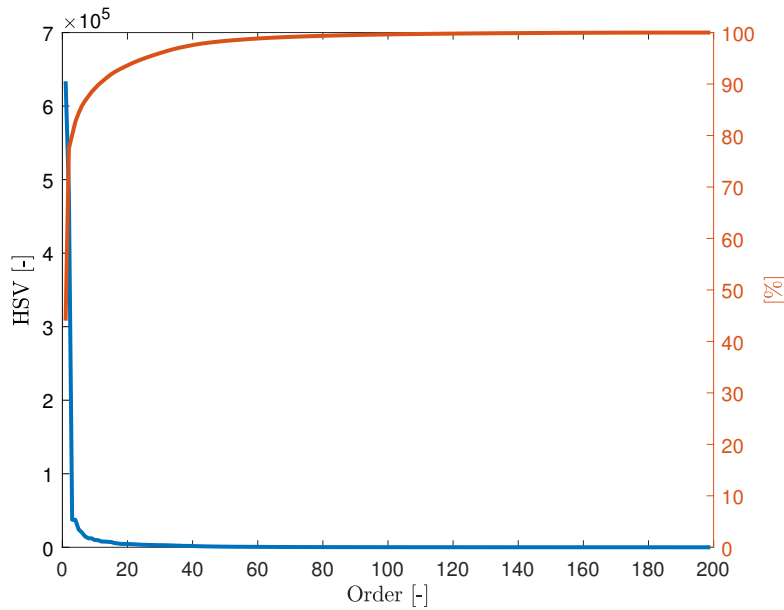
Figure 2.2: Hankel Singular Values distribution (HSVs) for the surge-surge wave-radiation-retardation kernel state-space approximation, $K_{11}(t)$.

the convolution approximation without losing accuracy. The model reduction is carried out in MATLAB by means of the function BALMR (balanced model reduction), which is based on truncation and Shur methods and implemented in Robust Control Toolbox (Kenney and Hewer, 1987; Kristiansen and Egeland, 2003).

Viscous Drag

In severe sea states, the hydrodynamic loads from linear potential flow theory may be augmented by a term accounting for flow separation (Jonkman, 2010). Morison's formulation, used in the analysis of fixed-bottom structures for offshore wind turbines, may be used to define viscous drag loads for cylindrical structures if 1) diffraction effects are negligible in severe sea states, 2) radiation damping is small, and 3) flow separation will occur in severe sea states (Jonkman, 2007). The fluid velocity in the platform surge and sway directions (1 for the surge direction, 2 for the sway direction) is defined from linear potential flow theory as (Faltinsen, 1993; Jonkman, 2007):

$$v_1(t, x, y, z) = \frac{cos\psi}{2\pi} \int_{-\infty}^{+\infty} W(\omega) \sqrt{2\pi S^{2-Sided}(\omega)}$$
$$e^{-jk(\omega)[x \cos \psi + y \sin \psi]} \frac{cosh[k(\omega)(z+h)]}{sinh[k(\omega)h]} e^{j\omega t} d\omega \tag{12}$$

$$v_2(t, x, y, z) = \frac{sin\psi}{2\pi} \int_{-\infty}^{+\infty} W(\omega) \sqrt{2\pi S^{2-Sided}(\omega)}$$
$$e^{-jk(\omega)[x \cos \psi + y \sin \psi]} \frac{cosh[k(\omega)(z+h)]}{sinh[k(\omega)h]} e^{j\omega t} d\omega \tag{13}$$

where h is the water depth and $k(\omega)$ is the wave number, defined through the following implicit equation (Faltinsen, 1993):

$$k(\omega)tanh[k(\omega)h] = \frac{\omega^2}{g} \tag{14}$$

The viscous drag load can be then defined as:

$$dF_i^{drag}(t, z) = \frac{1}{2}C_d\rho_{water}Ddz[v_i(t, 0, 0, z)] - \dot{q}_i(z)]$$
$$|\underline{v}(t, 0, 0, z) - \underline{\dot{q}}(z)| \tag{15}$$

where C_d is the drag coefficient, D is the spar diameter, dz is the vertical spar section height, and $i = 1$ or 2.

Preprocessing

Numerical-panel codes are generally employed to solve the frequency-domain hydrodynamic problem of floating platforms. The hydrodynamic quantities needed are the added mass matrix $[A(\omega)]$, linear damping matrix $[B(\omega)]$, and the vector of wave loads per unit wave amplitude, $\underline{X}(\omega, \psi)$. In this work, the frequency-domain hydrodynamic problem is solved by means of the industry-
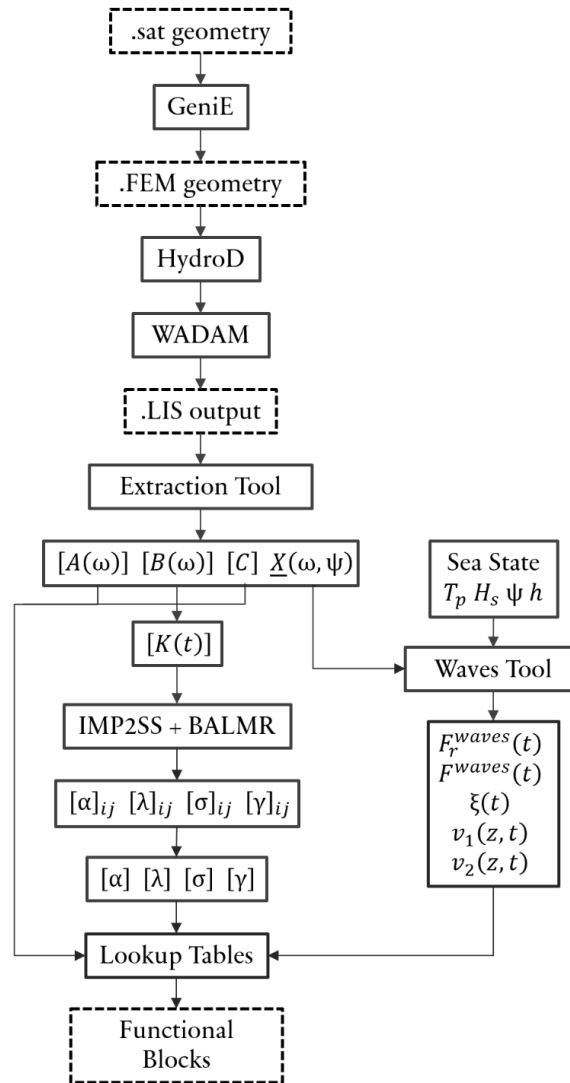
Figure 2.3: Hydrodynamic preprocessing workflow (see Section 2.2.1).

standard numerical-panel code WADAM, available within the DNV software SESAM (DNV, 2017). Figure 2.3 shows the preprocessing workflow. First, the wetted surface geometry, in general of arbitrary shape, is provided to the SESAM built-in CAD software GeniE. The extension *.sat* is compatible with the package and can be exported by most commercial CAD software. The geometry may also be developed directly in GeniE. Next, the frequency-domain hydrodynamic analysis is carried out in WADAM. All the hydrodynamic quantities are computed at the SWL. The resulting output file, with extension .LIS, is processed through an extraction tool developed for the purpose. The tool gives the hydrodynamic quantities in canonical form. The wave-radiation-retardation

kernel matrix is obtained from the frequency-domain damping matrix, $[B(\omega)]$. The state-space approximation of each kernel matrix component ij is carried out through the employment of the functions IMP2SS and BALMR within MATLAB. The single state-space matrices are assembled, giving rise to the final state-space formulation, $[\alpha]$, $[\lambda]$, $[\theta]$, and $[\gamma]$. A tool for the generation of wave quantities is also developed. Inputs of the tool are parameters describing the sea state (T_p, H_s, ψ, h) and the vector of wave-excitation loads on the platform per unit wave amplitude, $\underline{X}(\omega, \psi)$. Outputs of the tool are the time realizations of wave quantities (incident wave loads, wave amplitude, and horizontal fluid velocities). All the quantities thus defined are stored in lookup tables communicating with the modules in Modelica.

2.2.2   Mooring Lines

Station keeping of floating platforms is achieved by means of mooring lines. Modeling of the mooring loads acting at the platform fairlead is often achieved by means of either quasi-static or dynamic models (Cruz and Atcheson, 2016). Quasi-static models assume dynamic equilibrium of the mooring lines. This allows the description of station-keeping loads as a function of the fairlead position only. The dynamic approach allows for the account of local line dynamics. Dynamic models are used in later stages where higher accuracy is needed, as in the case of extreme responses and fatigue loads (Azcona et al., 2017). This work implements a quasi-static mooring model for taut or slack catenary mooring lines given its computational efficiency and sufficiently accurate results in the context of prototypal analysis (Masciola et al., 2013). In this formulation, the fairlead position is known from the global system dynamics, while the mooring tension is computed at each instant as lookup relationship. Figure 2.4 shows a schematization of a single mooring line. The implicit nonlinear formulation computes the horizontal and vertical loads at the fairlead point, H_F and V_F, as a function of the mooring stretching. Linear yaw stiffness is added to take into account the rigidity given by the mooring lines and bridles (Jonkman, 2009b). The formulation assumes a portion of the mooring line near the anchor point laying on the seabed, x_S. The mooring stretching is described by means of the
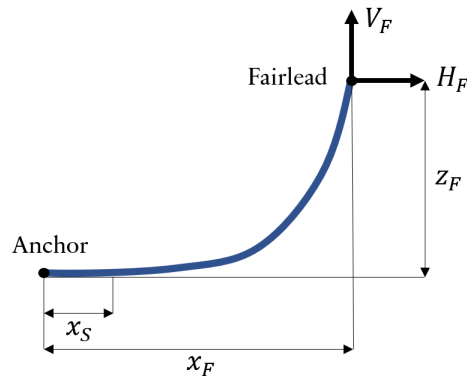
Figure 2.4: Mooring line schematization.

fairlead horizontal and vertical distance from the anchor point, x_F, and z_F. Figure 2.5 shows the mooring line load characteristic as a function of the fairlead horizontal and vertical distance from the anchor point. Both horizontal and vertical mooring loads experience a steep rise when the mooring line gets tauter - the nonlinear increment is particularly visible for horizontal distances higher than 90 % of the unstretched mooring line length. Assuming a fairlead vertical distance from the anchor point of about 250 m, the mooring line will be completely detached from the seabed ($x_S = 0$ m) if the horizontal fairlead distance from the anchor point exceeds 858.5 m.

2.2.3 Aerodynamics

Simplified Aerodynamics

Most numerical codes for the design FOWTs, such as FAST, HAWC2, and SIMA, employ the blade-element momentum theory to model aerodynamic loads. The aerodynamic loads acting on tower and blades are instantaneously computed from the integration of finite-element based drag and lift forces, allowing for very good response precision (Cruz and Atcheson, 2016). Simplified models are also used for feasibility and conceptual studies when the effects of rotor dynamics are negligible. Karimirad and Moan (2012a) investigated the response of a dynamic link library called TDHMill (Thrust-Dynamic-Horizontal-Mill), where the aerodynamic loads are defined as an overall concentrated thrust load act-
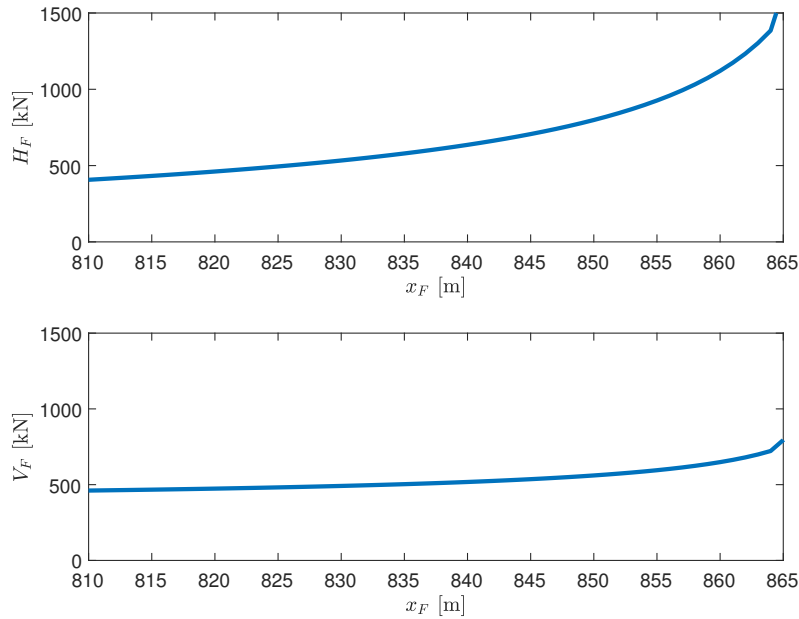
Figure 2.5: Mooring line load characteristic (unstretched length 902.2 m, mass density 77.71 kg/m, vertical length 250 m, diameter 0.09 m).

ing on the rotor hub. The response was compared with the HAWC2 BEM-based code, showing good agreement for operational conditions. Nielsen et al. (2008) analyzed the response of an integrated code for FOWTs loads employing similarly simplified aerodynamics. They compared the code response against experimental data, showing good agreement. Rotor dynamics, distributed aerodynamic loads, and detailed control dynamics are neglected. This type of simplified aerodynamics computes the thrust force acting on the hub as:

$$F = \frac{1}{2}\rho_{air}C_t(U_{rel})AU_{rel}^{\,2} \tag{16}$$

where ρ_{air} is the air density, C_t is the thrust coefficient, A is the total aera swept by the rotor, and U_{rel} is the relative velocity between the incoming wind flow and hub:

$$U_{rel} = U_{wind} - U_{hub} \tag{17}$$

U_{wind} and U_{hub} are local projections, transversal to the rotor plane, of the wind and hub velocities referred to the global reference frame. U_{wind} incorporates the 3-dimensional turbulent wind field at the hub. Figure 2.6 shows the thrust co-
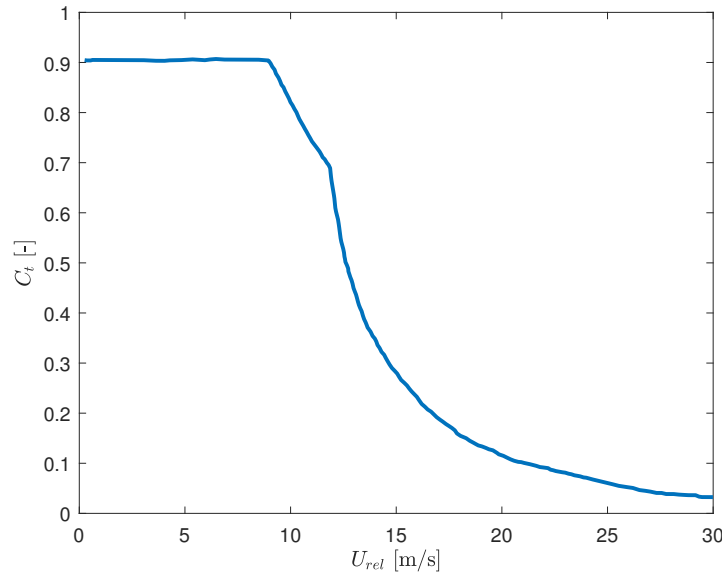
Figure 2.6: Thrust coefficient as function of relative wind velocity used in simplified aerodynamic codes (Nielsen et al., 2008).

efficient used in simplified aerodynamic codes. The thrust coefficient profile incorporates the effect of blade-pitch control. A notch filter on the tower velocity signal is also incorporated to consider resonant motions above the rated wind speed.

Steady-State Aerodynamics

This work implements steady-state rotor aerodynamics, including a simplified rigid-rotor EoM to define the aerodynamic state of the system. The rotor equation of motion is (Jonkman, 2007):

$$(I_{rotor} + \gamma^2 I_{generator})\dot{\omega}_{rotor} = T - \gamma T_{generator} \tag{18}$$

where I_{rotor} is the rotor inertia, $I_{generator}$ is the generator inertia, γ is the gearbox ratio, ω_{rotor} is the low-speed shaft rotational speed, T is the aerodynamic torque acting on the low-speed shaft, and $T_{generator}$ is the generator torque acting on the high-speed shaft. Table 2.1 shows the main drivetrain properties. $T_{generator}$ is a characteristic of the wind turbine, incorporating variable-speed torque control and given as a tabulated function of the generator rotational speed (Jonkman,

Table 2.1: Drivetrain properties NREL Baseline 5MW Wind Turbine (Jonkman, 2007).

I_{rotor}	kgm²	3.86×10^7
$I_{generator}$	kgm²	534.12
γ		97
$\omega_{generator,rated}$	rpm	1173.7

2007).

The aerodynamic loads acting on the system are composed of a concentrated thrust load at the hub and a torque acting on the rotor's low-speed shaft. The aerodynamic loads are defined by means of steady-state aerodynamic coefficients. The aerodynamic loads can be written as:

$$F = \frac{1}{2}\rho_{air}C_t(\lambda, \beta)A{U_{rel}}^2 \tag{19}$$

and:

$$T = \frac{1}{2}\rho_{air}RC_q(\lambda, \beta)A{U_{rel}}^2 \tag{20}$$

where β is the rotor-collective blade-pitch angle, R is the rotor radius, and λ is the tip speed ratio, defined as:

$$\lambda = \frac{\omega_{rotor}R}{U_{rel,filtered}} \tag{21}$$

where $U_{rel,filtered}$ is the low-pass filtered relative velocity between incoming wind and hub:

$$U_{rel,filtered} = U_{wind,filtered} - U_{hub} \tag{22}$$

The effective decoupling of the blade-pitch angle from the aerodynamics makes this method also suitable for the analysis of blade-pitch control strategies - not possible with simplified tools such as TDHMill. The aerodynamic coefficients are steady-state quantities. In order to avoid unrealistic fluctuations, the wind velocity used to define λ accounts for relatively steady velocity
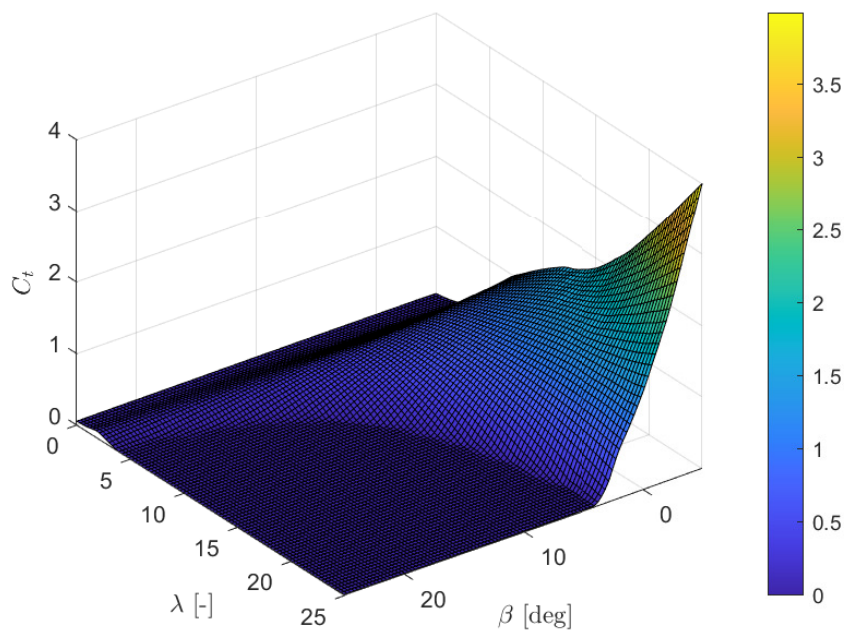
Figure 2.7: Thrust coefficient (NREL 5MW Baseline Onshore Wind Turbine).

variations by filtering out high-frequency content. The wind velocity profiles are obtained through the NREL code TurbSim. The turbulence model considered is the standard Kaimal. An IEC Class B normal turbulence model (NTM) is used. The steady-state aerodynamic coefficients are obtained through the NREL code FAST for the NREL 5 MW baseline wind turbine. AeroDyn v15 is used to solve the aerodynamic loads. A steady wind profile is used (WindType = 1). A time step of 0.001 s is used. The rotor is assumed to be rigid (CompElast = 1). A steady blade airfoil aerodynamic model is used (AFAeroMod = 1). Blade-pitch control is deactivated. A batch analysis is carried out in order to collect the aerodynamic profiles of the coefficients. λ is varied between 0 and 25, and β between -5° and 25°. Figures 2.7 and 2.8 show the obtained thrust and torque coefficients, respectively.

The modeling of aerodynamic loads by means of steady-state coefficients naturally leads to unavoidable limitations. Aerodynamic effects induced by unsteady dynamic motions are neglected, such as the effects given by the dynamic inflow, the rotor yaw motion, and the airfoil spatial orientation of the blades. This method is generally suitable to assess only the overall dynamic response
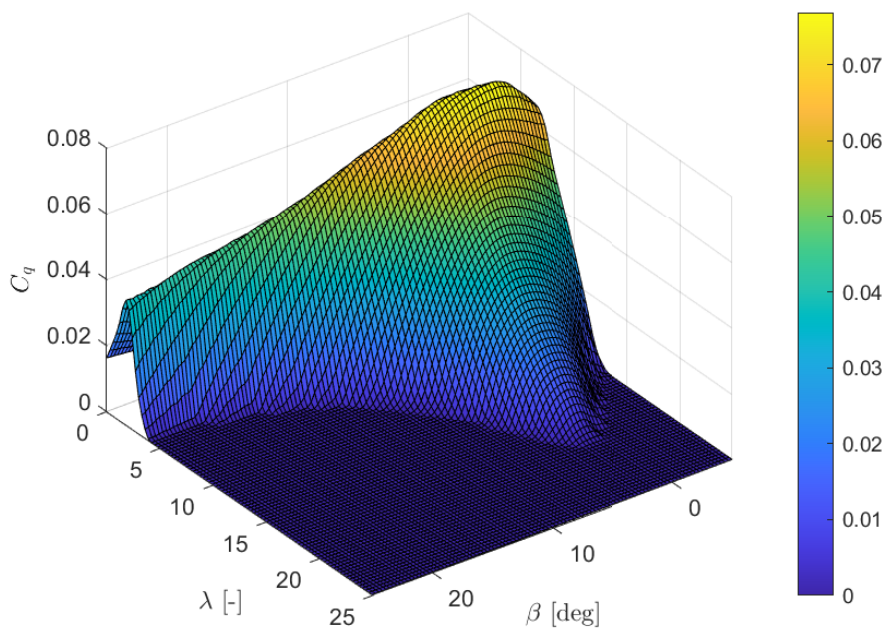
Figure 2.8: Torque coefficient (NREL 5MW Baseline Onshore Wind Turbine).

of FOWTs and leads to accurate results only when considering operational environmental conditions (Karimirad and Moan, 2012a).

2.2.4 Servo System

Control of variable-speed wind turbines is achieved by regulating blade-pitch angles and generator torque (Bossanyi, 2000). Control is generally divided into four regions as a function of the control objective:

- Region 1. Below cut-in wind speed. In this region, no generator torque allows drivetrain acceleration for start-up.

- Region 2. Between cut-in wind speed and rated wind speed. In this region, aerodynamic power is optimized by regulating generator torque.

- Region 3. Between rated and cut-out wind speed. In this region, generator speed is maintained equal to the rated value by actuating blade-pitch angles. Generator torque control allows for either constant electric power output or constant generator torque.

Table 2.2: Major class specialization types.

Models	Deploy classes, generic in nature, into a specific instance
Functions	Algorithmic imperative sections within the declarative Modelica environment
Connectors	Exchange variable information among functional blocks
Packages	Organize complex class hierarchies

- Cut-off region. Above cut-out wind speed. In this region, blades are fully pitched for parking the wind turbine by disrupting the aerodynamic loads.

The blade-pitch angle β is commonly computed by means of a rotor-collective PI control on the error between the generator rotational speed and its rated speed value. The control system is based on the baseline NREL 5 MW wind turbine PI controller (Jonkman, 2007). If the generator rotational speed error is defined as:

$$f = (\omega_{generator} - \omega_{generator,rated}) \tag{23}$$

the blade-pitch angle can be computed as:

$$\beta = K_p(\beta)f + K_I(\beta) \int_0^t f dt \tag{24}$$

where $K_p(\beta)$ and $K_I(\beta)$ are the proportional and integral gain-scheduling, respectively. The gains vary to account for a reduction of aerodynamic power sensitivity to blade-pitch angles (Jonkman, 2007).

2.2.5   Modelica

Modelica packages are organized as a set of hierarchically-structured reusable classes. Simple code structures can be used as fundamental classes and deployed in the definition of complex classes. Specializations may be assigned to general classes. Table 2.2 lists the major class specialization types with a brief description of their functionality. Classes deployed in a model are called functional blocks in this work. Functional blocks are characterized by input/output

connectors that allow the exchange of functional quantities. Each functional block is semi-independent, meaning that it only needs the definition of the necessary input quantities to be operative. The object-oriented nature of this approach allows for great flexibility - once the code structure is developed, modeling can be achieved graphically. The same code functionality can be employed in a virtually unlimited number of physical configurations. Specific models are constructed by the deployment of functional blocks. Models are generally used for the compilation of specific analysis cases. Versions of Modelica and Open-Modelica used in this work are, respectively, v3.2.3 and v1.16.2. Figure 2.9 shows the diagram view of the Phase IV OC3 simplified model implemented in Modelica. All the major functional blocks and their interactions are depicted.

2.3 Development

2.3.1 Baseline Design

The baseline single-rotor spar-type NREL 5 MW Phase IV OC3 design is used throughout the tool development process (Jonkman et al., 2009; Jonkman, 2010). This design has been extensively studied by researchers in the last decade and literature focusing on its dynamic response is plenty (for reference see Cruz and Atcheson (2016)). Moreover, the OC3 design is by default implemented in FAST v8, resulting in reasonably straightforward benchmark studies. Figure 2.10 shows a schematization of the NREL 5 MW baseline wind turbine. Major properties of the design are listed in Table 2.3. Tower properties are adjusted for floating deployment (Jonkman, 2010). Figure 2.11 depicts the Phase IV OC3 spar-type platform geometry. The platform is characterized by a draught of 120 m, and a center of gravity (CoG) depth from the sea water level (SWL) of about 89.92 m. Station-keeping is achieved by means of three catenary mooring lines. Table 2.4 summarizes the geometrical, inertial, and hydrostatic properties of the system.

Figure 2.12 shows a top-view schematization of the mooring system employed in the Phase IV OC3 platform. The angle δ is equal to $30°$. Three independent mooring lines are considered, installed at $120°$ from one another. The
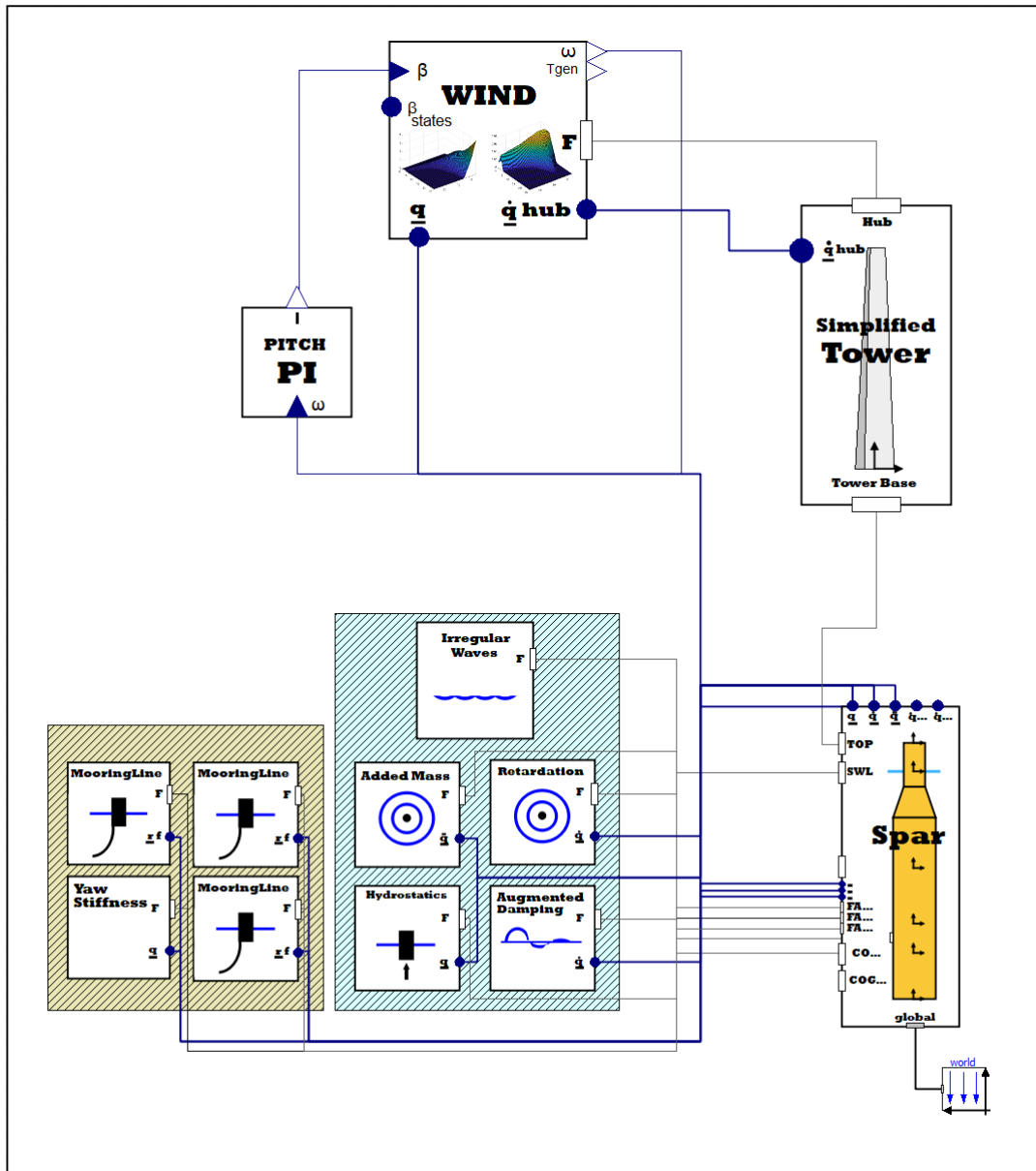
Figure 2.9: Diagram view of the Phase IV OC3 simplified model implemented in Modelica.
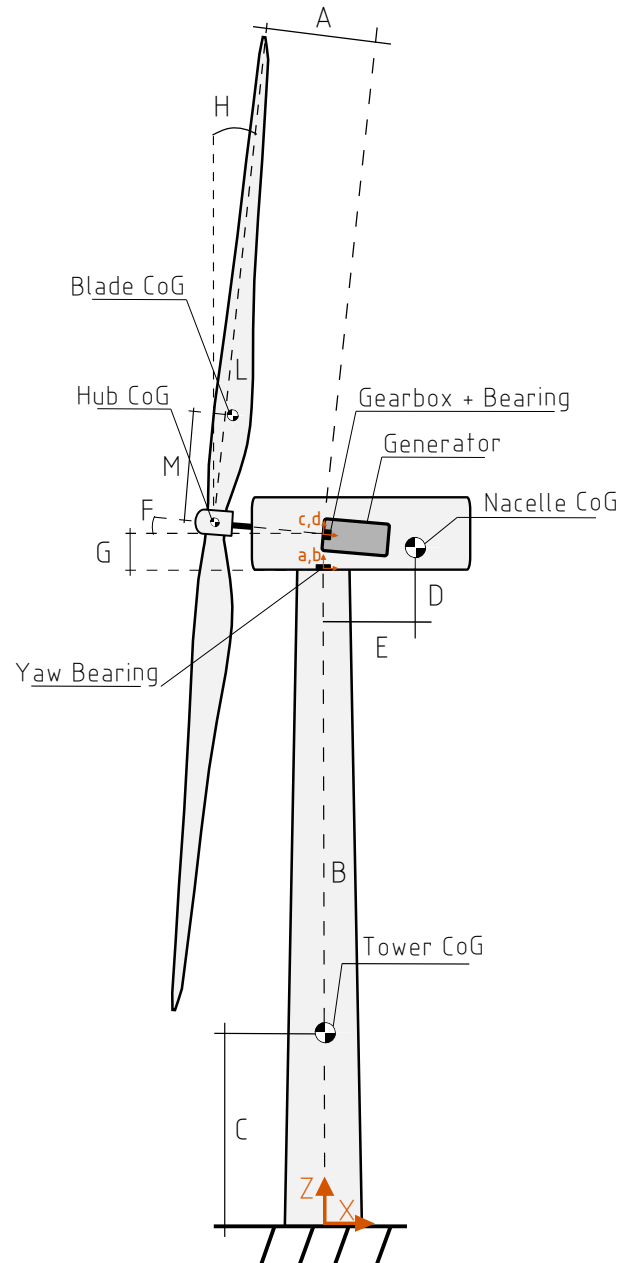
Figure 2.10: NREL 5 MW baseline wind turbine.

Table 2.3: NREL 5 MW Baseline Wind Turbine Specifications (tower adjusted for floating deployment) (Jonkman et al., 2009; Jonkman, 2010).

Rating		MW	5
Rotor Orientation, Configuration			Upwind, 3 Blades
Control			Variable Speed, Collective Pitch
Drivetrain			High Speed, Multiple-Stage Gearbox
Cut-In, Rated, Cut-Out Wind Speed		m/s	3, 11.4, 25
Cut-In, Rated Rotor Speed		rpm	6.9, 12.1
Rotor, Hub Diameter	P	m	126, 3
Hub Height (w.r.t tower base)	O	m	80
Overhang	A	m	5
Tower Height (w.r.t tower base)	B	m	77.6
Tower CoG Z-axis Location (w.r.t tower base)	C	m	33.4
Nacelle CoG X-axis Location	D	m	1.9
Nacelle CoG Z-axis Location	E	m	1.75
Drivetrain Shaft Tilt	F	deg	5
Distance Z-axis from Yaw Bearing to Shaft	G	m	1.96
Precone	H	deg	2.5
Blade Length (w.r.t blade root)	L	m	61.5
Distance between blade root and rotor axis		m	1.5
Blade CoG Location (w.r.t blade root)	M	m	20.650
Blade Mass		kg	1.75×10^4
Rotor Mass		kg	1.10×10^5
Nacelle Mass		kg	2.40×10^5
Tower Mass		kg	2.49×104^5
Blade Moment of Inertia (w.r.t blade root)		kgm²	1.17×10^7
Nacelle Moment of Inertia (w.r.t Z-axis)		kgm²	2.60×10^6
Generator Moment of Inertia (w.r.t shaft)		kgm²	5.34×10^2
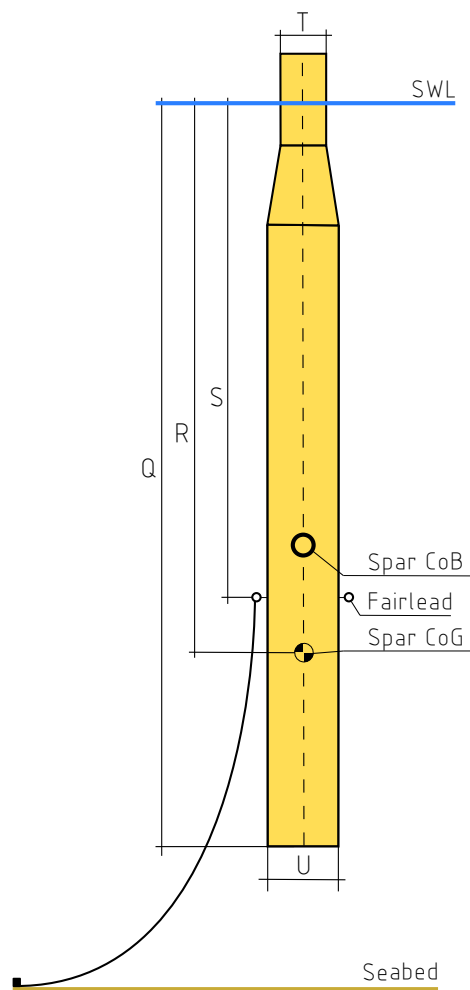
Figure 2.11: Phase IV spar-type OC3 geometry.

Table 2.4: Phase IV OC3 spar-type platform specifications (Jonkman et al., 2009; Jonkman, 2010).

Draught	Q	m	120
Depth to CoG	R	m	89.92
Depth to fairlead	S	m	70
Diameter	T-U	m	6.5 to 9.4 (tapered)
Water Displacement		m^3	8029
Mass (including ballast)		kg	7.4×10^6
Roll Moment of Inertia about CoG		kgm^2	4.2×10^9
Pitch Moment of Inertia about CoG		kgm^2	4.2×10^9
Yaw Moment of Inertia about Centerline		kgm^2	1.6×10^8
Number of mooring lines		-	3
Angular distance between adjacent mooring lines		deg	120
Unstretched line length		m	902.2
Static mooring line horizontal length		m	848.67
Radius to fairlead		m	5.2
Line diameter		m	0.09
Line mass density		kg/m	77.71
Mooring Line Weight in Water		N/m	698.09
Mooring Line Extensional Stiffness		N	3.8×10^8
Yaw Spring Mooring Stiffness		Nm/rad	9.8×10^7
Water Depth		m	320
Water Density		kg/m^3	1025
Drag Coefficient		-	0.6
Heave Hydrostatic restoring stiffness		N/m	3.3×10^5
Roll Hydrostatic restoring stiffness		Nm/rad	1.3×10^9
Pitch Hydrostatic restoring stiffness		Nm/rad	1.3×10^9
Surge added linear damping		N/(m/s)	1×10^5
Sway added linear damping		N/(m/s)	1×10^5
Heave added linear damping		N/(m/s)	1.3×10^5
Yaw added linear damping		Nm/(rad/s)	1.3×10^7

Figure 2.12: Phase IV OC3 mooring lines schematization (top-view).

unstretched mooring line length is about 902.2 m. The static mooring line horizontal length, l_0, is about 848.67 m, while the static mooring line vertical length, v_0, is about 250 m (Jonkman, 2010). The horizontal and vertical distance of the fairleads from the anchor points need to be defined to determine the mooring loads. To this end, the fairleads displacements in the platform surge and sway directions computed from the global system dynamics (r_{ij}, where i is the ith mooring line and j is the jth direction) can be projected in the mooring lines local directions. The effective horizontal distances of the fairleads from the associated anchor points can be written as:

$$x_{F,i} = l_0 + \Delta_1(i)r_{i1} + \Delta_2(i)r_{i2} \tag{25}$$

where:

$$\Delta_1(i) = \begin{cases} sin\delta, & \text{if } i = 1 \\ sin\delta, & \text{if } i = 2 \\ -1, & \text{if } i = 3 \end{cases} \tag{26}$$

and:

$$\Delta_2(i) = \begin{cases} cos\delta, & \text{if } i = 1 \\ -cos\delta, & \text{if } i = 2 \\ 0, & \text{if } i = 3 \end{cases} \tag{27}$$

The effective vertical distances of the fairleads from the associated anchor points are determined through the vertical fairleads displacements:

$$z_{F,i} = v_0 + r_{i3} \tag{28}$$

The mooring line horizontal loads, referred to the mooring line local reference frames, need to be referred to the fairlead global reference frame. The transformation can be expressed as:

$$\begin{cases} H_{Fi,1} = \Delta_1(i)H_{Fi} \\ H_{Fi,2} = \Delta_2(i)H_{Fi} \end{cases} \tag{29}$$

where $H_{Fi,1}$ is the i-th mooring line horizontal load projected in the platform surge direction. Vertical mooring line loads do not need any transformation.

2.3.2 Single Rigid Body Dynamics

Standard code from the multibody Modelica Standard Library is used to implement the system dynamics. A rigid body with mass and inertia tensor is used to define the equations of motion of the full system. Five frame connectors are defined, three at the fairlead locations, i.e., where mooring lines loads are applied, one at the COG location, i.e., where hydrostatic restoring loads are applied, and one at the SWL location, i.e., where the linear hydrodynamic loads are applied. The body is referred to the global reference frame, placed at the seabed location, by means of a free motion joint, where the system states are initialized. The body velocity in the platform surge and sway directions as a function of water depth ($\dot{\underline{q}}_1(z)$ and $\dot{\underline{q}}_2(z)$) are computed through a two-point linear interpolation.

2.3.3 Hydrodynamics

Five modules are used to define the hydrodynamic loads, one for each load component. Each hydrodynamic module makes use of a single frame connector where the associated load is applied. Hydrodynamic loads must be applied in the same reference frame used by the panel-code to solve the linear hydrodynamic problem. The default frame used in WADAM is at the SWL. Modules are fed by the associated platform state information, i.e., q, $\dot{q}$, and $\ddot{q}$, and loads are applied to the platform. FAST v8 hydrostatics separates the contribution of body weight from the contribution given from hydrostatic restoring as the global CoG may be subjected to significant displacements given by structural flexibility (Jonkman et al., 2009). This effect has been assumed negligible. As a consequence, hydrostatic quantities are defined as overall metacentric height relationships (Faltinsen, 1993), and hydrostatic loads are applied to the global CoG of the system.

Linear Relationships

Input state vectors ($\underline{q}$, $\underline{\dot{q}}$, or $\underline{\ddot{q}}$) are exchanged from the platform module to each hydrodynamic loads functional block. The related linear loads are obtained by scaling the input state vector with the associated matrix. Loads are defined as external forces and resolved globally. All linear hydrodynamic load contributions need to be applied at the location where the frequency-domain hydrodynamic problem is solved, i.e., at the SWL. Hydrostatic relationships are applied at the COG as hydrostatic restoring torques are also defined through metacentric height relationships. The total buoyancy force from Archimedes' principle is implemented by means of a static world force directed upwards and resolved globally.

Wave-Radiation Damping

The wave-radiation damping functional block is implemented by means of the Modelica standard state-space module, solving a state-space system given the input vector. State-space variables are initialized at zero. The input vector is

set equal to the input velocity state vector, $\underline{\dot{q}}$. All the loads are defined as world forces and resolved globally.

Incident Wave Loads

Lookup tables in the time domain are used to compute the incident wave loads. Modelica standard lookup modules allow for linear-periodic interpolation. Lookup start time is set to 0.1 s to aid the integrator initialization process. A continuous-derivative smoothness of table interpolation is used.

Viscous Drag

Time realizations of the water velocity fields in platform surge and sway directions, varying with water depth, are implemented by means of lookup tables in the time domain. Morison's definition of drag loads included the variation of platform diameter. The platform discretization step, dz, is set equal to 1 m.

2.3.4   Mooring Lines

The quasi-static mooring load module uses a single frame connector where the mooring load at the fairlead is applied. Lookup tables in two dimensions are used to compute the horizontal and vertical load components as a function of the fairlead horizontal and vertical position. The variation of the vertical mooring loads as a function of farilead position is implemented as an optional feature. The module is generalized to account for arbitrary mooring configurations. The angle between the surge direction and the mooring line axis (positive counterclockwise) is considered, and four cases (one for each plane quadrant) are implemented to adjust horizontal mooring load projections. Trigonometric load projections account for high platform surge displacements, i.e., they account for cases where surge displacement is big enough to significantly affect layout angles. The following equations hold for mooring configurations within the sec-

ond plane quadrant:

$$H = \sqrt{\left(H_0 cos\beta\right)^2 + \left(H_0 sin\beta + u[1]\right)^2}$$

$$F_x = F\frac{H_0 sin\beta + u[1]}{H} \qquad\qquad (30)$$

$$F_y = F\sqrt{1 - \left(\frac{H_0 sin\beta + u[1]}{H}\right)^2}$$

where H is the mooring line length, H_0 is the static mooring line length, β is the angle between the mooring line angle and the sway axis, $u[1]$ is the platform surge displacement, F is the horizontal mooring load at the fairlead, and F_x and F_y are, respectively, the horizontal mooring loads at the fairlead projected in surge and sway direction. The additional yaw stiffness module implements a linear relationship between platform yaw motion and yaw restoring moment due to station-keeping. The restoring moment is applied in the frame at fairlead depth in the platform centerline. Mooring loads are applied to the system at time 0.1 s to aid the integrator initialization process.

2.3.5 Tower

The simplified tower module is used to define a reference frame local to the rotor hub. The hub velocity vector, $\underline{\dot{q}}_{hub}$, is exchanged from the simplified tower functional block to the aerodynamic module.

2.3.6 Steady-State Aerodynamics

Table look-up in two dimensions is carried out to compute the aerodynamic thrust and torque coefficients given the tip speed ratio, λ, and the rotor-collective rotor-pitch angle, β. Time realizations of the wind turbulent velocity field, obtained in TurbSim, are implemented by means of lookup tables in the time domain. The input state vector, $\underline{q}$, is exchanged from the platform functional block to the aerodynamic functional block to project the wind and hub ve-

locity transversal to the rotor plane. The filtered turbulent wind velocity needed to compute λ is implemented by means of a lowpass butterworth filter with a cut-off frequency set to 0.0033 Hz (5 minutes cut-off period). Table lookup in one dimension is carried out to compute the generator torque given the generator rotational speed. The rotor-collective blade-pitch angle β is exchanged from the PI control functional block to the aerodynamic functional block. Conversely, the generator speed, $\omega_{generator}$, is exchanged from the aerodynamic functional block to the PI control functional block. The thrust force is defined as external force and resolved locally to the hub. A smooth initialization of the aerodynamic module is implemented by adjusting initial values of λ and thrust force. λ is imposed equal to 1 for the first 5 s of the analysis. The thrust force is set equal to 0 N for the first 2 s of the analysis, and equal to $2x10^5$ N for the next 200 s.

2.3.7 Servo Systems

The blade-pitch PI control and variable-speed torque control modules implement servo algorithms in a manner similar to the NREL FAST baseline control system (Jonkman et al., 2009). FAST models implement their controllers as an external Dynamic Link Library (DLL) in the DNV Bladed code style (DNV, 2021). The blade-pitch PI control module uses input and output real variable connectors for the feeding of the generator speed and rotor-collective blade pitch angle signals. Low pass filter of the generator speed is implemented by means of a butterworth filter. A range limiter is used to saturate the total blade pitch angle signal, and a slew rate limiter is used to implement the blade pitch rate saturation. The variable-speed generator torque module implements the low pass filter of generator speed, the saturation of generator torque, and the saturation of generator torque rate in a similar fashion to the blade-pitch PI control module. Definition of generator speed regions is implemented in a manner similar to the Bladed-style DLL controller (see Appendix C in Jonkman et al. (2009)).

Table 2.5: Summary of the modeling capabilities of the major codes used in the code-to-code comparative analysis (Jonkman et al., 2010; Cruz and Atcheson, 2016; Leimeister et al., 2020). (T: Turbine. P: Platform. Mod: Modal dynamics. MBS: Multi-Body System. FE: Finite-Element. SS: Steady-State. QS: Quasi-Static. BEM: Blade Element/Momentum. PF: Potential Flow. ME: Morison's Equation.)

	Developer	Structural Dynamics	Aerodynamics	Hydrodynamics	Mooring Dynamics	Identifier
Present Model	-	T: Simplified P: Rigid	SS	PF + ME	QS	■
FAST	NREL	T: Mod/MBS P: Rigid	BEM	PF + ME	QS	■
Simo-Riflex	MAR-INTEK	T: FE P: FE	BEM	PF + ME	FE	■
HAWC2	DTU	T: MBS/FE P: MBS/FE	BEM	ME	FE	■
Bladed	DNV	T: Mod/MBS P: Rigid	BEM	PF + ME	QS	■

2.4 Numerical Setup

The integration method used is the standard *dassl*, with a tolerance equal to $1x10^{-6}$ and time step equal to 0.1 s. The time step is associated with a Nyquist-bounded maximum dynamic frequency of 5 Hz, higher than the system natural frequencies and therefore suitable to cover the rigid body dynamics.

2.5 Benchmark

In this section, a code-to-code comparative analysis is performed by contrasting the dynamic responses of major design codes against the dynamic response of the present model.

Table 2.5 summarizes the modeling capabilities of the major codes used in the validation analysis. Modeling capabilities are described in terms of methods for structural dynamics, aerodynamics, hydrodynamics, and mooring dynamics

Table 2.6: Load cases (LCs) used in code-to-code comparative analysis, based on IEA Phase IV (Jonkman et al., 2010).

	Wind Conditions	Wave Conditions	Type
1.2	None: air density = 0	Still Water	Eigenanalysis
1.4	None: air density = 0	Still Water	Free-decay test time series
4.1	None: air density = 0	Regular Airy: H_s = 6 m, T_p = 10 s	Periodic time series
4.1[*]	None: air density = 0	Regular Airy: H_s = 2 m, T_p = *variable*	RAOs
4.2	None: air density = 0	Irregular Airy: H_s = 6 m, T_p = 10 s, JONSWAP spectrum	Power spectra
5.1	Steady, uniform, no shear: V_{hub} = 8 m/s	Regular Airy: H_s = 6 m, T_p = 10 s	Periodic time series
5.3	Turbulent: V_{hub} = 18 m/s, I = 0.18	Irregular Airy: H_s = 6 m, T_p = 10 s, JONSWAP spectrum	Power spectra

modeling. The load cases (LCs) used for the analysis are based on the standard International Energy Agency (IEA) Wind Task 23, Phase IV (Jonkman et al., 2010; Leimeister et al., 2020). The main reference code used for the comparative analysis is NREL FAST. The comparison is carried out in terms of eigenvalue analysis, free-decay time series tests, and time series and power spectra associated with different load conditions.

Table 2.6 outlines the load cases used in the comparative analysis. The eigenvalue analysis is performed by linearizing the system in the neighbourhood of its static equilibrium position when neither wind nor wave is acting (system stationary in still water). A drag coefficient C_d= 0 is used for free-decay analysis. The total simulation time is set to 600 s. The values of H_s and T_p in LC 4.1[*] are employed in order to compute the RAOs of the system. RAOs are frequency response functions defined as the ratio of a given DOF response amplitude to a given regular wave amplitude. RAOs are used in the offshore oil

and gas industry to assess the frequency-domain linear wave-body response of floating platforms. RAOs of spar-buoy platforms are significant only in platform surge, heave, and pitch directions. OC3-Hywind RAOs computed by means of NREL FAST-HydroDyn are used as main reference (Ramachandran et al., 2013; SeaFEM, 2018; Lin et al., 2019). Regular waves are employed to compute the RAOs (LC 4.1*). For each wave period considered, the hydrodynamic loads related to a 1 m amplitude regular wave are applied to the system. Because the procedure is based in the time-domain and only a limited number of wave periods is considered, the obtained RAOs are discrete. A drag coefficient C_d= 0 is used. The first 600 s are not considered in order to discard initial transients. In order to compute the PSDs of the system response to irregular waves and turbulent wind (LC 4.2 and LC 5.3), a simulation time of 4000 s is carried out. The first 400 s are not considered to discard initial transients so that a net 1-h simulation time is used in the analysis. A 15th order one-dimensional median filter is used to smooth the PSD responses.

2.5.1   Wind-Wave Dynamic Response

Figures 2.13 and 2.14 present an example of dynamic response of the system subjected to irregular waves and turbulent wind in terms of platform surge and pitch response. The dynamic loading of the system is relative to JONSWAP irregular airy waves (H_s = 6 m and T_p = 10 s), and turbulent wind (V = 18 m/s, I = 0.167). The figures present time series at the SWL and smoothed PSDs based on 1-h time history in the case of turbulent wind, constant wind, and wave-only conditions. Mean displacement values of the system can be inferred from the time histories. PSDs distribution clearly highlights energy peaks at platform surge, pitch, and wave excitation frequencies.

2.5.2   LC 1.2 - Full-System Eigenanalysis

Figure 2.15 shows the natural frequencies of the rigid motions of the system calculated through eigenvalue extraction. Most of the codes agree in their prediction, except for higher platform roll/pitch natural frequency computed with
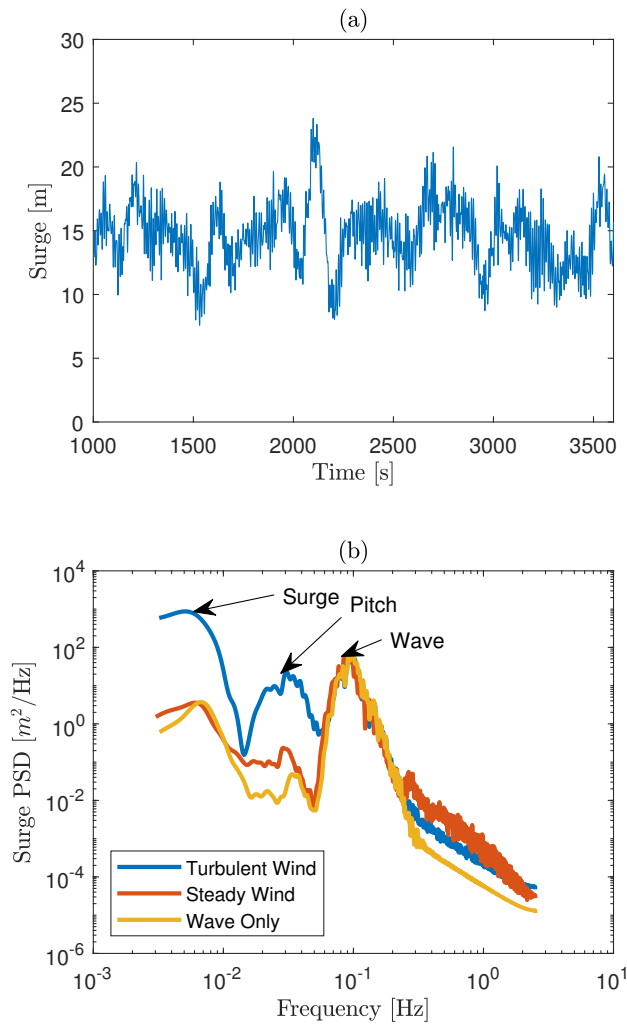
Figure 2.13: Surge response for coupled wave-wind analysis. a) Surge time history at SWL for irregular waves and turbulent wind (JONSWAP H_s = 6 m and T_p = 10 s, V = 18 m/s, I = 0.167). b) Surge smoothed power spectral densities based on 1-h time history in the case of turbulent wind, constant wind, and wave-only conditions.
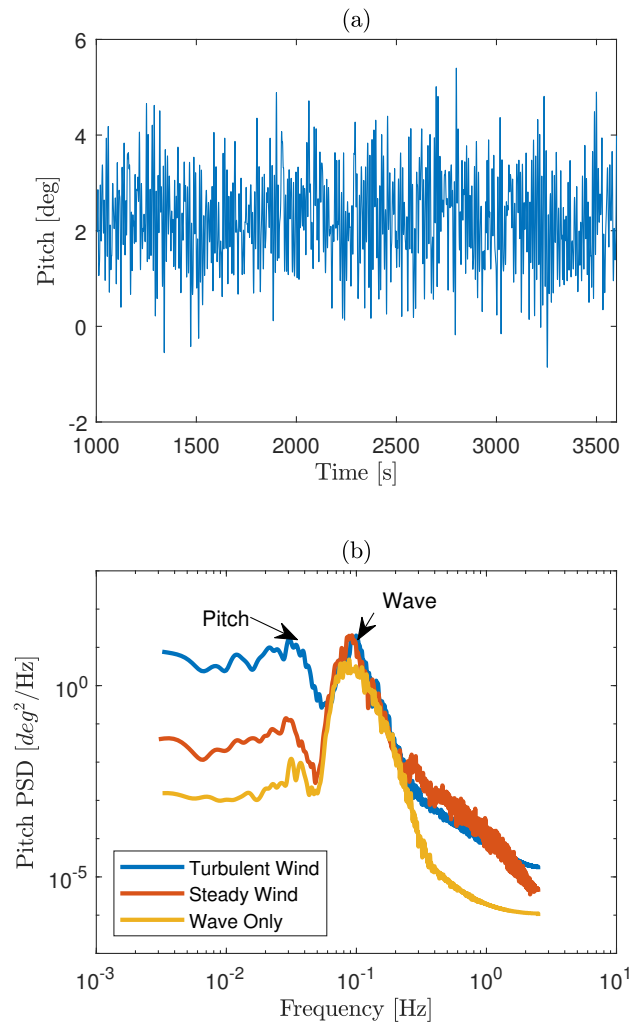
Figure 2.14: Pitch response for coupled wave-wind analysis. a) Pitch time history at SWL for irregular waves and turbulent wind (JONSWAP H_s = 6 m and T_p = 10 s, V = 18 m/s, I = 0.167). b) Pitch smoothed power spectral densities based on 1-h time history in the case of turbulent wind, constant wind, and wave-only conditions.
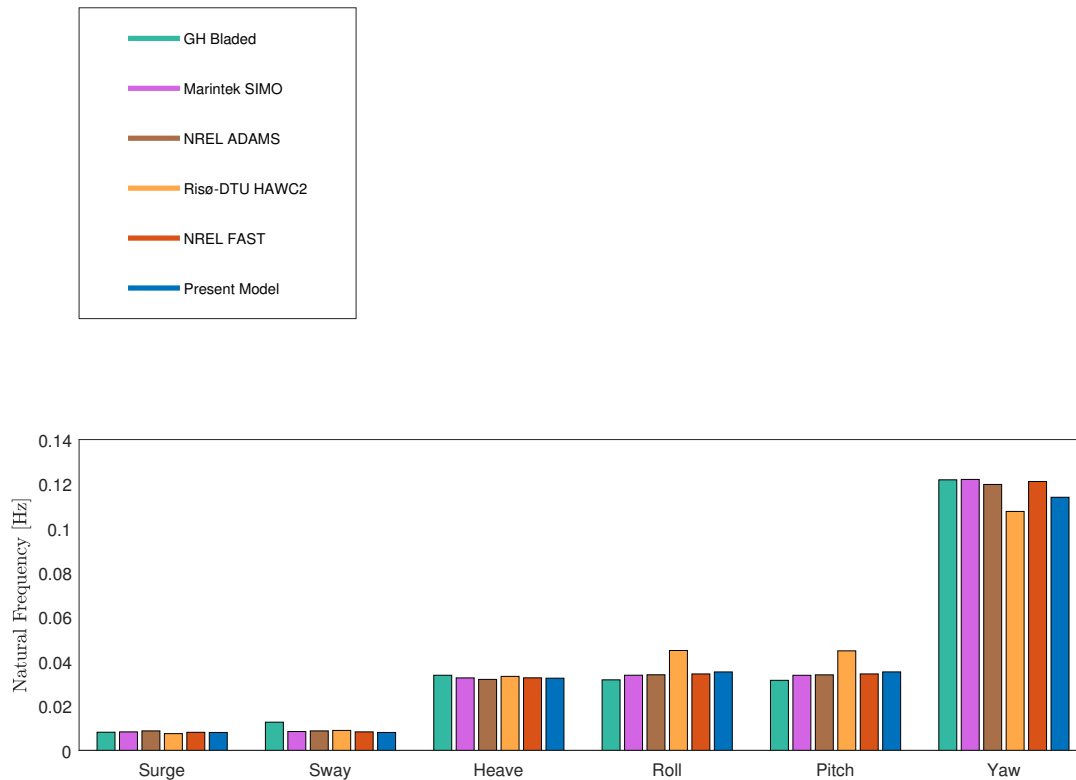
Figure 2.15: Full-system hydro-elastic natural frequencies from LC 1.2 (Jonkman et al., 2010; Leimeister et al., 2020)

HAWC2. Results obtained from present model are in good agreement with most codes and match very well with the results obtained from the main reference, NREL FAST.

2.5.3 LC 1.4 - Free Decay

Figure 2.16 shows the free decay time series comparison in platform heave, pitch, and surge directions. The free-decay time series obtained from present model are compared against NREL FAST and other codes whose free decay responses are available. A certain degree of variability is to be expected among responses obtained through different design codes. For the platform surge free-decay test, most of the codes agree well with each other. POSTECH FAST shows less hydrodynamic surge damping. This discrepancy is due to the lack of additional linear damping in POSTECH results (Jonkman et al., 2010). Results obtained from present model agree very well with FAST results. For the platform

Table 2.7: Natural frequencies of the OC3-Hywind floating wind turbine obtained from present model through free decay tests.

	Natural frequency [Hz]
Surge/Sway	0.0081
Pitch/Roll	0.035
Heave	0.0314
Yaw	0.122
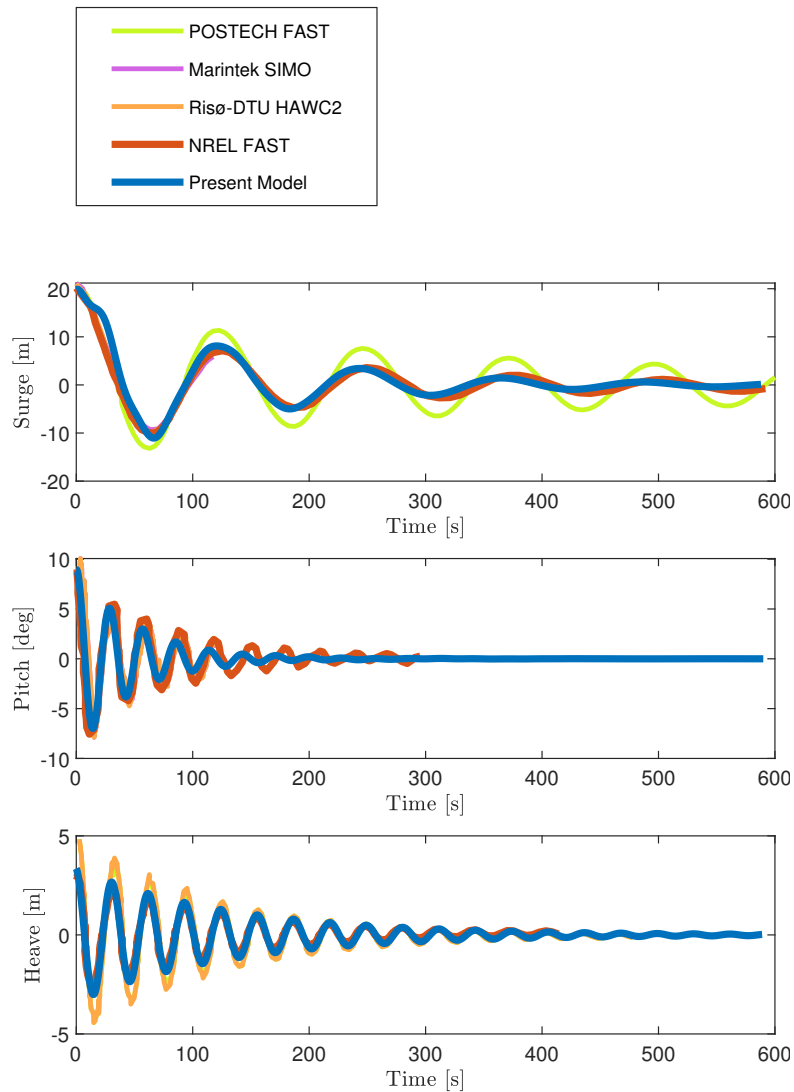
Figure 2.16: OC3-Hywind free decay time series comparison in platform heave, pitch, and surge directions from LC 1.4 (Jonkman et al., 2010; Leimeister et al., 2020).
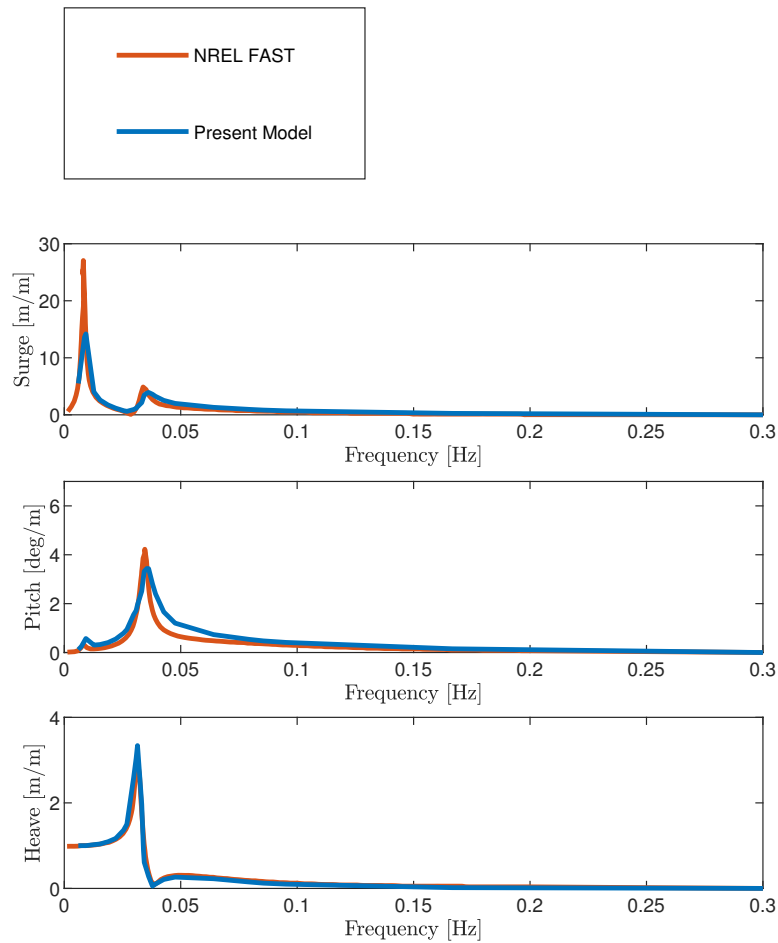
Figure 2.17: Response amplitude operators from LC 4.1* (Ramachandran et al., 2013).

pitch free-decay test, most codes agree. Present model results show a slight difference of platform pitch natural frequency with respect to results obtained with FAST - about 2.5 % higher from the present model. The difference is reasonably limited (δ: 9e-4 Hz, *min*: 0.0316 Hz, *max*: 0.0448 Hz, σ: 0.0047 Hz). For the platform heave free-decay test all codes agree, except HAWC2 results which show less hydrodynamic damping. Table 2.7 shows the natural frequencies of the OC3-Hywind system obtained in the present model through free decay tests. The results agree with eigenanalysis.

2.5.4   LC 4.1* - Response Amplitude Operator (RAO)

Figure 2.17 shows the RAOs comparison in platform heave, pitch, and surge motions. The blue line represents the discrete RAOs obtained from present model. The red line represents the main reference RAOs obtained from FAST-HydroDyn (Jonkman, 2010; Ramachandran et al., 2013). RAOs computed in present model and the ones computed from FAST are in good agreement. The platform heave RAO approaches unity in the quasi-static region, which is a good quality check for RAOs estimation and agrees well with the reference. Platform pitch-surge coupling is clearly visible and is correctly detected both in platform surge and pitch motions. A marginally higher amplitude response is experienced in present model in the upper-resonance region, which is most likely associated with the minor shift in the platform pitch natural frequency between the two codes.

2.5.5   LC 4.1 - Hydro-Elastic Response with Regular Waves

Figure 2.18 shows the time series of platform surge, pitch, and heave motions, and downstream fairlead tension (mooring line #3 - see Figure 2.12) under conditions given in LC 4.1. All of the platform initial transients obtained from all codes are removed from the results. All codes agree except HAWC2 platform surge response, which may simply have output the wrong parameter (Jonkman et al., 2010). SIMO results are phase-shifted relative to the other codes. Present model response agrees very well with NREL FAST response.

2.5.6   LC 4.2 - Hydro-Elastic Response with Irregular Waves

Figure 2.19 shows the power spectral densities for the same parameters used in Figure 2.18, computed under conditions given in LC 4.2. All codes removed initial transients from the results. A net 1-h simulation time history is used in the PSD computation. Spectral shape estimates obtained from present model
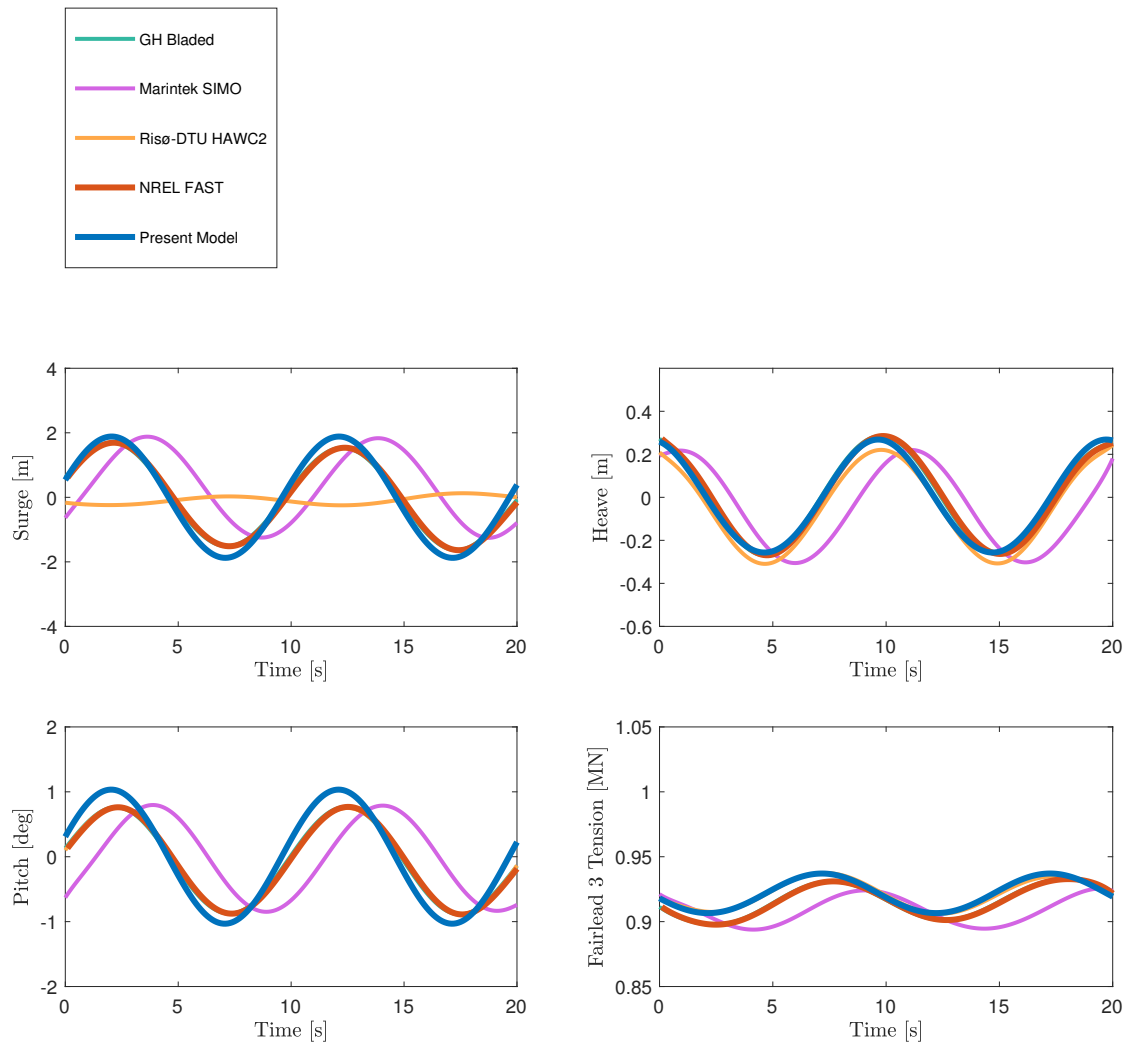
Figure 2.18: Hydro-elastic time series with regular waves from LC 4.1 (Jonkman et al., 2010; Leimeister et al., 2020).
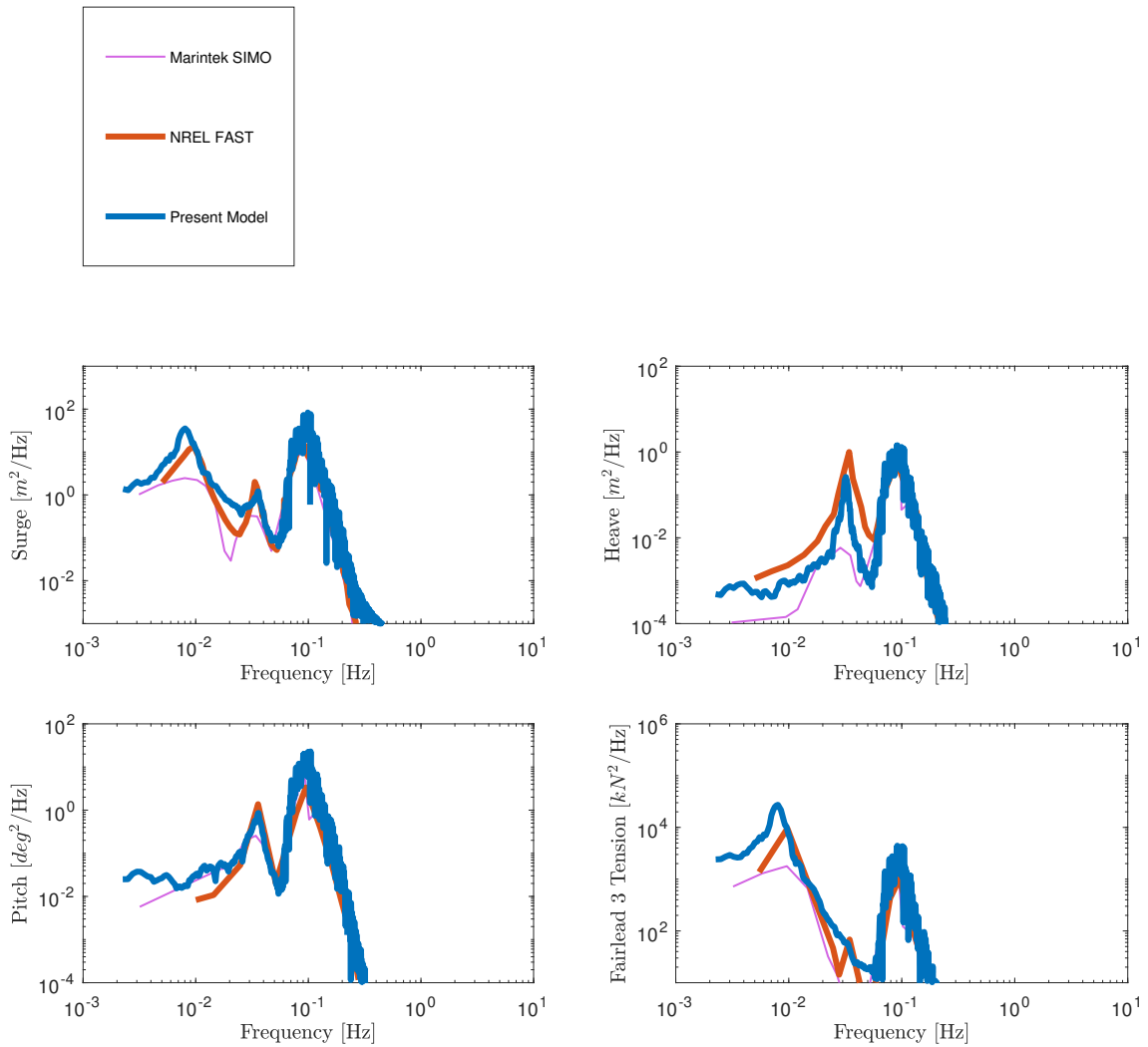
Figure 2.19: Hydro-elastic power spectral densities with irregular waves from LC 4.2 (Jonkman et al., 2010; Leimeister et al., 2020).

agree well with the main reference FAST. Wave energy is mainly distributed at wave excitation frequency, i.e., 0.1 Hz. The distribution of energy at platform surge, pitch, and wave frequencies obtained with present model agrees well with NREL FAST.

2.5.7 LC 5.1 - Fully-Coupled Response with Regular Waves

Figure 2.20 shows the time series of platform surge, pitch, heave, and yaw motions, and downstream and upstream fairlead tensions (mooring line #2 and #3 - see Figure 2.12) under conditions given in LC 5.1. Thrust associated with the steady wind causes nonzero mean loads and displacements. SIMO results are phase-shifted relative to the other codes. For the platform surge displacement, all codes except HAWC2 agree well on the oscillation amplitude. The mean platform surge displacement varies slightly among codes. The mean platform surge displacements obtained with SIMO and with present model are in a similar fashion slightly higher than the same results obtained from FAST. These differences are, however, reasonably limited (δ = 1.5 m, *min*: 8.37 m, *max*: 15.10 m, σ: 2.66 m). The significant difference in platform yaw response among codes is clearly visible in the figure. Present model platform yaw response is significantly lower than the response obtained from FAST. The difference is due to the simplified rotor dynamics assumptions employed in the present model. Lack of platform pitch-yaw coupling given by rotor gyroscopic effects leads to significant difference in platform yaw dynamics.

2.5.8 LC 5.3 - Fully-Coupled Response with Irregular Waves

Figure 2.21 shows the PSDs for the same parameters used in Figure 2.20, computed under conditions given in LC 5.3. Initial transients from the results obtained from all codes are removed. A net 1-h simulation time history is used in the PSD computation relative to present model. Spectral shape estimates obtained from present model, given in terms of distribution of energy at plat-
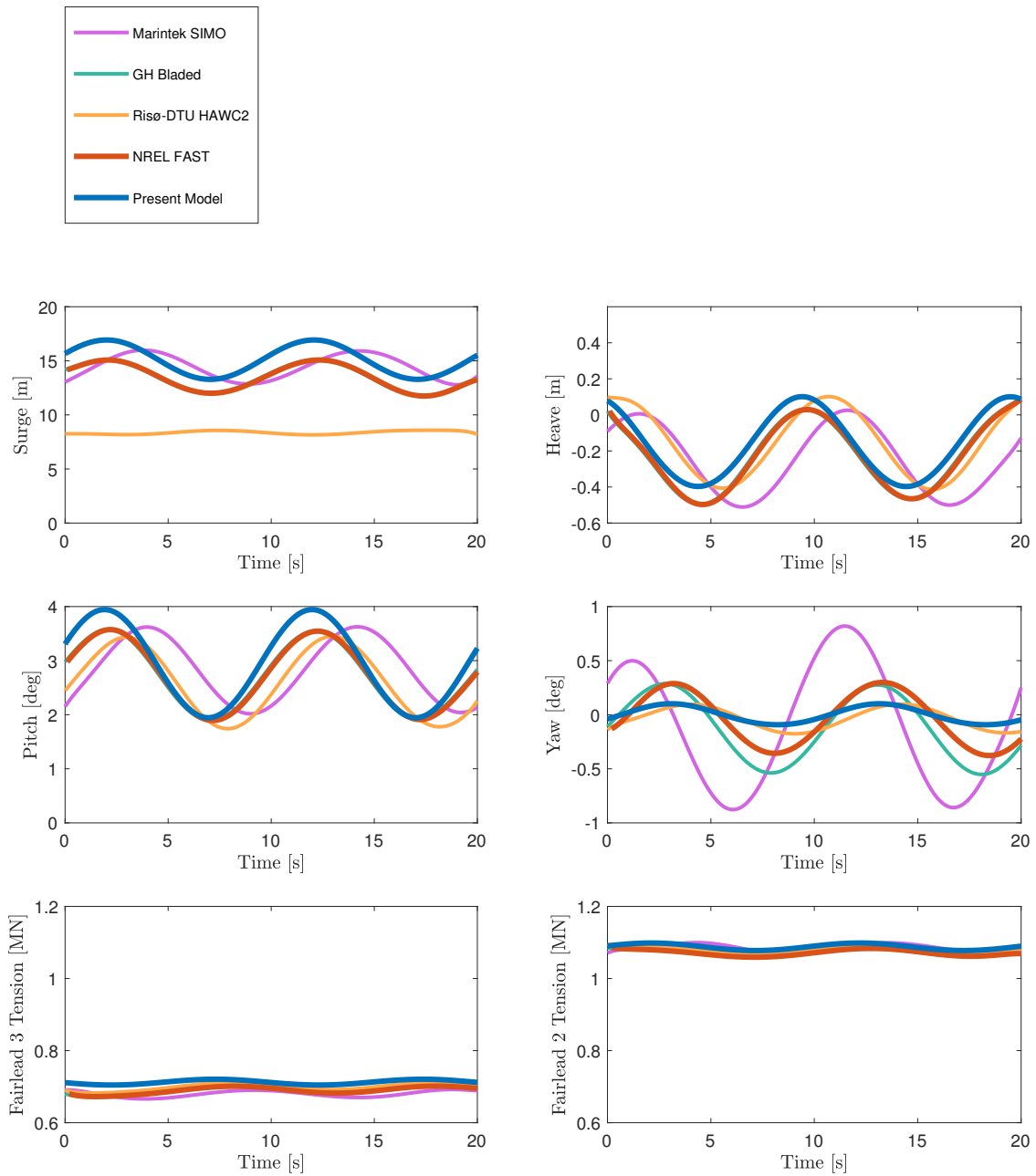
Figure 2.20: Fully-coupled time series with regular waves and steady wind from LC 5.1 (Jonkman et al., 2010; Leimeister et al., 2020).
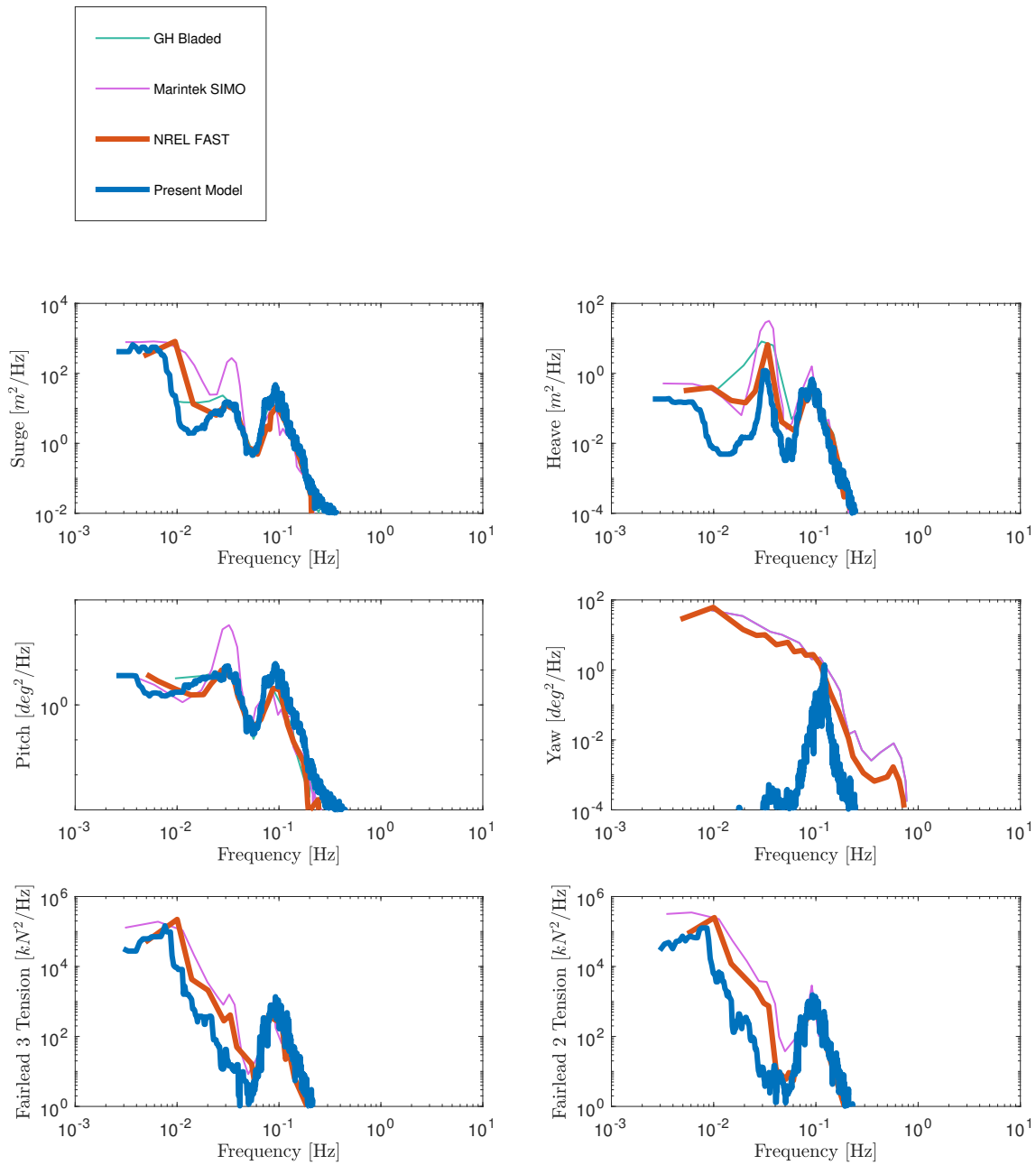
Figure 2.21: Fully-coupled power spectral densities with irregular waves from LC 5.3 (Jonkman et al., 2010; Leimeister et al., 2020).

form surge, pitch, and wave frequencies, agree well with those obtained from FAST. As previously noted in LC 4.2, wave energy is highest at wave excitation frequency, i.e., 0.1 Hz, and most are in good agreement on wave energy distribution. Wind energy is mainly distributed in the low-frequency region, corresponding to the highest energy of the wind (Jonkman et al., 2010). Platform yaw response deviates significantly due to simplified rotor dynamics. The low-frequency platform yaw response is negligible in present model due to the lack of platform pitch-yaw coupling induced by the rotor dynamics. The high-frequency platform yaw response is negligible in present model, also affected by the lack of drivetrain dynamics. Platform yaw dynamics is then effectively decoupled from the overall wind-induced response in the present model, and the energy content in the platform yaw PSD is mainly associated with the wave loads. Therefore, platform yaw inaccuracy should be considered as one of the major limitations of this method when considering OC3-Hywind applications.

2.6   Conclusions

This chapter presented a novel object-oriented approach to model the fully-coupled dynamic response of floating offshore wind turbines (FOWTs). The code accounts for hydrodynamic loads, station-keeping loads, aerodynamic loads, and servo systems in an integrated environment. The key features offered by the method are the following:

1. Its structure naturally allows for easy implementation of arbitrary platform geometries and platform/rotor configurations.

2. The analysis time is significantly faster than that of standard codes and results are accurate in situations where rotor dynamic contribution is negligible.

3. An extremely flexible modeling environment is offered by the object-oriented nature of Modelica. Moreover, the current modeling facility used for code development is open-source and is naturally suitable for code sharing.

The aerodynamic model computes the aerodynamic loads through the mapping of steady-state aerodynamic coefficients. This modeling approach can be placed at the intersection between simplified aerodynamic methods, such as TDHMill, and full beam-element momentum aerodynamic methods. Aerodynamic loads are composed of a concentrated thrust and a concentrated torque. The thrust acts at the hub, while the torque is applied at the rotor low-speed shaft of a simplified rigid rotor equation of motion (EoM) used to account for the rotor response. Code-to-code benchmark considered the response of the Phase IV OC3 system to standard load cases, resulting in a good agreement. The next chapter will present the development of a complete multi-body dynamics environment, the structural dynamics of tower and blades, and blade-element momentum aerodynamic load capabilities.

Chapter 3

Numerical Model – BEM Aerodynamic Loads and Structural Dynamics

Omar El Beshbichi [a], Yihan Xing [a], Muk Chen Ong [a]

[a] Department of Mechanical and Structural Engineering and Materials Science, University of Stavanger, Stavanger, Norway.

3.1 Introduction

This chapter presents the second development stage of the thesis. This stage defined the structural dynamics of tower and blades and the aerodynamic loads acting on blades based on the blade-element momentum approach.

The slender geometry of blades and tower allows to assume them as flexible beams with mass and stiffness continuously varying along their span. Major methods based on classical beam theory used to model the structural dynamics of wind turbine blades and tower are 1) the assumed modes (AM) formulation (also called normal mode summation method) (Jonkman, 2003), 2) the finite element (FE) formulation, and 3) the multibody (MB) formulation (also called lumped parameter formulation). The AM method describes the elastic flexibility of beam structures by considering a truncated vibration mode series. This method is computationally efficient and allows for sufficient accuracy. FAST relies on AM for blades and tower structural dynamics modeling. However, AM requires accurate re-processing of modal quantities each time the structural system is modified. The FE method divides the structure into finite elements specifying the local stress and deformation field (Liu and Quek, 2014). DNV Bladed uses a FE formulation for structural dynamics modeling (DNV, 2021). Examples of Modelica implementation of flexible beams by means of the FE formulation are present in literature (Ferretti et al., 2005; Murua et al., 2006). FE procedure is the most accurate, but the implementation procedure is cumbersome and computationally demanding. In this work, the system dynamics and structural dynamics are modeled by means of an MB-based approach, and the MSL multi-body environment is employed. Further information concerning the MB approach employed can be found in Section 3.2.2.

Full blade-element momentum capabilities are achieved by integrating into Modelica the well-established aerodynamic module AeroDyn v15 and wind-profile processor InflowWind developed by NREL and utilized within FAST. FAST v8 (Fatigue, Aerodynamics, Structures, and Turbulence) is a comprehensive open-source tool written in Fortran 90 and used for the fully-coupled aero-hydro-servo-structural analysis of two and three bladed horizontal-axis wind turbines (HAWTs) (Jonkman and Buhl, 2005). OpenFAST, a new version of the
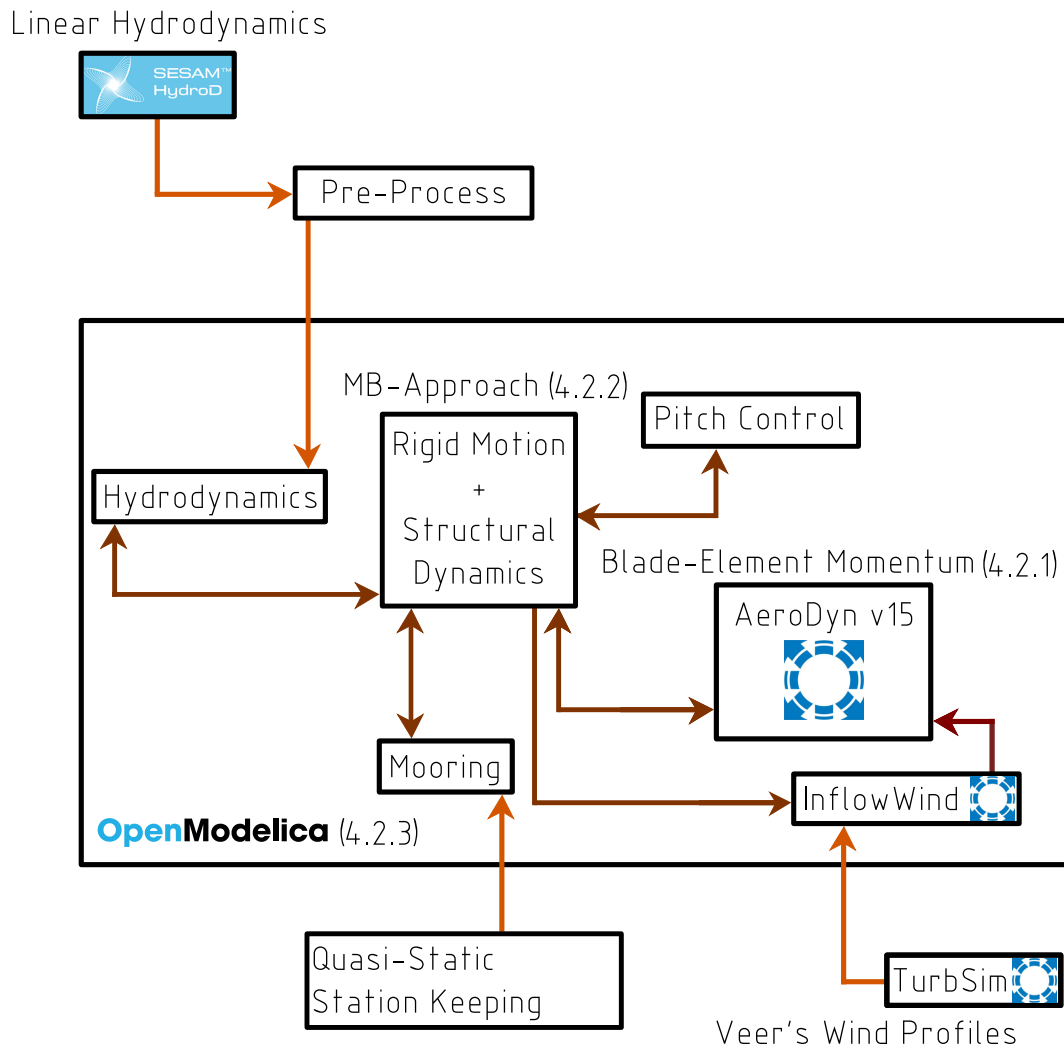
Figure 3.1: Modularized schematization of the tool developed in this work.

code, has recently been released (NREL, 2020). FAST couples different codes in a single structure within the so-called modularization framework.

A thorough code-to-code benchmark study is carried out for validation by considering the baseline Phase IV OC3 spar-type single-rotor design against FAST, showing almost identical results between the codes.
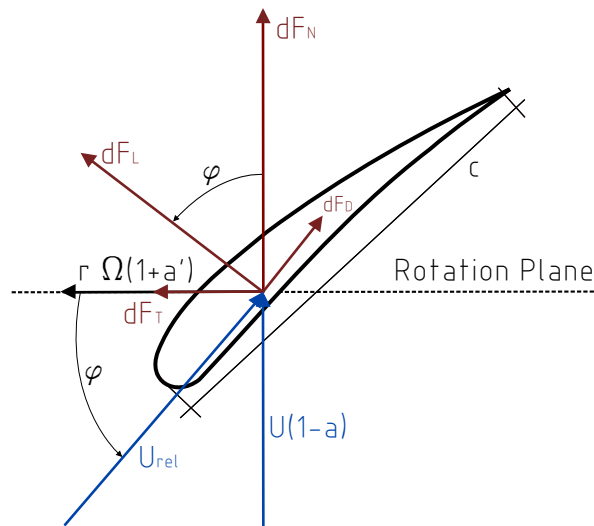
Figure 3.2: Relationship between local flow condition parameters and local aerodynamic loads of a single blade element.

3.2 Methodology

Figure 3.1 depicts a schematization of the tool developed in this work, where the major theories and external tools employed are highlighted. The next sections present in detail the development methodology of the multibody package, the structural dynamics of tower and blades, and blade-element momentum aerodynamics.

3.2.1 Aerodynamics

The blade-element momentum theory (BEMT), also called strip theory, is widely utilized to compute the aerodynamic state of wind turbines due to its simplicity, reasonable accuracy, and computational efficiency. AeroDyn v15 implements BEMT with the inclusion of Prandtl tip and hub losses, as well as Pitt-Peters skewed flow and Gaulert corrections (Moriarty and Hansen, 2005). In the blade element theory, the blades are discretized in finite independent elements. The relationship between local flow condition parameters and local aerodynamic loads of a blade element is typically depicted as in Figure 3.2, where Ω is the rotor angular speed, φ is the relative wind angle, U is the inflow wind speed, U_{rel} is the relative local wind speed, a is the local axial induction

factor, a' is the local tangential induction factor, c is the blade element chord length, r is the distance of the blade element from the rotor center, dF_L and dF_D are, respectively, the differential local lift and drag forces, and dF_N and dF_T are, respectively, the differential normal and tangential forces referred to the rotation plane. The relationship between the total local aerodynamic loads and the local flow condition can be easily derived and expressed as:

$$dF_N = \frac{1}{2}b\rho U_{rel}^2(C_l cos\varphi + C_d sin\varphi)cdr \qquad (1)$$

$$dQ = \frac{1}{2}b\rho U_{rel}^2(C_l sin\varphi - C_d cos\varphi)crdr \qquad (2)$$

where dQ is the differential torque acting on the rotor, b is the number of blades, ρ is the air density, C_l is the airfoil lift coefficient, C_d is the airfoil drag coefficient, and dr is the radial differential thickness of the control volume.

BEM capabilities are achieved by means of the solver AeroDyn v15 within FAST v8 (Moriarty and Hansen, 2005). This version of the code implements classic BEM theory as wake model. Prandtl tip and hub losses are included, as well as Pitt-Peters skewed flow and Gaulert corrections. Steady airfoil aerodynamics is used throughout the work, although AeroDyn v15 is able to consider Beddoes-Leishman unsteady model. AeroDyn presented itself as a natural choice for the task at hand given its widespread use and open-source platform. The next chapters present in greater detail the AeroDyn v15 code structure and how the coupling with the dynamic code implemented in Modelica has been achieved. Turbulent wind profiles are computed by means of the NREL routine TurbSim (Jonkman, 2009a). TurbSim generates turbulent wind fields from the selection of a given spectral model and spatial coherence model. TurbSim is based on Veer's method to generate the wind profiles, which is based on the factorization of the spectral matrix. AeroDyn v15 is not able to take into account aerodynamic interactions, as each blade element is independent of the flow condition and from other elements. This may have a significant effect on the fully-coupled analysis of two-rotor FOWT systems. A correction may be extracted from CFD-based models by assessing the steady-state velocity field around the rotors for different states of the system and later coupling the re-

sulting wind velocity deficit to the undisturbed wind profile. To date, the issue is left as a subject for future work.

3.2.2 Structural Dynamics

Wind turbine blades generally vibrate in flapwise, edgewise, and torsional directions, while wind turbine towers vibrate in longitudinal (fore-aft) and transversal (side-side) directions. Structural vibrations given by aeroelasticity negatively affect the system performance and its structural reliability (Xu et al., 2020).

The structural dynamics of tower and blades are modeled by means of an MB-based approach. HAWC2, developed and distributed by DTU Wind Energy, makes use of an MB formulation for the structural dynamics of blades and tower (Larsen and Hansen, 2007). Literature focusing on the application of the MB method in the structural dynamics of wind turbine blades is plenty. For instance, Zhao et al. (2007) presented the MB modeling procedure of wind turbine blades based on rigid bodies connected through cardanic joints. Mo et al. (2015) presented a blade aeroelastic coupling based on the MB procedure. Jiang and Duan (2011, 2016) performed vibration analysis of wind turbine blades and tower using an MB approach.

The MB approach employed in this work assumes small, linear, and elastic structural deformations, and makes use of a collection of discrete flexible units approximating the local structural dynamics of slender bodies (in this work they are called generalized beam elements, GBEs) (Miller et al., 2017). Each GBE is composed of two rigid bodies coupled with connecting springs and dampers defining its stiffness and dissipative properties. If bending deformations are considered, the equivalent spring coefficient of the GBE can be obtained from equalling the spring torque at the elastic joint and the bending moment of an equivalent continuous beam. The joint torque T can be defined as:

$$T = k_R \theta \tag{3}$$

where k_R is the spring coefficient, and θ is the deflection angle. On the other
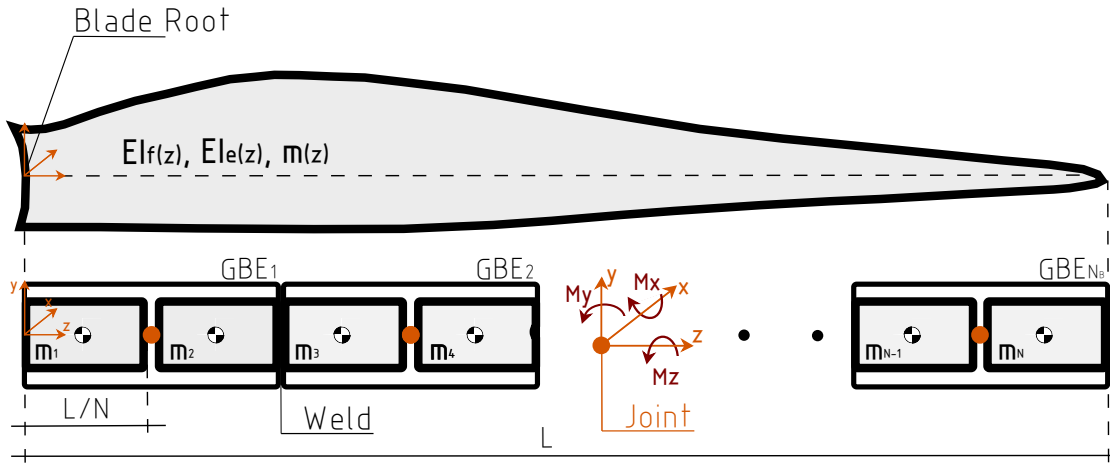
Figure 3.3: Blade structural discretization into generalized beam elements through MB approach.

hand, the bending moment M of a continuous beam unit can be computed as:

$$M = \frac{EI_b}{R} \tag{4}$$

where EI_b is the beam flexural rigidity, and R is the bending radius of curvature. For small angles $\theta \simeq l_b/R$, where l_b is the undeformed beam unit length. The spring coefficient can be thus computed as:

$$k_R = \frac{EI_b}{l_b} \tag{5}$$

The procedure is similar in the case of elastic torsional deformations. Figure 3.3 depicts the blade structural discretization into GBEs (N bodies, N_B GBEs). Joints have no spatial attribute and can enable all the local structural DoFs of the blade. More commonly, however, only the most important modes are enabled, i.e., the flapwise (y), the edgewise (x), and the torsional (z) mode. The flexural and torsional stiffness associated with a single GBE can be computed
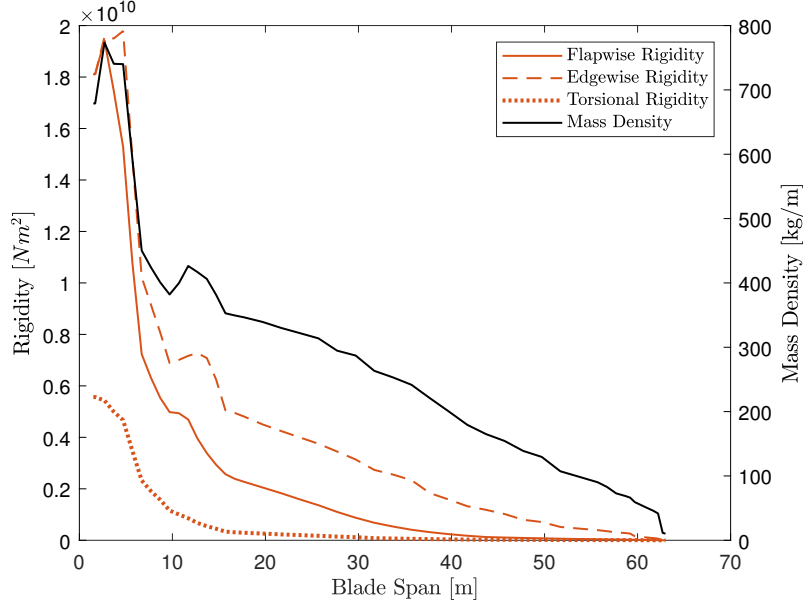
Figure 3.4: NREL 5 MW baseline wind turbine blade distributed structural properties as function of blade span (Jonkman et al., 2009).

as (Xu et al., 2020):

$$K_x = EI_x/l \tag{6}$$

$$K_y = EI_y/l \tag{7}$$

$$K_z = GJ/l \tag{8}$$

where K_x and K_y are, respectively, the flexural stiffness in the edgewise and flapwise direction, K_z is the torsional stiffness, EI and GJ are, respectively, the blade flexural and torsional rigidity, and l is the GBE length, L/N_B [where L is the blade length]. Rigidities and mass density vary significantly as a function of the blade span, and their variation is normally determined experimentally. For instance, Figure 3.4 shows the variation of flexural/torsional rigidities and mass density as a function of blade span for the NREL 5 MW baseline wind turbine, determined from experimental data of LMH64-5 blades (Lindenburg, 2002; Jonkman et al., 2009). Rigidities and mass per unit length associated with each GBE are computed assuming mean values interpolated from the distributed quantities.

The reason for employing the GBE-based MB approach in this work for struc-
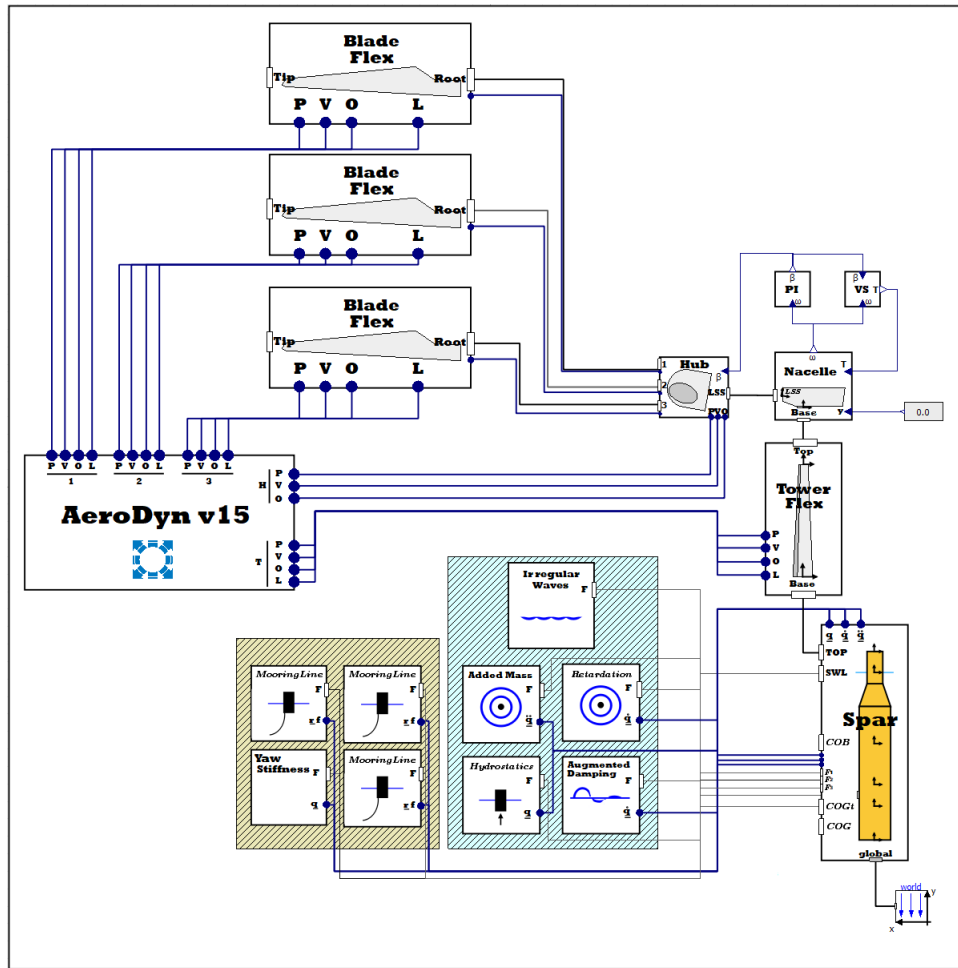
Figure 3.5: Graphical representation of the Phase IV OC3 model implemented in Modelica.

tural dynamics is twofold. Firstly, the multi-body environment within the Modelica Standard Library makes it the most straightforward approach to implement. Secondly, MB allows for higher modeling flexibility and fidelity if compared to the AM approach, while keeping computational economy if compared to the FE approach.

3.2.3 Modelica

Figure 3.5 depicts the graphical representation of the fully-coupled Phase IV OC3 model as implemented in Modelica. The model is structured as a set of functional blocks communicating through connections graphically represented
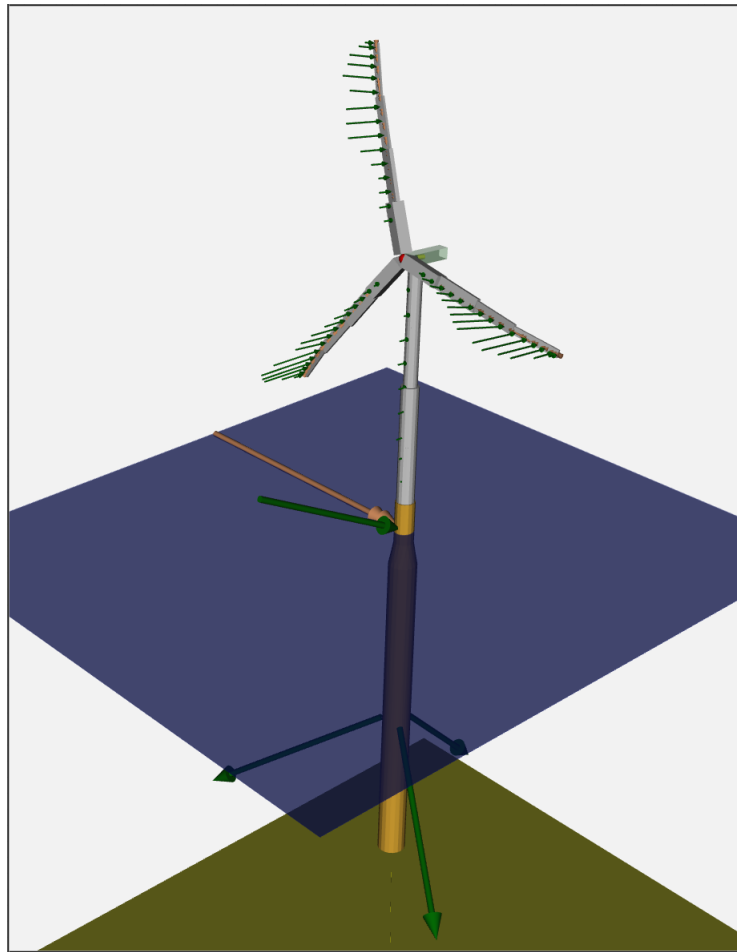
Figure 3.6: OpenModelica animation of the Phase IV OC3 model implemented in Modelica.

as wirings. The variables P, V, O, and L, stand for, respectively, the position, velocity, orientation, and applied loads of each aerodynamic node of the system. Blue wirings are associated with the exchange of variable information between functional blocks, while black wirings connect reference frames of the multibody environment. For instance, each blade is connected to the hub at the blade root through a reference frame connection. Additional variable exchange is also used between blades and hub to obtain the orientation of the unpitched blade root frame to compute in-plane and out-of-plane deflections. Further information can be found in the next sections. OpenModelica also features a 3D animation environment for MB models, a particularly useful development tool. Figure 3.6 depicts an animation render of the fully-coupled Phase IV OC3 model.

3.3   Development

3.3.1   Baseline Design

The baseline single-rotor spar-type NREL 5 MW Phase IV OC3 design is used throughout the tool development process, as presented in Section 2.3.1.

3.3.2   Multi-Body Dynamics

The multi-body code library implements distinct modules for each structural component type. Moreover, two well-distinct modules are implemented to handle rigid and flexible structures and are used independently in relation to the modeling necessity.

Rigid Tower

The rigid tower module is composed of two frame connectors at the tower base and tower top connected to a rigid body with mass.

Nacelle

Two frame connectors are used in the nacelle module. One frame is placed at the tower top for communication with the tower module, and one at the shaft bearing location for communication with the hub module (frames a and c in Figure 2.10, respectively). Frame a is connected to a revolute joint to enable yaw dynamics. This is achieved by imposing a forced movement to the associated axis flange. Yaw dynamics is modeled by means of a second-order transfer function between the yaw angle input signal and the flange movement ($f_n = 3$ Hz, $\zeta = 2$ %). The maximum yaw rate limit is implemented by means of a slew rate limiter. The nacelle and generator equations of motion are implemented by using rigid bodies with mass and inertia tensor. The nacelle body is connected to the frame at the tower top rotating as prescribed by yaw dynamics (frame b in Figure 2.10). A prescribed rotation and translation between frame b and frame c are used to implement the shaft tilt (F in Figure 2.10) and the distance

in the z-axis from the tower top to shaft (G in Figure 2.10). Shaft bearing is implemented by means of two revolute joints grounded to frame c and rotating about the shaft axis. An ideal gearbox without inertia and friction losses is used between the flange axes to implement the low and high speed sides of the shaft (LSS and HSS, respectively). The generator body is connected to the HSS frame, while the LSS frame is used as frame connector (frame d in Figure 2.10). An external torque acting at the HSS and resolved locally is used to implement the generator torque.

Hub

The hub module takes into account hub and shaft. Four frame connectors are used, i.e., one at the LSS frame and three at each blade root location. The shaft is modeled as a rigid body with negligible inertia. Drivetrain torsion is implemented by means of a revolute joint connecting the LSS frame and the shaft. Torsion properties are implemented by means of a rotational spring and damper in parallel. The hub equations of motion are included by means of a rigid body with mass and inertia tensor. Two prescribed rotations are used to implement the precone angle and relative orientation angle of each blade root frame. A revolute joint is used to implement blade pitch angle dynamics. Similar to the nacelle yaw dynamics, the implementation is achieved by means of a forced movement coupled with a second-order transfer function ($f_n = 5$ Hz, $\zeta = 2$ %).

Rigid Blade

The rigid blade module is composed of a rigid body with mass and inertia tensor and a frame connector at the blade root. Modelica resolves the inertia tensor in the CoG of the rigid body. Therefore, the blade moment of inertia referred to the blade root must be transported to the blade CoG by means of the classic transportation formula $I_G = I_R - M_b C_G{}^2$ [where I_G and I_R are, respectively, the blade moment of inertia referred to the CoG and blade root, M_b is the blade overall mass, and C_G is the CoG location referred to the blade root].

Floating Platform

The platform module is composed of a number of frame connectors placed at particular locations by means of prescribed translations. The locations considered are the global reference frame, SWL, CoB, total CoG, CoG of spar only, platform top, each fairlead, and fairlead depth in the platform centerline. The platform equations of motion are implemented by using a rigid body with mass and inertia tensor. The platform body is connected to the global reference frame by means of a free motion joint where the system states are initialized. Several real variable connectors are used to feed modules with platform states information (q, $\dot{q}$, $\ddot{q}$, fairlead displacement, platform displacement as function of depth).

3.3.3   Structural Dynamics

The flexible blade and tower modules implement the structural flexibility by means of lumped elasto-inertial parameters. Arbitrary mesh refinement is achieved by implementing single beam units composing the overall slender structures. Figure 3.7 depicts the general Modelica representation of the beam unit module, together with a depiction of the aerodynamic node structure. The structural beam unit makes use of four frame connectors. Connectors of the type *B* are used to connect beam units to one another. Connectors of the type *A* are instead used to connect the aerodynamic nodes to the structural system. The A-type frame connected to a given aerodynamic node changes in relationship to the number of beam units considered (span length per beam unit decreases by increasing the number of units). For this reason, A-type frame connectors are defined in array form to automatize the connection process. The beam unit deploys two rigid bodies with mass and inertia tensor (not used) and two revolute joints to enable flapwise (fore-aft) and edgewise (side-side) motion. Torsion and axial stiffness are not included to date. Linear rotational springs and dampers are used to implement local structural stiffness and damping. Frame connectors are used to define the aerodynamic nodes (*Nds[i]* in Figure 3.7 [where i is the ith aerodynamic node]), which are placed at the local aerodynamic center of the blade. The associated aerodynamic loads ($F[i]$ and
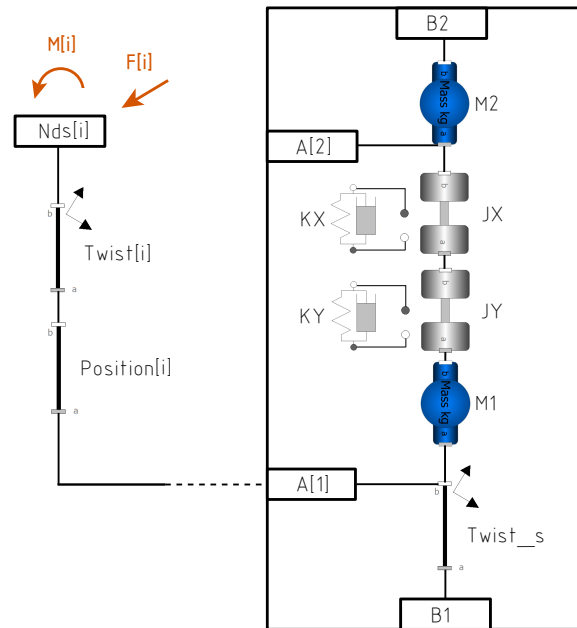
Figure 3.7: Beam unit module for structural dynamics implementation in Modelica with aerodynamic node structure in addition. Twist implementation is associated with blade unit only. Aerodynamic node twist accounts for adjustment of local structural twist angle.

$M[i]$) are implemented by means of an external force and torque and are resolved globally. A prescribed translation and rotation are used for each aerodynamic node to define its global position. The prescribed translation *Position[i]* takes into account the node span along the blade-pitch axis and the local out-of-plane offsets of the aerodynamic center as a result of blade curvature and blade sweep. On the other hand, the prescribed rotation *Twist[i]* considers the local aerodynamic twist angle of the airfoil adjusted for the approximated local twist used in the structural system, *Twist_s*. The tower beam unit and the definition of tower aerodynamic nodes clearly do not account for twist, curvature, and sweep. The blade module uses frame connectors at the blade root, blade tip, and undeflected blade tip (the latter is rigidly connected to the blade root frame by means of a prescribed translation). Blade tip deflection referred to the undeflected position is computed as the difference between tip displacement and undeflected tip displacement. Deflection is projected according to the orientation of the unpitched blade root frame, obtained from the hub module, to obtain in-plane and out-of-plane quantities. Tower deflections are defined similarly.

3.4   Modelica-AeroDyn Integration

FAST v8 is structured as a set of independent modules implementing different physical domains of bottom-fixed and floating wind turbine systems. The development language is Fortran 90. The standardized structure, called modularization framework, enables easy access and manipulation of source code (Jonkman, 2013). Each module is featured by associated dynamic states, input and output variables, and internal parameters. Two approaches exist for module coupling - loose and tight coupling. Loose coupling integrates the modules states by means of independent solvers and achieves coupling by exchanging input and output variables at each time step. Tight coupling, on the other hand, integrates all the dynamic states with a common solver. Loose coupling is implemented in FAST due to major benefits such as modularity, software reuse, independent modeling, and customization (Felippa et al., 2001). Tight coupling is not yet supported in the latest OpenFAST releases (NREL, 2020). Loose coupling can lead to numerical errors or numerical instability in some cases (Jonkman, 2013). Numerical stability of loosely-coupled algorithms is studied, for instance, by Gasmi et al. (2013). FAST employs a fixed coupling time step common to all modules to aid convergence performance. Modules are composed of subroutines, which can be either public or local. Public subroutines are used to control the module, while local subroutines implement the underlying numerical computations. Subroutines manipulate variables defined by means of specialized type structures. Figure 3.8 shows the typical flow of public subroutines used to call a general module in FAST v8, where u and y are, respectively, the input and output variables, p are the module parameters, s are the generalized module states, and t is the integration time step. The first subroutine initializes all the module variables, states, and parameters according to input info (user-defined from .dat file) and it is called only at the simulation start. The second subroutine interpolates the module states at the current time step from the information of system states at previous time steps. The third subroutine performs the main module computations and returns the output variable y at the current time step given the module states s and the input variable u. Finally, the last subroutine performs cleaning procedures, and it is

Input Info

Init $\rightarrow$ u_0, y_0, p, s_0

u_{t-1}, u_t, p

Update States $\rightarrow$ s_t

u_t, p, s_t

t

Compute Output $\rightarrow$ y_t

End
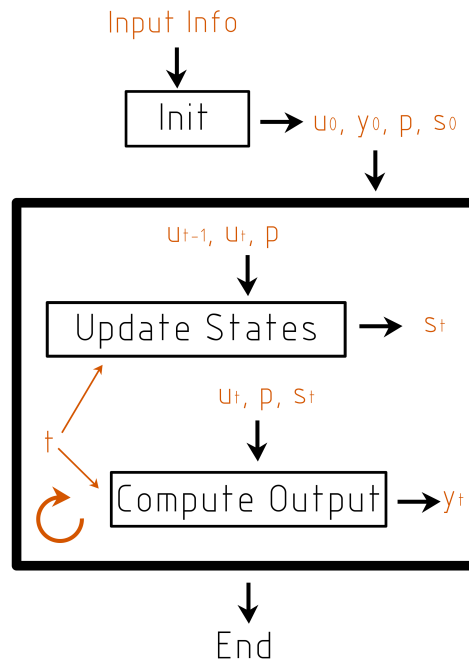
Figure 3.8: Public subroutines flow used in the call of a general module in FAST v8.

called only at the simulation end.

AeroDyn v15 makes use of three different modules within FAST v8, i.e., NWTC_Library, InflowWind, and AeroDyn itself. NWTC_Library contains major algorithmic implementations and is commonly used throughout FAST v8. InflowWind computes the wind velocity components undisturbed from structure proximity at the location of the aerodynamic nodes along blades and tower. Turbulent input wind profiles are preventively computed by means of the routine TurbSim (Jonkman, 2009a). InflowWind input data contain the position of the aerodynamic nodes, while the output data hold the associated wind velocity components.

AeroDyn v15 uses input data from the structural dynamic code (ElastoDyn in FAST) and from the turbulent wind flow code, InflowWind, to compute the aerodynamic loads acting on each aerodynamic node. AeroDyn v15 input data contain information about the orientation, the translational displacement, and the translational velocity of each aerodynamic node, and wind velocity components at the location of the aerodynamic nodes along blades and tower. Orientations are defined as 3x3 direction-cosine matrices. All quantities are referred

to the inertial reference frame located at the tower base. Aerodyn v15 output data, on the other hand, contain information about the aerodynamic force and moment acting on each aerodynamic node. Loads are given referred to the inertial reference frame. It is clear how proper AeroDyn coupling with arbitrary structural dynamic codes can be achieved by feeding the necessary information to the AeroDyn input data structure and employing the AeroDyn, InflowWind, and NWTC_Library modules according to their own function.

Modelica is able to interface with routines written in external libraries by means of external functions (The Modelica Association, 2017). Direct support is available for routines written in C and Fortran 77. To date, direct support for Fortran 90 routines is not available. As a result, the most robust strategy to integrate AeroDyn v15 and InflowWind modules in Modelica is by means of a dedicated DLL. The approach can be stated as follows. A general aerodynamic subroutine can be developed in Fortran 90 and compiled in DLL to call the public subroutines needed to control the AeroDyn v15 and InflowWind modules. In other words, the aerodynamic subroutine implements the direct functional relationship between the dynamic state of the system at a given time and the resulting aerodynamic loads. A buffer, written in C, can be used to load the external DLL and link the stored aerodynamic subroutine to a C function. Lastly, the C function can be easily imported into Modelica achieving the desired interface.

3.4.1 C-Buffer Architecture

Two types of variables are used in the C-buffer, i.e., pointers and local variables. Pointers refer to the address occupied by another variable and are used to interface the C-buffer to the input/output variables defined in Modelica and in the F90 aerodynamic subroutine, as shown in Figure 3.9. Local variables, on the other hand, are used to carry out the specific local computations and to call the external subroutine. Input variables originating from the Modelica structural dynamic code, u_m, are the position vector, orientation matrix, and velocity vector of the hub, the blade roots, and the aerodynamic nodes at the tower and blades. On the other hand, output variables computed by the aerody-
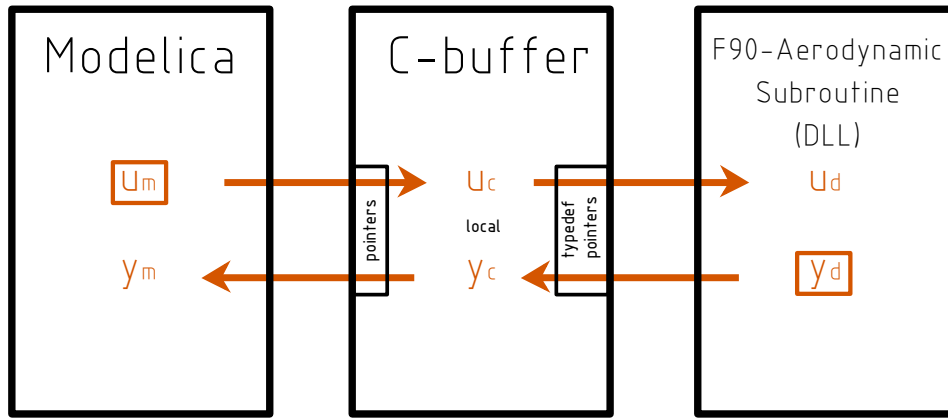
Figure 3.9: Variable flow between Modelica, C-buffer, and the aerodynamic subroutine (stored in DLL).

namic subroutine, y_d, are the aerodynamic loads computed at the aerodynamic nodes of the tower and blades. The definition of the C function structure follows Modelica-specific argument type mapping (The Modelica Association, 2017).

AeroDyn v15 handles fixed time steps only, while Modelica can accommodate variable time steps. Therefore, the C-buffer is developed in such a way as to allow for AeroDyn calls at fixed time steps regardless of the time steps used by the Modelica solver, as shown in Figure 3.10 [where Δt is the fixed aerodynamic time step, N is the current aerodynamic simulation time step, $time$ is the current Modelica simulation time, and P, O, V, L stand, respectively, for nodes position, orientation, velocity, and aerodynamic loads]. AeroDyn computation is carried out only while $N\Delta t < time$.

3.4.2 Aerodynamic Subroutine Architecture

Two variables declaration, i.e., passed and local, are used in the aerodynamic subroutine to handle incoming variables from the C-buffer. Passed variables are used to interface the subroutine to the C-buffer, while local variables are used to perform local operations. Passed variables are further specialized into two intent types, i.e., input type (IN) or output type (INOUT). Fortran 90 stores multidimensional arrays in column-major while C stores them in row-major. As such, the variables passed from the C-buffer to the aerodynamic subroutine must be properly rearranged to keep array structure consistency. The same pre-
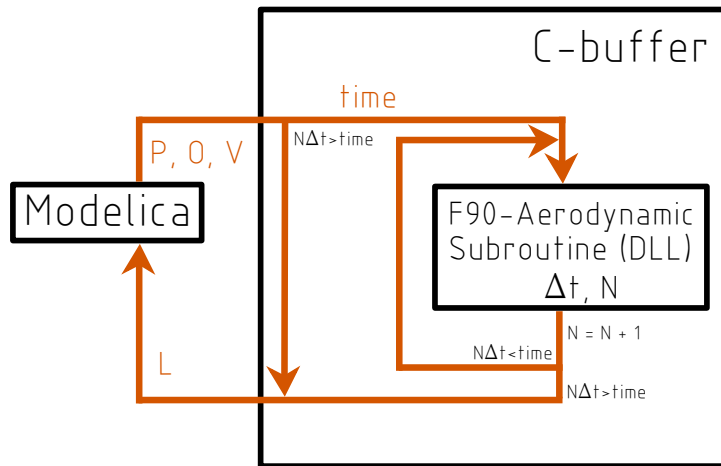
Figure 3.10: Scheme used to accomodate the AeroDyn v15 solver (fixed time steps) in Modelica (variable time steps).

cision kind must also be used for variables exchanged between Modelica and Fortran 90. Since Modelica exports variables in double precision only, it is important to define all the variables of the aerodynamic subroutine as double precision. Figure 3.11 depicts the functional flow of the aerodynamic subroutine. The initialization block is executed only at the simulation start. First, proper allocations are given to initialization variables. Modules variables, parameters, and dynamic states (if present) of AeroDyn v15 and InflowWind are initialized according to user-defined input information. Position and orientation of hub and blade roots from Modelica are used to initialize the aerodynamic nodes mesh of blades and tower in AeroDyn v15. Hub position is also used to initialize InflowWind. Input information not needed during the main calculations are finally deallocated.

The functional flow at each time step can be presented as follows. The structural variables incoming from Modelica are used to update the AeroDyn v15 input data. The position of the aerodynamic nodes at blades and tower is also used to update the InflowWind input data. Next, the wind velocity components at the position of the aerodynamic nodes are computed. The inflow variables in the AeroDyn v15 input data are then updated with the new wind velocity profile. An array of Aerodyn v15 input data is then updated with input information corresponding to the previous and the current time step. A linear interpola-
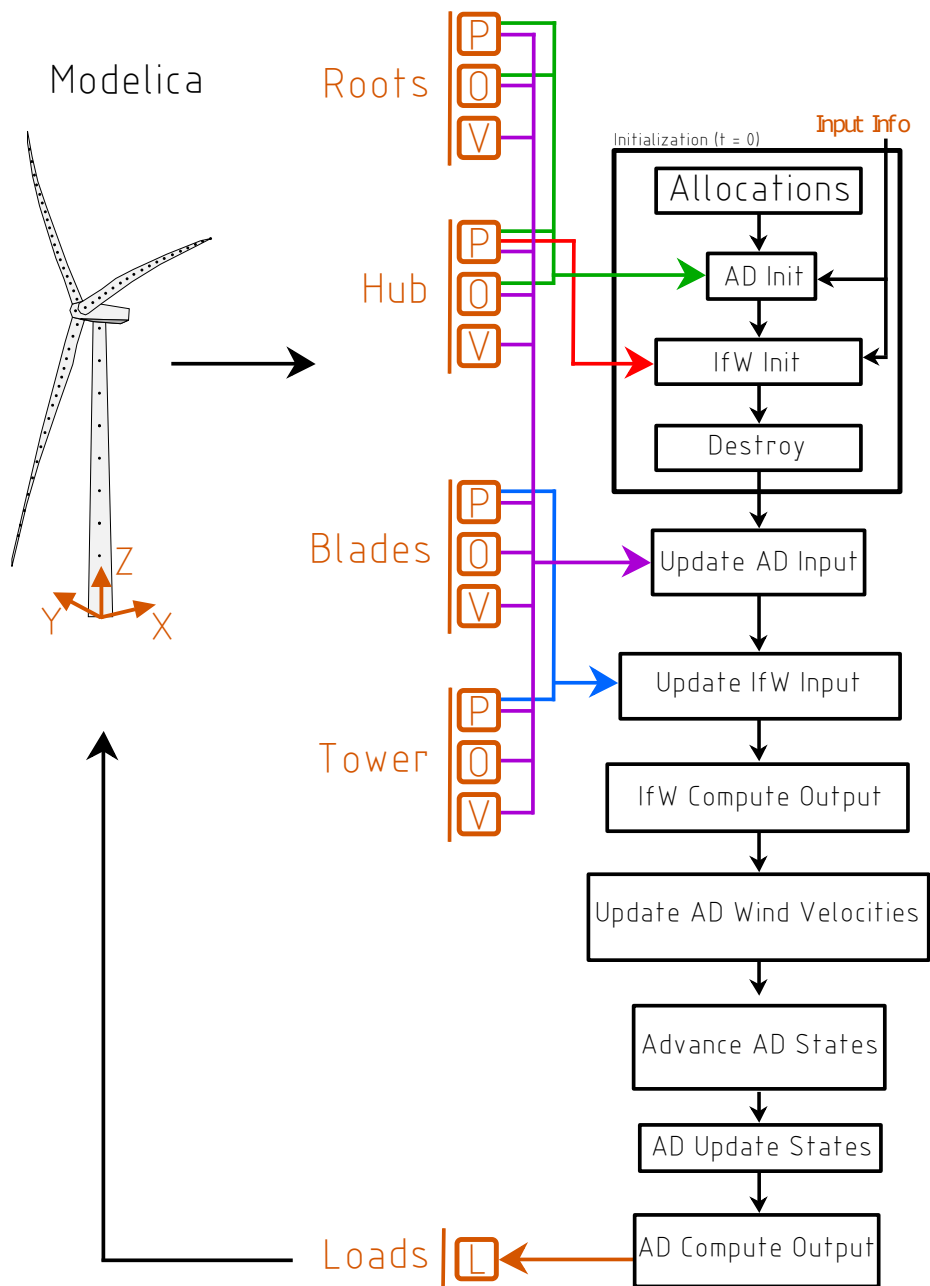
Figure 3.11: Functional schematization of the aerodynamic subroutine used for integration of AeroDyn v15 and InflowWind in Modelica. AD: AeroDyn v15. IfW: InflowWind.

Table 3.1: Numerical integration setup.

Integration Method	ida
Tolerance	10^{-4}
Linear Solver	total pivot
−maxSizeLinearTearing	0
Non linear Solver	kinsol

tion order is hence assumed. Since the aerodynamic subroutine is called from the Modelica structural code, the system states are known beforehand. As a consequence, interpolation is not strictly necessary. However, the associated computation is retained to maintain source code consistency. Next, the Aero-Dyn v15 dynamic states at the current time step are determined by means of the interpolated data previously defined. InflowWind module, on the other hand, does not feature any dynamic state. Lastly, the AeroDyn v15 output channels are computed, corresponding to the aerodynamic forces and moments acting at the aerodynamic nodes. The loads are returned normalized per unit length. Dimensionalization of the aerodynamic loads can be achieved by making use of the equivalent structural length associated with each node.

3.5 Numerical Setup

The default integration method implemented in OpenModelica is DASSL (Differential/Algebraic System Solver) (Petzold, 1982), an implicit higher-order solver with variable step-size. The solver IDA, however, is found to give a more robust performance in the context of this work. IDA is part of the solver family SUNDIALS (Suite of Nonlinear and Differential/Algebraic equation Solvers) (Hindmarsh et al., 2005). Similar to DASSL, IDA is an implicit higher-order solver with variable step size. Table 3.1 lists the numerical integration setup found to give reasonable stability and robustness. Total pivot, method using a total LU factorization for undetermination systems, is used as linear solver. Linear tearing is disabled. This is known to significantly improve the performance of large systems in combination with sparse solvers. Kinsol, on the other hand, is used as nonlinear solver. Kinsol implements a combination of Newton
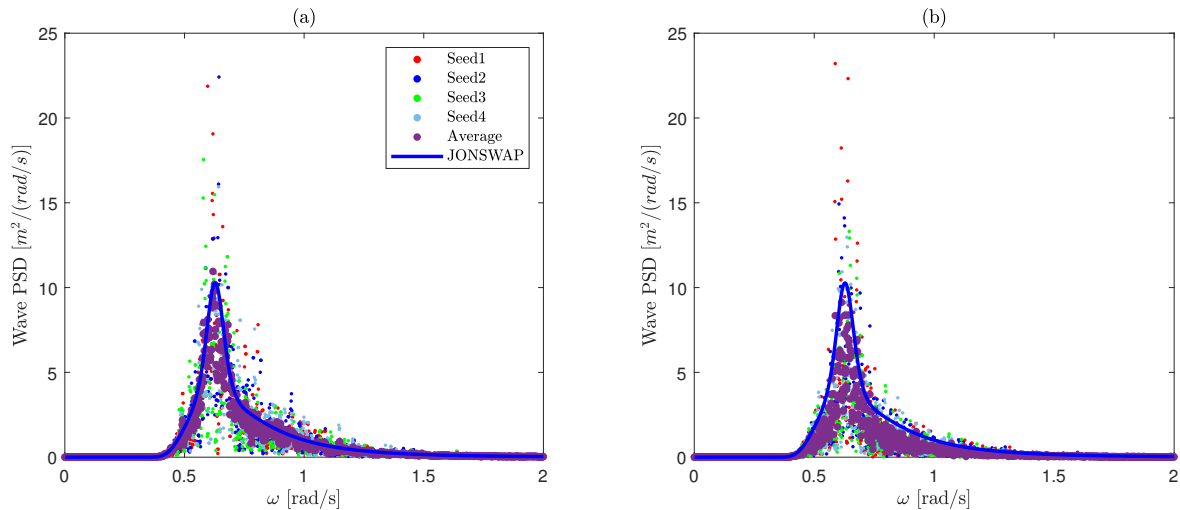
Figure 3.12: Power spectral densities of irregular wave amplitude (H_s = 6 m, T_p = 10 s). Blue line represents the target JONSWAP spectrum. Dots represent estimates from four different seeds. Green crosses depict the seed average. a) OM Hydrodynamic pre-processor. b) FAST-HydroDyn.

Krylov, Picard, and fixed-point solver (Taylor and Hindmarsh, 1998).

3.6   Benchmark

The baseline Phase IV OC3 design is also used for benchmark analysis. In the following sections, results obtained with the present code are compared with those computed in FAST v8. Identical turbulent wind and irregular wave time realizations are used.

3.6.1   Hydrodynamic Pre-Processing & Mooring Lines

Estimation of power spectral densities (PSDs) associated with the time realization of wave elevation profiles and incident wave loads are used to benchmark the hydrodynamic pre-processing module. Figures 3.12 and 3.13 depict, respectively, the PSDs of irregular wave amplitude and wave load in the platform pitch direction estimated from time realizations (H_s = 6 m, T_p = 10 s). Four different seeds are considered. The time series are obtained with the hydrodynamic pre-processing module (a) and FAST-HydroDyn (b). Good power distri-
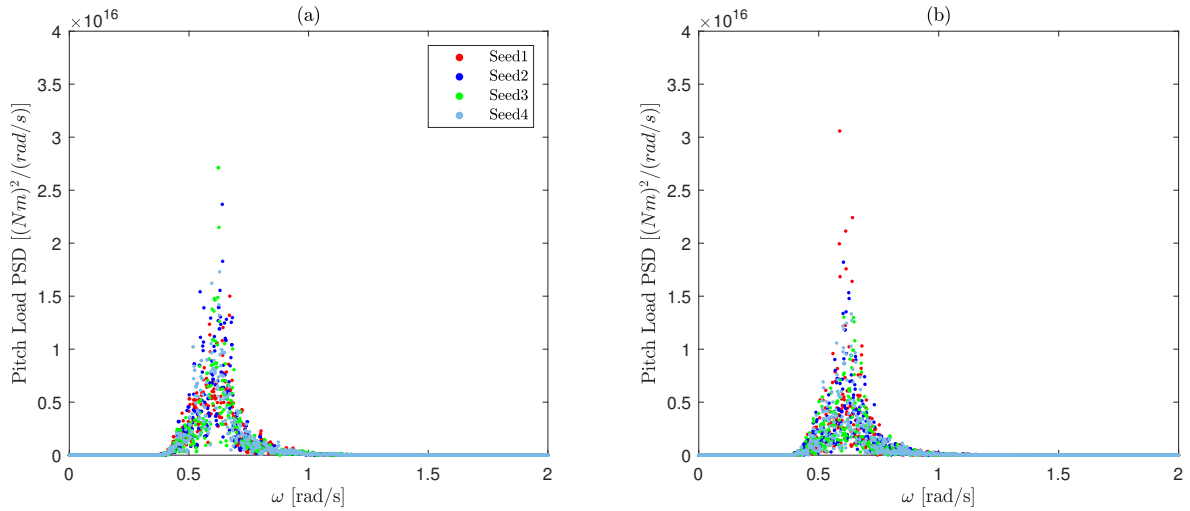
Figure 3.13: Power spectral densities of wave load in the platform pitch direction (H_s = 6 m, T_p = 10 s). Four different seeds are considered. a) OM Hydrodynamic pre-processor. b) FAST-HydroDyn.

bution is obtained. As coarse time sampling leads to PSD scatter, the seed average is used to reduce the relative effect of noise. As expected, the seed-averaged wave amplitude PSD converges to the target JONSWAP spectrum.

The radiation damping is approximated in the time domain by means of a state-space representation. Only two states are used to approximate each kernel component (thus reducing the kernel dynamics to a second-order ordinary differential equation). A unit platform velocity impulse can be fed to the state-space model to reconstruct the kernel components associated with the corresponding exciting impulse direction. Figure 3.14 shows the wave-radiation retardation kernel components obtained by exciting the state-space model with velocity unit impulses. The resulting kernels are then compared with the reference. It is clear how two states are sufficient to cover most of the impulse dynamics. Additional states may be necessary in cases where radiation damping is characterized by high-frequency energy content, for instance in the OC4 semi-submersible hydrodynamic response (Robertson et al., 2014a).

The benchmark of mooring lines is often assessed in terms of the non-linear relationship between static platform displacements and the resulting mooring restoring loads (Jonkman et al., 2009). Figure 3.15 shows the load-displacement relationship as computed in OM and FAST (Jonkman, 2010).
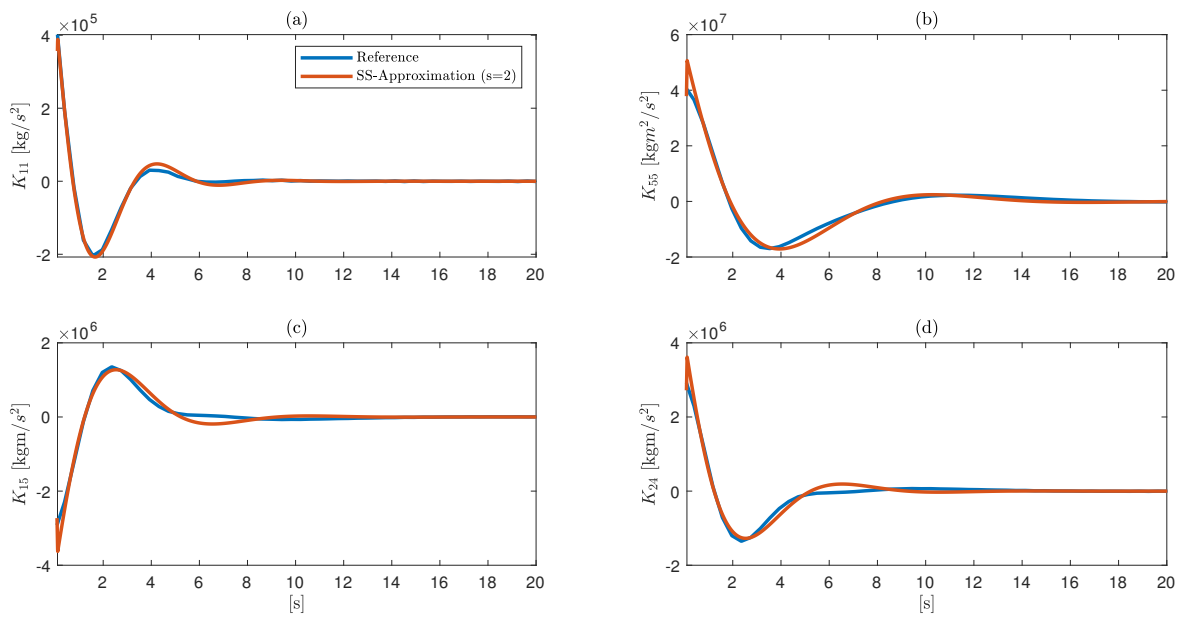
Figure 3.14: Wave-radiation retardation kernel components obtained by using velocity unit impulses in the state-space radiation damping approximation. Comparison with reference kernel components. Two states are used for the state-space approximation of each kernel component (s=2).
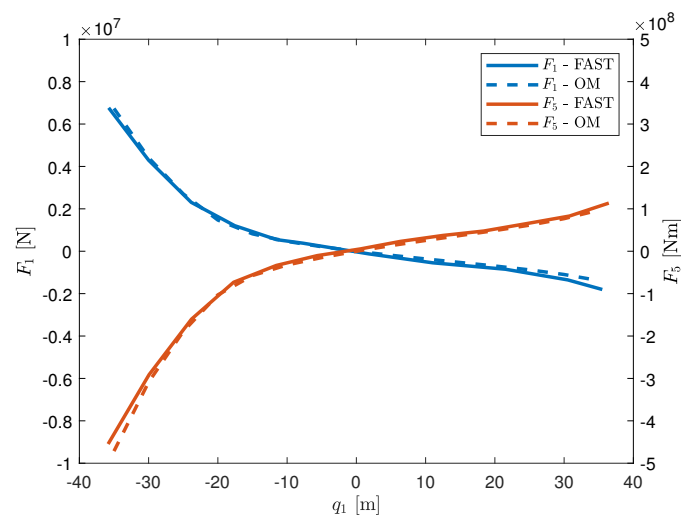
Figure 3.15: Load-displacement relationships of the Phase IV OC3 mooring system as computed in OM and FAST (Jonkman, 2010). Only surge/pitch mooring loads due to surge displacement are depicted.

Table 3.2: Full-system natural frequencies of the Phase IV OC3 system as computed in OM ($N_T = 2$, $N_B = 6$) against reference FAST frequencies (Jonkman et al., 2010; Matha, 2010; Lupton and Langley, 2017). OM frequencies are computed in the time domain through free-decay and sweep-sine tests.

	OM [Hz]	FAST [Hz]
Surge	0.008	0.008
Sway	0.008	0.008
Heave	0.0314	0.032
Roll	0.035	0.034
Pitch	0.035	0.034
Yaw	0.122	0.121
Tower fore-aft 1_{st}	0.490	0.473
Tower side-side 1_{st}	0.490	0.457
Drivetrain torsion (free-free)	1.667	1.700
Tower fore-aft 2_{nd}	3.632	3.751
Tower side-side 2_{nd}	4.312	4.258
Blade flapwise 1_{st}	0.634	0.666
Blade flapwise 2_{nd}	1.951	1.920
Blade flapwise 3_{rd}	4.204	N.A.
Blade edgewise 1_{st}	1.126	1.080
Blade edgewise 2_{nd}	4.144	N.A.

Only mooring loads in the platform surge and pitch direction due to a static displacement in the surge direction are depicted. A very good match is clearly obtained between the two codes. Mooring nonlinearities are thus well described with the present implementation. Moreover, the platform surge natural period computed from free-decay tests, which is strongly associated with mooring stiffness, is also agreeing very well between the codes, as shown in Section 3.6.3.

3.6.2 Structural Dynamics

As the structural model of blades and tower is composed of lumped elements, accuracy will depend on the number of blade/tower units employed. As a consequence, the benchmark consists in evaluating the convergence of the structural response to reference values. Convergence is given for the components inertia properties and for the associated structural frequencies. OM frequencies are computed in the time domain. Table 3.2 presents the full-system natu-
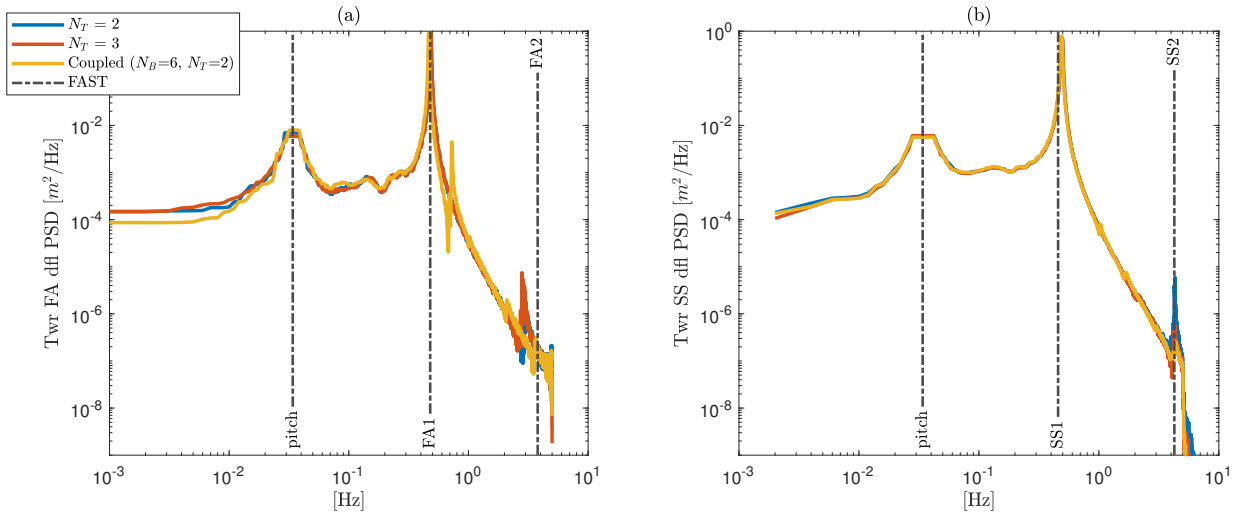
Figure 3.16: a) Power spectral densities of tower fore-aft deflection computed by means of sweep-sine excitation at the SWL in the platform surge direction. b) Power spectral densities of tower side-side deflection computed by means of sweep-sine excitation at the SWL in the platform sway direction. Uncoupled PSDs (rigid blades) are obtained for different number of tower units employed, N_T. Coupled PSD (flexible blades) is also included ($N_B = 6$, $N_T = 2$). Comparison with reference FAST frequencies (Jonkman et al., 2010; Matha, 2010; Lupton and Langley, 2017).

ral frequencies as computed in OM, together with reference FAST frequencies (Jonkman et al., 2010; Matha, 2010; Lupton and Langley, 2017). Values are relative to two tower units and six blade units ($N_T = 2$, $N_B = 6$). Platform natural frequencies are determined from free-decay tests, as presented in Section 3.6.3. The structural frequencies of blades, tower, and drivetrain are determined from free-decay and sweep-sine tests. Drivetrain torsion is relative to a generator-rotor free-free condition. Figure 3.16a and Figure 3.16b show, respectively, the uncoupled (rigid blades) PSDs of tower top fore-aft (FA) and side-side (SS) displacement determined for different number of tower units, N_T. Coupled PSD (flexible blades) is also included for $N_B = 6$. Sweep sine excitation is applied at the SWL in the platform surge and sway direction, respectively. Linear sweep rate is used. Pitch natural frequency is visible, as well as the frequencies associated with the first two tower FA/SS modes. It is clear how two units are sufficient to obtain full tower convergence. Tower inertia convergence is negligible given geometric regularity. Blades and tower structural coupling signif-
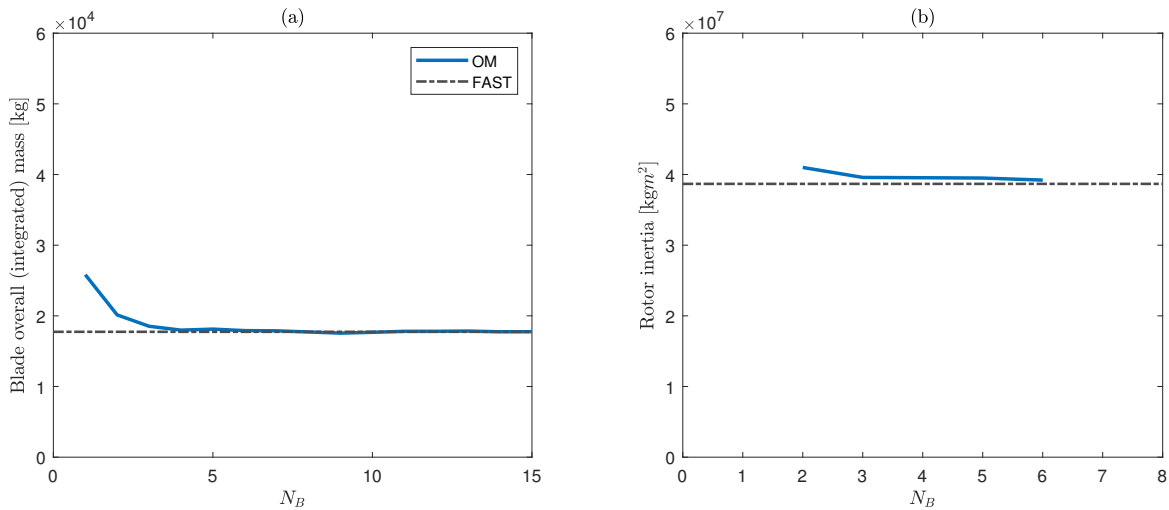
Figure 3.17: Convergence of blade overall (integrated) mass (a) and rotor inertia (b) as function of blade units employed (N_B) against reference FAST.

icantly affect the second tower FA frequency, shifting from about 2.79 Hz to about 3.63 Hz. On the other hand, the second tower SS frequency is found to be only marginally affected by structural coupling.

Due to the complex distributed structural properties, the blade structural dynamic benchmark must consider both the convergence of the blade mass/inertia and of the associated structural frequencies. The overall rotor inertia can be estimated in the time domain by assessing rotor acceleration due to a prescribed external torque. Figure 3.17 shows the blade overall mass and rotor inertia convergence as a function of the number of blade units employed. Five blade units are sufficient to reach full mass/inertia convergence (maximum 2% deviation from reference). Figure 3.18a and Figure 3.18b show, respectively, the uncoupled PSDs (rigid tower) of blade (zero azimuth) out-of-plane (OoP) and in-plane (IP) deflection determined for different number of blade units, N_B. Sweep sine excitation in the platform surge direction (a) and the platform sway direction (b) is applied at the SWL. Resonance peaks at the platform pitch natural frequency as well as at the flapwise and edgewise structural modes are clearly visible. It is clear that a good frequency convergence is achieved regardless of the number of blade units employed. The third flapwise and second edgewise modes are also detected at about 4.3 Hz and 4.1 Hz, respectively.
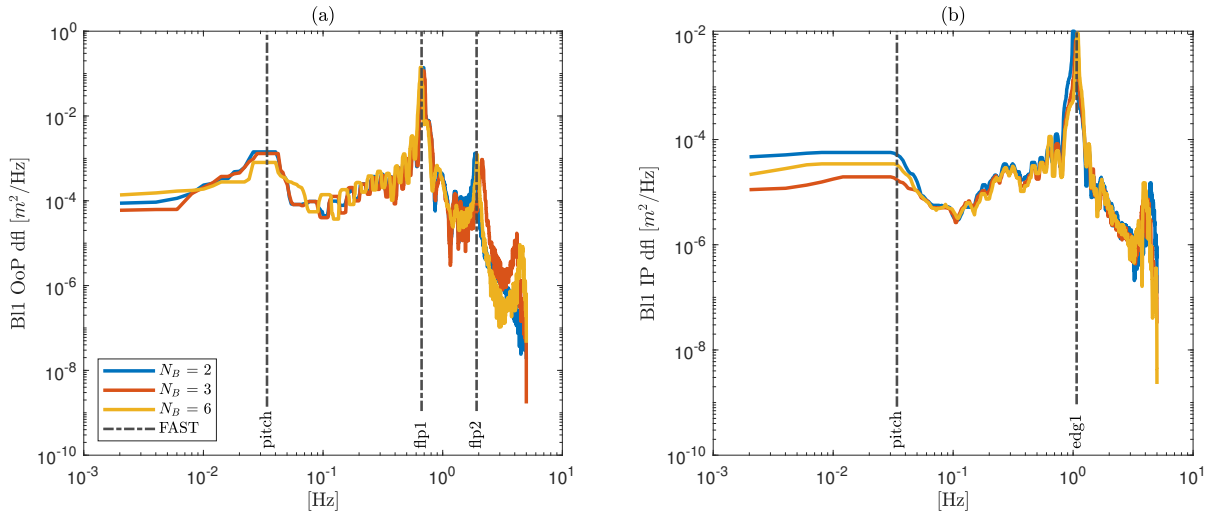
Figure 3.18: a) Power spectral densities of blade out-of-plane deflection computed by means of sweep-sine excitation at the SWL in the platform surge direction. b) Power spectral densities of blade in-plane deflection computed by means of sweep-sine excitation at the SWL in the platform sway direction. Uncoupled PSDs (rigid tower) are obtained for different number of blade units employed, N_B. Comparison with reference FAST frequencies (Jonkman et al., 2010; Matha, 2010; Lupton and Langley, 2017).

3.6.3 Global Dynamics

Throughout the dynamic benchmark exercise, six blade units and two tower units are used ($N_T = 2$, $N_B = 6$). Table 3.3 shows the load cases considered for the present dynamic benchmark, which are based on Phase IV Offshore Code Comparison Collaboration (Jonkman et al., 2010). The load cases are characterized by the associated enabled DoFs, the wind condition, the wave conditions, and the resulting analysis type. The first two load cases consider the fully-flexible wind turbine deployed onshore (retaining offshore tower geometry), under steady-state and turbulent wind conditions. Aerodynamic loads acting on the tower are not considered. A selection of steady-state operational curves from load case 2.1 is shown in Figure 3.19. The codes perform almost identically. A marginal deviation of blade out-of-plane deflection is detected at rated operational conditions (about 0.3 m higher in FAST at 11.4 m/s). Small deviations in blade deflections are to be expected given the different modeling assumptions used. Fully-coupled response time series from load case 2.2 are shown in Figure

Table 3.3: Summary specifications of load-case simulations used in benchmark study, based on IEA Phase IV Offshore Code Comparison Collaboration (Jonkman et al., 2010).

	Enabled DoFs	Wind Conditions	Wave Conditions	Analysis Type
2.1	Tower, Blades	Steady. V_{hub} = 3–25 m/s	N.A.	Operational curves
2.2	Tower, Blades	Turbulent (Kaimal, NTM B). V_{hub} = 11.4 m/s	N.A.	Time series
2.3	Platform	None	Still Water	Free-decay time series
2.4	Platform, tower	None	Regular Airy: H_s = 6 m, T_p = 10 m	Time series
2.5	Platform, tower	None	Irregular Airy (JONSWAP): H_s = 6 m, T_p = 10 m	Time series, PSDs
2.6	Platform, tower, drivetrain, blades	Steady. V_{hub} = 8 m/s	Regular Airy: H_s = 6 m, T_p = 10 m	Time series
2.7	Platform, tower, drivetrain, blades	Turbulent (Kaimal, NTM B). V_{hub} = 11.4 m/s	Irregular Airy (JONSWAP): H_s = 6 m, T_p = 10 m	PSDs

NTM: normal turbulence model
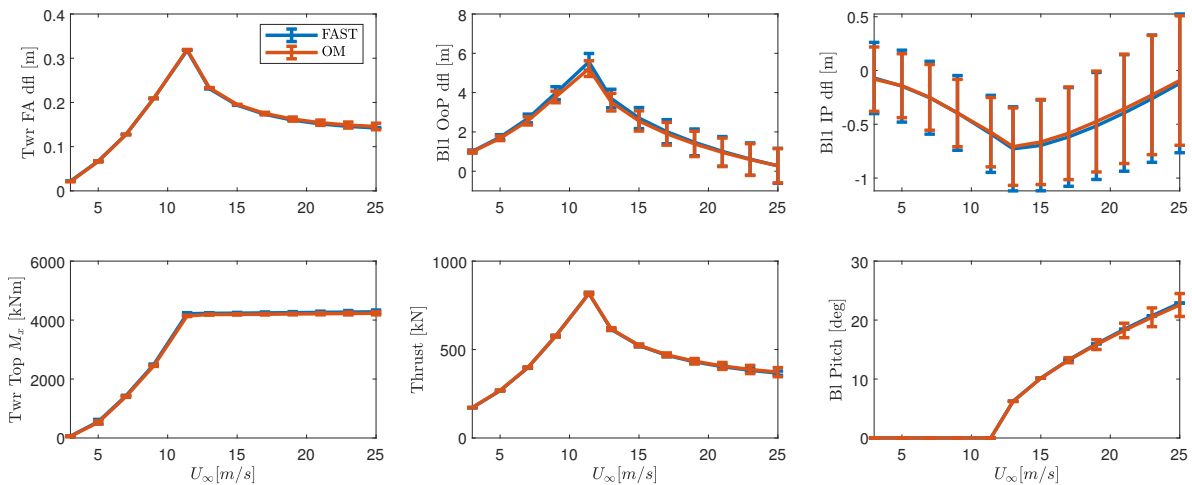
Figure 3.19: Steady-states operational curves from load case 2.1 (offshore tower geometry is used in both codes).
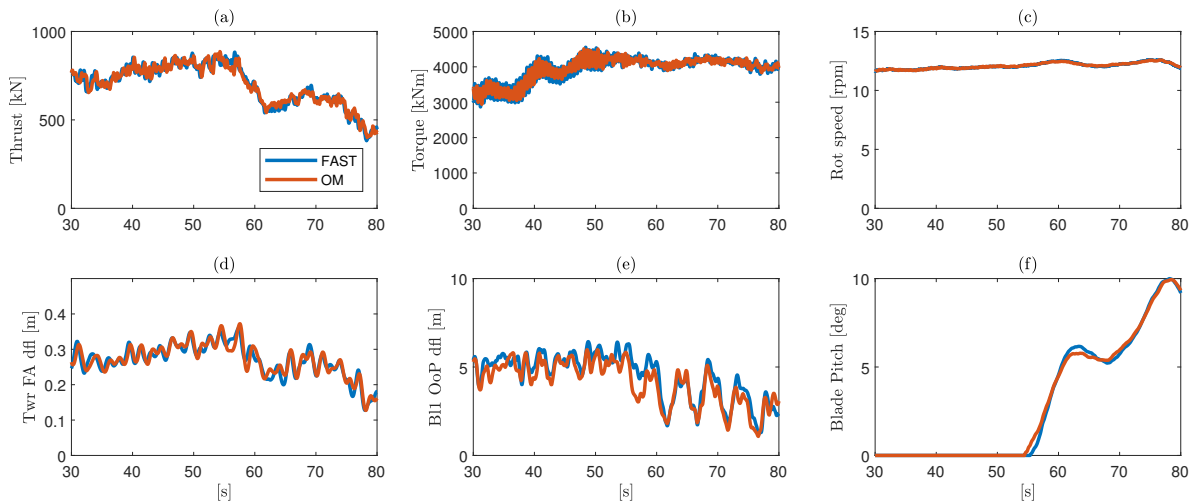
Figure 3.20: Fully-coupled response time series from load case 2.

3.20. The same turbulent input file (.bts) is used in the two codes. As it is clear, the codes result in almost identical responses. Figure 3.21 shows the free-decay time series from load case 2.3 associated with the platform surge (a), heave (b), and pitch (c) directions. Initial displacements of 10 m and 10 deg are used. A good response is obtained. Platform heave free-decay yields identical results. No significant hydrodynamic radiation is present for spar-type structures in the heave direction (Jonkman, 2010). Thus, heave dynamics is fully determined by the system inertia and the dynamic loads from incident waves. Some variability in the system damping is found in the platform surge and pitch directions. The damping ratio from logarithmic decrement in the surge direction found in FAST and OM is, respectively, about 0.097 and 0.143. In the platform pitch direction, the damping ratio from logarithmic decrement is, respectively, about 0.063 and 0.088. As radiation damping is approximated by means of a state-space representation, a certain degree of variability in damping properties is expected. Resulting time series from load case 2.4 are given in Figure 3.22. Also in this case, codes perform almost identically. Load case 2.5 is a variation of load case 2.4 where external loads are relative to prescribed irregular waves realized from JONSWAP spectrum. The same realization is used in both codes (same pseudorandom seeds). The resulting time series are given in Figure 3.23. The associated power spectral densities are shown in Figure 3.24. Energy content is distributed in a similar fashion between the codes. The major peak around
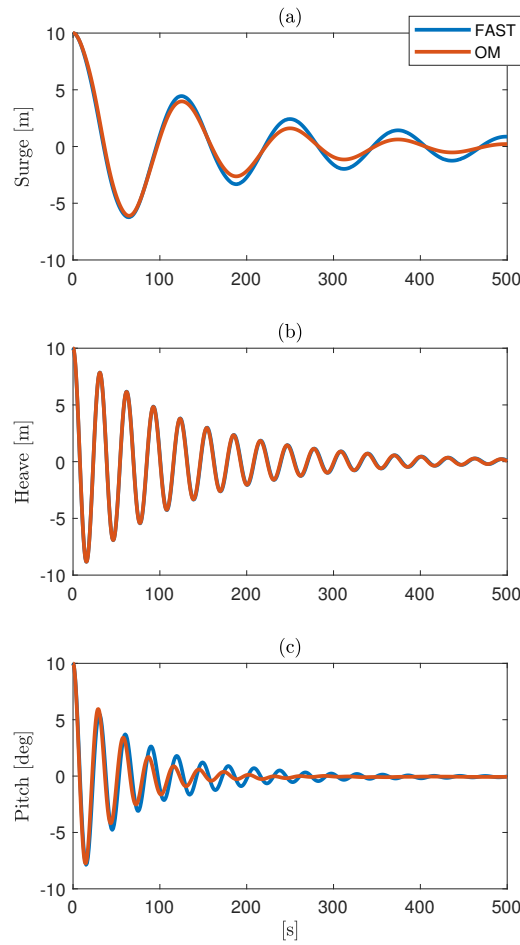
Figure 3.21: Free-decay time series from load case 3.
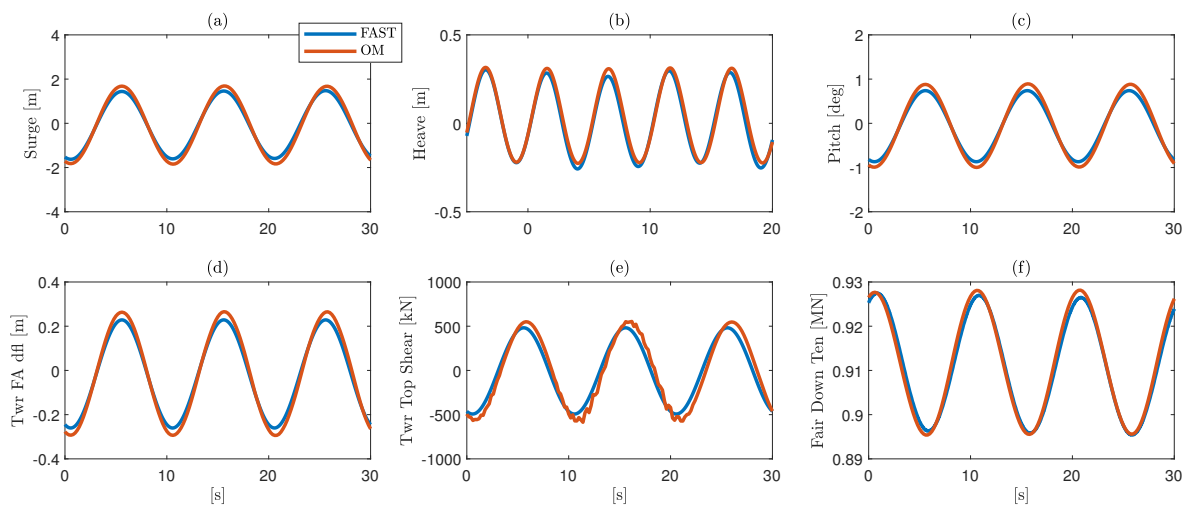
Figure 3.22: Fully-coupled response time series with regular waves from load case 4.
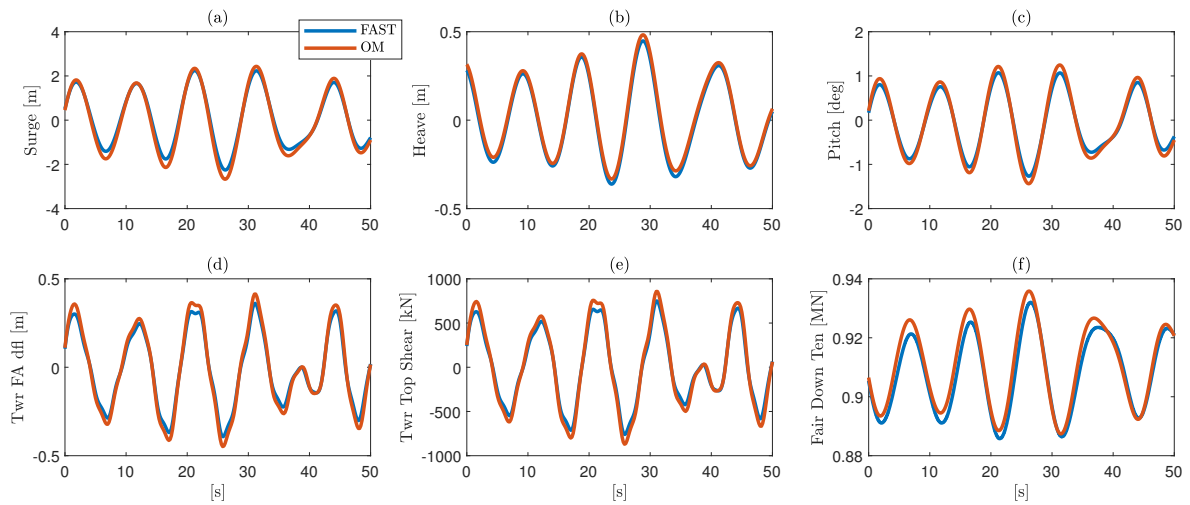
Figure 3.23: Fully-coupled response time series with irregular waves from load case 5.
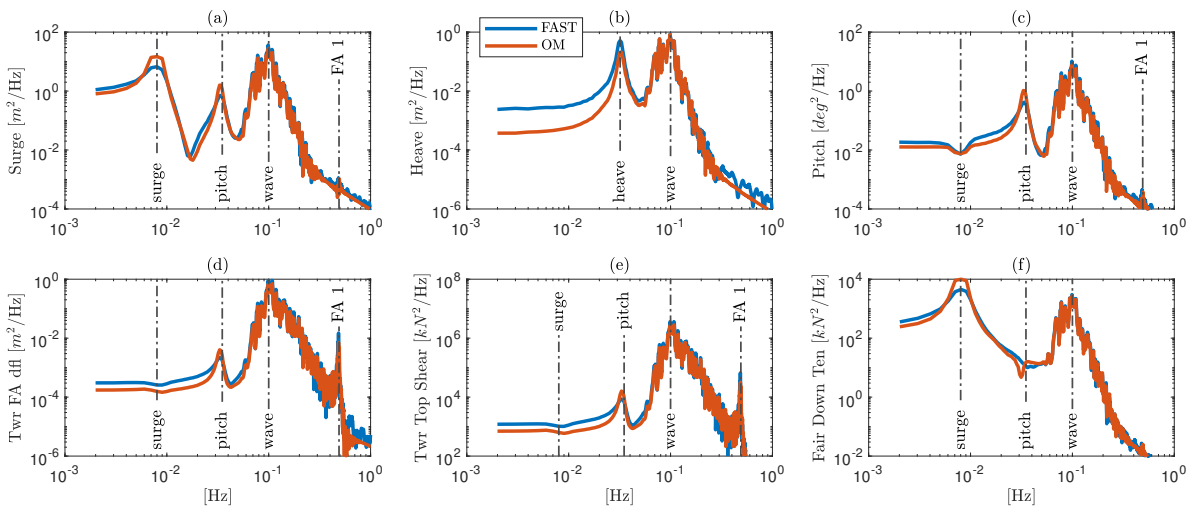
Figure 3.24: Fully-coupled response power spectral densities with irregular waves from load case 5.
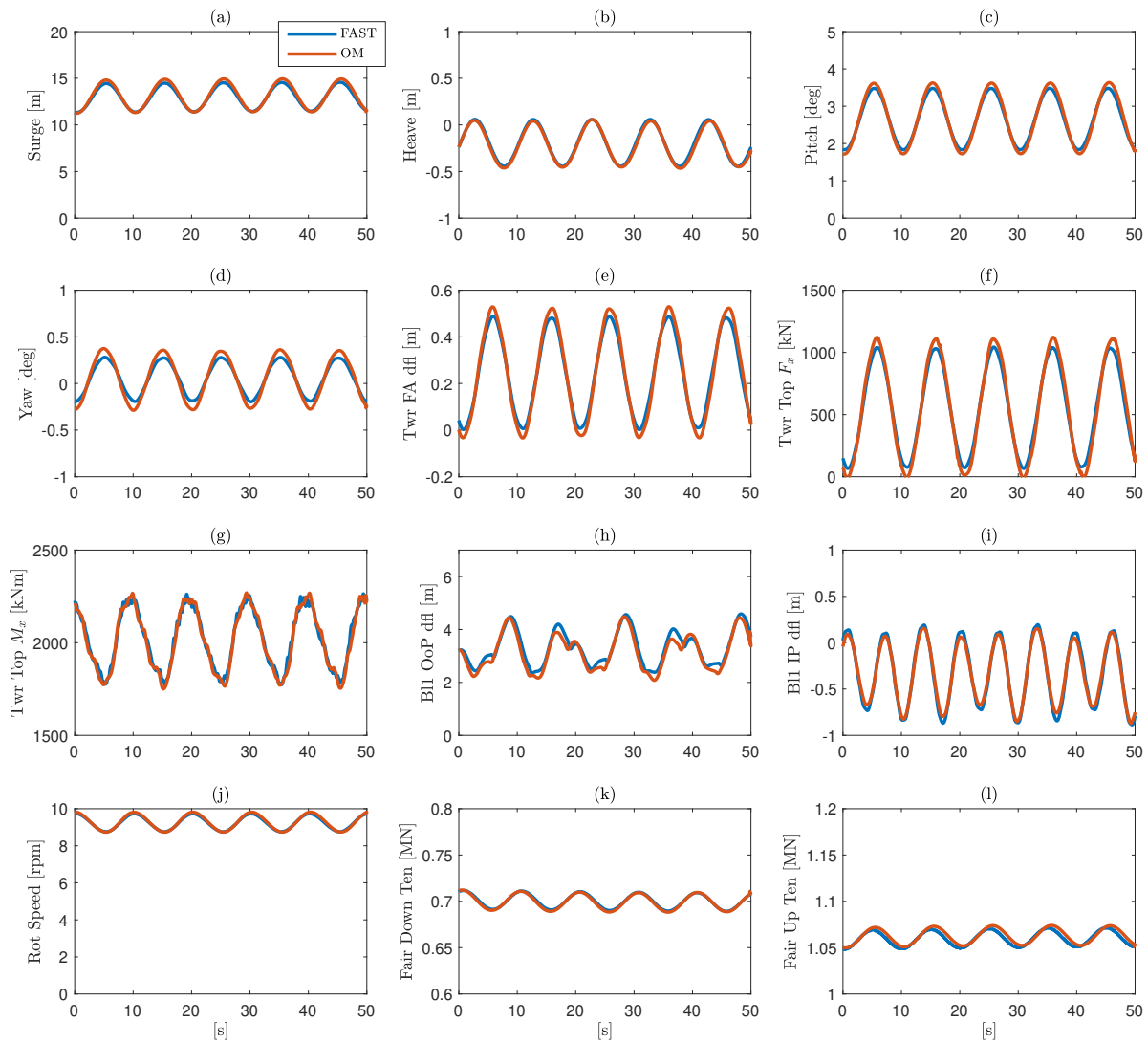
Figure 3.25: Fully-coupled response time series with regular waves from load case 6.

the characteristic wave period is clearly visible (0.1 Hz), as well as energy peaks at the platform surge (0.008 Hz), platform heave (0.032 Hz ca.), and platform pitch (0.035 Hz) motions, and the first tower fore-aft mode (0.49 Hz). Load case 2.6 considers the full-system dynamics, i.e., platform motion, drivetrain and control systems, and tower/blades structural dynamics. The response is due to steady-state wind conditions and prescribed regular waves. Figure 3.25 shows the resulting time series in terms of platform surge motion (a), platform heave motion (b), platform pitch motion (c), platform yaw motion (d), tower fore-aft deflection (e), tower-top shear (f), tower-top bending moment (g), blade

Table 3.4: Specifications for computing unit used in performance analysis.

CPU	Intel®Core™i7-9700 3.00 GHz
RAM	64 GB DDR4 2666 MHz SO-DIMM
Drive	512GB M.2 2280 PCIe SSD NVMe

out-of-plane deflection (h), blade in-plane deflection (i), rotor speed (j), down-wind fairlead tension (k), and upwind fairlead tension (l). Very good results are clearly obtained. Load case 2.7 considers full-system response due to turbulent wind and irregular waves. The same wind-wave realizations are used in both codes (same pseudorandom seeds). Rated wind condition is considered, i.e., 11.4 m/s. Results are given in terms of power spectral densities for the same parameters introduced in load case 2.6, as shown in Figure 3.26. Also in this case, the match between the codes is very good. Reference values for the system natural frequencies are depicted (from Table 3.2), as well as the mean rotor revolution frequencies. Match of blade flapwise modes with references are relative to the collective modes, which do not change natural frequency significantly at 11.4 m/s (Johnson et al., 2019).

3.7 Performance

Table 3.4 lists the specifications of the computing unit used to estimate the present code performance. The latest available OpenModelica compiler is used (v1.18.1). Conditions prescribed in load case 2.7 are used. The performance index considered is the time ratio, i.e., simulated time versus CPU time. The time ratio is evaluated as a function of the structural dynamic fidelity of the system, i.e., the number of units used for blades structural dynamic modeling. The effect of the radiation damping state-space approximation order on the code performance is also evaluated. Simulation settings used are listed in Table 3.1. Performace of the reference code FAST is also evaluated. FAST performance evaluation only takes into account radiation damping as computed from convolution in the time domain (RdtnMod=1). Moreover, FAST performance evaluation only considers a purely rigid and a fully-flexible case. In the flexible case,
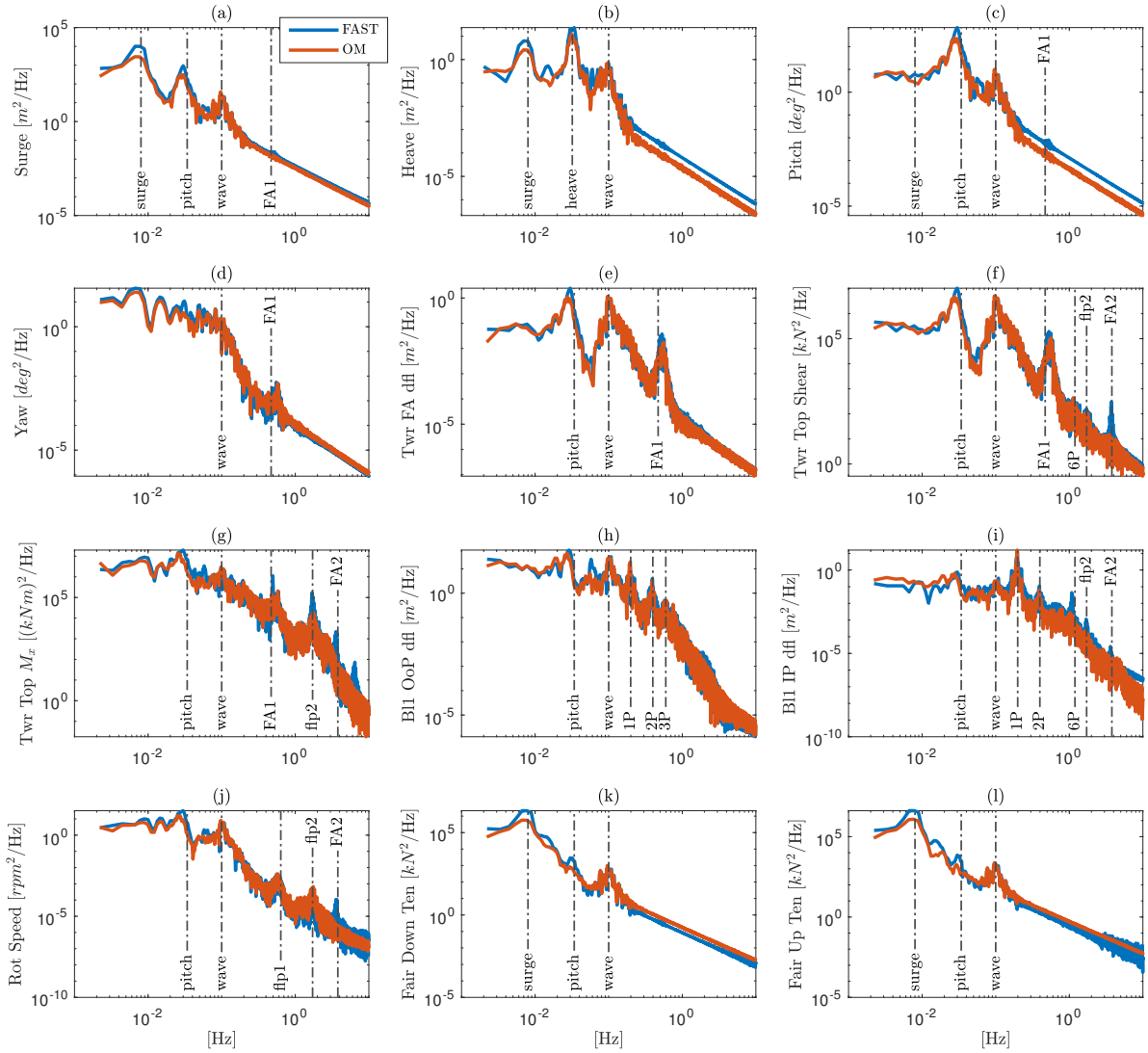
Figure 3.26: Fully-coupled response power spectral densities with irregular waves from load case 7 ($\overline{\omega_r} = 11.4$ m/s). Reference FAST frequencies and rotor revolution frequencies are also depicted (Jonkman et al., 2010; Matha, 2010; Lupton and Langley, 2017).
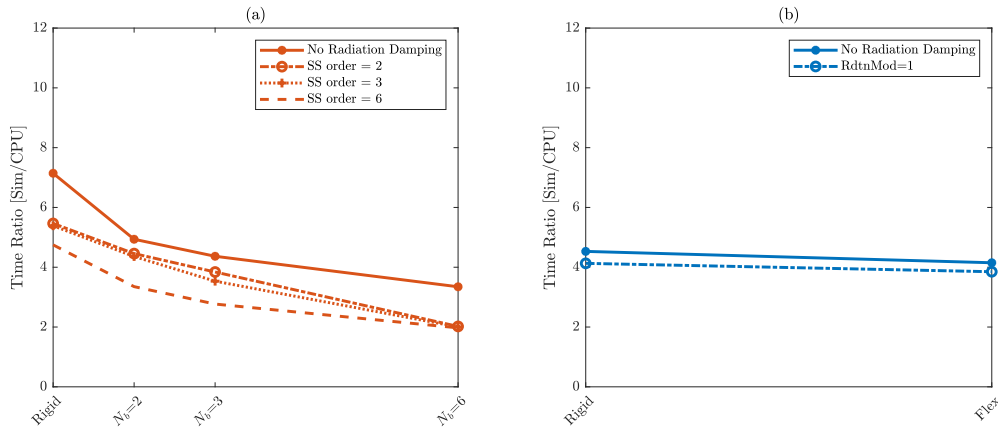
Figure 3.27: Performance study. a) OM Time Ratio (simulated time versus CPU time) as function of structural dynamic fidelity (tower/blade units N considered). The effect of the radiation damping state-space approximation order on the system performance is also considered. b) FAST Time Ratio as function of structural dynamic fidelity (flex case considers all tower/blades modes DoFs). The radiation damping effect on the system performance is also depicted.

all rigid and structural modes DoFs are enabled. Results are depicted in Figure 3.27. Figure 3.27a shows the time ratio for the present code, while Figure 3.27b shows the performance of reference code FAST. The present code performance is comparable with FAST. FAST time ratio does not vary significantly (max: 4.53, min: 3.85). The present code performance, on the other hand, varies as a function of structural dynamic fidelity and the state-space radiation approximation order. If no radiation damping is considered, the purely rigid dynamics time ratio is about 7. The time ratio reduces to about 2 if six blade units and a sixth-order state-space approximation are used. A lower time ratio is expected given higher modeling fidelity. However, computational improvement may be achieved by optimizing the blade structural code. Future work will address code performance optimization.

3.8 Conclusions

This chapter presented the further development of a fully-coupled aero-hydro-servo-elastic tool able to easily accommodate arbitrary platform and tower ge-

ometries and number of wind turbines employed. Development is carried out in Modelica, making use of the modelica standard library and the associated multi-body environment. Key implementations are the following:

- A complete multibody environment accounting the the major system components has been developed.

- Full beam-element momentum capabilities were achieved by integrating into Modelica the NREL open-source aerodynamic module AeroDyn v15 and wind-profile processor InflowWind within FAST v8. To establish this interface, a dedicated aerodynamic subroutine is written in Fortran 90 and compiled in a dynamic link library. A code buffer is also developed in C to bridge Modelica and Fortran 90.

- Structural dynamics of tower and blades is implemented by means of an MB-based approach, thus discretizing such structures with a series of concentrated masses and stiff joints.

The standard single-rotor Phase IV OC3 design is used throughout the development and benchmark process. A thorough code-to-code benchmark is performed by assessing the present code accuracy against FAST v8, and positive results and good performance of the present tool are obtained. To date, no aerodynamic interaction between rotors is included, as well as the tower influence on the wind field and aerodynamic loads on the tower. Aerodynamic interaction between adjacent rotors may be handled within BEM aerodynamics by first employing CFD-based models to assess the steady-state velocity field around the rotors for different states of the system, and later coupling the resulting wind velocity deficit to the undisturbed wind velocity field computed in InflowWind.

Chapter 4

Dynamics of a Two Rotor Floating Wind Turbine

Omar El Beshbichi [a], Yihan Xing [a], Muk Chen Ong [a]

[a] Department of Mechanical and Structural Engineering and Materials Science, University of Stavanger, Stavanger, Norway.

Abstract

The dynamic response of a two-rotor wind turbine mounted on a spar-type floating platform is studied. The response is compared against the baseline OC3 single-rotor design. Structural design shows how the two-rotor design may lead to a mass saving of about 26% with respect to an equivalent single-rotor configuration. Simulations predict significant platform yaw response of the two-rotor floating wind turbine - about 6 deg standard deviation at the rated operating wind speed. It is shown how the platform yaw response is directly caused by the turbulence intensity at the hub coupled with the transversal distribution of thrust loads on the structure. A coupled control strategy for the rotor-collective blade pitch controller is proposed, in which a simple proportional control mitigating platform yaw motion is superimposed to the baseline OC3 PI controller. Numerical simulations show how platform yaw response is reduced by about 60%, at the cost of mean power loss at below-rated wind speeds of about 100 kW and maximum increase of the rotor-collective blade-pitch angles standard deviation of about 2 deg. Parametric analysis of mooring lines design shows how an equivalent mass density of the line of at least 190 kg/m is needed to avoid vertical loads at the anchors.

Keywords: Floating offshore wind turbines, Dynamic analysis, Multi rotor wind turbines, Spar-buoy platform, Modelica.

4.1 Introduction

Offshore wind energy is a steadily growing industry, reaching in 2019 a total worldwide offshore wind power capacity of 30 GW out of a total worldwide wind power capacity of 600 GW (GWEC, 2019). Offshore wind energy is appealing since wind speed is much greater offshore than inland, and since many of the drawbacks of wind turbine deployment derives from interaction with populated areas (Cruz and Atcheson, 2016). Ideal wind energy sites are mostly locations where water depth far exceeds 50 m, while bottom-fixed offshore wind turbines are economically feasible to be deployed only in shallow water depths (Jonkman, 2007). Floating wind turbines (FOWTs), able to be deployed in deep waters, offer a technological solution, and may thus help in the reduction of the overall levelized cost of energy (LCoE) associated with wind energy.

Reduction of the overall LCoE may in principle be achieved also by means of downscaling wind turbines into equivalent multi-rotor systems (two or more wind turbines installed on the same structure). The development of multi-rotor wind turbines is an old idea, first developed early in the 20th century when the lack of advanced glass fiber composite materials made the manufacturing of large rotors unfeasible (Jamieson and Branney, 2012). The rated power of a wind turbine is proportional to the net area swept by the rotor blades - it thus scales with the square of the rotor radius. However, the blade mass generally increases with the cube of the rotor radius, thus making an array of smaller turbine units advantageous (Jamieson and Branney, 2012). Multi-rotor wind turbine concepts are also interesting from an economical and logistical perspective, since small blades are easier to manufacture, transport, and deploy with respect to state of the art blade sizes. Vestas Wind Systems A/S installed a multi-rotor demonstrator at the Technical University of Denmark, named 4R-V29, composed of four 225kW wind turbines mounted on a single structure and in operation between 2016 and 2019. van der Laan et al. (2019) recently compared numerical results obtained from several Reynolds-Averaged Navier-Stokes equations (RANS) tools against field measurements of power performance and wake deficit, showing faster wake recovery and marginally higher power output at below-rated environmental conditions given by the rotors aerodynamic inter-

action. Bastankhah and Abkar (2019) also performed a large-eddy simulation to study the wake flow properties of a similar four-rotor concept. They found out that the wake recovery is faster at short downwind distances with respect to a single-rotor system. The EU-funded project InnWind (INNWIND, 2015) proposed a 20 MW configuration composed of 45 turbines 444 KW each. Conclusions claimed a reduction of the LCoE against an equivalent single-rotor configuration of about 15%. Kirchner-Bossi and Porté-Agel (2020) showed that the optimization of the layout of multi-rotor wind farms may lead to significant benefits also in terms of overall power density compared to a baseline single-rotor wind farm layout. Research of multi-rotor concepts mounted on floating platforms is to date scant. First concepts date back to the time of the earliest works in the field, such as the work of Heronemus (1972). Multiple Unit Floating Offshore Windfarm (MUFOW) (Barltrop, 1993) was a UK based project started in 1993 aiming at the investigation of the feasibility of arrays of wind turbines mounted on a single floating platform. However, the idea has yet to be studied thoroughly and its feasibility has yet to be analyzed in detail. The overall dynamic response of the floating system must be carefully studied, as well as the aerodynamic interaction of the rotors under operative and extreme environmental conditions.

In this work, the dynamic response of a two-rotor wind turbine mounted on a spar floating platform is studied. The study relies upon a reduced aerodynamic model, simplified yet adequate to get the overall dynamic characteristics of the two-rotor FOWT concept. The advantageous stability and relatively simple design and manufacturing of spar-type platforms made it one of the most studied designs over the years, and the abundance of reference designs makes it suitable to be used in conceptual analyses. Phase IV OC3, for instance, is widely used as a major reference design (Jonkman, 2009b, 2010). Full-scale deployment of floating wind turbines also utilized spar-type design, as in Hywind Demo (Equinor, 2020a), the first full-scale prototype of a FOWT deployed in Norway in 2009, as well as in Hywind Scotland (Equinor, 2020b), the first floating wind farm situated in Scotland and commissioned in 2017.

The analysis of this work relies on an in-house tool for the simplified fully-coupled analysis of FOWTs concepts. The predictive tool is developed in Mod-

elica, a non-proprietary, declarative, object-oriented language developed by the non-profit Modelica Association and employed to conveniently model multi domain systems (The Modelica Association, 2020). The two-rotor FOWT system is modeled as a rigid body. A dummy degree of freedom (DOF) describing the simplified rigid rotor dynamics is added to the system equations of motion (EQM) in order to determine the aerodynamic state of the system. The aerodynamic loads are then modeled as concentrated thrusts acting on the rotor hubs and as concentrated torques acting on the rotor low-speed shafts. The aerodynamic loads are computed by considering the relative velocity between the hub and wind transversal to the rotor plane and mapping the steady-state aerodynamic coefficients of the wind turbine. This method is thought of as a simplified alternative to more complex beam-element/momentum (BEM) models, and previous work showed how results obtained are accurate in terms of overall dynamic response in operative environmental conditions (El Beshbichi et al., 2021b). The method, however, presents major limitations when considering more complex dynamic interactions. The rotors flexibility and dynamic contributions to the overall system dynamics are neglected. The aerodynamic interaction between rotors, as well as the aerodynamic effects induced by skewed flows are also not considered.

The present work is structured as follows. First, the two-rotor wind turbine concept (2WT) is presented. A simple structural study is carried out in order to define first-attempt tower dimensions and inertial properties. Moreover, the spar platform design is carried out by setting forth general hydrostatic performance considerations. Next, the dynamic response of the 2WT system is analyzed and contrasted with the response of the reference OC3 floating wind turbine. The response of the 2WT system is analyzed by means of two different rotor-collective blade pitch control strategies: the baseline OC3 controller, and a coupled controller that incorporates mitigation of yaw response. Finally, remarks about mooring lines dimensioning applied to the 2WT system are given.

Table 4.1: NREL offshore 5-MW Baseline Wind Turbine Specifications (Jonkman, 2007).

Rotor Diameter	m	126
Hub Height	m	90
Rotor Mass	kg	110×10^3
Nacelle Mass	kg	240×10^3
Cut-In, Rated, Cut-Out Wind Speed	m/s	3, 11.4, 25
Cut-In, Rated Rotor Speed	rpm	6.9, 12.1
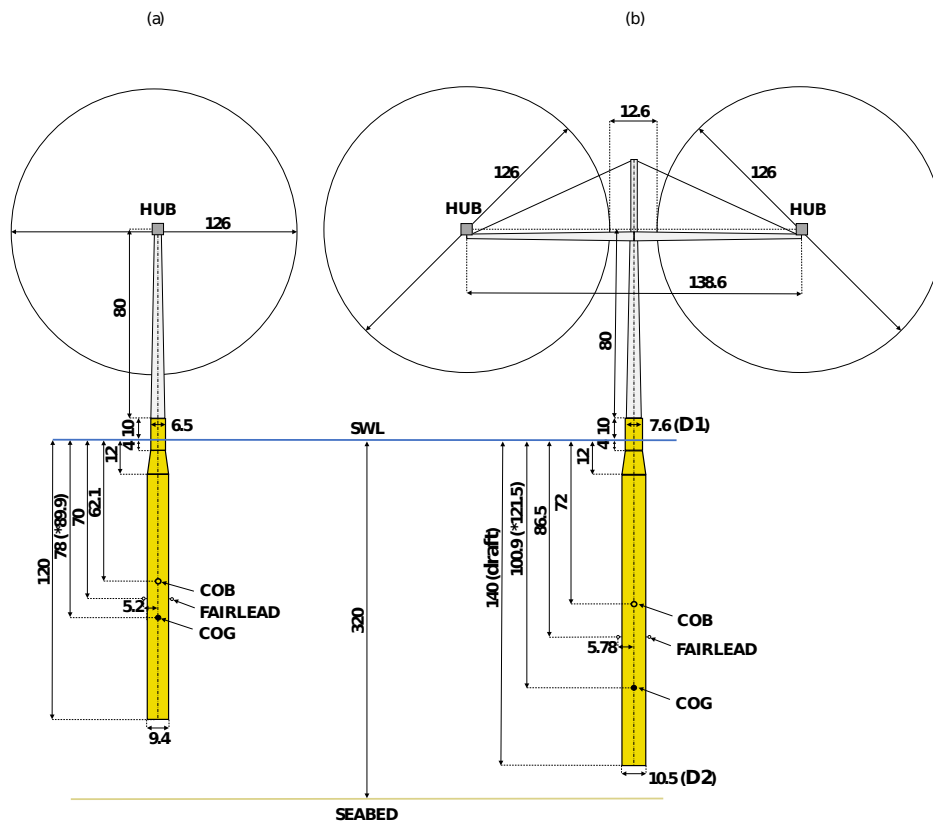
Figure 4.1: a) OC3 geometry [m] (Jonkman, 2007, 2010). b) 2WT configuration selected in the present study [m]. (* When only the floating platform is considered, the depth to COG is 89.9 m for the OC3 platform, and 121.5 m for the 2WT configuration.)

4.2   Multi-Rotor Wind Turbine Concept

Figure 4.1 shows the two-rotor wind turbine concept defined in the present work in relation to the standard OC3 design (Jonkman, 2007, 2010). The concept is composed of a two-rotor wind turbine mounted on a spar-buoy floating platform. As in any new technology development, the two-rotor FWT will eventually converge to the most optimal concept. This means that the OC3 spar design might not be the most optimal concept for the two-rotor WT. However, the OC3 spar design has been studied extensively by a large number of researchers over the last decade. Using this concept in the present paper offers the advantage of greatly aiding result assessment.

The hub height from the sea water level (SWL) is about 90 m, while the horizontal distance between the hubs is about 138.6 m. The center of gravity (COG) of the OC3 system is about 78 m from the SWL, while it is about 100.9 m for the 2WT system. Standard NREL 5-MW wind turbines are used in this study, whose main specifications are listed in Table 4.1. The horizontal rotor spacing is assumed to be 10% of the rotor diameter, inspired by the multi-rotor turbine concept installed at DTU Risø by Vestas A/S (Bastankhah and Abkar, 2019). The 2WT tower is composed of a main vertical tapered cylinder, a secondary vertical cylinder mounted on top of it, and two horizontal tapered cylindrical arms supporting the rotor nacelle assemblies (RNAs). Wires are used to connect the end of the horizontal arms to the top of the vertical structure. The inclination angle of the wires is 30 deg. This structural geometry allows for distribution of the aerodynamic loads on the horizontal arms as bending loads, while the wires distribute the static loads given by the arms self-weight and RNAs concentrated weight at the hubs as compression loads on the main structure. The assessment of local buckling resistance is neglected at this stage.

In the context of the present work, a simple structural dimensioning of the tower is carried out with the aim of defining first-attempt global inertia properties of the FOWT system. The following study is thus simplified and not intended to focus on detailed structural design. Table 4.3 summarizes the selected tower geometry in terms of cross-sectional dimensions of each tower sub-domain. Data are given in terms of inner diameter, outer diameter, and

Table 4.2: Parameters used in simple tower structural design (European Standard, 2006).

ρ_{steel}	kg/m^3	8500
S_{yield} (JIS SS400)	MPa	230
Wire Grade, R_r	MPa	1960
Wire Fill factor, f	-	0.8
Wire Spinning loss factor, k	-	0.9
Wire Self weight	N/mm^3	830x10^{-7}
Safety factor, γ	-	1.4

Table 4.3: Tower geometry selected in simple structural design, maximum loads and utilization ratio.

		Vertical tower	Horizontal arms	Top cylinder	Wire
Inner diameter (base)	m	6.22	4.732	3.26	-
Outer diameter (base)	m	6.28	4.79	3.29	-
Thickness (base)	m	0.03	0.028	0.014	-
Inner diameter (top)	m	4.75	1.79	3.26	-
Outer diameter (top)	m	4.79	1.77	3.29	-
Thickness (top)	m	0.0215	0.014	0.014	-
Diameter	mm	-	-	-	107
Effective load, S_e (bending/axial)	MPa	135	94	-	1058
S_e/S_{yield}	-	0.58	0.40	-	0.54

related thickness, and are given both at the base and top of the sub-structure. Intermediate cross-sections are defined through linear tapering. The structural computation assumes the maximum aerodynamic thrust acting at the hub, i.e., 808kN for the NREL 5-MW wind turbine (Jonkman, 2007). The wire tension and the reaction forces acting at the horizontal arms base are readily computed by solving the associated statically indeterminate beam problem. The loaded cross-section area must be big enough to prevent yield (S_{yield}). Yield assessment is performed at the most stressed sections of the structure, i.e., at the tower base and at the horizontal arm base. A safety factor (γ) of 1.4 is used to obtain a conservative design. The yield assessment can be prescribed as follows:

$$\frac{4r_{out}M}{\pi(r_{out}{}^4 - r_{in}{}^4)} \leq \frac{S_{yield}}{\gamma} \tag{1}$$

where M is the bending load acting at the base of the tower sub-domain, and r_{out} and r_{in} are the outer and inner radii at the base cross-section, respectively. Maximum and minimum values of thickness are considered, equal to 0.04 m and 0.001 m, respectively. The bending moment acting at the base of the horizontal arms is assumed given by the action of the aerodynamic thrust, the RNA weight concentrated at the hub, and the horizontal arm self-weight. On the other hand, the bending moment acting at the base of the vertical tower is assumed chiefly related to the action of the aerodynamic thrusts. Effective loads, as well as the ratio between effective and yield stress, are listed in Table 4.3. The bending stress obtained is equivalent to about 94 MPa at the horizontal arms base and about 135 MPa at the vertical tower base, following an utilization ratio close to 50%. The total concentrated mass of the tower thus defined is about 536.9 tonnes. The wire dimensioning is carried out in accordance with the recommended guidelines of the standard EN1993-1-11 (based on EN 1990) (European Standard, 2006). The wire cross-section must be big enough to prevent yield under maximum external load. A value of γ equal to 1.4 is used also in this case. The wire diameter can be estimated as follows (European Standard, 2006):

$$d_{wire} \geq \sqrt{\frac{4T\gamma}{\pi f k R_r}} \tag{2}$$

where T is the wire tension, R_r is the wire grade, f is the wire fill factor, and k is the spinning loss factor. The obtained wire tension is about 7730kN, while the obtained wire diameter is about 107 mm. The wire concentrated mass is about 4.94 tonnes. Table 4.2 summarizes the parameters used for preliminary tower and rope design.

4.3   Platform Design Criteria

The dimensioning process of a floating platform is mainly driven by 1) the maximization of pitch stiffness in order to reduce maximum static pitch angle, 2) the maximization of natural heave period in order to reduce wave-induced motion, and 3) the reduction of the overall cost, chiefly driven by the platform mass and dimensions (Cruz and Atcheson, 2016). Fatigue criteria are also applied in later design stages but may be neglected in conceptual design. The design space of a spar-buoy platform is generally composed of the platform draft, the upper diameter D_1, and the lower diameter D_2 as major design parameters. Platform design parameters associated to the final system geometry adopted in this work are those depicted in Figure 4.1. The distance between the SWL and the top of the platform is equal to the value used in the standard OC3 design, that is, 10 m. The distance between SWL and the top of the lower spar section is also equal to the standard OC3 value, 12 m. Spar thickness is assumed constant and equal to 0.05 m. The platform design is carried out in terms of hydrostatic performance, and simple computations can at this stage be employed in order to obtain useful predictions. The following sections present a brief discussion of the common criteria used in platform design.

4.3.1   Hydrostatic Considerations

The major criteria used in platform design can be described as follows:

1. The floating platform must achieve hydrostatic equilibrium. In order to enforce the constraint, the mass of the spar-buoy ballast is imposed by means

of the following hydrostatic vertical equilibrium:

$$m_{ballast} = \frac{\rho_{water}V_w g - 3F_{m,v} - m_s g - m_{t,n,r}g}{g} \tag{3}$$

where ρ_{water} is the water density, V_w is the water displaced volume, g is the acceleration due to gravity, $F_{m,v}$ is the total vertical mooring line static load, m_s is the spar-buoy mass, and $m_{t,n,r}$ is the mass of tower, nacelles, and rotors. In the design process, the ballast center of gravity is assumed to be located at 5 m from the bottom of the spar-buoy platform. $F_{m,v}$ is assumed equal to the vertical mooring line static load of the OC3 standard design.

2. The maximum static pitch angle must be sufficiently small, in order to avoid an excessive pitch dynamic response and to limit the loss of annual energy production (AEP) due to the skewed flow conditions (Cruz and Atcheson, 2016). According to Zambrano et al. (2006), the maximum static pitch angle must not exceed 5 deg with ±15 deg of dynamic amplitude. The static pitch angle can be estimated as follows (Pham and Shin, 2019):

$$\theta_5 = \frac{F_{thrust}HB}{C_{55}} \tag{4}$$

where θ_5 is the static pitch angle, F_{thrust} is the overall thrust force acting at the hubs, HB is the vertical distance from the hubs to the center of buoyancy (COB) of the spar-buoy platform, and C_{55} is the hydrostatic restoring pitch stiffness, which can be derived from metacentric height relationships (Faltinsen, 1993).

3. The pitch and heave natural periods must be larger than 25-30 s in order to avoid resonance motions with first-order wave effects (Bachynski and Moan, 2012). The heave period is estimated as follows:

$$T_{33} = 2\pi\sqrt{\frac{m_{tot} + A_{33}}{\rho_{water}g A_w}} \tag{5}$$

where m_{tot} is the overall FOWT mass, A_{33} is the added mass component in heave direction, and A_w is the waterplane area. The value used to estimate A_{33} is assumed in the design stage constant and equal to the value associated with the standard OC3 platform (Jonkman, 2010). The pitch period is estimated by considering surge-pitch coupling. The estimation is carried out by solving the associated surge-pitch characteristic equation:

$$\left(-\omega^2 \left(\begin{bmatrix} m_{tot} & z_{cog}m_{tot} \\ z_{cog}m_{tot} & I_{55} \end{bmatrix} + \begin{bmatrix} A_{11} & A_{15} \\ A_{51} & A_{55} \end{bmatrix}\right) + \left(\begin{bmatrix} 0 & 0 \\ 0 & C_{55} \end{bmatrix} + \begin{bmatrix} C_{m,11} & C_{m,15} \\ C_{m,51} & C_{m,55} \end{bmatrix}\right)\right)\underline{\phi} = \underline{0} \tag{6}$$

where ω and $\underline{\phi}$ are the eigenvalues and eigenvectors of the system, z_{cog} is the vertical location of the overall center of gravity of the FOWT system, I_{55} is the overall pitch inertia, A_{11}, A_{15}, A_{51}, and A_{55} are, respectively, the added mass in surge, surge-pitch, pitch-surge, and pitch directions, and $C_{m,11}$, $C_{m,15}$, $C_{m,51}$, and $C_{m,55}$ are, respectively, the mooring linear stiffness values in surge, surge-pitch, pitch-surge, and pitch directions. The pitch period is simply computed as:

$$T_{55} = \frac{2\pi}{\omega_5} \tag{7}$$

where ω_5 is the eigenvalue associated with the pitch direction. The values used to estimate the added mass and mooring lines linear stiffness are assumed in the design stage constant and equal to the value associated with the standard OC3 platform (Jonkman, 2010). The mooring lines stiffness is relative to an unstretched length of 902.2 m, a mass density of 77.71 kg/m, a vertical static length of 250 m, and a diameter of 0.09 m. The platform draft affects the vertical static length of the mooring lines, and consequently the mooring lines stiffness. Hence, a difference is to be expected between the dynamic response of the system and the hydrostatic results. The difference is assumed to be small in pitch and heave directions and therefore tolerable in a preliminary design context.
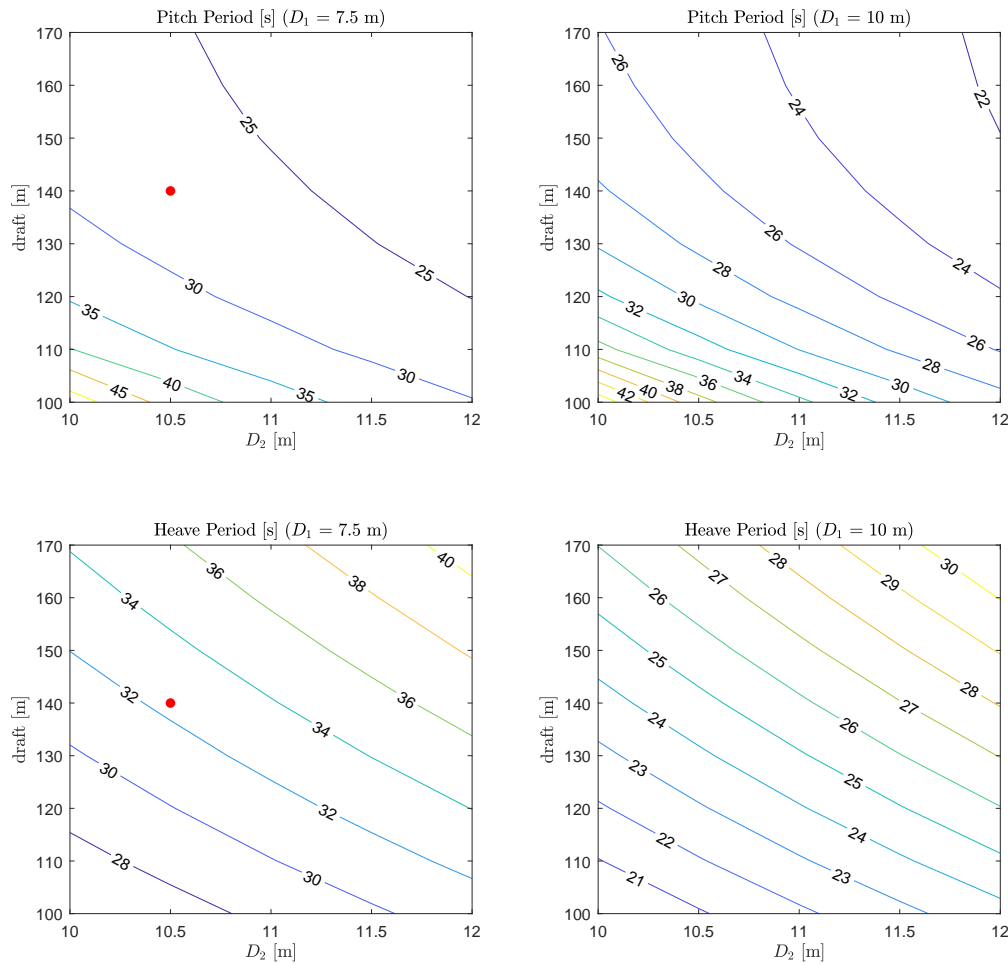
Figure 4.2: Pitch and Heave periods as a function of platform design parameters. Left plots are relative to an upper diameter $D_1 = 7.5$ m. Right plots are relative to an upper diameter $D_1 = 10$ m. The red dot denotes the design point selected in this work.

Periods

Figure 4.2 shows the variation of heave and pitch periods of the 2WT system as a function of the draft, lower diameter D_2, and higher diameter D_1 within 100 m<draft<170 m, 10 m<D_2<12 m, and D_1 either equal to 7.5 m (left-hand side plots) or equal to 10 m (right-hand side plots). The red dot denotes the final spar design configuration selected in the present work. As shown, the pitch period tends to increase in configurations with shorter draft and D_2 lengths, while it does not vary substantially with variations of D_1. Values obtained indicate that only for unrealistic configurations given by extremely long draft and
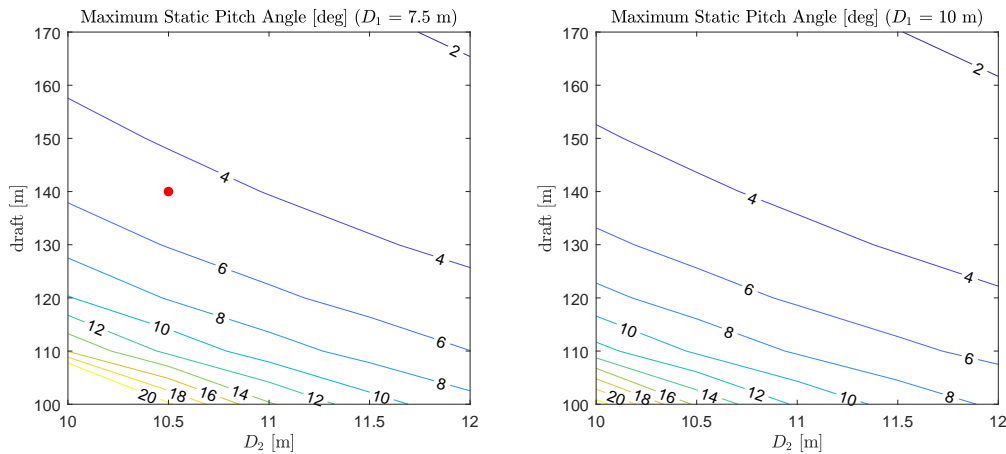
Figure 4.3: Maximum static pitch angle as a function of platform design parameters (maximum thrust is assumed). Left plot is relative to an upper diameter D_1 = 7.5 m. Right plot is relative to an upper diameter D_1 = 10 m. The red dot denotes the design point selected in this work.

D_2 the pitch period becomes unacceptably short. The heave period tends to increase in configurations with longer draft and D_2 lengths and reduces substantially in configurations with longer D_1 lengths. Note that in the case of D_1 = 10 m, the heave period reduces to values close to 25 s for feasible values of draft and D_2. Also for this reason, longer D_1 lengths should be avoided.

Maximum Static Pitch Angle

Figure 4.3 shows the maximum static pitch angle of the 2WT system as a function of platform design parameters within the same value range used in Figure 4.2. As it is clear, a greater maximum static pitch angle is obtained for shorter lengths of draft and D_2. Longer lengths of D_1 reduce to a minor extent the static pitch angle. The isoline relative to 4-5 deg should be considered as a threshold for acceptable platform configurations. Note that the maximum static pitch angle is the most stringent constraint in the design of two-rotor floating wind turbines, given that it eliminates most of the design space.
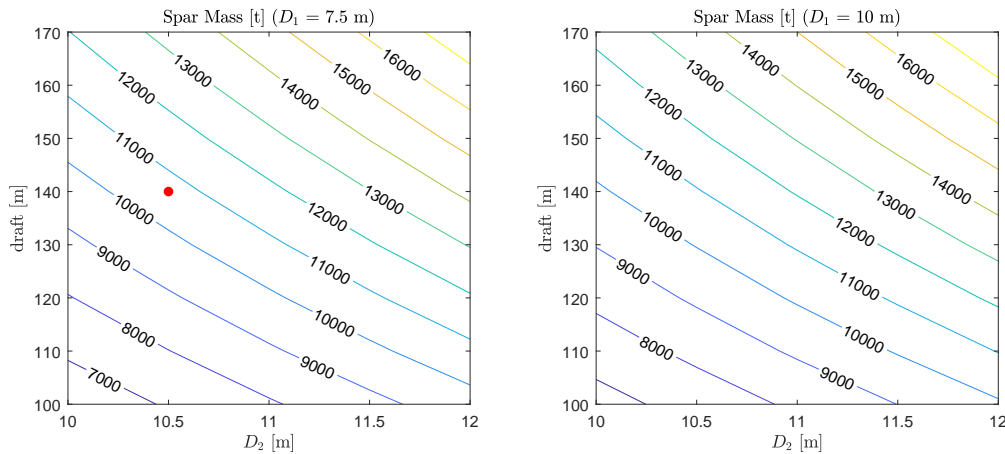
Figure 4.4: Overall spar-buoy mass (including ballast) as a function of platform design parameters. Left plot is relative to an upper diameter D_1 = 7.5 m. Right plot is relative to an upper diameter D_1 = 10 m. The red dot denotes the design point selected in this work.

Mass Sensitivity

Figure 4.4 shows the overall spar-buoy mass (including ballast) as a function of platform design parameters within the same value range used in Figure 4.2. The spar mass should always be minimized in order to reduce the construction, material, and deployment cost.

4.3.2 Platform Configuration

The selection process of a feasible platform configuration is based on a trade-off among the design constraints previously mentioned. The main design objective is to achieve acceptable hydrostatic performance and to minimize the platform mass to be employed. Drafts longer than 140 m are unfeasible to deploy and are susceptible to fatigue loading, while higher D_2 lengths generally lead to excessive manufacturing and deployment costs (Cruz and Atcheson, 2016). From design considerations several conclusions can be drawn. For a two-rotor FOWT employing multi-MW wind turbines, such as the 2WT concept considered in the present study, heave and pitch periods are generally not a stringent constraint within the region of feasible designs in view of the greater inertia involved. For draft lengths shorter than 130-140 m the maximum static pitch angle exceeds

Table 4.4: Geometrical-inertial-hydrostatic specifications for the platform configuration selected in the present work and for the standard OC3 spar platform (Jonkman, 2007).

		OC3	**2WT**
D_1	m	6.5	7.6
D_2	m	9.4	10.5
draft	m	120	140
Depth to COG	m	89.92	121.5
Water Displacement	m^3	8×10^3	11.7×10^3
Mass (including ballast)	kg	7.4×10^6	10.6×10^6
Roll Moment of Inertia about COG	kgm^2	4.2×10^9	1.13×10^{10}
Pitch Moment of Inertia about COG	kgm^2	4.2×10^9	1.13×10^{10}
Yaw Moment of Inertia about Centerline	kgm^2	1.6×10^8	1.7×10^8
Heave Hydrostatic restoring stiffness	N/m	3.3×10^5	4.56×10^5
Roll Hydrostatic restoring stiffness	Nm/rad	1.3×10^9	3.42×10^9
Pitch Hydrostatic restoring stiffness	Nm/rad	1.3×10^9	3.42×10^9
Mass (platform, ballast, tower, nacelle, rotor)	kg	8.06×10^6	11.8×10^6

Table 4.5: Mass saving between two OC3 units and a single 2WT concept.

		2-OC3	**2WT**	**Variation**
Mass (platform, ballast, tower, nacelle, rotor)	kg	16.12×10^6	11.8×10^6	-26.30%

the limit imposed of 5 deg. This constraint is the most stringent of the design process. Higher D_1 lengths are slightly beneficial in terms of maximum static pitch angle, but significantly reduce the heave period and increase the platform mass of about 500 tonnes. In the present work, the platform configuration selected is characterized by a draft of 140 m, D_1 = 7.5 m, and D_2 = 10.5 m. Table 4.4 summarizes the geometrical, the inertial, and the hydrostatic specifications of the configuration selected, together with the specifications of the baseline OC3 spar-buoy platform. The fairlead depth from SWL is assumed to be equally distanced from the COG and the COB, as in the case of the baseline OC3 design. The fairleads depth from SWL is thus equal to 86.5 m. The ratio between the fairlead radius and D_2 is set equal to the one used in the baseline OC3 design. The fairlead radius from the centerline is thus equal to 5.78 m. The overall concentrated mass of the 2WT system is about $11.8x10^3$ tonnes. The moments of inertia are computed by employing a CAD model of the FOWT system. The RNA mass is assumed to be concentrated at the hub. The associated inertia tensor of the 2WT system computed at the COG can be written as follows:

$$[I]_{,2WT} = \begin{bmatrix} 6.13x10^{10} & -5.93x10^5 & 1.67x10^7 \\ -5.93x10^5 & 5.77x10^{10} & 1.47x10^5 \\ 1.67x10^7 & 1.47x10^5 & 3.69x10^9 \end{bmatrix} kgm^2 \quad\quad (8)$$

Table 4.5 shows the relative variation of mass between two standard OC3 wind turbine units and an equivalent 2WT concept. Even without performing structural optimization, the present 2WT design brings about a significant mass saving of about 26.3% with respect to an equivalent single-rotor configuration. Equivalently, the rated power-to-weight ratio associated to the 2WT concept is about 0.85 W/kg, in place of 0.61 W/kg of the OC3-Hywind design. However, the power-to-weight ratio does not consider the overall power performance of the system but assumes rated power for each rotor as independent systems. The aerodynamic performance of the 2WT design must be carefully studied by considering all the major aerodynamic effects and interactions before an accurate statement on power performance can be drawn.

Table 4.6: Load cases (LCs) (Bachynski and Moan, 2012).

		1	2	3
Significant wave height, H_s	m	2.5	3.1	4.4
Peak wave period, T_p	s	9.8	10.1	10.6
Mean wind speed at hub, U	m/s	8	11.4	18
Turbulence intensity at hub, I	-	0.20	0.17	0.15

4.4 Fully-Coupled Dynamic Analysis

In this work, the coupled dynamic behavior of the 2WT concept is studied by employing an in-house code implemented by means of the object-oriented language Modelica. The approach allows for easy implementation of arbitrary platform geometries and platform/rotor configurations. Previous benchmarking work (El Beshbichi et al., 2021b) based on the International Energy Agency (IEA) code-to-code comparisons for the baseline OC3 design (Jonkman et al., 2010) has also shown how this method gives good agreement to well established dynamic codes in situations where rotor dynamic contribution can be neglected. The system is assumed to be rigid. The hydrodynamic added damping values employed are assumed equal to those associated with the baseline OC3 design. Albeit yaw mooring stiffness is associated with the mooring lines design, in this work its value is assumed constant and equal to the one characterizing the baseline OC3 design. The rotor inertial effects, including the contribution of gyroscopic effects on the system dynamics, are not considered.

4.4.1 Environmental Conditions

Three specific load cases (LCs) are considered in this work. Each case is characterized by directionally congruent turbulent wind and irregular waves based on standard JONSWAP spectra. Table 4.6 summarizes the characteristics of the LCs selected. The cases considered are relative to different environmental severity regions. The first case (LC1) is relative to a below-rated operational wind speed, the second case (LC2) is relative to the rated operational wind speed, and the last case (LC3) is relative to above-rated operational wind speed.

Wave energy content increases accordingly. The turbulence intensity at the hub follows the Kaimal spectrum with IEC Class B normal turbulence model (NTM), based on the standard IEC 61400-1 (International Electrotechincal Commission, 2005).

4.4.2   Hydrodynamic Modeling

The hydrodynamic loads are computed from linear (Airy) wave theory. Airy theory can be applied if the water depth is sufficiently deep (DNV, 2010). The numerical panel code Sesam-Wadam (DNV-GL) (DNV, 2017) is used to solve the frequency-domain linear hydrodynamic problem relative to the selected platform geometry. Time realizations of irregular wave loads are preventively computed by means of Inverse Fourier Transformations (IFT). The additional load contribution associated with hydrodynamic viscous drag is not considered in this work ($C_d = 0$). However, it should be noted that viscous drag loads may be significant in extreme environmental situations where much larger waves and current effects are considered (Zheng et al., 2020a).

4.4.3   Mooring Lines Modeling

Mooring lines design is assumed in this work equal to the standard OC3 design, that is, three catenary mooring lines mounted at 120 deg from one another (Jonkman, 2010). Figure 4.5 shows a top-view schematization of the standard mooring system employed in the 2WT spar-buoy platform, based on the OC3 design. $H_{F,1,2,3}$ are the horizontal mooring loads acting at the fairleads. Even though the delta catenary mooring lines used in the OC3-Hywind platform are not subject to significant yaw moments, their designs allow for yaw stiffness, which may be easily increased by increasing the fairlead length. A quasi-static formulation of the mooring lines loads is employed in order to obtain the loads-displacements relationship at the fairleads (Jonkman, 2007). The effect of the mooring lines design on the yaw stiffness is neglected, and a constant equivalent yaw stiffness of $9.8x10^7$ Nm/rad is used throughout the results to account for the effect of the delta lines. Moreover, the OC3-Hywind load-displacement
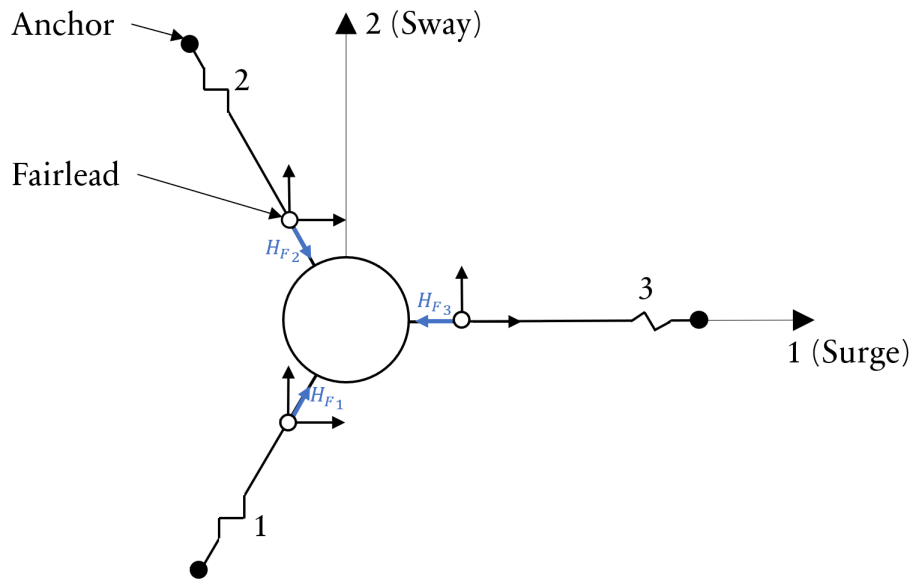
Figure 4.5: Mooring lines schematization (top-view) (El Beshbichi et al., 2021b).

relationship in the platform's yaw direction is found to be linear at least up to a platform's yaw angle of about 20 deg (Jonkman, 2010). A linear stiffness relationship can then be used also where the platform's yaw motion is considered significant. The mooring lines mass density used is set in this work equal to 200 kg/m.

4.4.4 Aerodynamic Modeling

In this work, the aerodynamic loads are computed by mapping the steady-state thrust and torque aerodynamic coefficients of each rotor. This approach is different to standard codes where a full BEM method is employed, and to simplified codes where the aerodynamic thrust is simply computed as function of the wind speed (Karimirad and Moan, 2012a). Integrated loads are used, and hence the distribution of the local aerodynamic loads and the associated local moments on the blades is neglected (Karimirad and Moan, 2012a). A simplified rigid rotor EQM is considered to emulate the rotors aerodynamic response. Aerodynamic concentrated thrusts are applied at the hubs, while aerodynamic concentrated torques are applied at the equivalent low-speed rotor shafts. The

relative velocity between hub and wind speed transversal to the rotor plane is used. The thrust loads are computed as (El Beshbichi et al., 2021b):

$$F = \frac{1}{2}\rho_{air}C_t(\lambda, \beta)A{U_{rel}}^2 \tag{9}$$

where ρ_{air} is the air density, C_t is the steady-state torque coefficient, λ is the tip speed ratio, β is the rotor-collective blade pitch angle, A is the rotor plane area, and U_{rel} is the relative speed between local wind and hub. The torque loads are computed as:

$$T = \frac{1}{2}\rho_{air}RC_q(\lambda, \beta)A{U_{rel}}^2 \tag{10}$$

where R is the rotor radius, and C_q is the steady-state torque coefficient. The three-dimensional wind velocity profiles at the hubs are computed in Turbsim (Jonkman, 2009a) and imported in the code. A 15X15 grid is used, wide enough to encompass the rotors space, and a time step of 0.05 s is used to generate the wind profiles. Wind time histories of 4000 s are computed for each environmental condition. This method, although generating accurate overall dynamic predictions in operational environmental conditions, is not able to detect more complex aerodynamic effects. For instance, the wind profile time realizations used for the computation of the concentrated aerodynamic loads are associated only with the hub locations. This assumption neglects the spatial turbulence variation on the rotors swept area. The effect of the horizontal arms on the local wind induction factors is also not considered. Moreover, skewed blade aerodynamics is not considered, as well as the aerodynamic interaction between the rotors. Albeit literature on similar two-rotor FOWTs is scant, research works in different fields concerning similar applications, such as the study of thrust deficit induced by the aerodynamic interaction among rotors of Unmanned Aerial Vehicles (UAVs) (Zhou et al., 2017; Alvarez and Ning, 2017), suggest that the effect of the rotor aerodynamic interaction on the overall system response may not be significant enough to compromise the general dynamic behaviour obtained in the present study. At any rate, the significance of these effects on two-rotor FOWT system dynamics can be quantified by employing corrected BEM aerodynamic capabilities in Modelica, which is a task
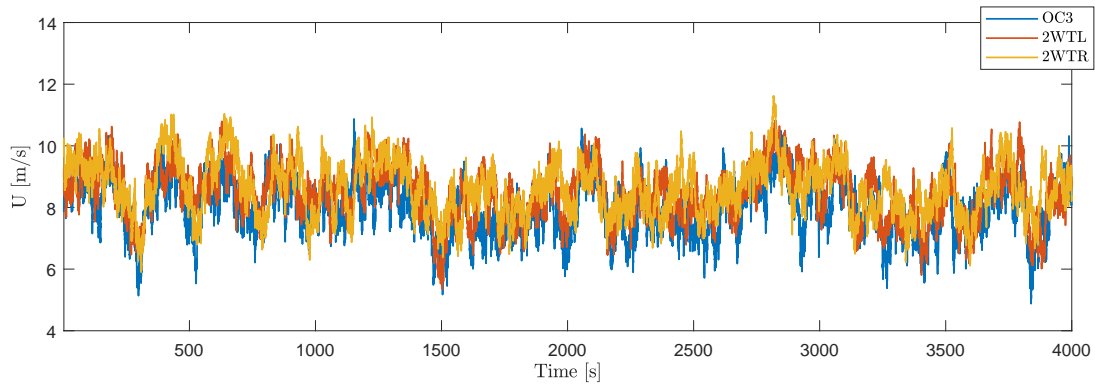
Figure 4.6: Wind profiles at the OC3, 2WT left turbine, and 2WT right turbine hub locations relative to the same realization (LC1 - Kaimal turbulence spectrum IEC Class B NTM).

currently under development.

The tower base local reference frame is assumed placed at the same inertial location for all configurations. Figure 4.6 shows the wind profiles relative to the same realization and attributed to the hub locations for the OC3 wind turbine, the 2WT left wind turbine (2WTL), and the 2WT right wind turbine (2WTR). The time histories are relative to a mean wind speed of 8 m/s (LC1).

4.4.5   Control Modeling

As it will be presented in detail in Section 4.5.4, the platform yaw motion response of the 2WT is particularly critical. For this reason, the quantification of the feasibility of mitigating the platform yaw motion by means of an optimized rotor-collective blade pitch control strategy is proposed. The pitch actuator dynamics is assumed fast enough to be neglected for rigid dynamics analysis. That is, there is no delay between the reference pitch angle and the actual pitch angle. A second-order low-pass filter can generally be used to represent pitch actuator dynamics. Common values for cut-off frequency and damping ratio are about 1 Hz and 0.7, respectively - fast compared to the system dynamics (Dunne and Pao, 2016). Two rotor-collective blade pitch control strategies are separately applied to the 2WT concept. The controls employed are the following:

- *OC3 baseline control.* The standard OC3 PI rotor-collective blade pitch
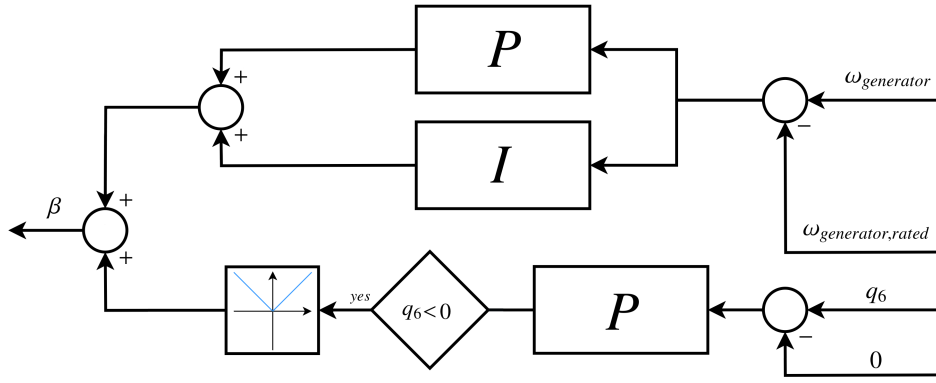
Figure 4.7: Block diagram of the 2WT coupled control concept for left wind turbine (right wind turbine condition: $q_6 > 0$).

control on the generator speed as described in Jonkman (2007) is used to independently control both rotors.

- *Coupled control.* The baseline OC3 baseline PI rotor-collective blade pitch control on the generator speed is linearly coupled with a proportional rotor-collective blade pitch control on the 2WT platform yaw motion.

The coupled control strategy proposed is designed to induce a reduction of aerodynamic thrust at the hub whose surge motion brought about by the yaw dynamics is positive. The rotor-collective blade pitch angle, β_i, where i denotes either the left (L) or the right (R) wind turbine, can be computed as:

$$
\begin{aligned}
\beta_i(t) =& K_P(\beta_i(t))\big(\omega_{i,gen}(t) - \omega_{gen,ref}\big) + \\
& K_I(\beta_i(t)) \int_0^t \big(\omega_{i,gen}(t) - \omega_{gen,ref}\big)dt + K_{q6,i}(q_6(t))|q_6(t)|
\end{aligned}
\tag{11}
$$

where $K_P(\beta)$ and $K_I(\beta)$ are, respectively, the proportional and integral gain-scheduling laws for the baseline OC3-Hywind PI control on the generator speed, $\omega_{gen}(t)$ is the generator speed, $\omega_{gen,ref}$ is the reference (rated) generator speed, $q_6(t)$ is the platform yaw motion in radians, and $K_{q6}(q_6)$ is the proportional gain-scheduling law for the P control on the platform yaw motion, which can be ex-

Proportional Gain at Minimum Blade-Pitch Setting (Generator speed control)	-	0.00627
Integral Gain at Minimum Blade-Pitch Setting (Generator speed control)	-	0.00089
Generator Torque at Rated Speed	Nm	43093
Proportional Gain (2WT yaw motion control)	-	1.5

pressed as:

$$
\begin{cases}
\text{if } i = L \begin{cases} K_{q6,i} = 0, & \text{if } q_6 > 0 \\ K_{q6,i} = K_{P,q6}, & \text{if } q_6 < 0 \end{cases} \\
\text{if } i = R \begin{cases} K_{q6,i} = K_{P,q6}, & \text{if } q_6 > 0 \\ K_{q6,i} = 0, & \text{if } q_6 < 0 \end{cases}
\end{cases}
\tag{12}
$$

where $K_{P,q6}$ is the constant gain to be determined from tuning analysis.

Figure 4.7 shows the block diagram representation of the coupled control strategy. Yaw motion is positive if counterclockwise. When the left rotor is considered, the yaw P control contribution is active only if yaw motion is negative. On the other hand, the right rotor yaw P control contribution is active only if the yaw motion is positive. The absolute value of the yaw control contribution is used to compute the final rotor-collective blade pitch angle induced by yaw dynamics. The standard OC3 variable-speed generator-torque control, as well as saturations of the rotor-collective blade pitch angles and pitch rates are also enforced in both cases (Jonkman, 2007). While the PI control on the generator speed is only active if the generator rotational speed reaches rated values, the P control on yaw motion is always activated.

Table 4.7 summarizes the control gains used in this work. As it will be described in detail in Section 4.5.2, a constant gain for the yaw control equal to 1.5 is selected. Figure 4.8 shows a time history of about 500 s of the rotor-collective blade pitch angle dynamics and thrust forces for both wind turbines of the 2WT concept with coupled control. The control dynamic response is associated to above-rated environmental conditions (LC3 - Table 4.6). The plot also shows the associated yaw response. The effect of the linear coupling between the base-
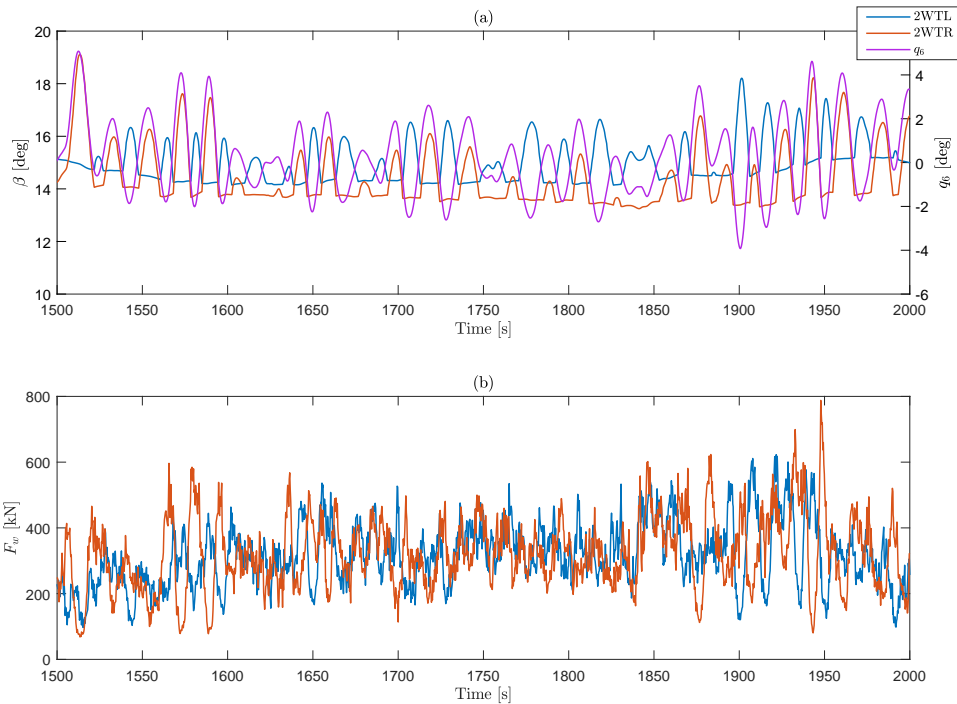
Figure 4.8: a) Rotor-collective blade pitch angles and platform yaw motion. b) Aerodynamic thrusts at hub. Coupled control schedule for 2WT at above-rated environmental condition (LC3).

line OC3 PI control and the yaw P control is clearly noticeable, as well as the associated influence on the rotor thrusts.

4.5 Results

The integration method *dassl* is employed to solve the equations of motion of the system, with a tolerance equal to $1x10^{-6}$ and a time step equal to 0.1 s. A simulation time equal to 4000 s is carried out. The first 400 s are discarded in order to let the initial transients of the system die out. The effective time series used to compute results are thus about 1-h long. Three systems are tested under the same environmental conditions: the baseline OC3 design, the 2WT concept with OC3 baseline control, and the same 2WT system with coupled control as described in Section 4.4.5. Every system employs mooring lines with a mass density of 200 kg/m. The dynamic response results are given in terms of platform motion $\underline{q}$, upstream fairlead tension T_2, and electric power production P_e,

Table 4.8: 2WT and OC3 damped natural periods, obtained from free decay tests in Modelica (note that mooring line mass density and yaw stiffness used with 2WT system are 200 kg/m and $9.8x10^7$ Nm/rad, respectively (Jonkman, 2007)).

		2WT	OC3 (200 kg/m)	OC3 (77.7 kg/m)
Surge	s	132.3	103.1	123.45
Heave	s	32.1	30.9	31.8
Pitch	s	29.7	28.2	28.5
Yaw	s	33.6	8	8.19

and are expressed in terms of overall mean values, μ, and standard deviations, σ.

4.5.1 System Natural Periods

Table 4.8 summarizes the damped natural frequencies of the 2WT system as computed from free decay tests in Modelica. The results obtained are compared against the damped natural frequencies of the OC3 system when the mooring mass density is equivalent to either the one used in the 2WT system (200 kg/m) or to the standard value found in the literature (77.7 kg/m) (Jonkman, 2007). The yaw stiffness of the OC3 system is assumed constant in the two cases. The assumption is reflected in a constant OC3 yaw period for different mooring characteristics. Higher inertia involved in the 2WT system lead to significantly higher surge and yaw periods with respect to the OC3 system. As expected from preliminary hydrostatic considerations, 2WT heave and pitch periods are for this configuration sufficiently longer than the limit imposed to avoid first-order wave excitations.

4.5.2 Effect of Yaw Control Proportional Gain Tuning (Coupled Control)

Generally, the tuning process of PI/PID wind turbine controllers is first obtained using methods such as pole-placement or Ziegler-Nichols and then refined by the employment of fully-coupled aeroelastic simulations to obtain an
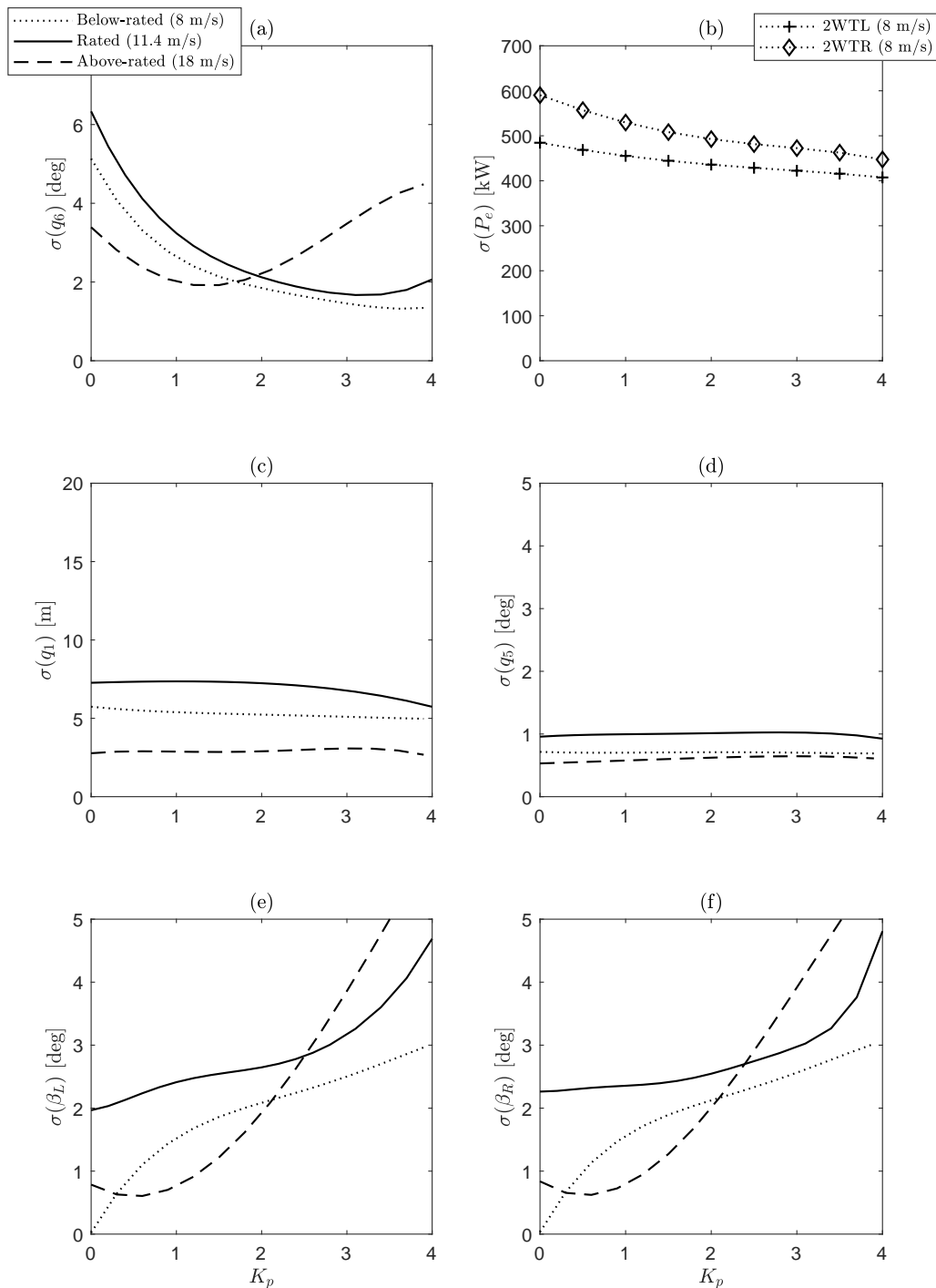
Figure 4.9: Standard deviation of (a) platform yaw motion, (b) electric power output, (c) platform surge motion, (d) platform pitch motion, (e) left rotor-collective blade pitch angle, and (f) right rotor-collective blade pitch angle of the 2WT system in relation to the yaw control proportional gain and under different operating wind speed (Table 4.6).

optimized tuning in terms of loads reduction and motion regulation (Ziegler and Nichols, 1993; Mirzaei et al., 2016). On this line, Hansen et al. (2005) determined the gains of a standard rotor-collective blade pitch PI controller by employing a minimization of the blade root flapwise bending moments. Tibaldi et al. (2012) performed a fine-tuning of two PI controllers respectively associated with below-rated and above-rated environmental conditions by minimizing a cost function based on fatigue loads, ultimate loads, annual energy production, and blade pitch actuator duty cycle. Control gain tuning is hence a trade-off analysis, necessary in order to identify the best tuning setup under contrasting objectives.

The main goal of the current analysis is to quantify the capability of a coupled control strategy to mitigate the platform yaw motion of the 2WT system. For this reason, a simple proportional control of the platform yaw motion is linearly superimposed to the OC3 baseline rotor-collective blade pitch PI control, as presented in Section 4.4.5. The tuning process is only focused on the additional proportional gain K_p, while the baseline PI controller retains the original OC3 gain-scheduling (Jonkman, 2007). The study of more advanced controllers, as well as the study of more thorough tuning strategies being able to further optimize the system response, are left as questions for further research.

The tuning is performed heuristically, and the main drivers are the following: 1) the minimization of platform yaw standard deviation, 2) the maximization of the mean electric power output, and 3) the minimization of the rotor-collective blade pitch angles standard deviation, which can be correlated with the aerodynamic thrust, torque, and the associated blade root loads standard deviation. Figure 4.9 illustrates the standard deviations of platform yaw, surge, and pitch motions, electric power output, and rotor-collective blade pitch angles of the 2WT system in relation to K_p for below-rated, rated, and above-rated environmental conditions. The platform yaw motion standard deviation reduces significantly for every environmental condition, reaching a minimum region at $K_p \simeq 2$. For above-rated environmental conditions, the yaw motion standard deviation increases significantly at high K_p values due to stalled-induced thrust fluctuations. Platform surge and pitch standard deviations are not notably affected by K_p. It can be noted how the rotor-collective blade pitch angles stan-

dard deviation is zero for $K_p = 0$ at below-rated environmental conditions, given by the lack of the PI controller contribution to the system response. The rotor-collective blade pitch angles standard deviation greatly increases with greater values of K_p, showing values higher than 2 deg for $K_p \geq 2$. Figure 4.10 illustrates the mean values for the same response parameters used in Figure 4.9. Platform surge and pitch mean motion reduces at high K_p values for below-rated environmental conditions, caused by the increased rotor-collective blade pitch mean angle and the associated reduction of aerodynamic thrust. The aerodynamic torque is reduced in the same manner, leading to a reduction of the overall electric power output. For $K_p = 4$ the electric power output loss is about 288kW. As listed in Table 4.7, the constant yaw control proportional gain selected for the present work is 1.5. Under this tuning schedule, platform yaw motion is minimized at the cost of an electric power output loss of 100 kW for below-rated environmental conditions and the increase of rotor-collective blade pitch angle standard deviation in the range of 0.5-2 deg.

4.5.3 Dynamic Response

Figure 4.11 shows the overall mean values for surge and pitch motion, electric power production, and upstream fairlead tension under different load cases for the OC3 system, the 2WT system configured with baseline OC3 control, and the 2WT system configured with the coupled control. Platform sway, heave, and roll motions are found to be small for each system and thus are not depicted in the results. Changing the rotor-collective blade pitch control strategy from the baseline OC3 to the coupled control strategy does not influence significantly the mean response of the 2WT system. As it is clear from the figure, the mean surge values are significantly lower in the OC3 system with respect to the 2WT concept, at each load case about twice the values obtained in the system. This is clearly associated with the doubling of aerodynamic thrust force in the 2WT concept. The maximum surge response in the 2WT concept is about 30 m and is obtained at the rated operating wind speed. The mean pitch values obtained in the OC3 system are higher with respect to the 2WT concept. The difference is of about 1 deg at the rated operating wind speed. As the pitch angle is one of the
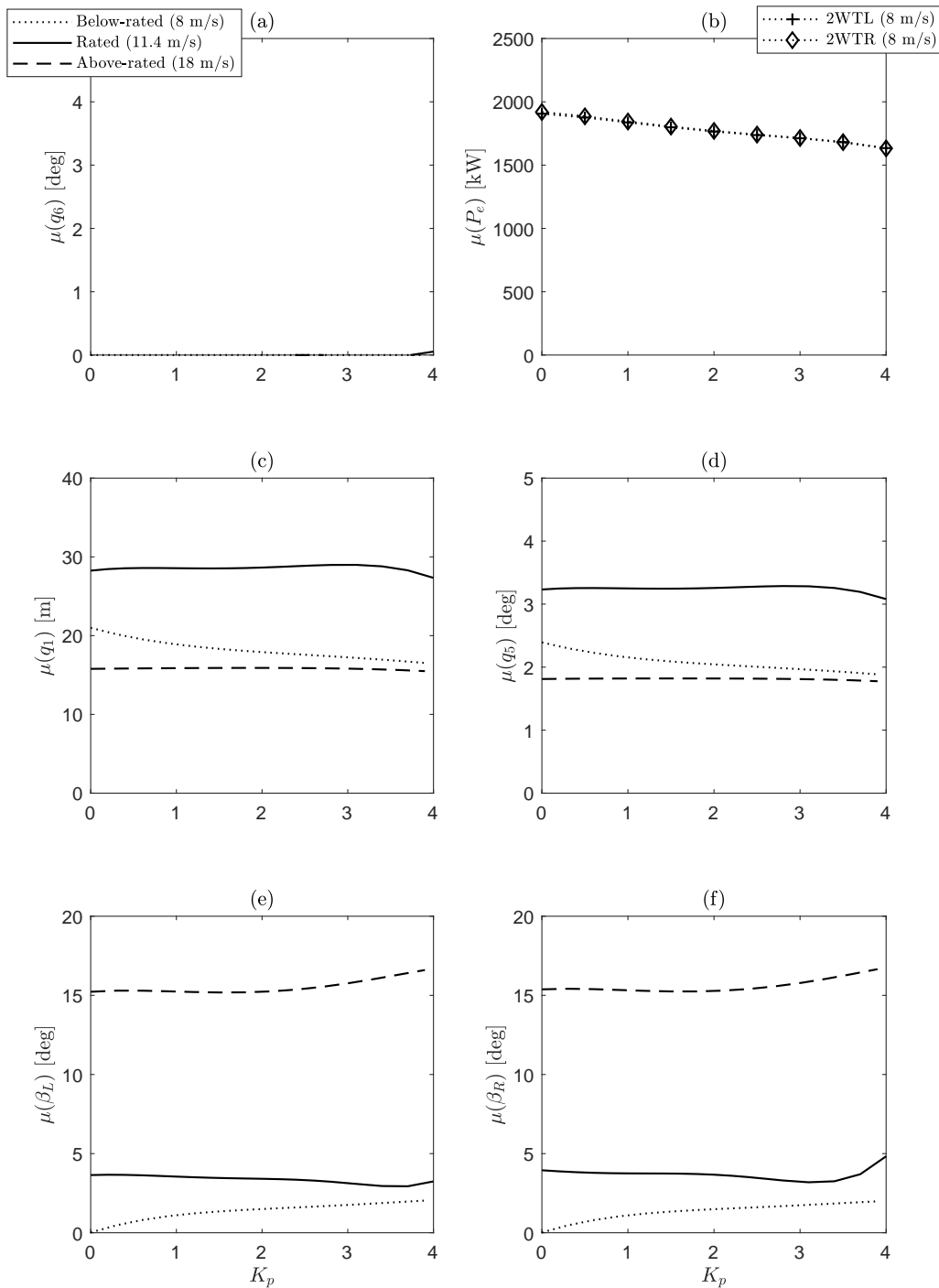
Figure 4.10: Mean of (a) platform yaw motion, (b) electric power output, (c) platform surge motion, (d) platform pitch motion, (e) left rotor-collective blade pitch angle, and (f) right rotor-collective blade pitch angle of the 2WT system in relation to the yaw control proportional gain and under different operating wind speed (Table 4.6).
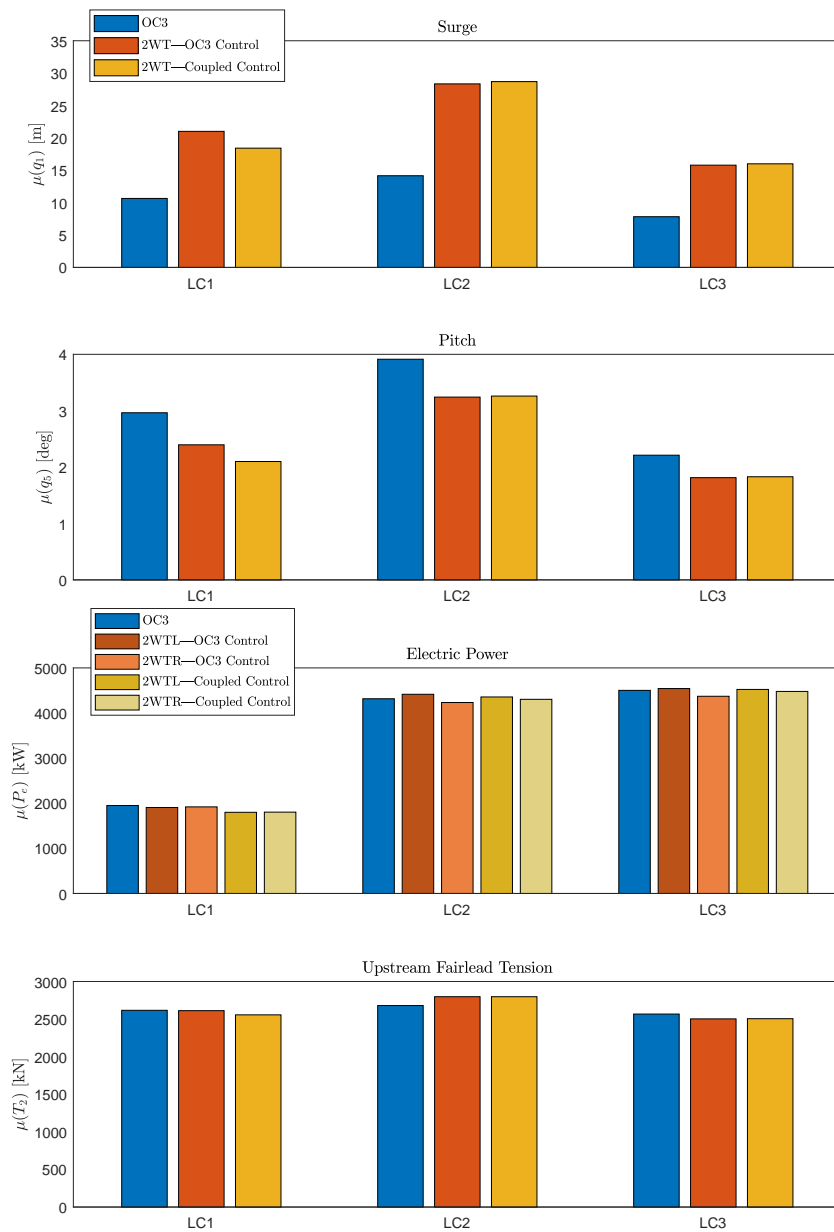
Figure 4.11: Mean surge, pitch, electric power production, and upstream fairlead tension (all configurations employ an equivalent mooring line mass density of 200 kg/m).

floating platform chief design drivers, it may be concluded that some margin is still available to further optimize the platform design. The mean electric power production is broken down into single rotor performance. Since the mean values are computed from single 1-h realizations of turbulent responses, the mean electric power production for all rotors at rated and above-rated operating wind speed is lower than the rated power of 5 MW (Clifton and Wagner, 2014). This is due to fluctuations of the generator speed in the below-rated region. Moreover, the aerodynamic model employed in this work does not allow for assessment of the contribution of complex aerodynamic effects on the system performance - especially with respect to aerodynamic efficiency and consequently electric power production. Consequently, the mean electric production obtained at below rated speed for the 2WT system with baseline OC3 control is similar to the one obtained in the OC3 system. The interaction effect may be significant and is therefore left at this stage as a question for further research.

Figure 4.12 shows the standard deviations for platform surge and pitch motion, electric power production, and upstream fairlead tension for the same load cases and system configurations given in Figure 4.11. The pattern obtained is similar to the one characterizing the mean values. Standard deviations obtained for the 2WT system under different control strategies are found to be similar. The electric power production standard deviations associated with the 2WT rotors are found to differ by about 100 kW, particularly at below rated wind speed. The difference is reasonably associated with the different wind velocity profiles at the hub locations. Tension standard deviation is important when evaluating the probability of line slack and fatigue life. In order to avoid slack conditions, the tension standard deviation must be sufficiently smaller than its associated mean value (Bachynski and Moan, 2012). The standard deviation of the upstream fairlead tension for the 2WT system at the rated operating wind speed is significantly higher than in the OC3 system. However, the tension standard deviation is relatively small if compared with its associated mean value (ratio $\sigma/\mu \approx 0.07$), implying that the current mooring layout may be sufficient to withstand survival environmental conditions (Cheng et al., 2017a).
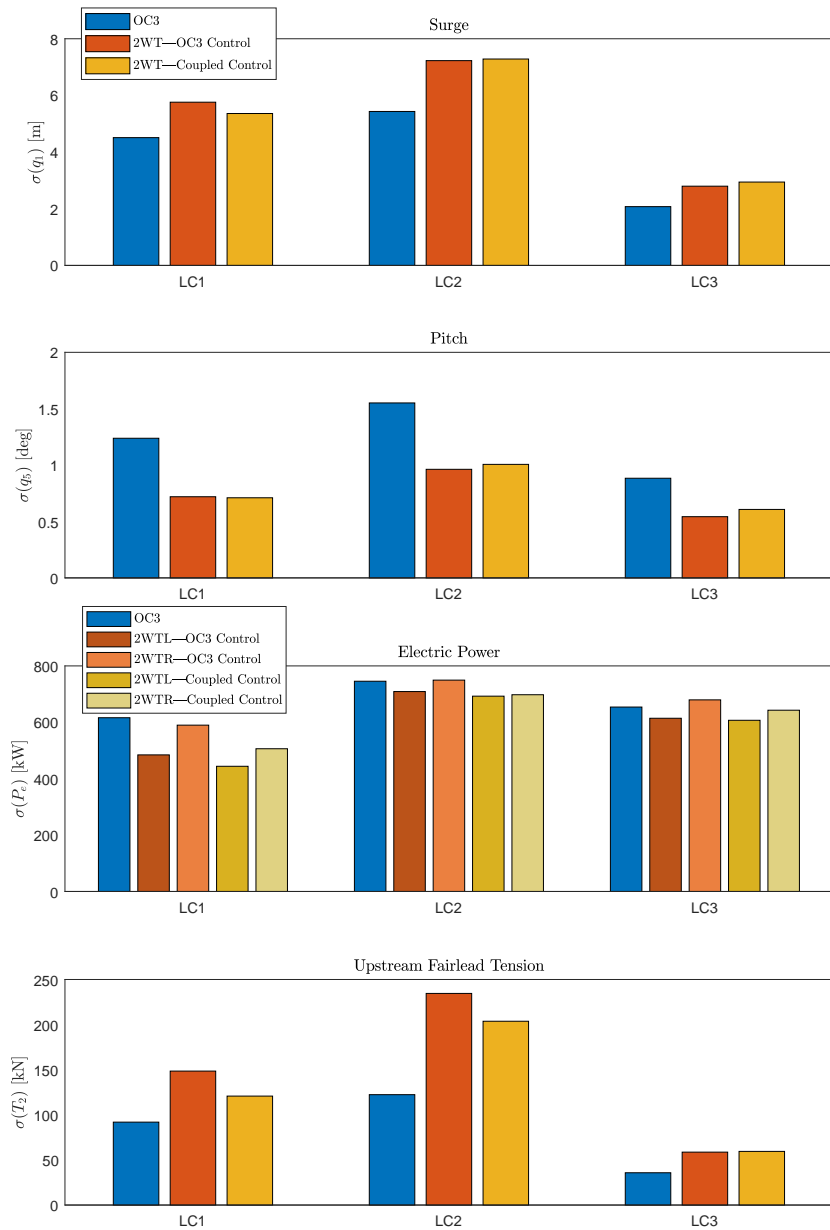
Figure 4.12: Standard deviations for surge, pitch, electric power production, and upstream fairlead tension (all configurations employ an equivalent mooring line mass density of 200 kg/m).
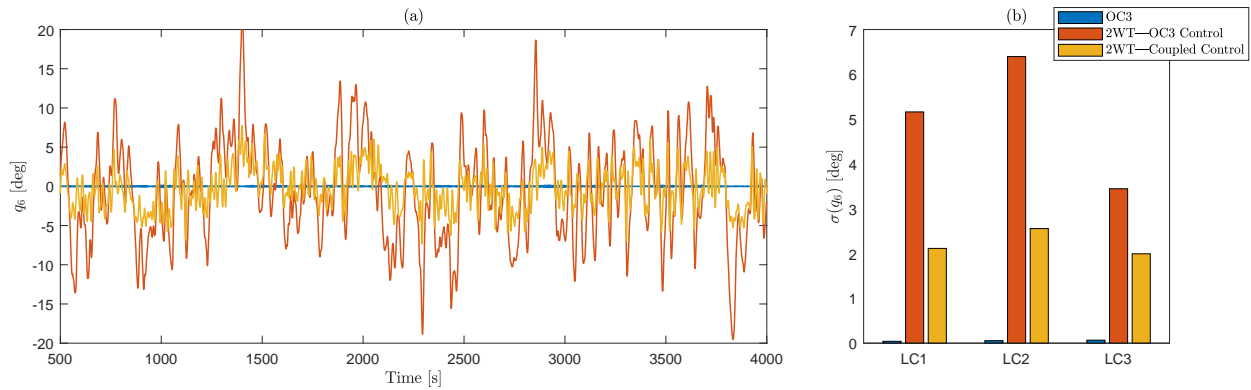
Figure 4.13: a) Time histories for platform yaw motion at the rated operating wind speed (LC2). b) Standard deviations for platform yaw motion (all configurations employ an equivalent mooring line mass density of 200 kg/m).

4.5.4 Yaw Response

Figure 4.13 shows the time histories for the platform yaw motion at the rated operating wind speed (LC2), and the standard deviations for the environmental conditions used in the analysis (see Table 4.6). The transversal distribution of thrust loads given by the two-rotor configuration significantly affects yaw motion. The response is characterized by long periods. This can be correlated with the concentration of wind turbulence energy in the low-frequency region (Li et al., 2019). The maximum yaw angle in the 2WT concept operating with the baseline OC3 control strategy is about 21.6 deg and it is obtained at the rated operating wind speed, while the associated standard deviation is about 6.5 deg. The coupled control strategy proposed in this work, albeit simply implementing a proportional control on the platform yaw motion, reduces the overall yaw response of about 60%. The maximum yaw angle at the rated operating wind speed reduces to about 7.7 deg, while the associated standard deviation reduces to about 2.5 deg. The thrust discrepancy at the hubs increases with turbulence intensity, thus increasing the standard deviation of platform yaw motion. Figure 4.14 shows the standard deviation for platform yaw motion as a function of the turbulence intensity I, computed at the rated operating wind speed (11.4 m/s). Platform yaw motion is nonlinearly correlated with the wind turbulence level. The significant reduction of the yaw standard deviation in the case the system operates with a coupled control strategy endures at varying turbulence
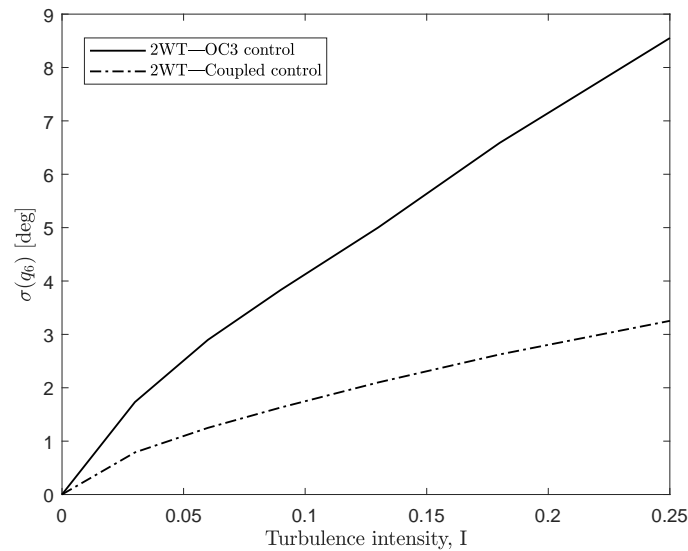
Figure 4.14: Standard deviation of platform yaw motion as function of turbulence intensity (11.4 m/s - Kaimal IEC 61400-1 turbulence spectrum).

intensities. It is also clear how the standard deviation for platform yaw motion is zero when the wind profile is not turbulent ($\sigma(q_6)|_{I=0} = 0$).

4.5.5 Mooring Configuration

A simple parametric mooring line design of the 2WT system is performed in terms of the effect of the mooring lines equivalent mass density on the system response computed at rated operating wind speed (LC2). The associated findings are illustrated in Figure 4.15. The mooring lines diameter is equal to 0.09 m, and the unstretched mooring line length is equal to 902.2 m. For an equivalent mass density of 170 kg/m the peak minimum seabed length is negative, i.e., no portion of the mooring line rests on the seabed and the anchor tension includes a nonzero vertical component. In order to ensure excess mooring line length, an equivalent mass density higher than 190 kg/m is thus necessary. Peak platform surge motion decreases with increasing mooring line weight.
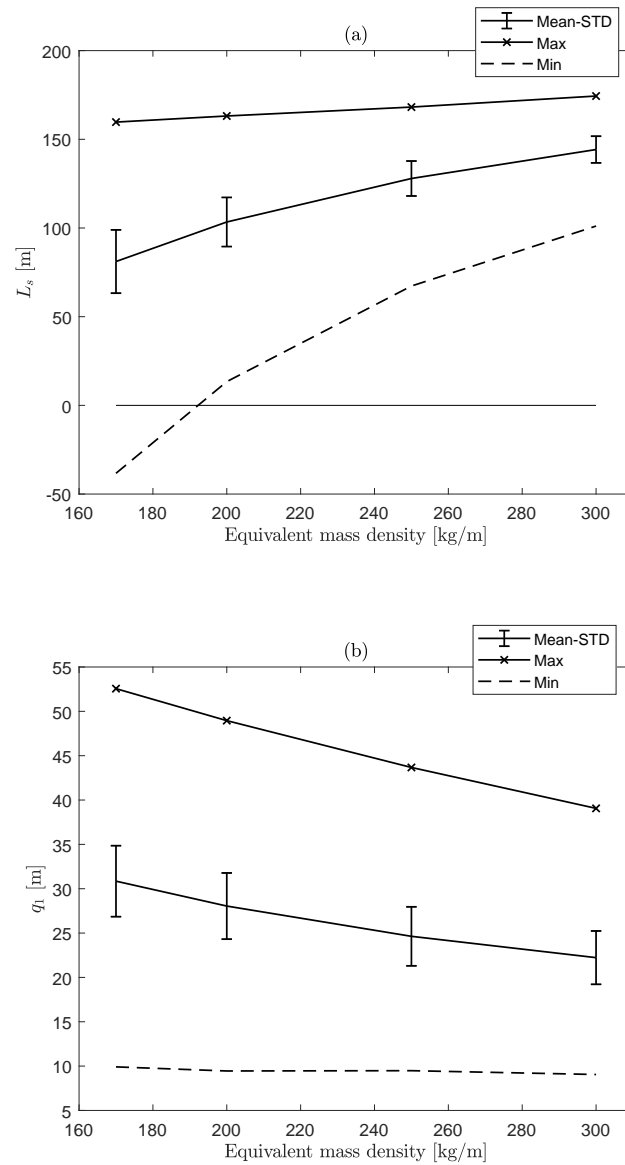
Figure 4.15: Effect of mooring line equivalent mass density on the upstream mooring line seabed length (a) and on the platform surge motion (b). Coupled control schedule for 2WT at the rated operating wind speed (LC2).

Table 4.9: Load Cases - 2WT dynamic analysis (Cheng et al., 2017b).

	U_w [m/s]	H_s [m]	T_p [s]	Wind Condition	Wave Condition	Simulation Length [s]
1.1	5	2.10	9.74	NTM+KAI/VKM	JSP	3600
1.2	8	2.55	9.86	NTM+KAI/VKM	JSP	3600
1.3	10	2.88	9.98	NTM+KAI/VKM	JSP	3600
1.4	12	3.24	10.12	NTM+KAI/VKM	JSP	3600
1.5	14	3.62	10.29	NTM+KAI/VKM	JSP	3600
1.6	18	4.44	10.66	NTM+KAI/VKM	JSP	3600
1.7	22	5.32	11.06	NTM+KAI/VKM	JSP	3600
1.8	25	6.02	11.38	NTM+KAI/VKM	JSP	3600

NTM: normal turbulence type; KAI: kaimal turbulence model; VKM: von karman turbulence model; JSP: JONSWAP

4.6 Dynamic Response Through BEM Loads and Structural Dynamics

This section presents the dynamic response of the 2WT system by means of full-system dynamics, blade-element momentum aerodynamic loads and the structural dynamics of tower and blades as presented in Chapter 3.

4.6.1 Load Cases

Table 4.9 lists the load cases (LCs) considered. Load cases are inspired by previous work by Cheng et al. (2017b). Each load case is characterized by directionally congruent wind and waves. The IEC-61400-1 standard (International Electrotechincal Commission, 2005) is currently adopted for FWTs, which proposes the employment of two possible wind turbulence models, i.e., the Kaimal spectral and exponential coherence model, and the Mann uniform shear model. The Kaimal spectral and exponential coherence model employs the Kaimal spectrum and a two-parameter exponential coherence model for the wind velocity in the average wind direction, while no coherence is assumed for the other directions. The Mann uniform shear model, on the other hand, is based on the Von Karman spectrum where a uniform, mean velocity shear and a three-dimensional coherence function are considered (International Electrotechincal
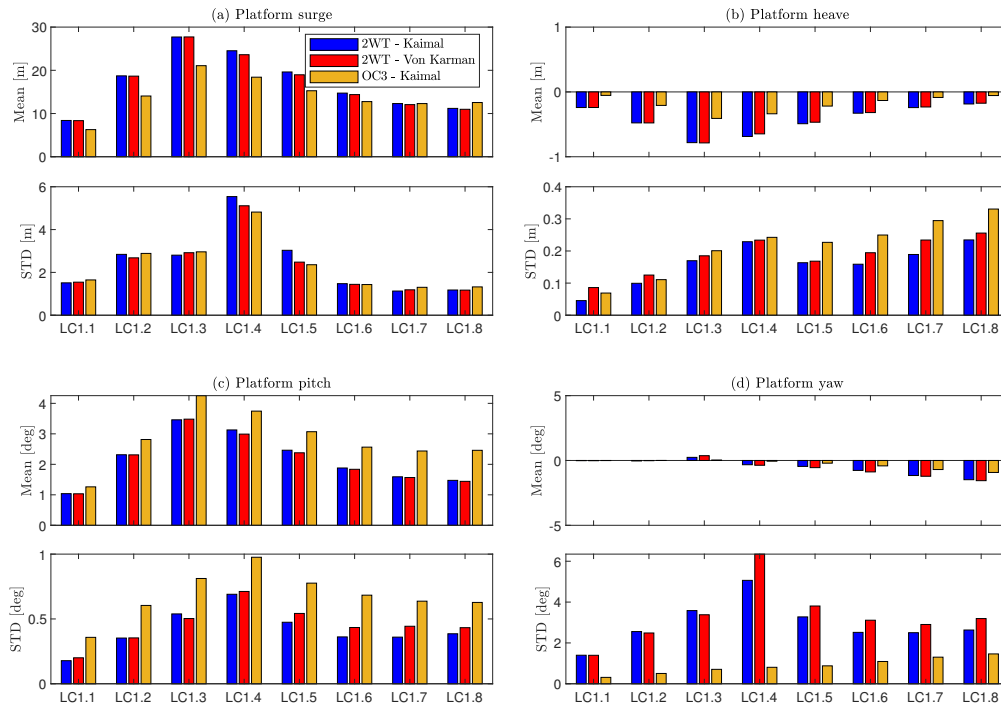
Figure 4.16: 2WT mean values and standard deviation (STD) of a) platform surge motion, b) platform heave motion, c) platform pitch motion, and d) platform yaw motion for Kaimal and Von Karman wind turbulence spectrums. OC3 single-rotor response for Kaimal spectrum is also shown for comparison.

Commission, 2005; Bachynski and Eliassen, 2019). See Bachynski and Eliassen (2019) for further details. Two different turbulence spectrums are thus assessed in the present dynamic evaluation, i.e., Kaimal and Von Karman, which are both readily available in the TurbSim package. Turbulent wind conditions are described by means of the normal turbulence type (NTM) of type B. The Joint North Sea Wave Project (JONSWAP) irregular wave spectrum is used for defining the wave conditions. Each simulation realizes time series of about 4000 s, where the first 400 s are removed to discard initialization transients. A net one-hour time is thus considered in the results.

4.6.2   Platform Motions

Figure 4.16 shows the mean and standard deviation (STD) values of the 2WT platform surge motion, platform heave motion, platform pitch motion, and platform yaw motion for the two different turbulence spectrums considered. The response of the single-rotor OC3 system for Kaimal spectrum is also shown for comparison. The response is similar in the two cases, showing maximum mean values in LC1.3 and maximum STD values in LC1.4. The response of the 2WT system as compared with the OC3 system response is in accordance with results from simplified analysis, showing smaller platform pitch motion and significant platform yaw motion STD. Von Karman turbulence spectrum leads to higher maximum platform yaw motion STD - in LC1.4 about 6.2 deg against 5 deg obtained by using Kaimal turbulence. This is expected, as the power spectral density is generally higher for Von Karman than for Kaimal at low to medium frequencies (Gontier et al., 2007). Figure 4.17 shows the 2WT power spectra of the same motion parameters depicted in Figure 4.16 and for the two different turbulence spectrums considered. The energy distribution is similar in the two cases. Platform yaw motion energy is concentrated at low frequencies as wind-induced.

4.6.3   Loads and Turbine Performance

Figure 4.18 shows the mean and STD values of the 2WT tower base fore-aft bending moment, downwind fairlead tension, electric power output, and rotor speed for the two different turbulence spectrums considered. The response of the single-rotor OC3 system for Kaimal spectrum is also shown for comparison. The response is similar in the two cases. Fairlead tension STD is significantly lower than the associated mean value even for maximum response at LC1.4, meaning that catenary slack is unreasonable (Bachynski and Moan, 2012). Figure 4.19 shows the 2WT power spectra of thrust, tower base fore-aft bending moment, blade root out-of-plane bending moment, and blade root in-plane bending moment for the two different turbulence spectrums considered. The energy distribution is similar in the two cases, with a marginally higher energy
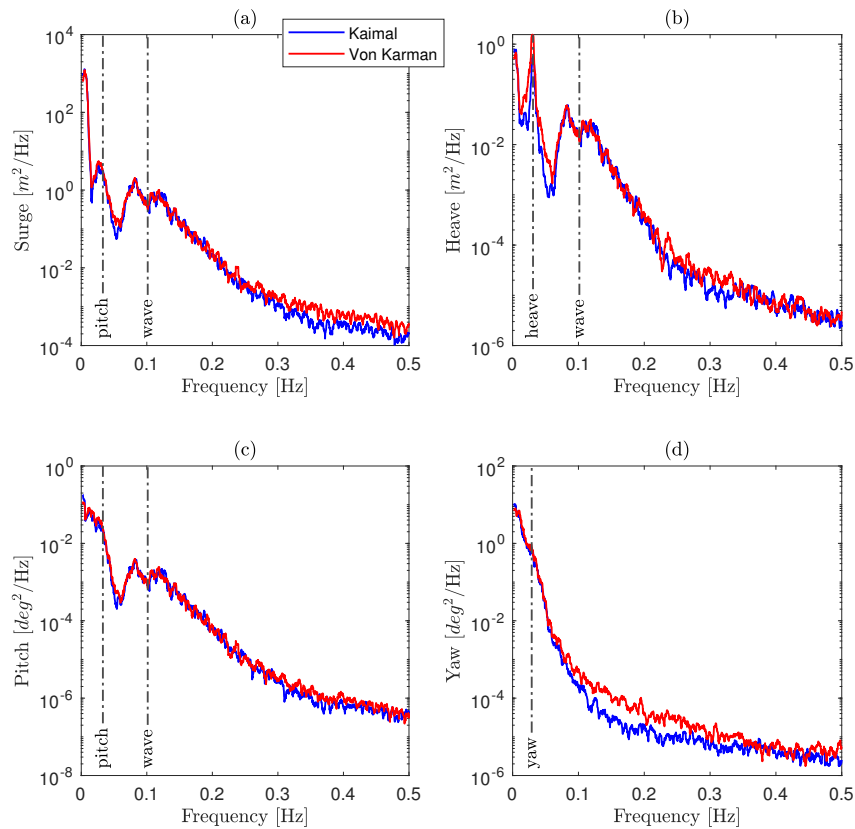
Figure 4.17: 2WT power spectra of a) platform surge motion, b) platform heave motion, c) platform pitch motion, and d) platform yaw motion for Kaimal and Von Karman wind turbulence spectrums (LC1.2).

content for blade root in-plane bending moment obtained with Von Marman turbulence.

4.7 Conclusions

The dynamic analysis of a two-rotor wind turbine mounted on a spar-type floating platform has been performed. A simple structural analysis showed how a mass saving of about 26% may be achieved by employing the two-rotor configuration instead of an equivalent single-rotor configuration. The numerical simulations showed an increased low-frequency yaw response of the two-rotor system compared with the response of a single-rotor configuration, of about 6
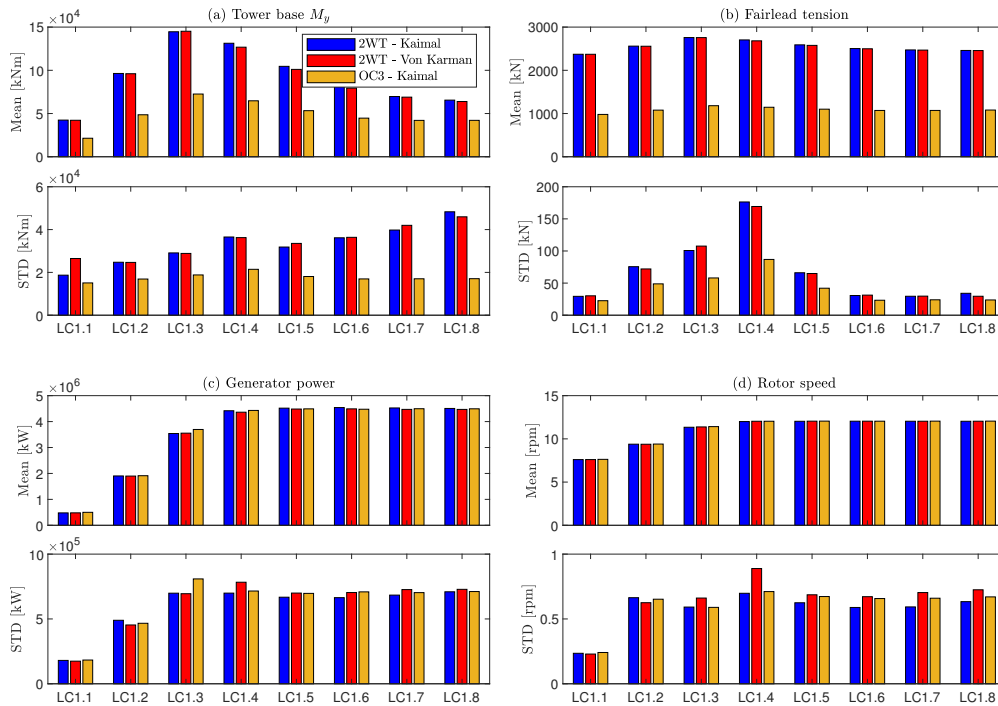
Figure 4.18: 2WT mean values and standard deviation (STD) of a) tower base fore-aft bending moment, b) downwind fairlead tension, c) electric power output, and d) rotor speed for Kaimal and Von Karman wind turbulence spectrums. Only data from the left turbine are shown, as turbines behavior is analogous. OC3 single-rotor response for Kaimal spectrum is also shown for comparison.

deg standard deviation at the rated operating wind speed. The yaw excitation is directly induced by the turbulence intensity at the hub and the transversal distribution of thrust loads on the structure. A rotor-collective blade pitch angle coupled control has been proposed for the mitigation of yaw response. The numerical simulations showed a reduction of the yaw response of about 60% at the cost of a reduction of mean power output at below-rated wind speed of about 100 kW. In addition, parametric analysis showed that an equivalent mass density of the mooring lines of at least 190 kg/m is necessary in the 2WT in order to avoid vertical loads at the anchors. Stiffer mooring lines configurations in yaw direction would also reduce platform yaw response.

The analysis is based on in-house code developed in Modelica. The aerody-
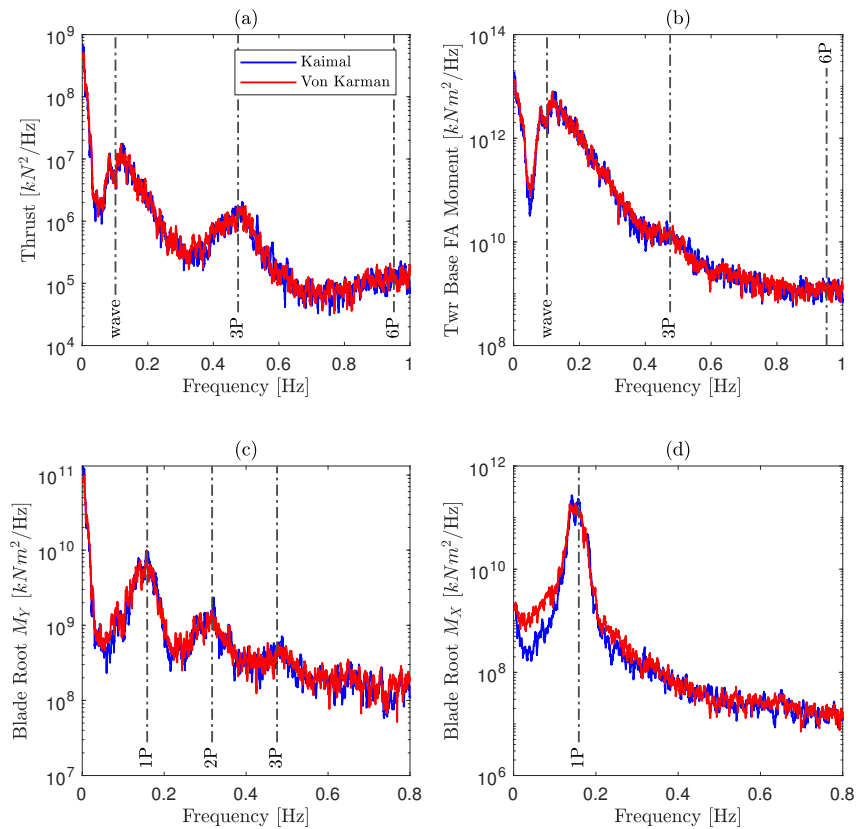
Figure 4.19: 2WT power spectra of a) thrust, b) tower base fore-aft bending moment, c) blade root out-of-plane bending moment, and d) blade root in-plane bending moment for Kaimal and Von Karman wind turbulence spectrums (LC1.2). Only data from left turbine are shown, as turbines behavior is analogous.

namic model is based on the mapping of the steady-state aerodynamic coefficients characteristic of the wind turbines employed. The approach is therefore not able to assess complex aerodynamic situations which may be significant. The dynamic response of the 2WT system is also investigated considering the full-system dynamics, blade-element momentum aerodynamic loads, and the structural dynamics of tower and blades. Results are in very good accordance with those obtained through the simplified approach, implying that the global dynamic response of the system is not significantly affected by distributed loads, structural elasticity, and skewed effects. However, the aerodynamic interaction between the rotors cannot be assessed in either case. This interaction should

later be investigated in more detail by means of high fidelity tools.

Acknowledgment

Chapter 5

Optimal Control of a Two-Rotor Floating Wind Turbine

Omar El Beshbichi [a], Yihan Xing [a], Muk Chen Ong [a]

[a] Department of Mechanical and Structural Engineering and Materials Science, University of Stavanger, Stavanger, Norway.

Abstract

Interest is steadily growing for two-rotor wind turbine concepts. This type of wind turbine offers a practical solution for scaling issues of large wind turbine components and for the reduction of costs associated with manufacturing, logistics, and maintenance. However, the literature lacks thorough knowledge of the dynamic performance of two-rotor wind turbine concepts installed on floating platforms. Previous research studied the dynamic response of a two-rotor wind turbine concept mounted on a spar-type floating platform (2WT). Platform yaw motion is a significant dynamic factor directly caused by differential turbulence intensity experienced by the two hubs coupled with the distribution of thrust loads on the tower structure. Blade-pitch control analysis also showed how the 2WT yaw response is extremely sensitive to the control strategy employed. In this work, a linear quadratic regulator (LQR) is used to design an optimal controller for the 2WT prototype. Three LQR gain schedules corresponding to three operation regions are considered. An in-house tool for the dynamic analysis of two-rotor floating wind turbines is used for linear state-space extraction and dynamic analysis. The control performance in different load conditions is assessed against the baseline OC3 PI control strategy and a PI-P control strategy in a previous paper presented by the authors.

Keywords: Linear quadratic regulator, Offshore wind, Spar, Floating wind turbines, Multi-rotor, Optimal control.

5.1   Introduction

The installed capacity of offshore wind energy has steadily increased in the last decade. Estimates from the global wind energy council (GWEC) account for a total installed capacity offshore of about 35 GW in 2021 out of a total wind energy capacity of about 600 GW (GWEC, 2019). Space availability, stronger and steadier winds, and less interference with populated areas, to name but a few reasons for the appeal of offshore wind installations (Cruz and Atcheson, 2016). Almost all of the offshore wind turbines currently installed are bottom-fixed. However, most wind potential is beyond the limit imposed by the maximum water depth at which bottom-fixed structures are economically feasible (around 50 m). Floating offshore wind turbines (FOWT) have been proposed as a technical solution, and several examples of FOWTs deployment are present (Equinor, 2015; Principle Power, 2016). Multi-rotor FOWTs have also been proposed, where the advantages are associated with more economical offshore operations and floating platform sharing. Two commercial examples of multi-rotor FOWTs currently under development are TwinWind™ by Hexicon (Hexicon, 2021a) and Flex2power by Rosenberg Worley AS (Flex2Power, 2022). The former is a two-rotor wind turbine mounted on a semisubmersible platform. Hexicon has recently signed an agreement for conditional site exclusivity with a reservation of 6 MW for deploying a demonstrator prototype at the Metcentre's deepwater site off Norway's coast (Hexicon, 2021b). Flex2power, on the other hand, is a modularized concept for combined wind, wave, and sun energy production. Another innovative multi-rotor floating wind technology is Nezzy[2], currently under development by EnBW and the North German engineering company Aerodyn Engineering (EnBW, 2021b; Aerodyn Engineering, 2021) and composed of two wind turbines supported by a Y-shaped semisubmersible platform anchored by six mooring lines (EnBW, 2021a). A 1:10 scale prototype has been recently tested in two-blades and three-blades variants. To date, the literature lacks knowledge on the dynamic performance of two-rotor FOWTs systems. Recent research evaluated the dynamic response of a two-rotor wind turbine prototype mounted on a spar-type floating platform (2WT) (El Beshbichi et al., 2021a). The concept was first defined as a first-
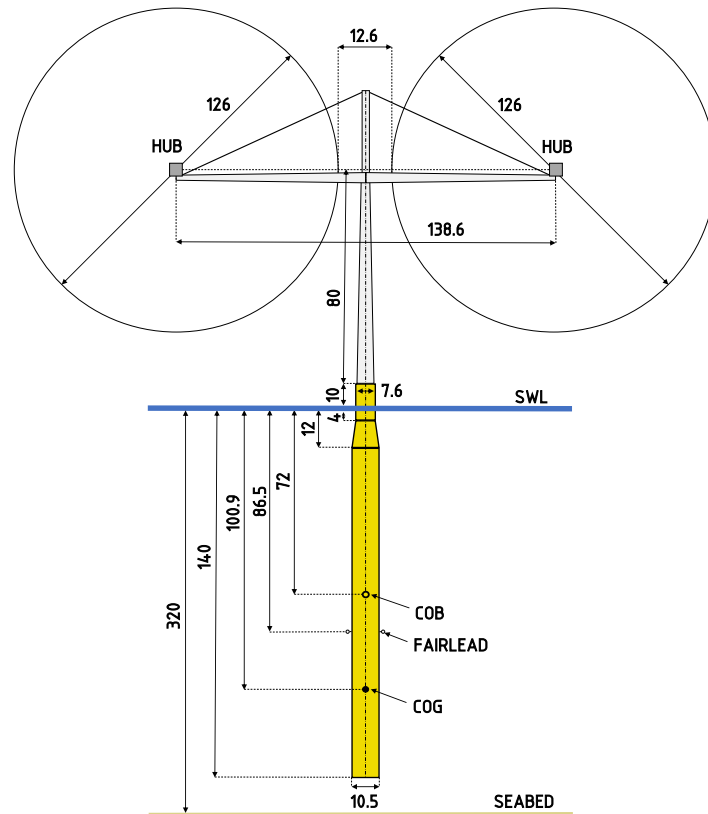
Figure 5.1: 2WT two-rotor FOWT prototype presented in El Beshbichi et al. (2021a) and considered in this work (lengths in m).

attempt prototype by seeking simplicity of platform design, great availability of data concerning similar platform performance in the literature, and easy result assessment. It was found that the 2WT design is subject to significant platform yaw motion associated with differential turbulence intensity at the hubs coupled with the distribution of thrust loads on the tower structure. A simple proportional control (PI-P) mitigating yaw motion was introduced in parallel with the baseline OC3 proportional-integral (OC3 PI) controller, significantly reducing platform yaw response. Figure 5.1 presents the 2WT system. The design considers two baseline NREL 5 MW wind turbines (Jonkman, 2007). Major system parameters are listed in Table 5.1. Three catenary mooring lines are consid-

Table 5.1: System parameters (Jonkman, 2007; El Beshbichi et al., 2021a).

Diameter at SWL	m	7.6
Diameter	m	10.5
Draft	m	140
Depth to COG		100.9
Water Displacement	m^3	$11.7x10^3$
Platform Mass (including ballast)	kg	$10.6x10^6$
Platform Roll Moment of Inertia	kgm^2	$1.13x10^{10}$
Platform Pitch Moment of Inertia	kgm^2	$1.13x10^{10}$
Platform Yaw Moment of Inertia	kgm^2	$1.7x10^8$
Heave Hydrostatic stiffness	N/m	$4.56x10^5$
Roll Hydrostatic stiffness	Nm/rad	$3.42x10^9$
Pitch Hydrostatic stiffness	Nm/rad	$3.42x10^9$
Total mass	kg	$11.8x10^6$
Rotor Diameter	m	126
Hub Height	m	90
Rotor Mass	kg	$110x10^3$
Nacelle Mass	kg	$240x10^3$
Cut-In, Rated, Cut-Out Wind Speed	m/s	3, 11.4, 25
Cut-In, Rated Rotor Speed	rpm	6.9, 12.1

Table 5.2: Natural frequencies and damping ratios of the two-rotor FOWT system computed through free-decay tests.

	Natural frequency [Hz]	Damping ratio [%]
Surge	0.0075	8.73
Sway	0.0075	8.73
Heave	0.031	1.96
Roll	0.033	3.81
Pitch	0.033	3.81
Yaw	0.029	4.12

ered for station-keeping, placed at 120 deg from one another starting from the downwind position. The mooring lines mass density is 200 kg/m, the static vertical length is about 250 m, and the unstretched static length is about 900 m. Additional concentrated stiffness in the platform yaw direction of about 9.8e7 Nm/rad is considered to account for yaw stiffness given by the delta line configuration (Jonkman, 2007). Hydrostatic quantities are relative to the static position of the system affected by the loading of the mooring lines. Table 5.2 lists the natural frequencies and damping ratios from logarithmic decrement of the 2WT system computed through free-decay tests. Control of variable-speed wind turbines is achieved by regulating blade-pitch angles and generator torque (Bossanyi, 2000). Control is generally divided into four regions as a function of control objective:

- Region 1. Below cut-in wind speed. In this region, no generator torque allows drivetrain acceleration for start-up.

- Region 2. Between cut-in wind speed and rated wind speed. In this region, aerodynamic power is optimized by regulating generator torque.

- Region 3. Between rated and cut-out wind speed. In this region, generator speed is maintained equal to the rated value by actuating blade-pitch angles. Generator torque control allows for either constant electric power output or constant generator torque.

- Cut-off region. Above cut-out wind speed. In this region, blades are fully pitched for parking the wind turbine by disrupting the aerodynamic loads.

The most common blade-pitch control implementation is employing a PI logic, for instance, in the case of the baseline OC3 PI controller (Jonkman, 2007). A linear quadratic regulator (LQR) may also be employed to design the control of FOWTs (Stol and Fingersh, 2004; Wright and Fingersh, 2008). Pham et al. (Pham et al., 2012) designed an LQR control for a multi-MW wind turbine. Christiansen et al. (2011, 2014) designed and analyzed an LQR controller applied to a spar-type FOWT.

This work presents the design of an LQR control for the 2WT system. Control objectives are the reduction of platform yaw motion while regulating the gener-

ators' speed. To date, no other examples of the employment of LQR as optimal control algorithm for mitigating platform yaw response in two-rotor FOWTs is present in the literature. Results are compared against 2WT performance controlled with the baseline OC3 PI controller and the coupled PI-P controlled as defined in El Beshbichi et al. (2021a).

5.2   2WT Dynamic Model

Dynamic assessment and linear state-space extraction for the 2WT prototype are performed through an in-house tool developed in Modelica (v3.2.3) (El Beshbichi et al., 2021b). Modelica is a non-proprietary, declarative, object-oriented language developed by the non-profit Modelica Association and used to conveniently model multi-domain systems (The Modelica Association, 2017). The open-source Modelica-based platform OpenModelica is also used for development (v1.16.2) (OSMC, 2021).

5.2.1   Nonlinear Model

Nonlinear dynamic analysis of the floating system assumes linear (Airy) hydrodynamics (Faltinsen, 1993). This assumption is valid in most practical cases, i.e., when the wave height is much smaller than the water depth. The frequency-domain hydrodynamic problem associated with the platform design is solved through the commercial code WADAM within DNV SESAM (DNV, 2017). The 2WT system is assumed to be a single rigid body with six degrees of freedom (DoF). The motions are then computed using rigid equations of motion (Jonkman, 2007):

$$[M]\underline{\ddot{q}} + [C]\underline{q} + C_{0,3} = -[A]_{inf}\underline{\ddot{q}} - \int_0^t [K(t-\tau)]\underline{\dot{q}}d\tau + \underline{F}_w + \underline{F} + \underline{F}_m + \underline{F}_g \qquad (1)$$

where $\underline{q}$ are the platform DoFs, $[M]$ is the total inertia tensor of the 2WT system, $[C]$ is the hydrostatic matrix, $C_{0,3}$ is the Archimede restoring load, $[A]_{inf}$ is the added mass term from hydrodynamic radiation computed at infinite wave frequency, $[K(t)]$ is the retardation-kernel matrix from hydrodynamic radiation,
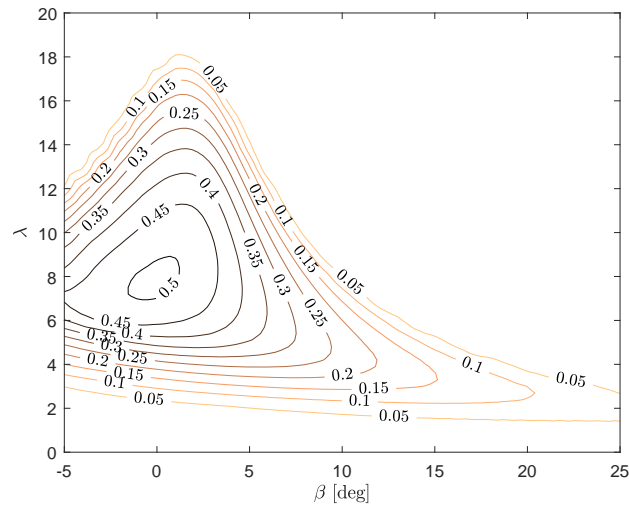
Figure 5.2: Power coefficient (C_P).

$\underline{F}_w$ are the loads from incident waves, $\underline{F}$ are the aerodynamic loads, $\underline{F}_m$ are the mooring loads, and $\underline{F}_g$ are the gravitational loads. Station-keeping loads from mooring lines are included by means of a non-linear quasi-static formulation, i.e., the effect of the acceleration and velocity of the mooring lines on station-keeping loads is disregarded. Aerodynamic loads are assumed composed of concentrated thrusts acting at the hubs and torques acting on the dynamics of the drivetrain. Additional DoFs are added to account for drivetrains dynamics and used to define the aerodynamic state of the system. Drivetrain dynamics is described as:

$$(I_r + \gamma^2 I_g)\dot{\omega}_r = T - \gamma T_g \tag{2}$$

where I_r is the rotor moment of inertia, I_g is the generator moment of inertia, γ is the gearbox ratio, ω_r is the low-speed shaft speed, T is the aerodynamic torque, and T_g is the generator torque. Aerodynamic loads are computed utilizing steady-state aerodynamic coefficients associated with the onshore NREL 5 MW wind turbine design. Aerodynamic coefficients of thrust, torque, and aerodynamic power are collected in FAST and Figures 5.2, 5.3, and 5.4 show the resulting mapping [where $\lambda = \omega_r R/U_{rel}$ is the tip speed ratio (TSR), U_{rel} is the relative wind velocity at the hub, and β is the rotor-collective blade-pitch angle].
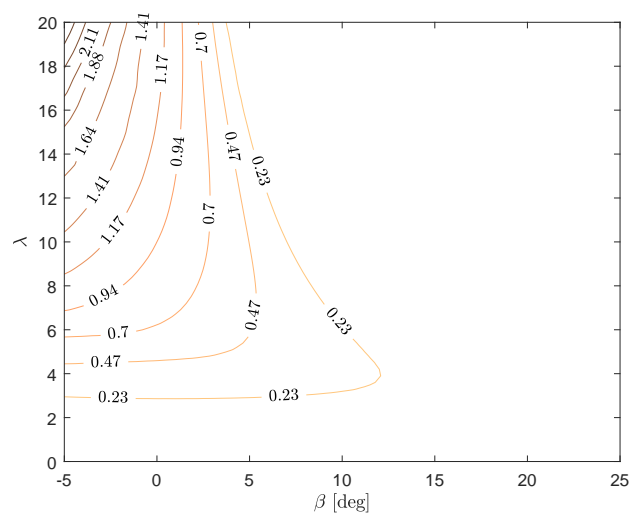
Figure 5.3: Thrust coefficient (C_T).
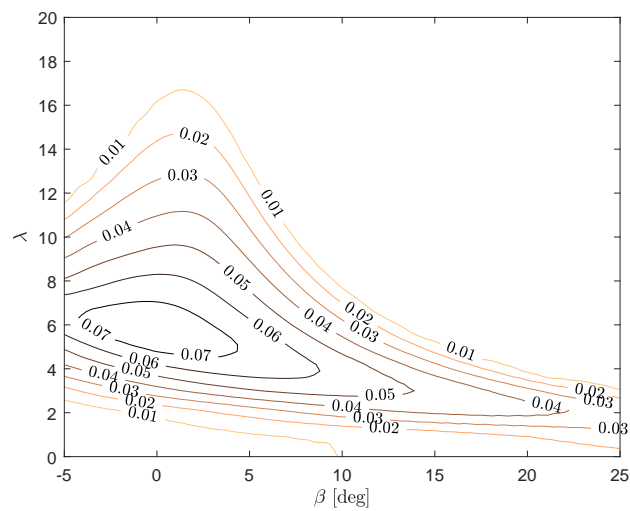
Figure 5.4: Torque coefficient (C_Q).

Aerodynamic loads are computed as:

$$F = \frac{1}{2}\rho_{air}C_T(\lambda, \beta)AU_{rel}^2 \tag{3}$$

and:

$$T = \frac{1}{2}\rho_{air}RC_Q(\lambda, \beta)AU_{rel}^2 \tag{4}$$

where ρ_{air} is the air density, C_T is the thrust coefficient, C_Q is the torque coefficient, A is the rotor-swept area, and R is the rotor radius. The effect of platform motion on the relative wind speed at the hub affects the computation of the TSR and the aerodynamic thrust and torque loads. Turbulent wind profiles are computed in TurbSim (Jonkman, 2009a). The dynamic response of the blade-pitch actuation system is described through a second-order transfer function (f_n = 5 Hz, ξ = 0.02).

Even though previous work demonstrated that the method is sufficiently accurate to determine the general dynamic response of FOWTs (Karimirad and Moan, 2012b; El Beshbichi et al., 2021b), more complex aerodynamic effects cannot be assessed. For instance, the aerodynamic interaction between rotors is not available. Concentrated loads effectively neglect wind shear. The effect of platform yaw motion on the aerodynamic performance of the wind turbine is also not directly assessed, as well as aerodynamic drag loads on the tower and the aerodynamic effects of the tower's proximity on the turbine blades. These effects may be significant and should later be investigated to determine optimal control weights.

5.2.2   Linear Model

The nonlinear model can be described as:

$$\begin{aligned} \dot{\underline{x}} &= f(\underline{x}, \underline{u}) \\ \underline{y} &= g(\underline{x}, \underline{u}) \end{aligned} \tag{5}$$

where $\underline{x}$ is the state vector, $\underline{u}$ is the input vector, $\underline{y}$ is the output vector, f is the nonlinear relationship describing the dynamic behavior of the system, and

g is the nonlinear output function (Prasad et al., 2014). Control design exploits the linearization of the system by using first order Taylor expansion about the neighborhood of a steady-state operation point. If $\underline{x}^*$ is the state vector at the operation point and $\underline{\tilde{x}}$ the infinitesimal variation about the operation point (such that $\underline{x} = \underline{x}^* + \underline{\tilde{x}}$) the linear system can be expressed as:

$$\dot{\underline{\tilde{x}}} = [A]\underline{\tilde{x}} + [B]\underline{\tilde{u}}$$
$$\underline{\tilde{y}} = [C]\underline{\tilde{x}} + [D]\underline{\tilde{u}}$$

(6)

where $[A] = \left.\frac{\partial f(\underline{x},\underline{u})}{\partial \underline{x}}\right|_{\underline{x}=\underline{x}^*}$, $[B] = \left.\frac{\partial f(\underline{x},\underline{u})}{\partial \underline{u}}\right|_{\underline{u}=\underline{u}^*}$, $[C] = \left.\frac{\partial g(\underline{x},\underline{u})}{\partial \underline{x}}\right|_{\underline{x}=\underline{x}^*}$ and $[D] = \left.\frac{\partial g(\underline{x},\underline{u})}{\partial \underline{u}}\right|_{\underline{u}=\underline{u}^*}$ are the Jacobian matrices of the system evaluated at the operation point. Jacobian components describe sensitivity relationships among states, inputs, and outputs. Modelica models can be linearized in OpenModelica by calling the function *linearize()* in the OMShell and specifying the simulation time at which linearization occurs. Only significant platform states have been enabled in the linearization process. Moreover, no wave loads are considered and radiation damping states are disabled. The state vector considered is:

$$\underline{\tilde{x}} = [\beta_L, \beta_R, \dot{\beta}_L, \dot{\beta}_R, \Omega_L, \Omega_R, q_5, \dot{q}_5, q_6, \dot{q}_6]$$

(7)

where Ω is the rotor speed, q_5 is the platform pitch angle, and q_6 is the platform yaw angle. Subscripts L and R stand for the left and right rotor, respectively. The input vector considered is:

$$\underline{\tilde{u}} = [\beta_L, \beta_R]$$

(8)

Moreover, external wind speed is considered as additional system input (Kumar and Stol, 2009):

$$\underline{\tilde{u}}_d = [U_{rel}]$$

(9)

Above-rated steady-state error of the rotor speed can be avoided by including states expressing the integral error between the reference and actual speed, as in linear-quadratic regulators with integral terms (LQI) (Feng et al., 2007).

Keeping LQI notation, the output variables are simply defined as the generators' speed:

$$\tilde{\underline{y}} = [\Omega_L, \Omega_R] \tag{10}$$

The integral error can be defined as:

$$\underline{\Omega}_{err} = \int_0^t \left(\Omega_{ref} - \tilde{\underline{y}} \right) dt \tag{11}$$

where Ω_{ref} is the reference (rated) rotor speed. From equations 6 and 11 (and assuming $[D] = [0]$) it follows:

$$\dot{\underline{\Omega}}_{err} = \Omega_{ref} - [C]\tilde{\underline{x}} \tag{12}$$

The augmented system can finally be obtained as:

$$\left\{ \begin{matrix} \dot{\tilde{\underline{x}}} \\ \dot{\underline{\Omega}}_{err} \end{matrix} \right\} = \begin{bmatrix} A & 0 \\ -C & 0 \end{bmatrix} \left\{ \begin{matrix} \tilde{\underline{x}} \\ \underline{\Omega}_{err} \end{matrix} \right\} + \begin{bmatrix} B \\ 0 \end{bmatrix} \tilde{\underline{u}} + \begin{bmatrix} B_d \\ 0 \end{bmatrix} \tilde{\underline{u}}_d + \begin{bmatrix} 0 \\ \Omega_{ref} \end{bmatrix} \tag{13}$$

which in compact form becomes:

$$\dot{\tilde{\underline{x}}}_T = [A_T]\tilde{\underline{x}}_T + [B_T]\tilde{\underline{u}} + [B_{d,T}]\tilde{\underline{u}}_d + [E] \tag{14}$$

where $\tilde{\underline{x}}_T$ is the global state vector:

$$\tilde{\underline{x}}_T = [\beta_L, \beta_R, \dot{\beta}_L, \dot{\beta}_R, \Omega_L, \Omega_R, q_5, \dot{q}_5, q_6, \dot{q}_6, \Omega_{L,err}, \Omega_{R,err}] \tag{15}$$

The final state-space system is hence composed of 12 states.

5.3   Control Design

5.3.1   LQR Blade Pitch Control Design

LQR control is based on the minimization of a quadratic cost function accounting for state control and control input usage (Prasad et al., 2014):

$$J = \int_{t_0}^{t_1} (\tilde{\underline{x}}_T^T [Q] \tilde{\underline{x}}_T + \tilde{\underline{u}}^T [R] \tilde{\underline{u}}) \, dt \tag{16}$$

where $[Q]$ and $[R]$ are symmetric positive semi-definite and positive definite weight matrices, respectively. The selection of weight parameters is typically left to the control system designer and is often resolved by rule of thumb or exhaustive search approaches. Sensitivity analysis and optimization methods may be employed to determine optimal weight parameters which maximize the control system performance according to the selected objectives (Miyamoto et al., 2018). In this work, weight matrices are determined heuristically by considering the associated control objectives and evaluating the ensuing system's performance. The full-state feedback minimizing J is given by:

$$\tilde{\underline{u}} = -[K] \tilde{\underline{x}}_T \tag{17}$$

where $[K]$ is the control gain matrix given by:

$$[K] = [R]^{-1} [B_T]^T [P] \tag{18}$$

where $[P]$ is a positive definite symmetric matrix obtained by solving the algebraic Riccati equation (ARE):

$$[A_T]^T [P] + [P][A_T] - [P][B_T][R]^{-1}[B_T]^T[P] + [Q] = 0 \tag{19}$$

LQR design is carried out in MATLAB by using the featured LQR function *lqr*.
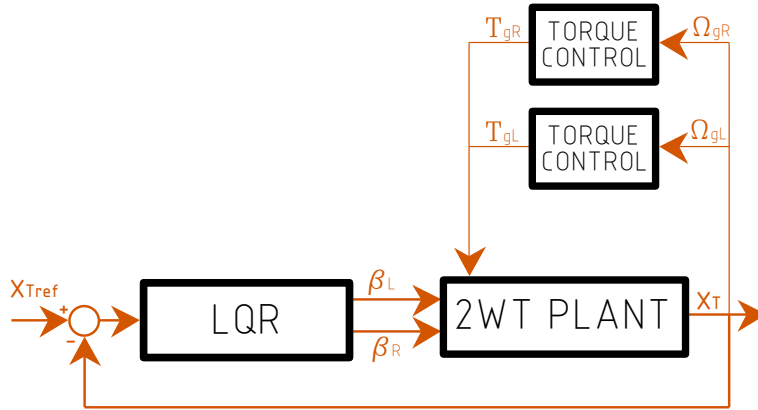
Figure 5.5: Control schematics.

5.3.2   Generator Torque Control

The generator torque control is excluded from linear control design, and a standard control schedule is employed in parallel as shown in Figure 5.5. Each wind turbine is controlled independently. Figure 5.6 shows the controlled generator torque as a function of generator speed. The regions depicted are the standard control regions as described in Introduction. Torque control scheme in Region 2 maximizes the wind turbine aerodynamic power (see Figure 5.2) for each aerodynamic state (Johnson, 2004; Johnson et al., 2004):

$$
\begin{aligned}
T_g &= C\Omega_g^2 \\
C &= \frac{1}{2}\rho_{air}\frac{C_{P,max}(\beta)}{\lambda^*(\beta)^3}\pi R^5
\end{aligned}
\tag{20}
$$

where Ω_g is the generator speed, λ^* is the optimal TSR at a given blade pitch angle, and $C_{P,max} = C_P(\lambda^*(\beta), \beta)$ is the optimal power coefficient. The blade pitch angle used to determine λ^* and $C_{P,max}$ is at present assumed constant and equal to the global optimal value (0 deg). The assumption is in consequence of small mean and standard deviation values of blade-pitch angles in Region 2 given by the present control design ($\mu \simeq 1$ deg, $\sigma \simeq 2$ deg). Torque control
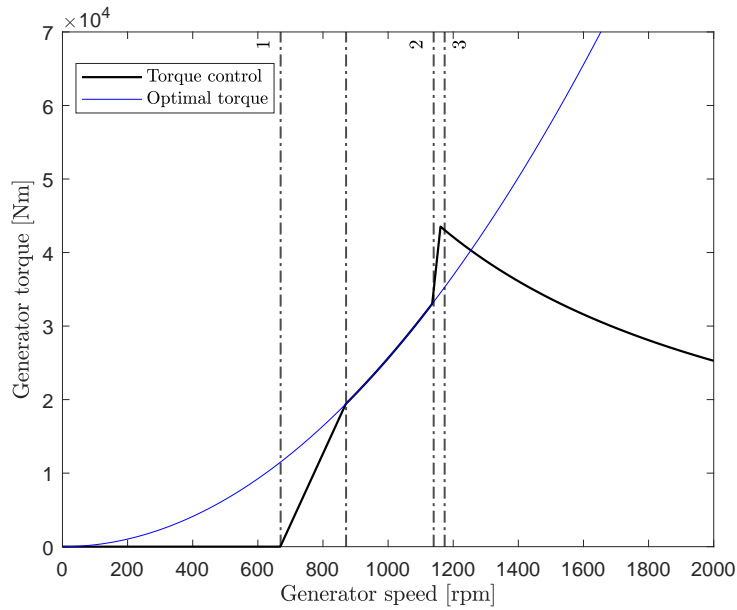
Figure 5.6: Generator torque control.

scheme in Region 3 keeps constant generator power output:

$$P_e = T_g \Omega_g \tag{21}$$

where P_e is the rated generator power.

5.3.3   LQR Blade Pitch Control Schedules

The 2WT system is considerably non-linear and exhibits different behavior in Region 2, Region 3, and around the rated wind speed. Moreover, control objectives change in relation to the operation regime considered. Three different LQR control schedules have thus been defined for the rotor-collective blade-pitch control. The operational wind speeds at which each controller operates are listed in Table 5.3. Control LQR-A operates at below-rated wind regimes (between 3 and 10 m/s). Control LQR-B operates close to the rated wind speed (between 11 and 12 m/s). Finally, control LQR-C operates at above-rated wind speeds (between 13 and 25 m/s). The wind speed gaps between control sched-

Table 5.3: Operational wind speeds associated with LQR controllers employed.

	U_{rel} **[m/s]**
LQR-A	3 - 10
LQR-B	11 - 12
LQR-C	13 - 25

Table 5.4: Steady-state operation points used for linearization.

		LQR-A	**LQR-B**	**LQR-C**
U_{rel}	m/s	9	11.3	13
β	rad	0.052	0.1	0.118

ules are associated with transitional conditions not considered in this work. Smooth transitioning between controllers may be employed to effectively automate the controller selection process (Lindeberg et al., 2012). This may be achieved by estimating the effective wind speed using a Kalman filter (KF) (Jena and Rajendran, 2015). As wind speed stationarity is commonly assumed (as in TurbSim (Jonkman, 2009a)), the controller employed is at present simply determined using the mean wind speed used to generate the wind profile realization.

Three different operation points (one for each controller) are used to linearize the system, as listed in Table 5.4. The control objectives used in this study are 1) the mitigation of platform yaw motion, and 2) the regulation of generators' speed at the rated value for rated and above-rated wind speeds. The employment of as few control objectives as possible has been adopted for two reasons. First, platform yaw motion is an important dynamic mode strictly associated with the 2WT system. Consequently, more emphasis has been given to its mitigation by means of an optimal control strategy. Secondly, fewer control objectives make the evaluation of the control system performance easier since fewer state couplings are taken into account. A much larger number of control objectives can be considered in later control design stages. LQR con-

Table 5.5: LQR control weigths.

	[Q]	[R]
LQR-A	*diag(0, 0, 0, 0, 0, 0, 0, 0, 500, 1, 0, 0)*	*diag(100,100)*
LQR-B	*diag(0,0,0,0,500,500,0,0,2500,2500,0.01,0.01)*	*diag(200,200)*
LQR-C	*diag(0, 0, 0, 0, 5, 5, 0, 0, 5000, 5000, 1, 1)*	*diag(100,100)*

Table 5.6: LQR control gain scheduling.

	[K]
LQR-A	$\begin{bmatrix} 0,0,0,0,-0.0241,0.0241,0,0,1.2244,5.4343,0,0 \\ 0,0,0,0,0.0241,-0.0241,0,0,-1.2244,-5.4343,0,0 \end{bmatrix}$
LQR-B	$\begin{bmatrix} 0,0,0,0,-0.87,-0.38,0,0,1.929,6.52,0.0071,0 \\ 0,0,0,0,-0.38,-0.87,0,0,-1.929,-6.52,0,0.0071 \end{bmatrix}$
LQR-C	$\begin{bmatrix} 0,0,0,0,-1.617,1,0,0,5.04,-0.8838,0.1,0 \\ 0,0,0,0,1,-1.617,0,0,-5.04,0.8838,0,0.1 \end{bmatrix}$

trol objectives are summarized as follows. Control LQR-A minimizes platform yaw motion. Control LQR-B minimizes platform yaw motion while controlling the generators' speed at rated values. Control LQR-C is similar in scope to control LQR-B, but more weight is given to the generator speed control to optimize power output quality.

LQR control weights and associated gains scheduling for each controller are selected heuristically by considering the associated control objectives and evaluating the resulting performance of the system. Values used in this work are listed in Tables 5.5 and 5.6.

5.4 Reference Blade Pitch Controls

5.4.1 OC3 PI control

The baseline OC3 PI control computes the rotor-collective blade-pitch angle using a gain-scheduled proportional-integral control on the error between generator speed and the rated generator speed value (Jonkman, 2007). The control

law can be expressed as:

$$\beta = K_P(\beta)\big(\omega_g - \omega_{g,ref}\big) + K_I(\beta) \int_0^t \big(\omega_g - \omega_{g,ref}\big)dt \tag{22}$$

where K_P and K_I are the proportional and integral gains scheduled as a function of the blade pitch angle. Gain scheduling takes into account the nonlinear relationship between blade-pitch and variation of aerodynamic power.

It is known that platform pitch instability may occur if the control system is too stiff. The gains proposed for control of the OC3-Phase IV floating system are designed to reduce the controller natural frequency from 0.6 rad/s (associated with baseline onshore gains) to about 0.2 rad/s – thus lower than the platform pitch natural frequency of about 0.21 rad/s (Jonkman, 2010). Reduction of controller frequency below the platform pitch natural period has been proved beneficial for the avoidance of negative damping in the platform pitch direction (Larsen and Hanson, 2007). Since the 2WT and OC3-Phase IV platform pitch motion natural frequencies are very similar (see Table 5.2) and the same drivetrain system is used, the same reduced gains can be employed without further modification, as listed in Table 5.7. No instability occurrence has been detected with this control setup. Moreover, the OC3 PI control configuration applied to the 2WT system may also determine negative damping in the platform yaw direction at above-rated wind speeds. This can be associated with the reduction of thrust at the hub moving upwind induced by higher relative wind speed. This effect may exacerbate the platform yaw motion, which is predominantly induced by wind turbulence intensity (El Beshbichi et al., 2021a).

5.4.2 PI-P Control

Previous work focusing on the dynamic response of the 2WT system proposed a simple coupled control strategy aiming at the mitigation of platform yaw motion (El Beshbichi et al., 2021a). This control strategy, called PI-P for brevity, is composed of a proportional control mitigating platform yaw motion superimposed to the baseline OC3 PI control. The control law associated with the

Table 5.7: Major reference controller parameters.

		OC3 PI	PI-P
Proportional gain (yaw mitigation), K_{q_6}	-	-	1.5
Proportional gain at min blade-pitch setting, $K_P(0)$	s	0.00627	-
Integral gain at min blade-pitch setting, $K_I(0)$	-	0.00089	-
Max blade pitch rate	deg/s	8	-
Min blade pitch	deg	0	-
Max blade pitch	deg	90	-

proportional control component can be expressed as:

$$
\begin{cases}
\text{if } L \quad \beta_{q_6} = max(0, -K_{q6}q_6) \\
\\
\text{if } R \quad \beta_{q_6} = max(0, K_{q6}q_6)
\end{cases}
\tag{23}
$$

where β_{q_6} is the blade-pitch angle associated with platform yaw motion control, and K_{q_6} is the associated proportional control gain. This control reduces thrust at the hub experiencing relative motion in the downwind direction. Heuristic control tuning showed best performance at around $K_{q_6} \simeq 1.5$. Table 5.7 summarizes the controller parameters.

5.5 Environment

The performance of the LQR control design is assessed by evaluating the fully-coupled nonlinear response of the 2WT system over a wide range of wind speeds at below-rated, rated, and above rated environmental conditions. Results are compared to the performance relative to the OC3 PI control and the coupled PI-P control. Environmental parameters are listed in Table 5.8. Wind speeds range from a minimum of 5 m/s to the cut-off value of 25 m/s. The turbulence model considered is Kaimal, and a normal turbulence type with characteristic B (NTM - type B) is considered (Jonkman, 2009a). All hydrodynamic loads are considered, where incident wave loads are relative to irregular waves from the

Table 5.8: Environmental parameters.

U_{rel}	m/s	5-25
$Turb$		Kaimal
I		NTM B
$S(\omega)$		JONSWAP
H_s	m	6
T_p	s	10

JONSWAP spectrum. The effect of current is neglected. A water depth of about 320 m is considered. Waves are aligned with the wind direction. Only one sea state is applied to the system, corresponding to a characteristic wave height H_s of 6 m and characteristic wave period T_p of 10 s.

5.6   Results

The integration method *ida* is used to solve the equations of motion of the system. Integration tolerance equal to $1x10^{-4}$ is used. A time interval equal to 0.3 s is used, sufficient to cover rigid motion response. The linear solver *totalpivot* and non-linear solver *kinsol* are also employed. Time realizations of about 4000 s are computed. The first 400 s are removed to avoid numerical transients, leaving a net 1 h simulation time to compute short-term results. A total of five response parameters are used to evaluate the LQR controller response and compare it with reference control strategies (Sarkar et al., 2021). The first parameter is the platform yaw motion. Standard deviation (STD) should be kept as low as possible. The second parameter is generator speed. More stable generator speed leads to higher power quality. The third parameter is the electric power output, which is directly related to the variation of generator speed. The fourth parameter is the platform pitch motion, which can induce significant tower fore-aft (FA) bending loads if too high. Finally, the fifth parameter is the blade pitch rate. This parameter is used as an indication of actuation usage. The assumptions employed in this work may have a significant impact on the performance parameters here considered. For instance, rigid structural dynamics

may significantly reduce STD values - especially of generator speed and electric power output. The neglect of the effect of blades' spatial orientation on the aerodynamic loads may also significantly influence platform yaw motion STD. Nonetheless, the results obtained are sufficiently accurate for global dynamic performance evaluation and control system design purposes. A detailed exposition of the dynamic response of the 2WT system will be the subject of future work.

Figure 5.7 shows the performance of LQR and coupled PI-P controllers as a function of wind speed. Platform yaw motion STD with OC3 PI controller is also included. It is clear that platform yaw motion is significant without a proper control strategy throughout the full wind speed range (OC3 PI). PI-P controller reduces the platform yaw motion significantly. LQR control is found to perform significantly better than the PI-P control, especially at rated and above-rated wind speeds. At below-rated wind speeds the advantage is present but small (about -8% LQR yaw motion STD and -11% LQR pitch motion STD if compared to PI-P response at 8 m/s). This is expected, since the only control objective of control LQR-A is platform yaw motion reduction, while the major advantage of LQR against PI strategies is the ability to control multiple objectives (Kumar and Stol, 2009). At near-rated and above-rated wind speeds the LQR controller performs significantly better than the PI-P controller. The advantage is significant also for operating conditions far from the one used for linearization. At 12 m/s the platform yaw motion STD is about -58% and the platform pitch motion STD is about -40% if compared to the PI-P controller. Marginally higher mean platform pitch motion is obtained around the rated wind speed (about +5% if compared to PI-P controller). LQR performance is stable also at very high wind speeds. Electric power quality is also increased with the LQR control. At 17 m/s, the electric power output mean and STD difference if compared to the PI-P control is about +100 kW and -17%, respectively. Excellent generator speed control at above-rated wind speeds is obtained, with a significant STD reduction obtained with the LQR controller (about -25% if compared to the PI-P controller). It can also be noted how the average generator speed reaches close-to-rated values at about 11 m/s, while the average electric power output stabilizes
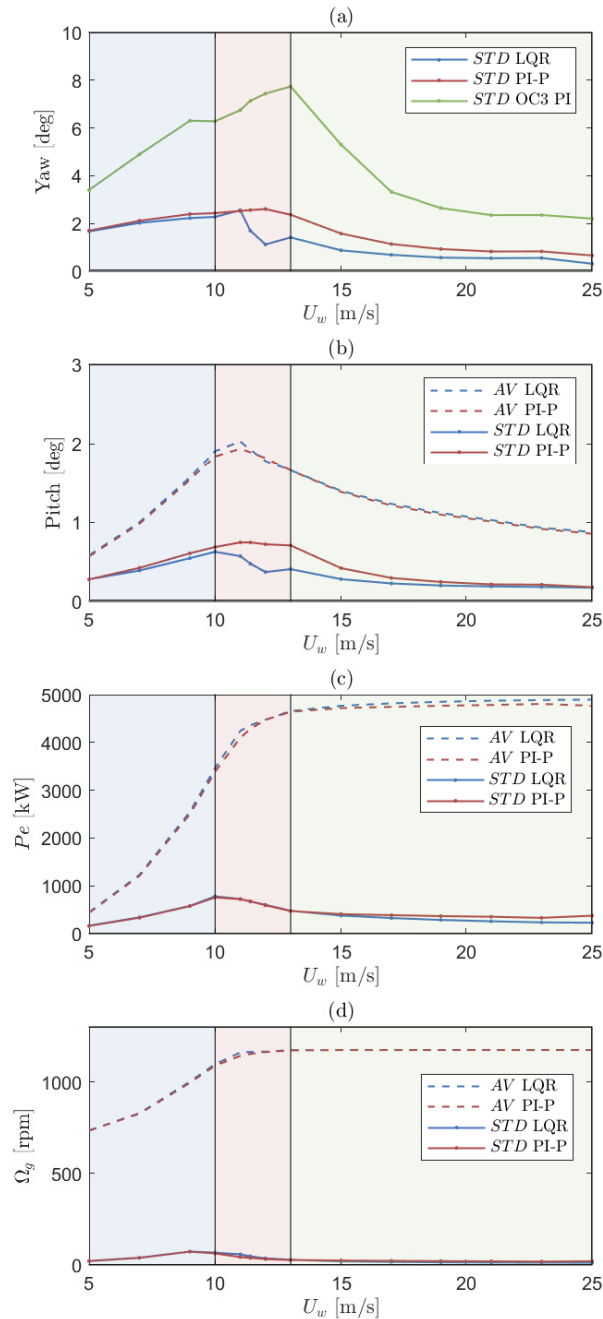
Figure 5.7: Performance of LQR and coupled PI-P controllers as a function of wind speed. Platform yaw response with OC3 PI controller is also included. Control regions associated with different LQR gain schedulings are highlighted with different box colors. Response given in terms of a) platform yaw STD, b) platform pitch motion, c) electric power, and d) generator speed. Only results relative to the left turbine are shown.
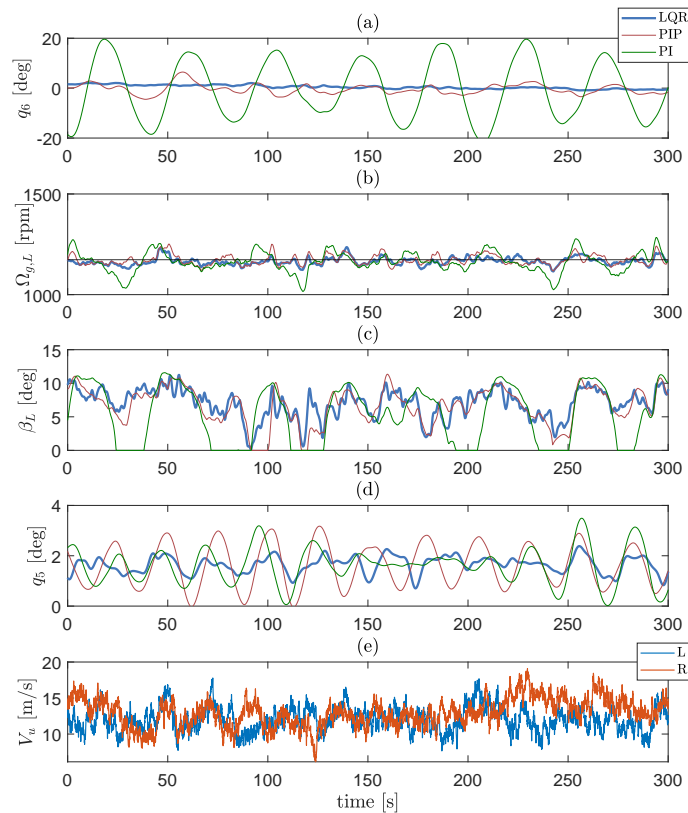
Figure 5.8: Above-rated 2WT response 300 s time series of a) platform yaw motion, b) generator speed, c) blade-pitch angle, and d) platform pitch motion for LQR (control LQR-C), baseline OC3 PI, and PI-P controllers. Mean wind speed 13 m/s. Only results relative to the left turbine are shown. Turbulent wind realizations at hubs are also depicted (e).

at close-to-rated values at about 13 m/s. This discrepancy is mainly associated with the relatively higher electric power STD close to the rated wind speed (17% of the mean value against the 5% associated with the generator speed). This can further be related to the fluctuating aerodynamic torque at the low-speed shaft given by wind turbulence.

Figure 5.8 and Figure 5.9 show time realizations of about 300 s of the 2WT response for LQR, the baseline OC3 PI, and the coupled PI-P controllers for above-rated (13 m/s) and below-rated (9 m/s) wind speed conditions, respectively. LQR control yields more stable results in terms of platform yaw and pitch
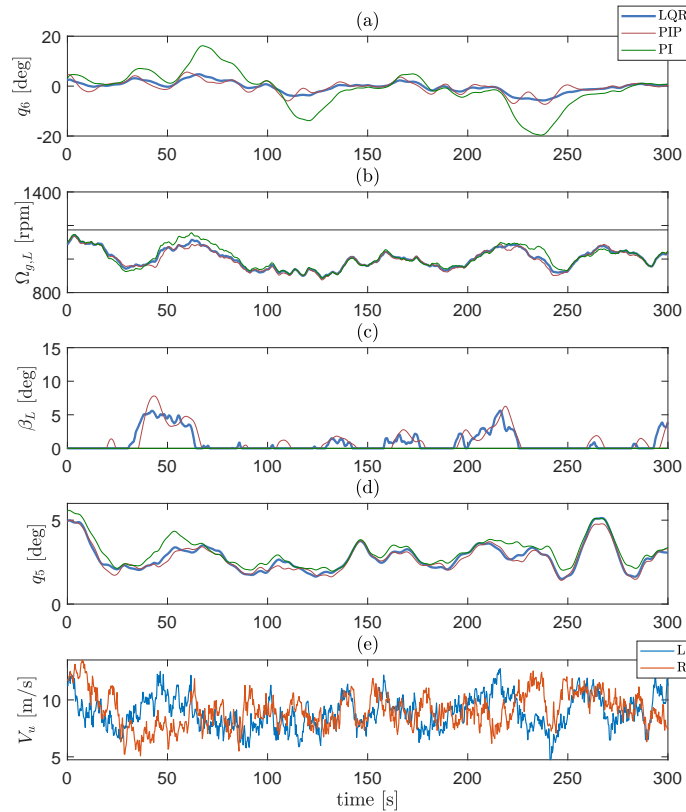
Figure 5.9: Below-rated 2WT response 300 s time series of a) platform yaw motion, b) generator speed, c) blade-pitch angle, and d) platform pitch motion for LQR (control LQR-A), baseline OC3 PI, and PI-P controllers. Mean wind speed 9 m/s. Only results relative to the left turbine are shown. Turbulent wind realizations at hubs are also depicted (e).

motions. LQR controller is able to reduce peak variations of generator speed from the rated value. It can be also noted that the blade pitch angle experiences a higher rate of change, associated with a more onerous actuator usage. The increase in blade pitch rate is not problematic, as long as subsequent detailed investigation of the loads and fatigue assessment associated with the blade pitch actuation system are carried out.

It is clear how the LQR controller gives most of its advantages around and above the rated wind speed. Four response parameters are used to further evaluate the LQR controller response and compare it with reference controllers. Response evaluation is given in terms of the root mean square (RMS) of platform yaw motion, generator speed error, electric power error, and blade-pitch

rate. Figure 5.10 shows the performance comparison for LQR, the baseline OC3 PI, and the coupled PI-P controllers at above-rated wind speeds. Moreover, Figure 5.11 shows the performance comparison for LQR, the baseline OC3 PI, and the coupled PI-P controllers at below-rated wind speeds. At above-rated wind speeds, LQR is the best performing controller. The PI-P controller leads to higher speed and power errors than the OC3 PI controller at higher wind speeds (about +10% RMS power error difference at 17 m/s). Performance must, however, be paid in terms of a higher actuation usage. The RMS of blade-pitch rate is significantly higher for the LQR controller (about +27% and +35% if compared to PI-P and OC3 PI controllers at 13 m/s, respectively). However, the increase in blade-pitch rate is well within the limits imposed by actuation rate saturation (max 8 deg/s (Jonkman, 2007)). At below-rated wind speeds, the LQR and PI-P performance is similar.

5.7 Conclusion

This work presented the design of an optimal LQR controller for a two-rotor floating wind turbine prototype. Three different LQR control schedules were defined, associated to below-rated, near-rated, and above-rated wind speeds. For each controller, a related operational point was used for linearization. Numerical evaluations were used to assess the performance of the LQR controller against the performance of baseline OC3 PI and coupled PI-P controllers. Suited control objectives were considered. It was shown how the LQR controller performs significantly better than both reference controllers. The advantage was found to be most significant at above-rated wind speeds. Platform yaw and pitch motion STD is reduced considerably. Mean platform pitch motion close to the rated wind speed is marginally higher for the LQR controller than the PI-P performance. Electric power output STD is also reduced, indicating higher power quality. Greater performance must be paid for higher actuator usage (estimated in terms of blade-pitch rate RMS). Nevertheless, peak values are well within saturation limits.
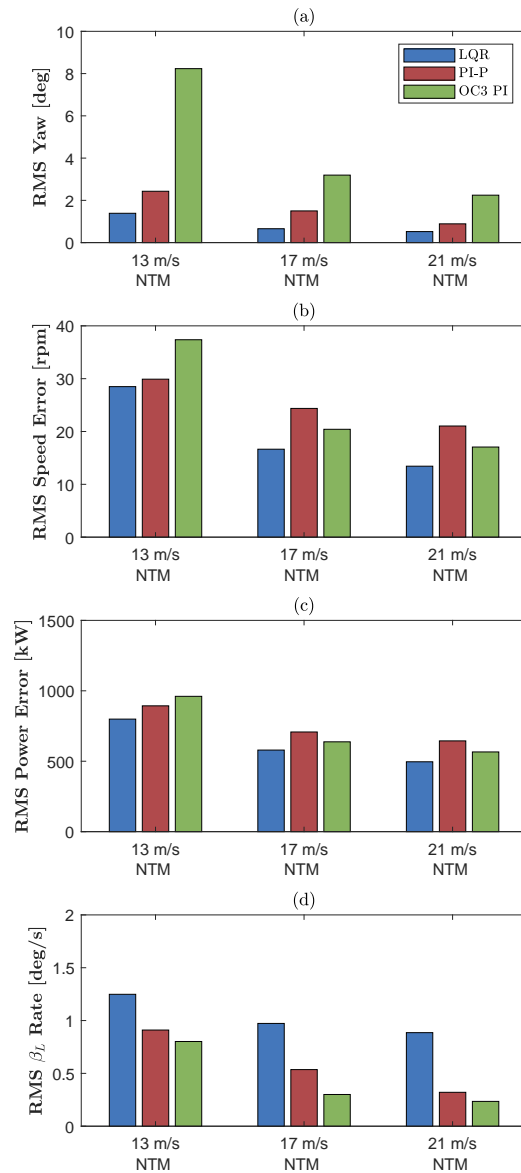
Figure 5.10: Performance comparison for LQR, baseline OC3 PI, and coupled PI-P controllers at above-rated wind speeds. RMS of a) platform yaw motion, b) generator speed error, c) electric power error, and d) blade-pitch rate. Only results relative to the left turbine are shown.
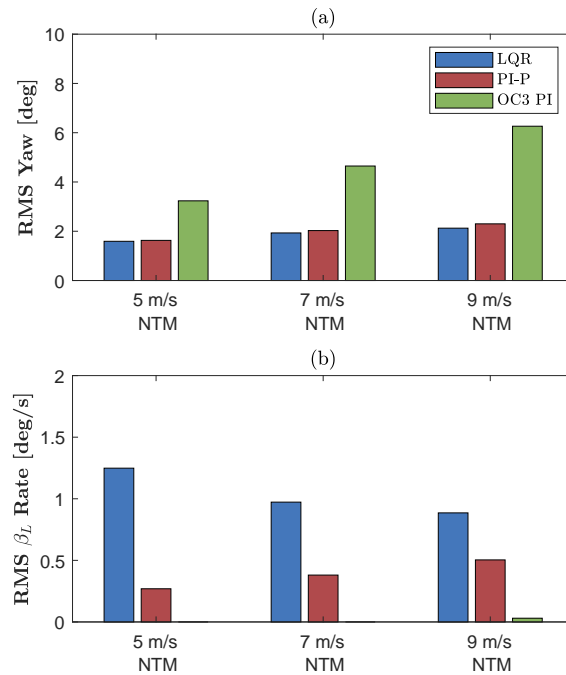
Figure 5.11: Performance comparison for LQR, baseline OC3 PI, and coupled PI-P controllers at below-rated wind speeds. RMS of a) platform yaw motion and b) blade-pitch rate. Only results relative to the left turbine are shown.

Acknowledgment

Chapter 6

Long-Term Exterme Response of a Two-Rotor Floating Wind Turbine

Omar El Beshbichi [a], Yihan Xing [a], Muk Chen Ong [a]

[a] Department of Mechanical and Structural Engineering and Materials Science, University of Stavanger, Stavanger, Norway.

Abstract

The modified environmental contour method (MECM) is assessed for the prediction of 50-year extreme response of a two-rotor floating wind turbine concept (2WT) deployed in two offshore sites in the northern North Sea (Norway 5) and the North Atlantic Ocean (Buoy Cabo Silleiro). The sites considered are in areas known for their floating wind development potential. The environmental contour method (ECM) is used to reduce the computational effort of full long-term analysis (FLTA) by only considering environmental conditions associated with a given return period. MECM is a modification of the ECM where additional environmental contours are included to account for discontinuous operation modes of dynamic structures. The results obtained in MECM are benchmarked against FLTA results and compared to ECM results. ECM leads to large underpredictions of responses governed by wind loads if compared to FLTA, as it is not capable of taking into account important operational modes of the 2WT. It is found that MECM, which includes the wind turbines cut-off contour, is able to reduce most response underpredictions within 15% difference compared to FLTA results. MECM may thus be considered as a sufficiently accurate and computationally efficient method for the long-term extreme analysis of 2WT concepts.

Keywords: Floating offshore wind turbines, Multi rotor, Long-term extreme response, Environmental contour method, Probabilistic design.

6.1 Introduction

Floating offshore wind turbine concepts (FOWTs) should be designed to withstand extreme environmental loading. The most accurate method for the prediction of long-term extreme responses is the full long-term analysis (FLTA). This approach directly integrates the probability distribution of all short-term extreme responses and their associated environmental conditions. However, FLTA is also computationally demanding due to the bulk response evaluation of all the relevant environmental conditions. In the last decade, more efficient methods able to evaluate extreme long-term responses with a sufficient level of accuracy have been investigated. The most widely used alternative to reduce the environmental cases to be evaluated is the environmental contour method (ECM) (Haver and Winterstein, 2008). This method predicts the long-term extreme response by considering the short-term extreme distribution of only significant conditions lying on the environmental contour surface with the same return period as the long-term extreme response. However, the operational space of offshore wind turbines (OWTs) is highly discontinuous. The cut-in and cut-out wind speed limits, as well as full loading at rated conditions, entail a discontinuity of the environment-structural load relationship. ECM assumes the design load cases to lie nearby the environmental contour surface. Consequently, pure ECM is found to greatly under-estimate the long-term extreme responses of OWTs and FOWTs (Saranyasoontorn and Manuel, 2004; Li et al., 2016).

The modified environmental contour method (MECM), proposed in Li et al. (2016), is a modification of the ECM that takes into account multiple contours in addition to the one associated with the ECM return period. The method allows for the employment of environmental contours in structures with a discontinuous environment-load condition.

MECM has been successfully employed to assess the long-term extreme response of a variety of offshore structures, including bottom-fixed OWTs (Li et al., 2016), semi-submersible FOWTs (Li et al., 2017), and combined wind turbine and wave energy converter systems (WECs) (Li et al., 2018). However, no MECM assessment for the analysis of two-rotor floating wind turbine sys-

tems is to date available in the relevant literature. Knowledge of the validity of MECM results is of great practical utility given the significant reduction of the time needed for simulation and analysis.

In this paper, the extreme long-term response of a spar-type two-rotor floating wind turbine concept (2WT) is analyzed by means of the MECM for two different offshore sites in the North Atlantic Ocean and the northern North Sea. The offshore sites considered in this work are in areas well known for their floating wind development potential (EWEA, 2013). The accuracy of MECM results is assessed by comparing them with results obtained from the complete FLTA and the more general ECM.

6.2 Overview of Environmental Long-Term Joint Distributions

A detailed exposition of long-term joint distribution assessment can be found in Li et al. (2013). Long-term extreme response analysis is based upon the joint distribution of the environmental parameters of a particular offshore site. That is, for each specific environmental condition it is necessary to define the associated long-term probability of occurrence given a return period, e.g., 50 years. A large amount of data is normally necessary to estimate the environmental distributions. To get accurate joint distribution fittings it is suggested to use at least ten years datasets (Bitner-Gregersen, 2011). It is assumed that the short-term responses are sequential and stationary (Li et al., 2013). It is customary to define the joint distribution given by the average wind speed, U_w, the significant wave height, H_s, and the significant wave period, T_p, by means of a marginal distribution of U_w, a conditional distribution of H_s given U_w, and a conditional distribution of T_p given both H_s and T_p:

$$f_{U_w,H_s,T_p}(u,h,t) = f_{U_w}(u)f_{H_s|U_w}(h|u)f_{T_p|U_w,H_s}(t|u,h) \tag{1}$$

where f denotes the probability density function operator (PDF). $f_{U_w,H_s,T_p}(u,h,t)$ is the joint PDF of environmental conditions at a specific

offshore site. In other words, $f_{U_w,H_s,T_p}(u,h,t)$ gives the relative likelihood that a specific offshore site will experience a given environmental condition (u,h,t). Integration of the joint PDF over the environmental space yields unity by definition, $\int f_s(s)ds = 1$ [where s is the generalized environmental variable].

The average wind speed marginal distribution is found to be best fitted by means of a two-parameter Weibull distribution, which can be described as:

$$f_{U_w}(u) = \left[\frac{\alpha_U}{\beta_U}\left(\frac{u}{\beta_U}\right)^{\alpha_U-1}\right]exp\left[-\left(\frac{u}{\beta_U}\right)^{\alpha_U}\right] \tag{2}$$

where α_U and β_U are the fitting shape and scale parameters of the distribution, respectively. The conditional PDF of H_s given U_w is also fitted by means of a two-parameter Weibull distribution:

$$f_{H_s|U_w}(h|u) = \left[\frac{\alpha_{HC}}{\beta_{HC}}\left(\frac{h}{\beta_{HC}}\right)^{\alpha_{HC}-1}\right]exp\left[-\left(\frac{h}{\beta_{HC}}\right)^{\alpha_{HC}}\right] \tag{3}$$

where α_{HC} and β_{HC} are the fitting shape and scale parameters of the distribution, respectively. They are fitted by means of power functions:

$$\alpha_{HC} = a_1 + a_2 u^{a_3} \tag{4}$$
$$\beta_{HC} = b_1 + b_2 u^{b_3} \tag{5}$$

where the constants $a_1, a_2, a_3, b_1, b_2, b_3$ are determined from data fitting. The conditional distribution of T_p given H_s and U_w is fitted by means of a lognormal distribution:

$$f_{T_p|U_w,H_s}(t|u,h) = \frac{1}{\sqrt{2\pi}\sigma_{ln(T_p)}t}exp\left[-\frac{1}{2}\left(\frac{ln(t)-\mu_{ln(T_p)}}{\sigma_{ln(T_p)}}\right)^2\right] \tag{6}$$

where $\mu_{ln(T_p)}$ and $\sigma_{ln(T_p)}$ are the mean value and standard deviation defining the lognormal distribution. They are defined as:

$$\mu_{ln(T_p)} = ln\left(\frac{\mu_{T_p}}{\sqrt{1 + \nu_{T_p}^2}}\right) \tag{7}$$

$$\sigma^2{}_{ln(T_p)} = \ln\left(\nu^2{}_{T_p} + 1\right) \tag{8}$$

$$\nu_{T_p} = \frac{\sigma_{T_p}}{\mu_{T_p}} \tag{9}$$

The mean value of T_p is computed as:

$$\mu_{T_p} = \bar{t}(h)\left[1 + \theta\left(\frac{u - \bar{u}(h)}{\bar{u}(h)}\right)^{\gamma}\right] \tag{10}$$

where θ and γ are fitting coefficients, and $\bar{t}(h)$ and $\bar{u}(h)$ are the expected peak period and average wind speed fitted as power functions:

$$\bar{t}(h) = e_1 + e_2 h^{e_3} \tag{11}$$

$$\bar{u}(h) = f_1 + f_2 h^{f_3} \tag{12}$$

where the constants $e_1, e_2, e_3, f_1, f_2, f_3$ are determined from data fitting. $\nu_{T_p}(h)$ may also be assumed only correlated with H_s. In this case the fitting can be described as follows:

$$\nu_{T_p}(h) = k_1 + k_2 exp(hk_3) \tag{13}$$

where the constants k_1, k_2, k_3 are determined from data fitting. Empirical fitting parameters for the marginal distribution of U_w, the conditional distribution of H_s given U_w, and the conditional distribution of T_p given both U_w and H_s at different offshore sites can be found in Li et al. (2013).

6.3   Overview of Long-Term Extreme Methods

6.3.1   Full Long-Term Analysis (FLTA)

The most accurate method to estimate the long-term extreme responses of off-shore structures is the full long-term analysis (FLTA). FLTA is mostly used as a benchmark reference to more simplified methods. The method combines the short-term extreme response distribution associated with all the environmental conditions for a given return period and their corresponding probability of occurrence. The long-term distribution can be established by integrating the product of the short-term extreme response cumulative distribution functions (CDF) and the long-term PDF of the environmental conditions associated with a particular offshore site:

$$F_X^{LT}(\xi) = \iiint F_{X|U_w,H_s,T_p}^{ST}(\xi|u,h,t) f_{U_w,H_s,T_p}(u,h,t) du dh dt \qquad (14)$$

Equation 14 is the standard representation of the full long-term analysis (Haver and Winterstein, 2008). X is a given response variable. F_X^{LT} and $F_{X|U_w,H_s,T_p}^{ST}$ are the long-term and short-term CDFs associated with the variable X. That is, they represent the probability that X will assume a value lesser or equal than ξ. The short-term extreme response probability distribution is often approximated by means of a Gumbel fit of the maxima of n realizations of random seeds (Haver and Winterstein, 2008). It is customary to use Gumbel distributions to fit extreme data (also denoted as extreme value distribution - type I) (Li et al., 2017). The Gumbel distribution can be defined as:

$$F^{ST}(x) \approx e^{-e^{-(x-\mu)/\beta}} \qquad (15)$$

where μ and β are, respectively, the location and scale parameters, which can be estimated by means of the method of moments (Mahdi and Cenac, 2012):

$$\mu = \overline{x} - \gamma\beta \qquad (16)$$

$$\beta = \sqrt{6}s_x/\pi \qquad (17)$$

where γ is the Euler-Mascheroni constant ($\gamma \approx 0.57722$), $\overline{x}$ is the mean of the extreme values, and s_x is the standard deviation of the extreme values. If a reference time duration of 1-h is used, the full-long term extreme response can then be estimated by means of the inverse relationship:

$$\xi^* = F_X^{LT^{-1}}(1 - 1/(N * 365 * 24)) \tag{18}$$

where N is a given return period in years. From Equation 14 it is clear that FLTA entails the integration of a large number of environmental states. This method is thus extremely time-consuming. A great effort has been put by many researchers in designing more cost-effective methods to estimate extreme responses of offshore structures, such as the ECM (Haver and Winterstein, 2008) and MECM (Li et al., 2016).

6.3.2 Environmental Contour Method (ECM)

ECM stems from the more general inverse first-order reliability method (IFORM) (Winterstein et al., 1993). In contrast to IFORM, ECM does not consider the variability of the extreme response (Li et al., 2017). Consequently, the contour can be fully described in the environmental space. As already discussed, ECM assumes that the extreme response is found along a surface constructed within the environmental space (i.e., U_w, H_s, T_p) and associated with the desired return period, e.g., 50 years. The environmental condition along the contour surface which yields the largest short-term response is designated as design point. High empirical percentiles are used in order to take into account the omission of the short-term extreme response variability (Madsen, 1988; Li et al., 2017). Percentiles values between 70% to 90% are normally used.

ECM is based on Rosemblatt transformation (Rosenblatt, 1952), whereby site-specific environmental PDFs are combined with the projection of a normal CDF into a gaussian space (U-space) associated with the desired return period. The U-space thus defined has the same number of dimensions of the environmental space. That is, the environmental space (U_w, H_s, T_p) is transformed into the U-space (U_1, U_2, U_3). Figure 6.1 depicts a graphical representation of the
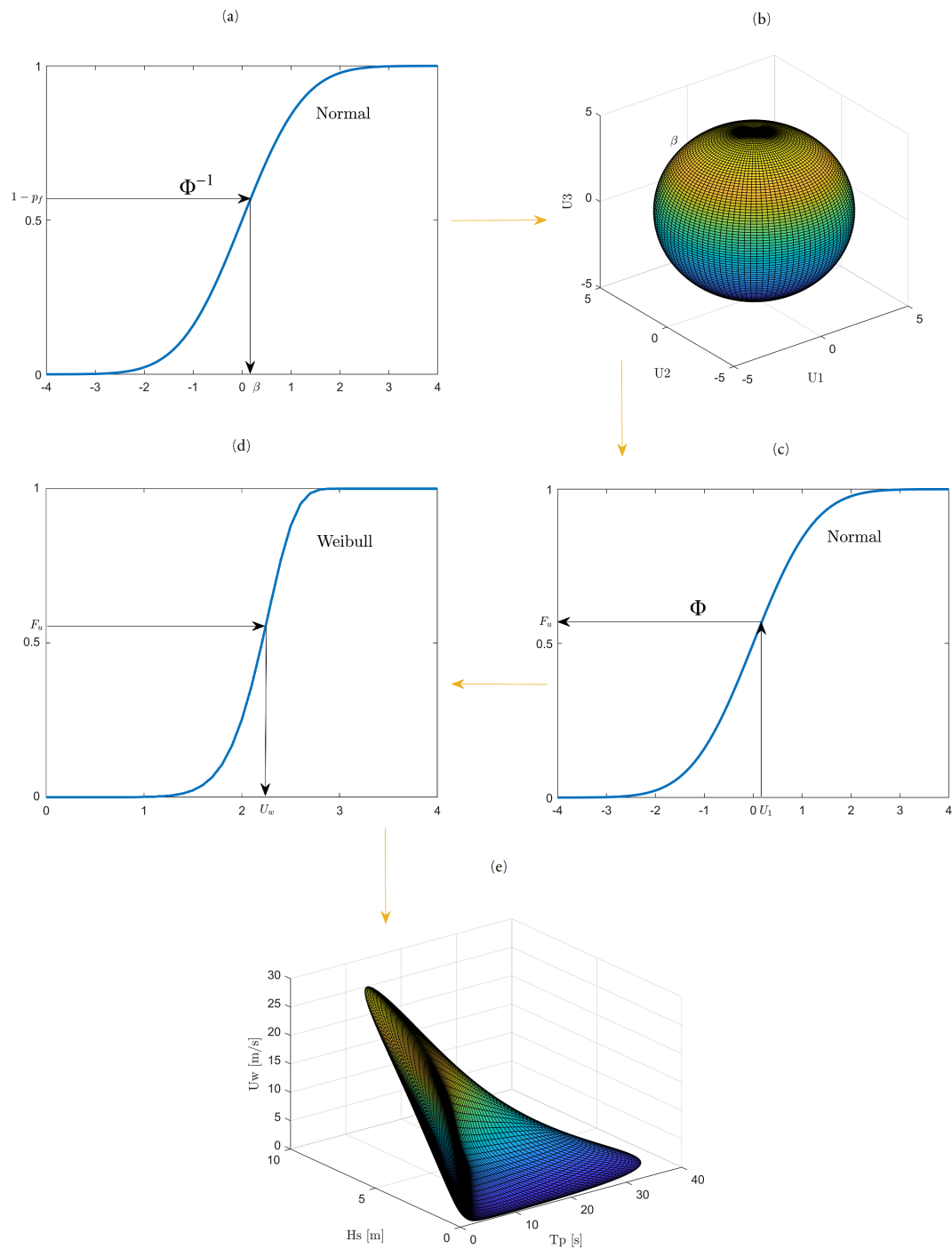
Figure 6.1: Graphical representation of the Environmental Contour Method (ECM), based on Rosemblatt transformation (Rosenblatt, 1952). Only the marginal (Weibull) distribution of U_w is shown, relative to a standard height of 10 m and site 14 (Table 6.3) (Li et al., 2013).

ECM procedure. The steps required to establish an EC may be described as follows. First, a desired return period N is defined, e.g., 50 years. The hourly exceedance probability, p_f, can then be defined as:

$$p_f = \frac{1}{365.25 * 24 * N} \tag{19}$$

The associated non-exceedance probability, $1 - p_f$, can then be used to compute the Gaussian variable, β, corresponding to the desired return period (Figure 6.1a):

$$\beta = \Phi^{-1}(1 - p_f) \tag{20}$$

where Φ is the standard Gaussian CDF operator ($\mu = 0, \sigma = 1$). In the U-space, the distance of a point to the origin corresponds to the associated return period. Therefore, a sphere of radius β may be established to define all the environmental conditions associated with the return period N (Figure 6.1b). The relationship between the environmental variables in the gaussian space (U_1, U_2, U_3) and the environmental variables in the physical space (U_w, H_s, T_p) can be described as follows:

$$F(U_w) = \Phi(U_1) \tag{21}$$
$$F(H_s|U_w) = \Phi(U_2) \tag{22}$$
$$F(T_p|U_w, H_s) = \Phi(U_3) \tag{23}$$

That is, the probability computed from normal CDF is bound to the probability computed from the environmental CDF associated with the environmental variable considered, e.g., Weibull for the marginal distribution of U_w (Figures 6.1c-d). For any given point in U-space, $(U_1{}^*, U_2{}^*, U_3{}^*)$, a corresponding point in the physical space can be thus established, $(U_w{}^*, H_s{}^*, T_p{}^*)$. As a consequence, the gaussian sphere in U-space can be transformed into a surface in physical space corresponding to the same return period N (Figure 6.1e).

ECM entails much fewer environmental conditions compared with FLTA. Moreover, the design points are naturally lumped either in the maximum wind speed region or in the maximum wave height region. Therefore, often only a

portion of the contour surface is of interest in long-term extreme analysis (Li et al., 2013).

ECM is often not suitable to accurately analyze the long-term extreme response of systems whose environment-structural load relationship is not monotonically increasing. Structures such as FOWTs, for instance, feature many discontinuities of the response which are associated with sudden operational changes. It is clear that for such systems, the largest extreme response is likely to occur during normal operational conditions.

6.3.3   Modified   Environmental   Contour   Method (MECM)

As previously discussed, ECM cannot be considered a reliable method to predict the extreme long-term response of structures with complex dynamics such as FOWTs. The MECM, proposed by Li et al. (2016), is a modification of the ECM which takes into account multiple contours to incorporate non-monotonic behaviour. For instance, a contour surface with a maximum wind speed corresponding to the FOWT cut-off wind speed condition can be superimposed to the global 50-years contour surface to account for the discontinuous behaviour. In the same manner, additional contour surfaces are included accounting for cut-in and rated conditions. The additional contours have a different return period, as a different constraint is used to define the surface in U-space. Since the different contours use different return periods, extrapolation is needed to get consistent values to the original N-year period. The largest extreme response obtained from the environmental contours is the final MECM result. This can be written as (Li et al., 2018):

$$\xi_1 = F_{X|U_w,H_s,T_p}^{ST(50yr)-1}(p_1|u_{contour1}, h_{contour1}, t_{contour1}) \tag{24}$$

$$\xi_2 = F^{ST(50yr)-1}_{X|U_w,H_s,T_p}(p_2|u_{contour2}, h_{contour2}, t_{contour2})$$

$$\dots$$

$$\xi_{ECM} = F^{ST(ECM)-1}_{X|U_w,H_s,T_p}(p_1|u_{ECM}, h_{ECM}, t_{ECM})$$

$$\xi = max[\xi_1, \xi_2, ..., \xi_{ECM}]$$

where p_i (i= 1,2,...) is the empirical percentile level for the additional contour (commonly equal to 50%), while p_{ECM} is the empirical percentile used in ECM (commonly equal to 90%). The expected value of the additional contours is relative to a lower return period compared to the ECM. The extrapolated distributions equivalent to a 50-year return period are thus computed as:

$$F^{ST(50yr)}_{X|U_w,H_s,T_p}(\xi) = F^{ST}_{X|U_w,H_s,T_p}(\xi|u_M, h_M, t_M)^{50/M} \tag{25}$$

where M is the return period of the additional contour. For a full methodological description of MECM refer to Li et al. (2016).

6.4 Two-Rotor Spar-Type Floating Wind Turbine (2WT)

The present study focuses on the response of a spar-type two-rotor floating wind turbine concept (2WT) proposed by El Beshbichi et al. (2021a). The system consists of two baseline NREL 5-MW wind turbines (Jonkman et al., 2009) mounted on a structure composed of horizontal arms connected to the main tower and supported by wires. The floating foundation used is a standard spar-buoy design. Figure 6.2 shows the 2WT structural geometry. Major specifications of the 2WT concept are listed in Table 6.1. The table includes geometrical and inertial specifications, station-keeping specifications, hydrostatic specifications, and specifications related to the wind turbine design considered.

Three catenary mooring lines are used as station-keeping systems. The unstretched length of the lines is 902.2 m, while the static vertical length is 250 m. The mooring line mass density used is equal to 200 kg/m, and a constant yaw

Table 6.1: Major specifications of the 2WT concept (Jonkman, 2007; El Beshbichi et al., 2021a).

Draft	m	140
Depth to CoG (full system)	m	100.9
Depth to fairlead	m	86.5
Diameter	m	7.6 to 10.5 (tapered)
Water Displacement	m^3	11.7x10^3
Platform Mass (including ballast)	kg	10.6x10^6
Tower Mass	kg	537x10^3
Rotor Mass (per unit)	kg	110x10^3
Nacelle Mass (per unit)	kg	240x10^3
Platform Roll Moment of Inertia about CoG	kgm^2	1.13x10^{10}
Platform Pitch Moment of Inertia about CoG	kgm^2	1.13x10^{10}
Platform Yaw Moment of Inertia about Centerline	kgm^2	1.7x10^8
Number of mooring lines	-	3
Angular distance between adjacent mooring lines	deg	120
Unstretched line length	m	902.2
Radius to fairlead	m	5.78
Line diameter	m	0.09
Line mass density	kg/m	200
Yaw Spring Mooring Stiffness	Nm/rad	9.8x10^7
Heave Hydrostatic restoring stiffness	N/m	4.56x10^5
Roll Hydrostatic restoring stiffness	Nm/rad	3.42x10^9
Pitch Hydrostatic restoring stiffness	Nm/rad	3.42x10^9
Surge added linear damping	N/(m/s)	1x10^5
Sway added linear damping	N/(m/s)	1x10^5
Heave added linear damping	N/(m/s)	1.3x10^5
Yaw added linear damping	Nm/(rad/s)	1.3x10^7
Rotor Diameter	m	126
Hub Height	m	90
Cut-In, Rated, Cut-Out Wind Speed	m/s	3, 11.4, 25
Cut-In, Rated Rotor Speed	rpm	6.9, 12.1
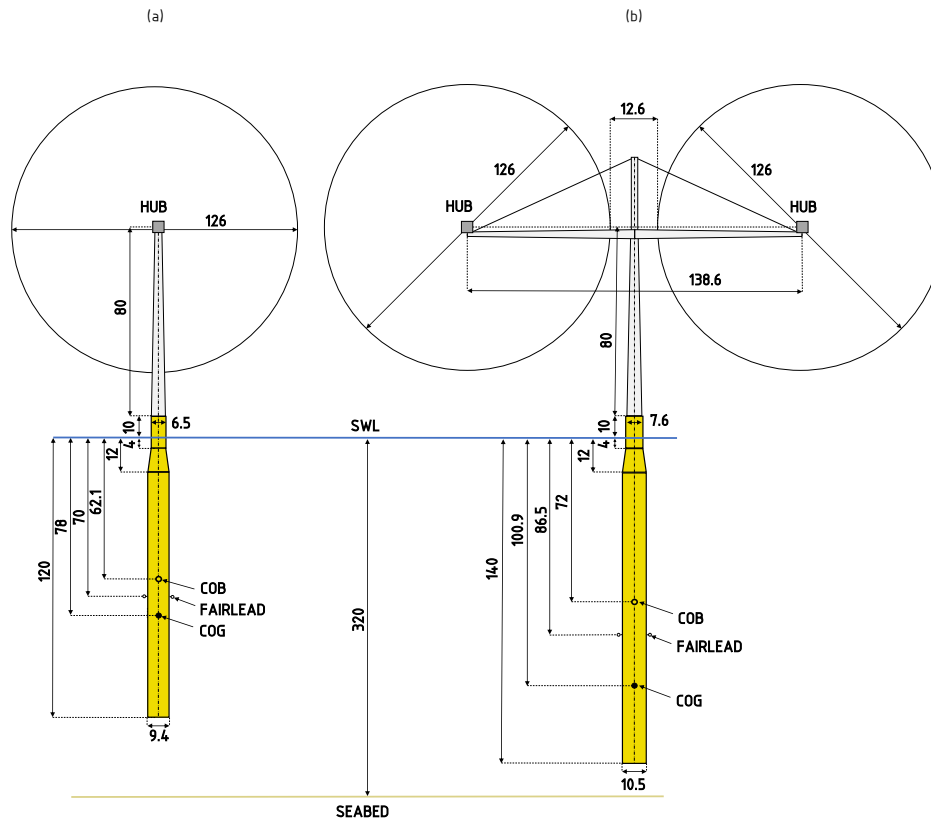
Figure 6.2: a) OC3 geometry [m] (Jonkman et al., 2009). b) 2WT configuration [m] (El Beshbichi et al., 2021a).

stiffness equal to $9.8x10^7$ Nm/rad is used. A proportional-integrative (PI) rotor-collective blade pitch control strategy on the generator speed is linearly coupled with a proportional rotor-collective blade pitch control on the 2WT platform yaw motion (El Beshbichi et al., 2021a). The coupled control strategy aims at mitigating the platform yaw response by reducing the thrust on the hub surging due to the positive yaw dynamics.

The numerical simulations rely on an in-house code for the simplified dynamics of two-rotor FOWTs concepts (El Beshbichi et al., 2021a,b). The tool is developed in Modelica, within the open-source platform OpenModelica (OSMC, 2021). Figure 6.3 depicts a flowchart describing the simulation tool structure. The system is assumed as a single rigid body, i.e., six equations of motion (EoMs) are used to solve the system dynamics. The linear hydrodynamic solver
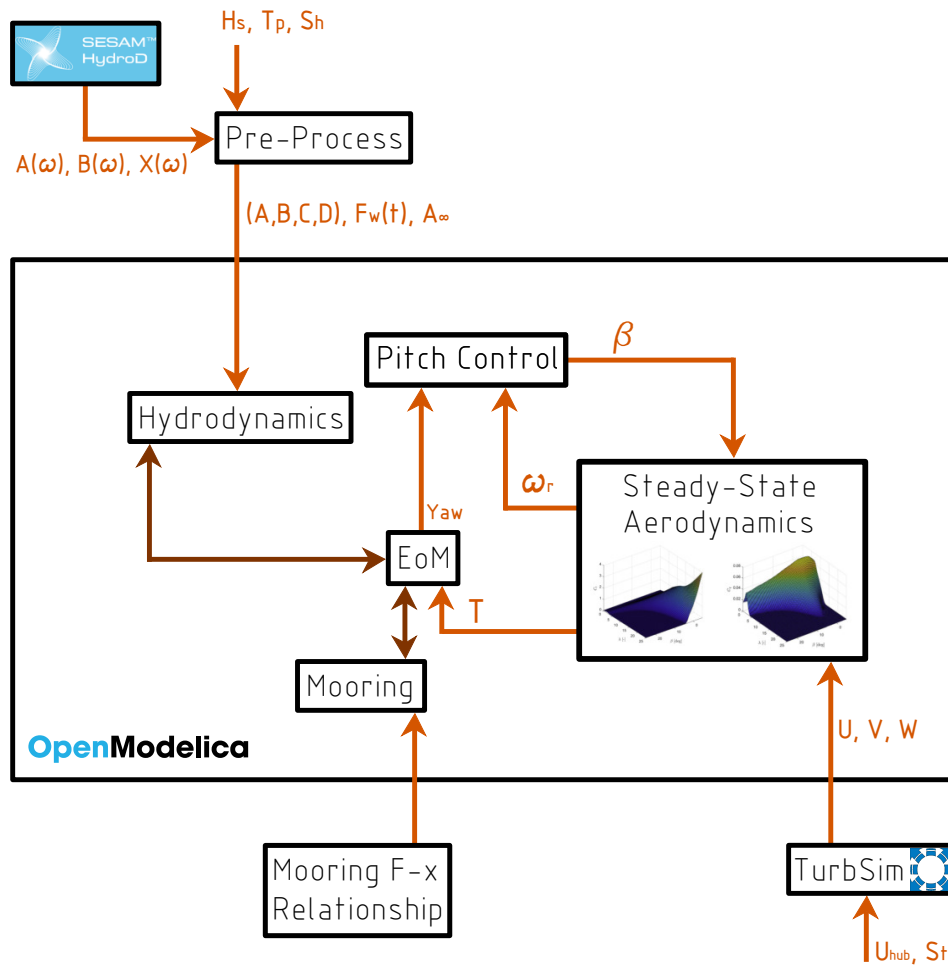
Figure 6.3: Flowchart describing the simulation tool structure used in the analysis.

WADAM within SESAM-HydroD is used to solve the first-order frequency-domain hydrodynamic problem (DNV, 2017). The frequency-domain added mass, $A(\omega)$, radiation damping, $B(\omega)$, and incident wave loads per unit wave amplitude, $X(\omega)$, can then be obtained for the given floating platform. Radiation damping is approximated by means of a state-space representation (El Beshbichi et al., 2021b). A pre-processor is used to obtain operational quantities from input information, such as the radiation damping state-space matrices (A, B, C, D), the linear hydrodynamic loads from incident waves, $F_w(t)$, included as realizations from look-up Inverse Fourier Transformations (IFT), and the added mass matrix computed at infinite frequency, A_∞. The characteristic wave height, H_s, characteristic wave period, T_p, and seed number, S_h, are

also used to define the hydrodynamic state of the system. Station-keeping loads given by mooring lines are modeled as quasi-static load-displacement relationships (Jonkman, 2007).

The aerodynamic loads are assumed as concentrated at the hub. The aerodynamic thrust loads, T, act at the hub locations. In order to obtain the aerodynamic state of the system, the aerodynamic torque is used to solve the rotor equivalent EoM, included in the aerodynamic module. The aerodynamic loads are computed by mapping the quasi-static aerodynamic thrust and torque coefficients. Turbulent wind realizations, (U, V, W), are computed by means of the NREL pre-processor TurbSim (Jonkman, 2009a). TurbSim input information are the mean wind speed at the hub height, U_{hub}, and the seed number, S_t. The thrust loads can be defined as:

$$F = \frac{1}{2}\rho_{air}C_t(\lambda, \beta)AU_{rel}^2 \tag{26}$$

where ρ_{air} is the air density, C_t is the steady-state thrust coefficient, λ is the tip speed ratio, β is the rotor-collective blade pitch angle, A is the rotor plane area, and U_{rel} is the relative speed between local wind and hub. The torque loads are defined as:

$$T = \frac{1}{2}\rho_{air}RC_q(\lambda, \beta)AU_{rel}^2 \tag{27}$$

where R is the rotor radius, and C_q is the steady-state torque coefficient. System response parameters considered in the present study are listed in Table 6.2. Due to limitations in the present modeling strategy, only the global rigid body motion responses are considered in the evaluation of long-term extremes. However, rigid motion responses may be used as indicators for structural responses.

Table 6.2: Response parameters in consideration for long-term extreme analysis of the 2WT system.

q_1	m	Surge
q_3	m	Heave
q_5	deg	Pitch
q_6	deg	Yaw
T_1	kN	Upstream Fairlead #1 Tension
T_2	kN	Upstream Farilead #2 Tension
T_3	kN	Downstream Fairlead Tension
$\dot{q}_1$	m/s	Surge velocity
$\dot{q}_3$	m/s	Heave velocity
$\dot{q}_5$	deg/s	Pitch velocity
$\dot{q}_6$	deg/s	Yaw velocity
$\ddot{q}_1$	m/s²	Surge acceleration
$\ddot{q}_3$	m/s²	Heave acceleration
$\ddot{q}_5$	deg/s²	Pitch acceleration
$\ddot{q}_6$	deg/s²	Yaw acceleration

6.5   Environment

The geographical sites and their environmental characteristics used in this work are based on information from Li et al. (2013). The sites considered are referred to as site 3 and site 14 and are located in the North Atlantic Ocean and the northern North Sea, respectively. The geographical location of the offshore sites used in the present study is shown in Figure 6.4. Locations are selected from wind and wave resource assessment performed within the EU-funded project MARINA Platform (Ferri et al., 2018). Offshore sites selected are locations well known for their floating offshore wind development potential (EWEA, 2013; WindEurope, 2019). Site 14 is first selected due to harsh long-term environmental conditions, while site 3 is selected as a reference site in Southern European waters. Both sites are sufficiently deep to host deep drafted platforms such as the spar-type 2WT platform. Table 6.3 shows the characteristic values of the offshore sites used in this study. Table 6.4 shows the basic information of the meteorological conditions used to compute turbulent wind profile realizations. The environmental cases in FLTA are initially limited to the ones listed in Table 6.5. The bin sizes are chosen from recommendations in the standard

Figure 6.4: Location of sites used in the present study (Li et al., 2013; Ferri et al., 2018).

Table 6.3: Characteristic values of site 3 and site 14.

		Site 3	Site 14
Location		Atlantic	North Sea
Water depth	m	449	202
Distance to shore	km	40	30
50-year U_w at 10 m	m/s	28.37	33.49
50-year H_s	m	10.19	10.96
Mean value of T_p	s	11.84	11.06

Table 6.4: Meteorological conditions used for simulations of wind speed profiles in Turbsim.

Turbulence model	Kaimal
IEC standard	IEC 61400-1-ED3
Turbulence type	Normal
Turbulence characteristics	B
Hub height [m]	90

Table 6.5: FLTA environmental conditions.

		Min	**Max**	**Bin**
U_w	m/s	4	50	2
H_s	m	1	20	1
T_p	s	2	34	2
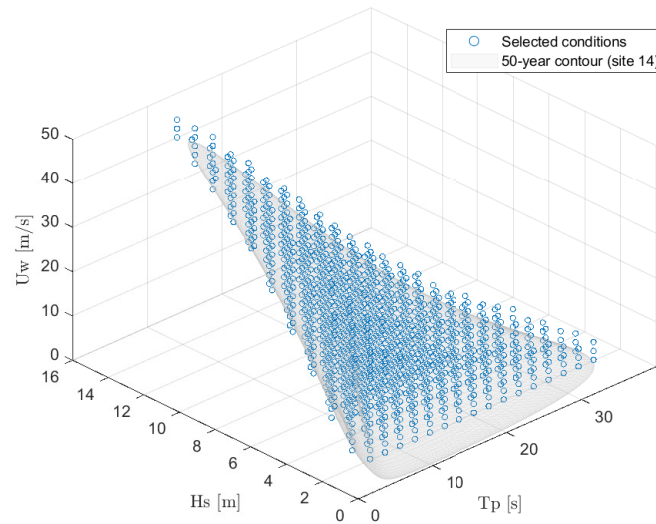
Figure 6.5: Environmental conditions used for FLTA. The 50-year contour surface of site 14 is included to visualize the threshold of the selected conditions.

DNVGL-RP-0286 (DNV-GL, 2019), which gives a total of 8160 environmental conditions. The simulation time is approximately 25 minutes for each case. In this work, the number of environmental conditions is reduced by selecting only the conditions with a return period of fewer than 1000 years. This ensures that conditions with low exceedance probability are considered while unimportant conditions are omitted. Figure 6.5 shows the selected conditions relative to the 50-year contour surface of site 14 and adjusted for the hub height wind speed. Based on this method, a total of 1205 environmental conditions are selected (about 85% fewer conditions).

As previously described, the present application of MECM makes use of two environmental contours. The first is associated with the standard ECM 50-years return period, while the second is associated with the wind turbines' cut-out
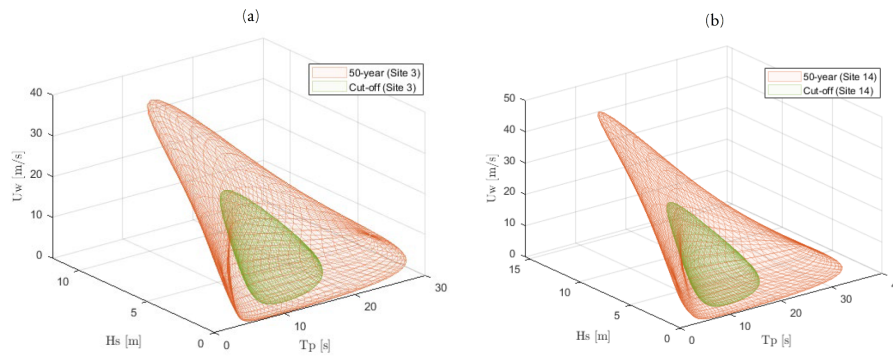
Figure 6.6: Environmental contours associated with the ECM 50-years return period and with the wind turbine cut-off wind speed. a) Site 3. b) Site 14 (Li et al., 2013).

Table 6.6: Comparison of number of cases and cumulative computational time needed to perform long-term analysis (CPU time needed for a single case is 25 minutes circa).

		N_{cases}		T_{sim} **[min]**	**Variation w.r.t. FLTA**
FLTA		1205		30125	-
MECM	50-years	101	170	4250	-86%
	cut-off	69			
ECM	50-years	101	101	2525	-91.6%

wind speed, i.e., 25 m/s. Figure 6.6 shows the ECM contour and the additional contour represented by the cut-off wind speed for site 3 and site 14. The latter is often referred to as the 'cut-off contour.' For site 14, the cut-off contour is created with a return period corresponding to approximately 105 hours, while 680 hours is used for site 3.

Table 6.6 shows a comparison of the number of cases and cumulative computational time needed to perform long-term analysis by means of the FLTA, the ECM, and the MECM. As it is clear, FLTA requires a large amount of environmental cases. The contour methods presently proposed significantly reduce the computational effort for long-term analysis. Total computational time is reduced of about 91.6% if ECM is considered, and of about 86% if MECM is considered.
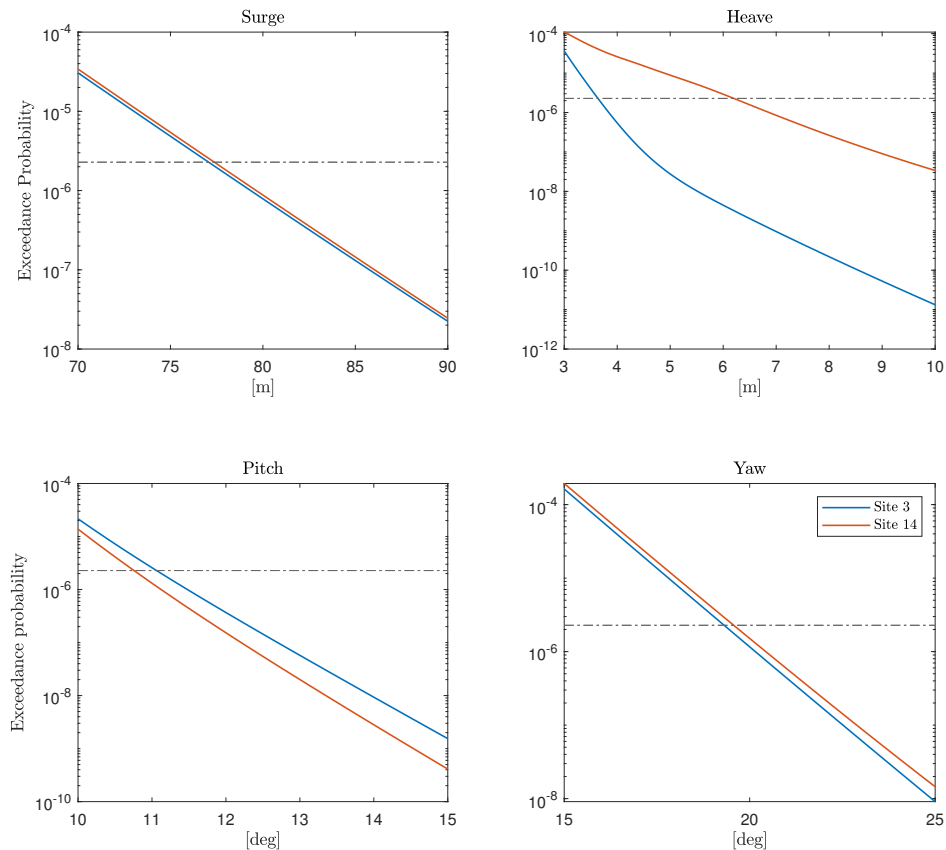
Figure 6.7: Full long-term extreme exceedance probability of platform surge, heave, pitch, and yaw motions computed for site 3 and site 14. The dashed line represents the exceedance probability associated with 50-years return period.

6.6 Results and Discussion

Figure 6.7 shows the FLTA 1-hour exceedance probability for platform surge, heave, pitch, and yaw platform motions computed for site 3 and site 14. The dashed line represents the 50-years return period threshold. Moreover, Table 6.7 summarizes the 50-year extreme responses obtained from FLTA. Results show how the responses predicted are very close for both sites. This indicates that the responses are not affected significantly by the harsher wind conditions of site 14. Heave motion is significantly reduced in site 3, with a 50-years extreme of about 3.6 m against 6.2 m in site 14. As heave is wave-dominated, it is reasonable to assume that the wave-induced loads, associated with lower

Table 6.7: 50-years long-term extreme responses obtained from FLTA for site 3 and site 14.

		Site 3	Site 14
q_1	m	77.06	77.37
q_3	m	3.64	6.20
q_5	deg	11.06	10.76
q_6	deg	19.31	19.57
T_1	kN	5122	5148
T_2	kN	4897	4902
T_3	kN	2827	2831
$\dot{q}_1$	m/s	5.03	5.72
$\dot{q}_3$	m/s	0.90	1.24
$\dot{q}_5$	deg/s	2.10	2.30
$\dot{q}_6$	deg/s	4.19	4.52
$\ddot{q}_1$	m/s^2	2.67	3.05
$\ddot{q}_3$	m/s^2	0.52	0.59
$\ddot{q}_5$	deg/s^2	1.09	1.26
$\ddot{q}_6$	deg/s^2	1.52	1.53

frequencies for site 3 if compared to site 14 (Table 6.3), are more prone to dynamically amplify heave motion. As previously stated, ECM takes into account the 50-years contour surface, while MECM considers both the 50-years contour and the contour corresponding to the wind turbines cut-off condition, that is, 25 m/s. It is challenging to locate the important conditions on the contour efficiently. The aim is to cover enough environmental conditions without compromising accuracy and efficiency. This may be achieved, for instance, by searching only areas of the contour in which the extreme response is expected to be located (Li et al., 2018). However, for conceptual systems as the 2WT, there is little evidence for dominant environmental regions. As such, the whole contour is included in the present study. Figure 6.8 and Figure 6.9 show the selected conditions on the 50-years environmental contour surfaces for sites 3 and 14, respectively. Figure 6.10 and Figure 6.11 show the selected conditions on the cut-off environmental contour surfaces for both sites. The design points obtained in the study are highlighted with filled black circles. Each design point is associated with one response variable, even though overlap of design points can occur. It can be noted how the design points found from the 50-year contour
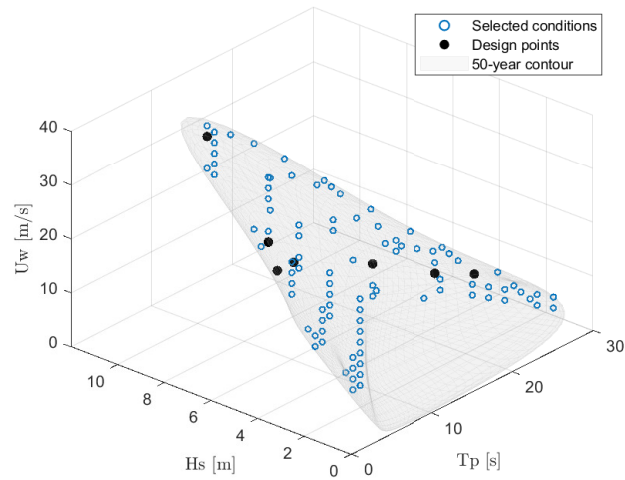
Figure 6.8: Discretized conditions for 50-years contour surface for site 3. The blue circles are the selected conditions, while the filled black circles are the design points.
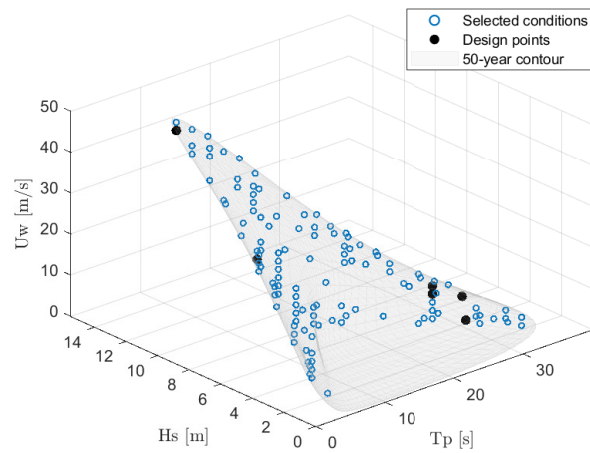
Figure 6.9: Discretized conditions for 50-years contour surface for site 14. The blue circles are the selected conditions, while the filled black circles are the design points.
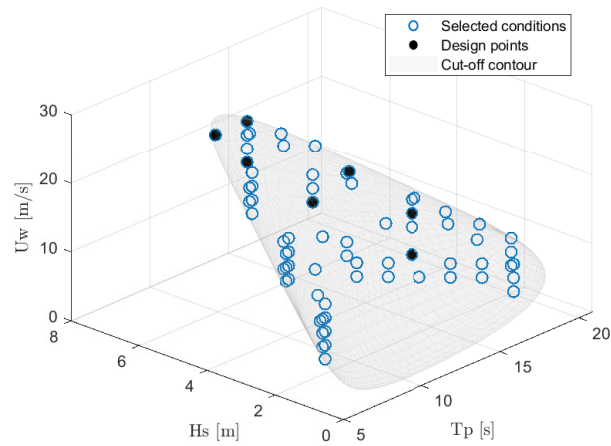
Figure 6.10: Discretized conditions for cut-off contour surface for site 3. The blue circles are the selected conditions, while the filled black circles are the design points.
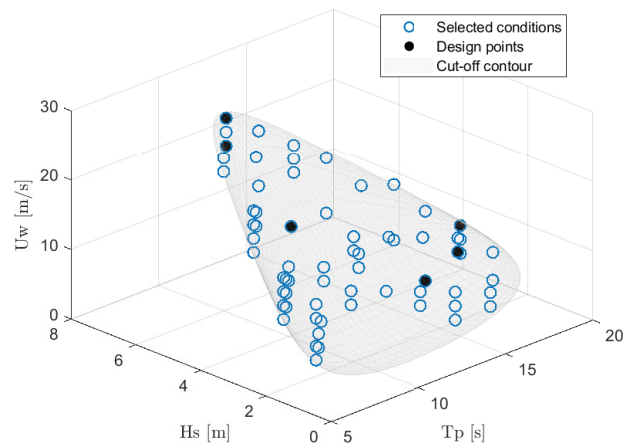
Figure 6.11: Discretized conditions for cut-off contour surface for site 14. The blue circles are the selected conditions, while the filled black circles are the design points.
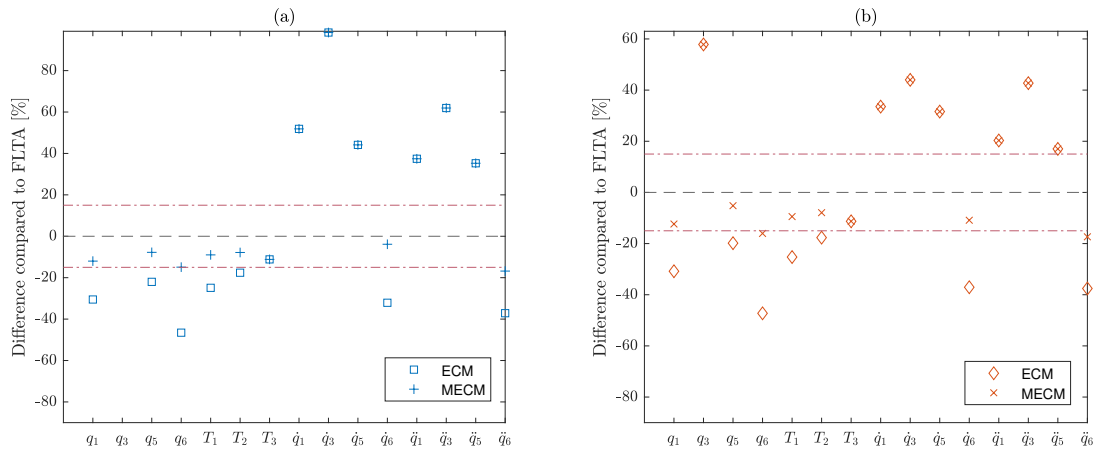
Figure 6.12: Percentage deviation of ECM and MECM results to FLTA results for site 3 (a) and site 14 (b). The 50-years contour uses a 90% percentile, while the cut-off contour uses a 50% percentile.

are generally located in the regions corresponding to rated wind speed, wave period close to the platform natural periods, maximum wind speed, and cut-off wind speed. For the cut-off contours, the design points are generally located at the wind-wave peak or close to rated wind conditions.

Common percentiles used in previous studies of long-term extreme responses of floating wind turbine concepts are 90% for ECM and 50% for additional contours for MECM (Li et al., 2016, 2017, 2018). Same percentiles values are thus used in this work. Figure 6.12 compares the results of ECM and MECM as percentage difference with respect to the FLTA results for site 3 (a) and site 14 (b). Negative values indicate underprediction, while positive values indicate overprediction. Response underprediction is clearly the major issue in using simplified methods such as the ECM. Overpredictions above 90%, exclusively associated with platform heave motion in site 3 (about 150% overprediction), are omitted for figure clarity. All MECM results lay within 15% difference compared to FLTA results. Table 6.8 and Table 6.9 list the resulting long-term extremes obtained from the 50-years contour (ECM) and cut-off contour for sites 3 and 14, relative to previously described percentiles. FLTA results are also presented to illustrate the value deviations. The color grade indicates deviation from FLTA results. Red grading indicates underprediction higher than about 30% compared to FLTA, while green grading indicates overprediction.

Table 6.8: Predicted 50-year extreme responses with ECM and MECM for site 3. Percentiles used are 90% for the 50-years contour and 50% for the cut-off contour. The color grade indicates deviation from FLTA results. Red grading indicates underprediction higher than about 30% compared to FLTA. Green grading indicates overprediction.

	FLTA	ECM (90%)	Cut-off (50%)	MECM	
q_1	77.06	53.49	67.82	67.82	m
q_3	3.64	9.78	2.71	9.78	m
q_5	11.06	8.62	10.22	10.22	deg
q_6	19.31	10.35	16.49	16.49	deg
T_1	5122	3847	4676	4676	kN
T_2	4897	4035	4596	4596	kN
T_3	2827	2512	2386	2512	kN
$\dot{q}_1$	5.03	7.63	4.28	7.63	m/s
$\dot{q}_3$	0.90	1.78	0.53	1.78	m/s
$\dot{q}_5$	2.10	3.02	1.71	3.02	deg/s
$\dot{q}_6$	4.19	2.84	4.04	4.04	deg/s
$\ddot{q}_1$	2.67	3.66	3.09	3.66	m/s²
$\ddot{q}_3$	0.52	0.84	0.43	0.84	m/s²
$\ddot{q}_5$	1.09	1.47	1.31	1.47	deg/s²
$\ddot{q}_6$	1.52	0.95	1.26	1.26	deg/s²

Table 6.9: Predicted 50-year extreme responses with ECM and MECM for site 14. Percentiles used are 90% for the 50-years contour and 50% for the cut-off contour. The color grade indicates deviation from FLTA results. Red grading indicates underprediction higher than about 30% compared to FLTA. Green grading indicates overprediction.

	FLTA	ECM (90%)	Cut-off (50%)	MECM	
q_1	77.37	53.53	67.81	67.81	m
q_3	6.20	9.79	2.75	9.79	m
q_5	10.76	8.63	10.20	10.20	deg
q_6	19.57	10.32	16.43	16.43	deg
T_1	5148	3847	4662	4662	kN
T_2	4902	4035	4514	4514	kN
T_3	2832	2511	2307	2511	kN
$\dot{q}_1$	5.72	7.64	4.28	7.28	m/s
$\dot{q}_3$	1.24	1.79	0.58	1.79	m/s
$\dot{q}_5$	2.30	3.03	1.71	3.03	deg/s
$\dot{q}_6$	4.52	2.84	4.02	4.02	deg/s
$\ddot{q}_1$	3.05	3.67	3.09	3.67	m/s²
$\ddot{q}_3$	0.59	0.84	0.43	0.84	m/s²
$\ddot{q}_5$	1.26	1.47	1.31	1.47	deg/s²
$\ddot{q}_6$	1.53	0.96	1.26	1.26	deg/s²

ECM performs inadequately for a wide range of the responses considered. The most notable underpredictions are relative to surge motion, and yaw motion, velocity, and acceleration. ECM underpredicts yaw motion of about 50% if compared to FLTA. Underpredictions of the extremes can be explained by considering the omittance of the wind turbine parking operational mode by using a simple ECM approach. The greatest deviations are relative to responses dominated by wind loading. From Figure 6.12, it can be noted how MECM either significantly improves or predicts the same results as ECM. In particular, long-term extreme prediction of platform yaw motion is significantly improved. Yaw motion, which in previous work is found to be one of the major dynamic modes of the 2WT concept, can be related to the transversal distribution of thrust loads and to wind turbulence intensity (El Beshbichi et al., 2021a). Since platform yaw motion is wind dominated, the inclusion of the cut-off contour in MECM aids the detection of long-term extremes near the cut-off wind condition. The significant over predictions for heave motion, surge, heave, and pitch velocities and accelerations - higher than 25% compared to FLTA responses - can be explained by considering that the relative extreme responses are already very close to the results obtained from FLTA. A percentile of 90% may thus be considered as too conservative (Li et al., 2018).

6.7 Conclusions

In this paper, the modified environmental contour method (MECM) is used to predict the 50-year extreme response of a two-rotor floating wind turbine concept (2WT) deployed in two different offshore sites. The standard contour method (ECM) is much faster than the complete full long-term analysis (FLTA) but performs poorly if the loads acting on the system are not monotonically increasing with the environmental state. The analysis considered the environmental conditions describing two specific offshore sites located in the North Sea and the North Atlantic Ocean, known to be suitable for floating offshore deployment. FLTA and ECM were carried out and used as a benchmark to assess the performance of MECM. MECM takes into account two environmental contours,

that is, the baseline 50-years return period contour used in ECM and an additional cut-off wind speed contour. ECM leads to significant underprediction of the system responses dominated by wind loading. In particular, underestimation of platform yaw motion, a typical dynamic mode of the 2WT system, is about 50%, while the underestimation associated with platform surge motion is about 30%. It is found that MECM significantly improves the accuracy of wind-dominated results while predicting the same accuracy for wave-dominated results. ECM over-estimates wave-dominated results, such as surge, heave, and pitch velocities and accelerations. Over-estimation can be associated with the high fractile level employed (90%), as results are already very close to the ones obtained in FLTA. Most MECM responses are within 15% difference with respect to FLTA results. Therefore, MECM may be assumed suited to be employed for the analysis of two-rotor FOWTs without the risk of underestimating long-term extreme responses. The conclusions offered in this study can be summarized as follows:

- MECM can predict the long-term extreme response of two-rotor floating wind turbine concepts within a maximum underestimation of about 15% compared to FLTA results.

- MECM wind-dominated results are especially more accurate if compared to those obtained by means of the standard ECM, while maintaining the same level of accuracy for wave-dominated results.

- MECM over-estimation of wave-dominated results can be associated with the high fractile level (90%) employed in the ECM environmental contour, as results are already very close to the ones obtained in FLTA.

The numerical simulations relied upon a simplified model assuming concentrated aerodynamic loads at the hubs. The model maps steady-state aerodynamic coefficients characteristic of the wind turbine employed. Therefore, this method is not able to cover more complex dynamic effects. For instance, the aerodynamic interaction effect between the rotors is not considered. Skewed effects are also not considered, such as the skewed conditions related to significant yaw motion. The results obtained in this study give useful indications about

the applicability of MECM for two-rotor floating systems and sufficiently accurate wave-dominated responses. However, wind-dominated responses may be significantly affected by the aforementioned assumptions. Future work will include the expansion of the analysis by means of a more sophisticated model including a blade-element momentum (BEM) implementation for two-rotor FOWTs and structural dynamics.

Acknowledgment

Chapter 7

Dynamics of a Two-Rotor Wind Turbine Mounted on Three Floating Platforms

Omar El Beshbichi [a], Yihan Xing [a], Muk Chen Ong [a]

[a] Department of Mechanical and Structural Engineering and Materials Science, University of Stavanger, Stavanger, Norway.

Abstract

Multi-rotor floating offshore wind turbines have been recently proposed as an innovative technology to further reduce the cost of offshore wind energy. Even though examples of commercial prototypes are present, the literature lacks studies on the dynamic performance of such systems. This work presents a comparative analysis of a two-rotor wind turbine concept mounted on spar-type, semi-submersible, and tension-leg platforms. Their short-term performance is assessed by considering five different load cases considering directionally congruent turbulent wind profiles and irregular sea states. The analysis is carried out through an in-house fully-coupled code developed in Modelica. AeroDyn v15 within FAST v8 by NREL is coupled to the Modelica code to achieve blade-element momentum capabilities. Results indicate that platform yaw motion is an important dynamic mode of the systems, particularly for the spar configuration. Stiffer station-keeping lines and longer fairlead distance to the platform centerline reduce significantly yaw motion, as in the case of the semi-submersible and tension-leg configurations. Large tower base bending moment standard deviations and the associated concentration of energy at the platform heave and pitch motion frequencies indicate an increased risk for fatigue damage for the TLP configuration, especially at above-rated wind speeds. Moreover, large tendon loads can pose concerns in terms of fatigue and limit state performance. Large mean platform pitch angle and yaw standard deviation contribute to the reduction of electric power output quality. Extreme storm conditions greatly increase the response standard deviation, especially for the semi-submersible configuration.

Keywords: Offshore wind, Spar, TLP, Semi-submersible, Floating wind turbines, Multi-rotor.

7.1 Introduction

The offshore wind industry has been experiencing significant expansion in the last decade, achieving in 2020 a total offshore wind capacity of about 6.1 GW (GWEC, 2019). Many are the advantages of employing wind turbines in the offshore environment. First, the wind speed is much greater and steadier than in inland environments. Moreover, offshore deployment allows for less intrusive interactions with populated areas. Most of the current wind energy exploitation is located in shallow waters, where bottom-fixed foundations are economically feasible. Floating offshore wind turbines (FOWTs) have been recently proposed as technological means to achieve wind energy deployment in offshore areas with significant water depth (exceeding the conventional limit of 50 m) without increasing the associated levelized cost of energy (LCoE) (Cruz and Atcheson, 2016). Hywind Scotland was the first FOWT farm to be commercially commissioned in 2017 by Equinor ASA off the coast of Peterhead, Scotland (Equinor, 2015). The farm is composed of five spar-type FOWTs of about 6 MW. More recently, many other commercial projects have been commissioned. Notable examples are the European projects initiated by Principle Power, where semi-submersible floating platforms are used (Principle Power, 2016).

Another means of reducing the LCoE of offshore wind energy is by means of multi-rotor floating configurations. Multi-rotor wind turbines have been put forward for the reduction of costs associated with exceptionally big wind turbine components, chiefly blades. The blade mass increases at a higher rate than the associated increase in net energy output (Jamieson and Branney, 2012). Scaling big wind turbines in an array of smaller wind turbines thus allows for a net reduction of the rotor mass employed and the associated final cost. Moreover, employing multiple wind turbines on the same floating platform leads to significant advantages such as, for instance, the reduction of costs associated with the manufacturing and sharing of platform and station-keeping systems, fewer installations, and cheaper offshore operations dealing with smaller mechanical components.

Vestas A/S deployed a four-rotor wind turbine 225 kW each (4R-V29) at the Technical University of Denmark from 2016 to 2019, demonstrating faster

wake recovery and marginally higher power production if compared to an analogous single-rotor configuration (van der Laan et al., 2019). Notable examples of multi-rotor FOWT systems under development are TwinWay by Hexicon (Hexicon, 2021a) and Flex2Power by Rosenberg Worley AS (Flex2Power, 2022). The first is a two-rotor wind turbine mounted on a semi-submersible platform. A TwinWay demonstrator is planned to be deployed in 2022 at the MetCentre area in Norway (Hexicon, 2021b). The second instance is a modularized platform for combined wind, wave, and solar energy production. Other conceptual examples are Wind Catching by Wind Catching Systems (WCS) (Wind Catching Systems, 2022) and Nezzy[2], under development by EnBW and Aerodyn Engineering (EnBW, 2021b; Aerodyn Engineering, 2021). The former is composed of a steel grid of 117 small turbines mounted on a semi-submersible floating platform, while the latter is composed of a two-rotor wind turbine supported by a light Y-shaped semi-submersible platform (EnBW, 2021a).

To date, the literature lacks a thorough depiction of the dynamic performance of two-rotor FOWTs. Previous work presented a novel object-oriented approach to model the fully-coupled dynamics of FOWTs, aiming at the dynamic analysis of two-rotor concepts (El Beshbichi et al., 2021b). The method was then employed to study the dynamics of a two-rotor wind turbine concept mounted on a spar-type floating platform (El Beshbichi et al., 2021a). Results showed significant platform yaw motion, associated with turbulence intensity and related with the thrust distribution on the structure. It was also shown how platform yaw motion can be mitigated by properly adjusting the rotor-collective blade-pitch control strategy.

In this work, the dynamic analysis of a two-rotor wind turbine concept (2WT) mounted on spar-type, semi-submersible, and tension-leg (TLP) platforms is performed. The 2WT concept makes use of baseline NREL 5-MW wind turbines and a tower structure as proposed in El Beshbichi et al. (2021a). The spar and TLP platforms considered are preliminary designs defined by means of simplified hydrostatic considerations, while the semi-submersible platform design is based upon the well-known OO-Star design (Berthelsen, 2015).

Currently available commercial and open-source fully-coupled tools for the dynamic analysis of floating wind turbines are not able to accommodate two-

rotor systems with the flexibility and performance needed for conceptual analysis. To address this gap, a novel tool has been developed which offers easy implementation of arbitrary floating platforms and number of turbines employed. The tool is developed in Modelica v3.2.3 through the open-source platform OpenModelica v1.16.2 and is based on the freely-available Modelica Standard Library (MSL) (The Modelica Association, 2017; OSMC, 2021). Modelica is a non-proprietary, object-oriented, equation-based language used for the convenient dynamic modeling of complex multi-domain systems. The tool implements industry-standard fidelity levels, and a benchmarking exercise of the code against FAST v8 showed an accurate response and good numerical performance. The blade-element momentum (BEM) package within FAST v8, i.e., AeroDyn v15, has been coupled to the Modelica code because of its widespread use in academic research (Jonkman and Buhl, 2005; Moriarty and Hansen, 2005). More complex aerodynamic effects, such as the aerodynamic interaction between rotors, are not considered to date. AeroDyn v15 is well-suited to be further modified, as it would be needed in future work for the implementation of a correction factor accounting for aerodynamic interactions between rotors within the BEM formulation. The tool will be released open-source in the next future. The structural code relies upon the multi-body systems (MBS) package within the MSL. Tower and blades are assumed rigid in this study.

A series of load cases (LCs) are used to assess the dynamic performance of the three FOWT concepts. Performance parameters, such as global rigid motions, tower base bending moment, and upstream mooring line tension are compared. This type of comparison is able to highlight important dynamic differences of the floating systems undergoing the same hydrodynamic and aerodynamic loads.

Table 7.1: NREL 5-MW Baseline Wind Turbine Specifications (Jonkman, 2007).

Rated Power	MW	5
Rotor Orientation, Configuration		Upwind, 3 Blades
Control		Variable Speed, Collective Pitch
Drivetrain		High Speed, Multiple-Stage Gearbox
Rotor, Hub Diameter	m	126, 3
Rated Tip Speed	m/s	80
Hub Height	m	90
Rotor Mass	kg	110×10^3
Nacelle Mass	kg	240×10^3
Cut-In, Rated, Cut-Out Wind Speed	m/s	3, 11.4, 25
Cut-In, Rated Rotor Speed	rpm	6.9, 12.1
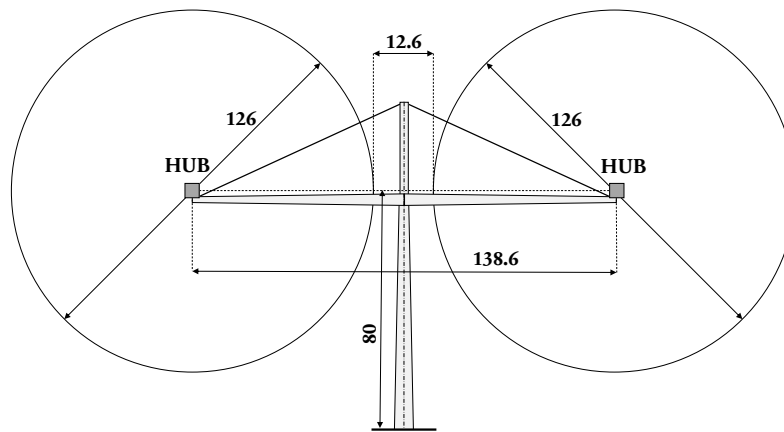
Figure 7.1: Multi-rotor wind turbine geometry [m] (El Beshbichi et al., 2021a).

7.2 Two-Rotor Wind Turbine Design

The 2WT structure employed corresponds to the design proposed in El Beshbichi et al. (El Beshbichi et al., 2021a). The structure is composed of a primary vertical tapered tower, two horizontal tapered arms, and an additional vertical cylinder as depicted in Figure 7.1. Wires are employed to distribute static bending loads as compression loads on the primary tower. The primary tower base outer diameter is about 6.28 m (thickness of about 0.03 m), while its top outer diameter is about 4.79 m (thickness of about 0.0215 m). A simplified structural design preventing yield is employed considering the RNAs weight acting at the
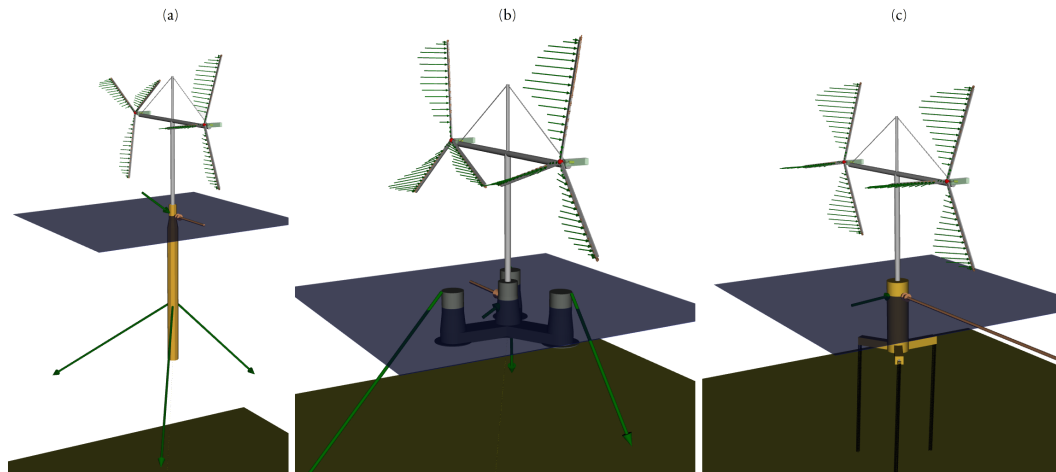
Figure 7.2: Multi-rotor floating wind turbine configurations selected in the present study. a) Spar-type platform. b) Semi-submersible platform (OO-Star design (Berthelsen, 2015)). c) TLP platform.

hubs, the horizontal arms self-weight, and the maximum environmental loading acting on the structure, i.e., maximum aerodynamic thrust at the hubs. A safety factor of 1.4 is also employed to obtain a conservative design. Further information about tower structural dimensioning and inertial specifications can be found in El Beshbichi et al. (2021a). More sophisticated considerations, such as fatigue, buckling, and inertial amplification effects, are not accounted to date. Nonetheless, a more detailed structural design may be defined in future work. Two standard NREL 5-MW wind turbines are also employed in the 2WT design (Jonkman, 2007). The space between rotors is set to 10% of the rotor radius, similarly to the multi-rotor concept by Vestas A/S installed at DTU (Bastankhah and Abkar, 2019). Major wind turbine specifications are listed in Table 7.1.

7.3   Floating Platforms

Three floating platform configurations are considered for this study, i.e., a spar-type, a semi-submersible, and a TLP, as depicted in Figure 7.2. The spar and TLP platforms are early designs that have been specified for use with the 2WT configuration under consideration. On the other hand, the semi-submersible design is the OO-Star Wind Floater Semi 10-MW (for brevity, OO-

Table 7.2: Spar platform configuration selected (El Beshbichi et al., 2021a).

Draft	m	140
Diameter (tapered at SWL)	m	10.5 (7.5)
Fairlead distance from SWL	m	86.5
Fairlead radius	m	5.78
Freeboard to tower base	m	10

Star) (Berthelsen, 2015). This design has been proposed within the second stage of the EU-funded LIFES50+ project (LIFES50+, 2022). The OO-Star design is also originally intended to be employed with the DTU 10-MW reference wind turbine (Bak et al., 2013).

The spar platform design is equal to the one proposed in El Beshbichi et al. (2021a). The structure is made of steel. Hydrostatic considerations are used to select an optimal spar geometry. The design criteria are 1) the enforcement of hydrostatic equilibrium of the full-system affected by mooring lines by properly adjusting the ballast mass, 2) the limitation of the static pitch angle to about 5 deg under maximum external loading, 3) the enforcement of pitch and heave natural periods larger than about 25-30 s in order to avoid first-order wave effects, and 4) the utilization of as little mass as possible. A complete account of the spar design can be found in El Beshbichi et al. (2021a), where platform design spaces are employed to determine the optimal configuration. Geometrical parameters relative to the specified spar platform configuration are listed in Table 7.2. The configuration employs three catenary mooring lines with a length of about 900 m, a diameter of 0.09 m, and an equivalent mass density of 200 kg/m. The lines are mounted at 120 deg from each other, starting from the downwind direction. The spar configuration is employed at a water depth of about 320 m.

The TLP platform design is carried out following preliminary considerations from Bachynski and Moan (2012). The design employs a main cylindrical hull and three rectangular pontoons supporting the tension legs. The structure is made of steel. The pontoons are mounted at the cylinder base and are displaced 120 deg from each other, starting from the downwind direction. A square pontoon cross-section is also assumed. Design is based on hydrostatic considera-

Table 7.3: TLP platform configuration selected.

Number of pontoons	-	3
Draft	m	43
Main hull diameter	m	16
Hull height	m	53
Pontoon length to axis	m	32.5
Pontoon square cross-section height	m	6
Pontoon vertical location from the SWL	m	40
Tendon outer diameter	m	1.3
Freeboard to tower base	m	10

tions. The design criteria used are 1) the enforcement of surge and sway natural periods longer than 25 s to avoid first-order wave excitation, 2) the enforcement of heave, roll, and pitch natural periods shorter than 3.5 s to avoid first-order wave excitation, 3) the limitation of the mean offset to about 5% of the water depth under maximum aerodynamic loading and hydrodynamic loading, 4) the yield assessment of the tendons with a safety factor (SF) equal to 2, and 5) the enforcement of a displaced volume higher than 2000 m^3 for increased stability under extreme environmental conditions. Major platform and tendon parameters are adjusted heuristically until a feasible configuration fulfilling all design constraints is obtained. Surge and pitch natural periods are computed by considering hydrodynamic coupling. Hydrodynamic loading for offset estimation accounts for a sea state with a significant wave height of 4 m and a period of 10 s. Geometrical parameters relative to the specified TLP platform configuration are listed in Table 7.3. The TLP configuration is employed at a water depth of about 130 m.

The description of the OO-Star platform design is public (Berthelsen, 2015; Pegalajar-Jurado et al., 2018). The platform is made up of a star-shaped pontoon connecting the central tapered column with the three outer tapered columns. The pontoons are displaced 120 deg from each other, starting from the upwind direction. The structure is made of concrete. The main geometrical parameters of the platform are listed in Table 7.4. The configuration employs three catenary mooring lines with a length of about 703 m, a diameter of 0.137 m, and an equivalent mass density of about 375 kg/m. The lines are mounted

Table 7.4: OO-Star platform main geometrical parameters (Berthelsen, 2015).

Draft	m	22
Pontoon length to axis	m	37
Pontoon height	m	6.5
Pontoon width	m	17
Outer column height (from pontoon)	m	24.5
Central column height (from pontoon)	m	26
Central column diameter (tapered)	m	16.2 (12.05)
Outer column diameter (tapered)	m	15.8 (13.4)
Fairlead radius	m	44
Fairlead distance from SWL	m	-9.5
Freeboard to tower base	m	11

at 120 deg from each other, starting from the upwind direction. Moreover, the original mooring system employs clumped masses, mounted at 118 m from the fairlead along the mooring lines, in order to achieve greater pre-tension per unit length. In this work, the clump mass is removed and equivalence is achieved by increasing the mooring line mass per unit length to get the same static fairlead tension. An equivalent mass density of 650 kg/m is thus obtained. The ballast mass has been also properly adjusted for utilization with the 2WT system. Additional ballasting of about 688 tonnes is included to achieve equivalent draft and water displacement. The OO-Star configuration is employed at a water depth of about 130 m.

Figure 7.3 gives a graphical representation of the design criteria used in preliminary platform design and the corresponding design performance. Red grading is used to highlight values outside the optimal design range. The figure shows both the TLP design parameters (a) and the spar design parameters (b). The OO-Star performance when employed together with the 2WT prototype is also included (b). To be noted the low heave period for the OO-Star configuration (about 18.5 s), which may lead to amplification of platform heave motion under extreme sea states.

Table 7.5 lists the inertial and hydrostatic properties of each platform. Hydrostatic restoring stiffness values are derived from metacentric height relationships and are referred to the total center of gravity (CoG) of the system (Faltin-
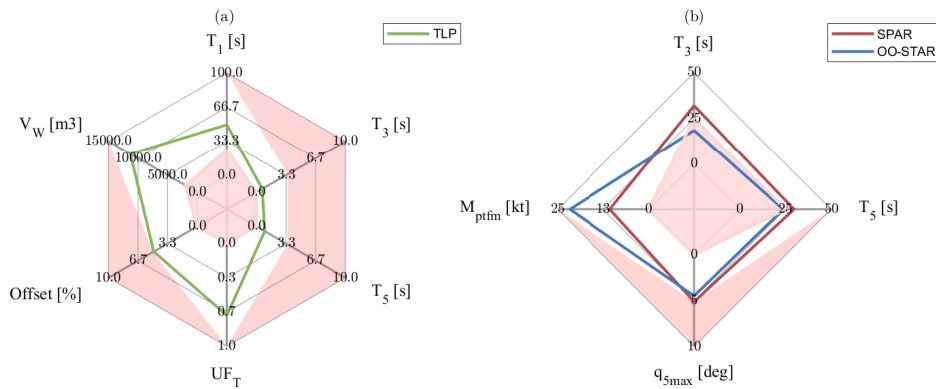
Figure 7.3: Design criteria used in preliminary platform design. Values outside of the optimal design range are within the red-graded area. a) TLP design criteria (Bachynski and Moan, 2012). b) spar design criteria (OO-Star performance when employed with 2WT prototype is also included) (El Beshbichi et al., 2021a).

Table 7.5: Platforms inertial and hydrostatic properties.

		SPAR	**OO-STAR**	**TLP**
Depth to CoG	m	121.5	15.2	27.9
Depth to CoB	m	72	14.2	25.83
Water displacement, V_w	m^3	1.17x10^4	2.35x10^4	1.13x10^4
Mass (including ballast)	kg	1.06x10^7	2.17x10^7	2.59x10^6
Roll moment of inertia about CoG	kgm^2	1.13x10^{10}	9.43x10^9	5.76x10^8
Pitch moment of inertia about CoG	kgm^2	1.13x10^{10}	9.43x10^9	5.76x10^8
Yaw moment of inertia about centerline	kgm^2	1.7x10^8	1.63x10^{10}	8.02x10^7
Waterplane area, A_{wp}	m^2	45.4	548.8	201
Roll waterplane second moment of area, I_{yy}	m^4	163.8	2.95x10^5	3.22x10^3
Pitch waterplane second moment of area, I_{xx}	m^4	163.8	2.95x10^5	3.22x10^3
Heave hydrostatic restoring stiffness, C_{33}	N/m	4.56x10^5	5.51x10^6	2.02x10^6
Roll hydrostatic restoring stiffness, C_{44}	Nm/rad	3.42x10^9	2.16x10^9	-1.42x10^9
Pitch hydrostatic restoring stiffness, C_{55}	Nm/rad	3.42x10^9	2.16x10^9	-1.42x10^9
Total mass (platform, ballast, tower, nacelle, rotor)	kg	1.18x10^7	2.36x10^7	8.82x10^6
Depth to total CoG (platform, ballast, tower, nacelle, rotor)	m	100.9	10.24	13.01
Distance between total CoG and CoB	m	28.9	-3.42	-12.82

sen, 1993). The restoring stiffness values can be estimated as:

$$C_{33} = \rho g A_{wp} \tag{1}$$

$$C_{44} = \rho g V_w(z_G - z_B) + \rho g I_{yy} \tag{2}$$

$$C_{55} = \rho g V_w(z_G - z_B) + \rho g I_{xx} \tag{3}$$

where C_{33} is the heave restoring stiffness, C_{44} is the roll restoring stiffness, C_{55} is the pitch restoring stiffness, ρ is the water density, g is the acceleration due to gravity, V_w is the water displacement, A_{wp} is the waterplane area, z_G is the depth to the total CoG, z_B is the depth to the center of buoyancy (CoB), I_{yy} is the roll waterplane second moment of area, and I_{xx} is the pitch waterplane second moment of area. This formulation assumes positive depths from the SWL. These formulations can be used as indicators for the stability of the unmoored floating system. The roll and pitch hydrostatic restoring stiffness values associated with the TLP platform are negative given the relatively small waterplane second moment of area and the negative difference between depth to total CoG of the system and depth to CoB. This clearly indicates hydrostatic instability of the TLP system if tendon loads are disregarded. On the other hand, hydrostatic coefficients relative to the spar and OO-Star configurations are positive. This indicates hydrostatic stability of the system even without considering the further stabilizing effect of the catenary system. It is assumed that the OO-Star platform CoG location is not significantly affected by the additional ballast mass employed.

7.4 Non-Linear Coupled Analysis

The non-linear fully-coupled dynamic responses of the FOWT concepts are obtained by means of an in-house code implemented in the language Modelica (The Modelica Association, 2017). The open-source platform OpenModelica is also employed (OSMC, 2021). The object-oriented coding approach allows for easy implementation of models relative to concepts of arbitrary platform configuration and number of wind turbines. The structural modeling is carried out

by using the MBS package within the freely-available MSL (The Modelica Association, 2008). Previous work described the method in some detail, where simplified aerodynamic loads computed by means of steady-state coefficients were employed (El Beshbichi et al., 2021b). More recently, full BEM capabilities have been achieved by integrating into Modelica the well-established code Aerodyn v15 within FAST v8 by NREL (Jonkman and Buhl, 2005; Moriarty and Hansen, 2005). An aerodynamic subroutine, written in Fortran 90 and compiled as a dynamic link library (DLL), has been developed to call AeroDyn v15 at each time step. The result is a direct functional relationship between the dynamic state of the system and the associated steady-state aerodynamic loads. An aerodynamic subroutine instance is called for each rotor considered in the model. The aerodynamic DLL has been interfaced with the Modelica code by means of a buffer written in C.

In this work, tower structure and blades are assumed to be rigid. The study of more complex aeroelastic effects is left as a subject for further investigation. The integration method *ida* is used to solve the equations of motion (EoM) of the system. A time interval of 0.1 s is used for time series storage, sufficient to cover rigid dynamics. Different tolerances are selected in a trade-off between simulation time and a sufficient level of accuracy and stability of the solver. It is found that the spar configuration needs a tolerance of at least $1x10^{-5}$ in order to avoid aerodynamic loads scattering. The OO-Star configuration, however, is found to be more stable and a tolerance of $1x10^{-3}$ is used without issues. A tolerance of about $1x10^{-6}$ is used instead in the TLP configuration, as lower tolerance levels are harder to solve. The linear solver *totalpivot* is used, as it is found to be the most robust algorithm available in this context. The non-linear solver *kinsol* is also used. The simulation time used is equal to 4000 s, where the first 400 s are removed to discard initial transients. A net 1-h simulation time is thus used to compute the resulting dynamic response parameters.

7.4.1   Aerodynamic Modeling

Aerodynamic loads are computed by means of the BEM formulation. The NREL code InflowWind within FAST is integrated into Modelica to compute the wind

velocity components at each aerodynamic node. Global turbulent wind velocity profiles are preventively generated in TurbSim and imported in InflowWind as binary .bts files (Jonkman, 2009a). A 15x15 grid-point matrix dimension is used. The grid height is 160 m and the grid width is 300 m, large enough to cover both rotors. A time step of 0.05 s is used, and a total usable time series of 4000 s is computed. A steady airfoil aerodynamic model is used in all cases considered. The aerodynamic interaction between the rotors due to their proximity is to date not considered. Previous work in different fields regarding similar systems, such as the study of thrust imbalance due to aerodynamic interactions in Unmanned Aerial Vehicles (UAVs), suggests that the effect of aerodynamic interactions on the aerodynamic loads acting on the system may not be significant enough to compromise the results obtained with the method employed in this work (Zhou et al., 2017; Alvarez and Ning, 2017). At any rate, this effect should later be investigated by means of higher fidelity methods. The tower influence on the local wind velocity profile is also not included, as well as the aerodynamic drag acting on the tower.

7.4.2 Hydrodynamic Modeling

In the simulations presented in this work, the hydrodynamic loads acting on the floating platforms are computed by means of linear wave theory. The commercial software DNV HydroD-Wadam within SESAM is used to solve the potential flow frequency-domain hydrodynamics (DNV, 2017). Loads are computed at the SWL. External lookup tables are used to store and import in Modelica time realizations of irregular wave loads. A state-space representation is employed to approximate the effect of radiation damping in Modelica (Cummins, 1962). A state-space approximation order equal to two is used. The added mass matrix from radiation is included by computing its value at infinite frequency. Motions of a rigid floater can then be computed by using the associated equations (Jonkman, 2007):

$$[M]\underline{\ddot{q}} + [C]\underline{q} + C_{0,3} = -[A]_{inf}\underline{\ddot{q}} - \int_0^t [K(t-\tau)]\underline{\dot{q}}d\tau + \underline{F}_w + \underline{F}_g \qquad (4)$$
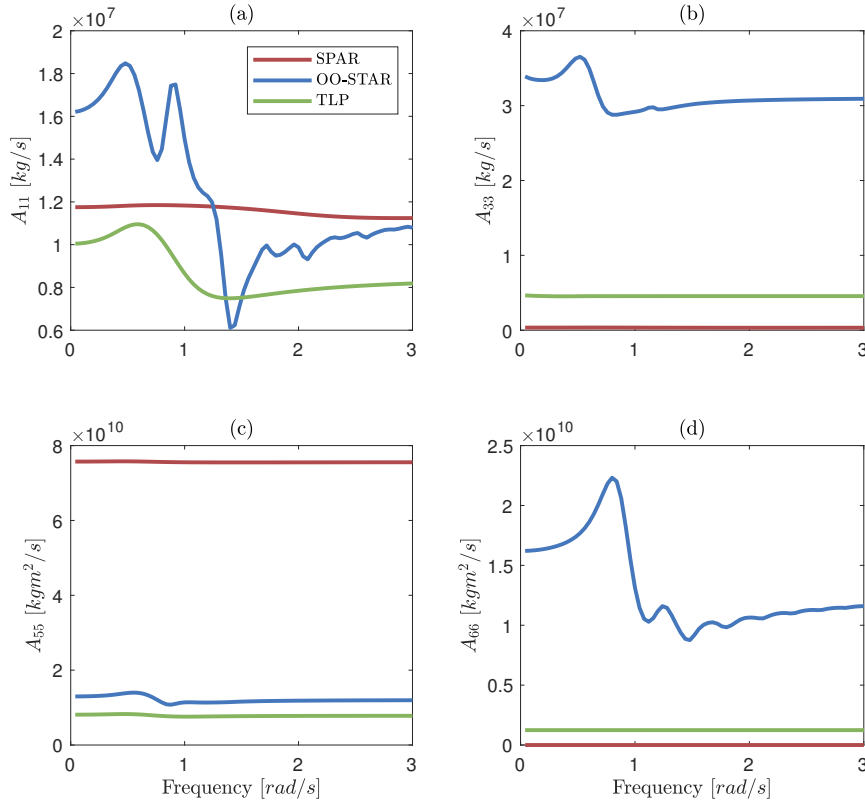
Figure 7.4: Major components of the radiative added mass matrix. Platform surge (a), heave (b), pitch (c), and yaw (d) directions.

where $\underline{q}$ are the platform degrees of freedom, $[M]$ is the inertia tensor of the system, $[C]$ is the hydrostatic matrix, $C_{0,3}$ is the restoring load, $[A]_{inf}$ is the added mass term from hydrodynamic radiation at infinite wave frequency, $[K(t)]$ is the retardation-kernel matrix from hydrodynamic radiation, $\underline{F}_w$ are the incident wave loads, and $\underline{F}_g$ are the gravitational loads. Further information about hydrodynamic modeling can be found in El Beshbichi et al. (El Beshbichi et al., 2021b).

Figures 7.4, 7.5, and 7.6 show, respectively, the major components of the radiative added mass, radiative potential damping, and incident wave loading for each FOWT configuration. Added mass in the platform pitch direction is highest for the spar configuration given the long-drafted geometry. The OO-Star configuration is subjected to the highest radiation damping in all directions. Radiation damping is especially high in the platform heave and yaw directions
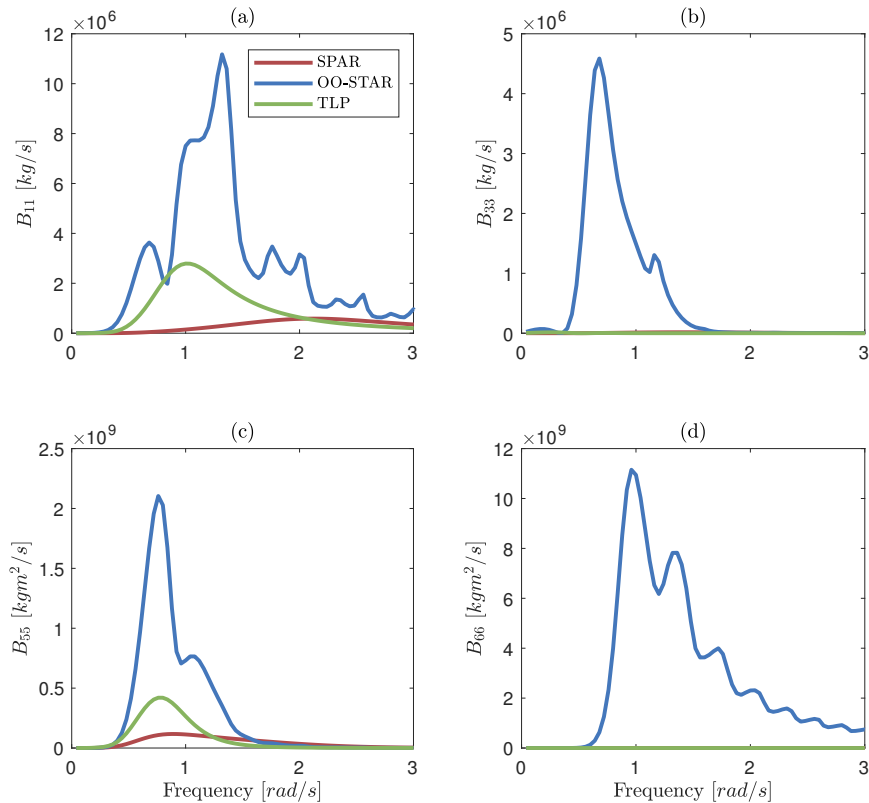
Figure 7.5: Major components of the radiative potential damping matrix. Platform surge (a), heave (b), pitch (c), and yaw (d) directions.

given the significantly greater waterplane area and mass distribution about the centerline.

7.4.3   Viscous Drag Modeling

Linear wave theory assumes the fluid to be inviscid, incompressible, and irrotational (Faltinsen, 1993). As a consequence, viscous drag is effectively neglected. Viscous drag can have a significant effect on the system response in extreme sea states, i.e., if waves and current effects are much larger than in operational conditions (Zhang et al., 2020; Zheng et al., 2020b). Viscous effects are typically included by means of the drag term of Morison's equation. For a slender structural component, the differential viscous load at a given water depth can
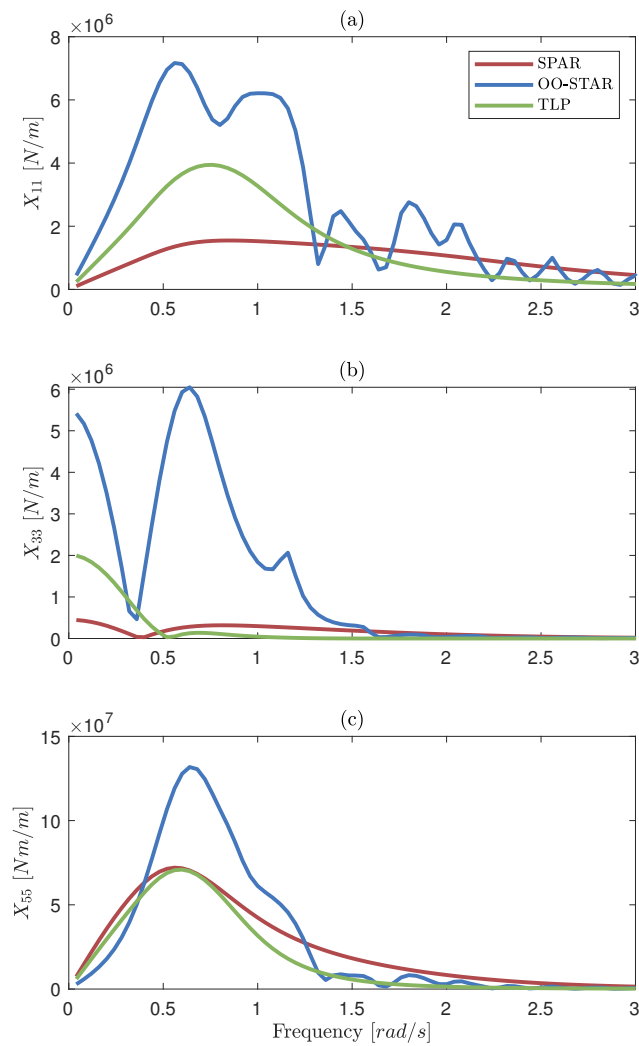
Figure 7.6: Major components of the incident wave loading matrix. Platform surge (a), heave (b), and pitch (c) directions.

be expressed as (Zhang et al., 2020):

$$dF_{viscous} = \frac{1}{2}\rho C_d A |u_f - u_c|(u_f - u_c)dl \tag{5}$$

where $dF_{viscous}$ is the viscous drag acting on a single differential element, C_d is the drag coefficient, A is the projected area per unit length of the component perpendicular to the direction of the flow, u_f is the fluid particle velocity, u_c is the component velocity, and dl is the longitudinal length of the differential element.

Viscous loads have been included in all configurations. In the spar configuration, the viscous load is applied to the main column. In the OO-Star and TLP configurations, the viscous loads are applied to all columns and pontoons. Only transversal viscous drag is assumed to be acting on the pontoons. A drag coefficient equal to 0.65 is used in all configurations.

7.4.4 Station Keeping

The spar and OO-Star configurations employ catenary mooring lines. The associated station-keeping loads are computed by means of a quasi-static formulation considering the fairleads load-displacement relationship. Additional yaw stiffness is applied to the spar system to account for the delta catenary configuration (about 9.8e7 Nm/rad, as in the Phase IV OC3 design (Jonkman, 2010)). The TLP configuration employs tendons. The tendon effect on the global system dynamics is approximated by means of a restoring axial stiffness acting between anchor and fairlead. Tendon stiffness is applied to traction loads only, i.e., compression loads are disregarded. Axial stiffness produced by tendons can be computed as:

$$k_t = \frac{E_t A_t}{l_0} \tag{6}$$

where k_t is the tendon axial stiffness, E_t is the tendon Young's modulus, A_t is the tendon cross-sectional area, and l_0 is the tendon unstretched length (Bachynski and Moan, 2012; Du Kim and Jang, 2016). Tendon structural damping is neglected.

7.4.5   Control System Modeling

The baseline NREL control system for the Phase IV OC3 design is employed (Jonkman, 2007, 2010). The control is composed of a rotor-collective blade-pitch proportional-integral (PI) logic on the error between generator speed and the rated generator speed, and it is active at above-rated environmental conditions. The PI-controlled rotor azimuth follows a second-order system dynamics with characteristic natural frequency and damping ratio. These dynamic parameters are often used to properly tune the PI control gains (Hansen et al., 2005; Jonkman, 2007). Recommended natural frequency and damping ratio values for the onshore single-rotor system are 0.6 rad/s and 0.7, respectively. The associated proportional and integral gains at zero blade-pitch angle are 0.0188 and 0.008, respectively. It is well-known how the gains optimized for onshore deployment must be reduced in floating applications to avoid negative damping in the platform pitch direction associated with unfavorable thrust coupling (Hansen et al., 2005; Jonkman, 2010). The PI-controlled rotor dynamics natural frequency must be sufficiently smaller than the natural frequency associated with platform pitch motion to avoid negative damping. As all configurations considered in this work have a platform pitch motion natural frequency higher than that of the reference single-rotor Phase IV OC3 system, the associated reduced gains for offshore application are employed (K_I=0.00089 and K_P=0.0062, associated with a natural frequency and damping ratio of 0.2 rad/s and 0.7, respectively) (Jonkman, 2010). As expected, pitch instability did not occur in the load cases considered in this study. The NREL generator torque control is also employed, aiming at the optimization of aerodynamic power at below-rated environmental conditions and allowing for constant electric power output at above-rated environmental conditions (Jonkman, 2007).

7.4.6   Load Cases

Six load cases are considered in this work, characterized by directionally congruent irregular waves and turbulent wind conditions (Bachynski and Moan, 2012). Table 7.6 lists the load cases selected. Irregular waves are produced by

Table 7.6: Load cases (LCs).

		LC1	LC2	LC3	LC4	LC5	LC6
U_W	m/s	8	11.4	14	18	25	50
H_S	m	2.5	3.1	3.6	4.4	5.9	12.7
T_P	s	9.8	10.1	10.2	10.6	11.3	14.1
Simulation time	s	3600	3600	3600	3600	3600	3600
Wind state		NTM/KAI	NTM/KAI	NTM/KAI	NTM/KAI	NTM/KAI	NTM/KAI
Wave spectrum		JSP	JSP	JSP	JSP	JSP	JSP

NTM: normal turbulence model (type B); KAI: kaimal turbulence; JSP: JONSWAP

Table 7.7: Damped natural periods obtained from free decay tests.

		SPAR	OO-STAR	TLP
Surge	s	132.3	147.5	44.3
Heave	s	32.1	18.5	0.65
Pitch	s	29.7	23.8	1.05
Yaw	s	33.6	108.6	25.1

JONSWAP spectra. LC1 is relative to below-rated environmental conditions, LC2 to the rated environmental condition, and LC 3-5 to above-rated environmental conditions. In LC5 the wind turbine is parked with fully-pitched blades. Finally, LC6 represents an extreme storm condition where the wind turbine is parked with fully-pitched blades. Wave energy content increases in accord with the wind condition. Kaimal wind turbulence model is used, based on the standard IEC 61400-2 (International Electrotechincal Commission, 2005). A normal turbulence model of class B (NTM-B) is used to define the turbulence intensity associated with each LC. The same wind and wave time realizations are applied to all FOWT configurations.

7.5   Results and Discussion

7.5.1   Natural Periods

Table 7.7 lists the damped natural periods of each configuration obtained through free decay tests in Modelica. Free decay tests are carried out in still

water and without incoming wind. The flexibility of the OO-Star and TLP pontoons and columns may have a significant effect on the natural periods of the system (especially in the platform heave and pitch directions) (Bachynski and Moan, 2012; Berthelsen, 2015). The TLP tendons mass and added mass may also have a significant effect on the natural period in the platform yaw direction (Bachynski and Moan, 2012). The OO-Star natural period in the platform heave direction is short relative to the spar configuration, given the larger waterplane area and the stiffer mooring lines employed. The large yaw inertia of the OO-Star configuration leads to a significantly longer natural period in the platform yaw direction if compared to the other configurations. TLP natural periods are well within the limits imposed by the design criteria considered (Bachynski and Moan, 2012).

7.5.2   Dynamic Response

Figure 7.7 shows the overall mean values of platform surge and pitch motions, electric power output, and nacelle horizontal acceleration for the considered load cases. Results are relative to the left wind turbine only. The mean values of platform surge motion are directly associated with the equivalent stiffness of the mooring system. As a consequence, the spar configuration experiences the highest mean response (about twice the values obtained in the OO-Star system) because it employs the softest station-keeping system. The mean values of platform pitch motion are instead mainly associated with the pitch hydrostatic stiffness and the configuration layout. The platform static pitch angle due to a given thrust can be estimated as (El Beshbichi et al., 2021a):

$$\phi_5 = \frac{F_T HB}{C_{55} + K_{55}} \tag{7}$$

where ϕ_5 is the platform pitch angle, F_T is the thrust acting on the structure, HB is the vertical distance between hub and CoB, and K_{55} is the stiffness due to the station-keeping system in the platform pitch direction. Although the hydrostatic pitch stiffness is highest for the spar configuration (Table 7.5), the associated mean platform pitch response is the highest due to the significant longer
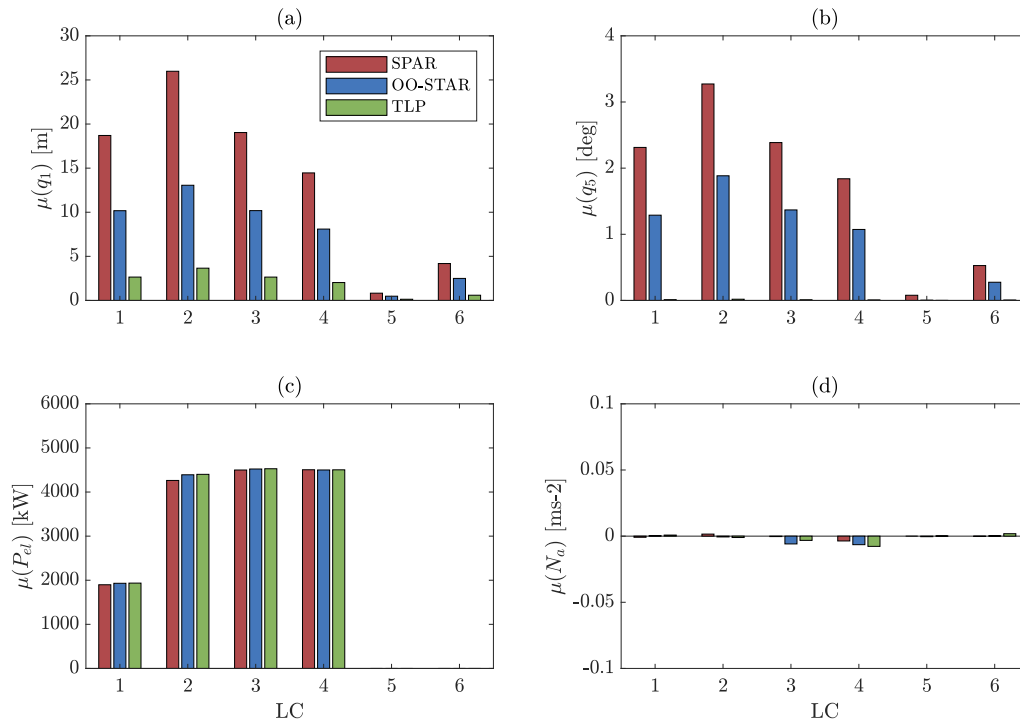
Figure 7.7: Mean values of a) platform surge motion, b) platform pitch motion, and c) electric power output, and d) nacelle horizontal acceleration. Results are relative to the left wind turbine.

distance HB and the low stiffness due to the station-keeping system. The TLP is clearly the best performing configuration, showing negligible mean platform pitch motion and mean platform surge motion well within the offset limit imposed in the design stage (about 3.6 m offset at the rated wind speed). Only the power output relative to the left wind turbine is depicted, as results associated with the right wind turbine are analogous. Electric power output close and above the rated wind speed is lower than the rated value, i.e., 5 MW, due to turbulent fluctuations of the generator speed to below-rated values (El Beshbichi et al., 2021a). The different configurations lead to similar electric power generated throughout the load cases considered. The spar configuration leads to a slight reduction of mean electric power at below-rated wind speeds (about -140 kW difference if compared to OO-Star and TLP at the rated wind speed). This may be associated with a larger global response of the system in the platform pitch and yaw directions, which can reduce the aerodynamic efficiency due to
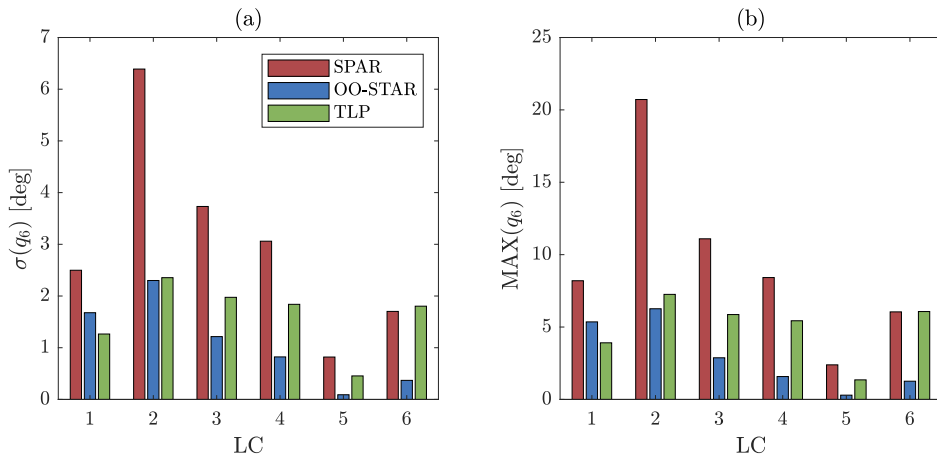
Figure 7.8: Platform yaw motion standard deviation and maximum values.

the skewed flow. The nacelle horizontal acceleration is characterized by near-zero mean values. The reduction of aerodynamic loads due to fully-feathered blades leads to overall negligible mean responses in extreme storm conditions.

Figure 7.8 shows the platform yaw motion standard deviation (STD) and maximum value (MAX) for the load cases considered. The figure shows clearly how platform yaw motion is significant for all configurations considered. Platform yaw motion is particularly significant in the spar configuration, showing a STD value of about 6.2 deg and MAX of about 20.4 deg at the rated wind speed. These values are in good accordance with results obtained in previous work by means of simplified aerodynamic methods (El Beshbichi et al., 2021a). In the same work, it was shown how platform yaw motion is directly caused by the wind turbulence intensity coupled with the transversal thrust distribution on the tower structure. Although the OO-Star and TLP configurations show a relatively appreciable platform yaw response, their magnitude is significantly lower than in the spar configuration. This can be directly associated with stiffer station-keeping systems and a markedly longer fairlead distance to the platform centerline, increasing the effective platform yaw stiffness (Faltinsen, 1993).

Figure 7.9 shows the overall STD values of platform surge and pitch motions, electric power output, and nacelle horizontal acceleration for the load cases considered. Whilst mean values are in the main associated with the mean wind speed, STD values are also affected by wind turbulence intensity and the hy-
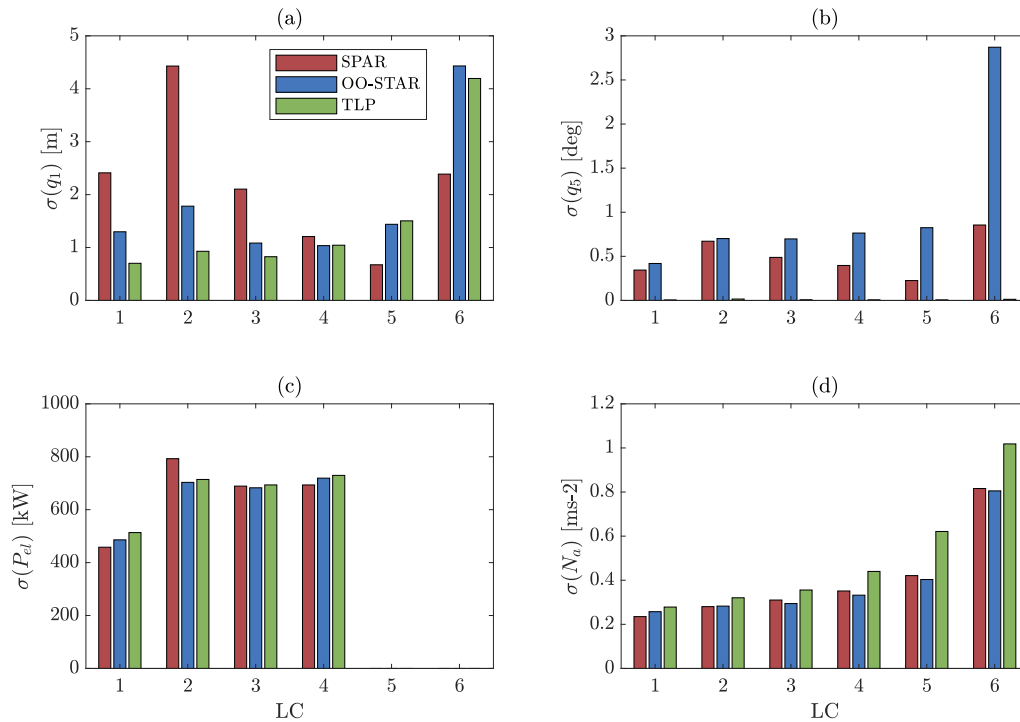
Figure 7.9: Standard deviation values of a) platform surge motion, b) platform pitch motion, c) electric power output, and d) nacelle horizontal acceleration. Results are relative to the left wind turbine.

drodynamic loadings acting on the floating platform (e.g., see the response in parked and extreme storm conditions). Within operational environmental conditions, the highest platform surge STD is obtained for the spar configuration at the rated environmental condition. Platform surge STD presents a similar trend with respect to its mean value. Moreover, platform surge STD is greatly increased in extreme storm conditions, with peak values obtained for the OO-Star configuration of about 4.5 m. Platform pitch STD is highest for the OO-Star configuration, and tends to increase with the severity of the sea state. This can be related to the significant increase in hydrodynamic loading at higher wind speeds, which compensate for the reduction of thrust-induced pitch torque and the reduction of the wind turbulence intensity. On the other hand, platform pitch STD for the spar configuration is reduced at above-rated wind speeds (excluding extreme storm conditions) because the increase of hydrodynamic loading is not sufficient to compensate for the reduction of thrust-induced pitch
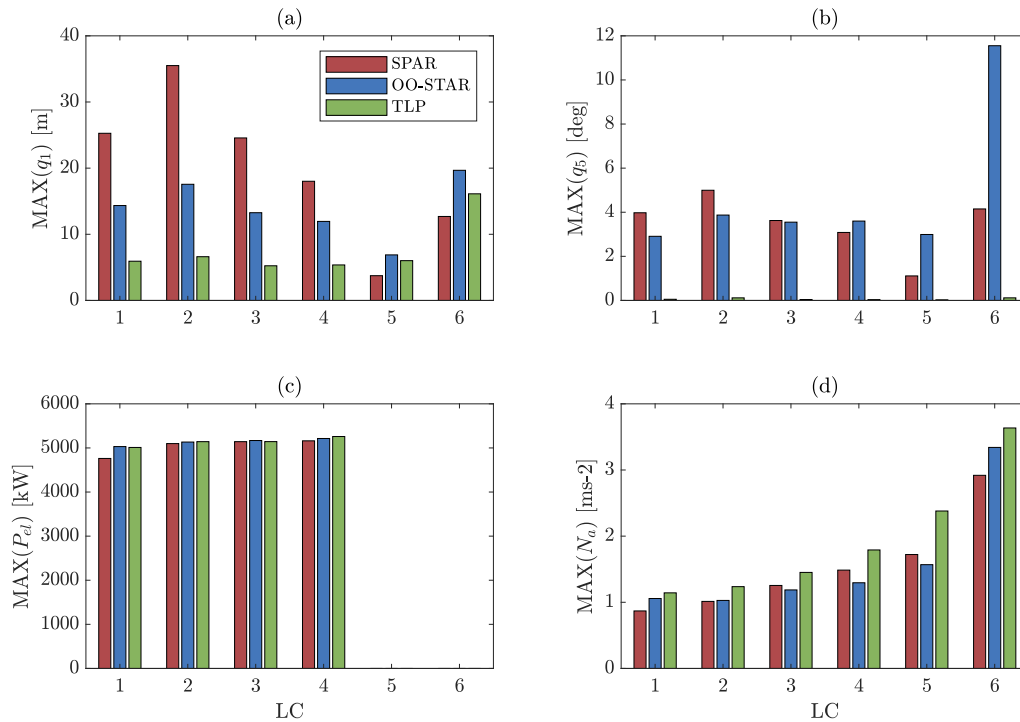
Figure 7.10: Maxima of a) platform surge motion, b) platform pitch motion, c) electric power output, and d) nacelle horizontal acceleration. Results are relative to the left wind turbine.

torque. Platform pitch STD is significantly higher for the OO-Star configuration in the extreme storm load case - about 2.5 times higher than in the spar configuration. A marginally higher electric power output STD for the spar configuration (about 100 kW at the rated wind speed) is a direct consequence of thrust fluctuations given by the large platform yaw and pitch responses, as discussed for Figure 7.9. The nacelle horizontal acceleration STD is significantly increased by increased severity of the sea state, with maximum values in the extreme storm condition of about 0.9 m/s^2. Moreover, results show similar acceleration values among the configurations considered.

Figure 7.10 shows the maxima of the performance parameters for the load cases considered. The trend depicted is in accordance with the considerations made for the mean values (especially in the case of the platform surge motion) and STD values (especially for the platform pitch motion). The highest value of the maximum platform pitch motion in the extreme storm condition is about

11 deg for the OO-Star configuration, while the maximum nacelle horizontal acceleration is about 3.5 m/s^2 and is obtained for the TLP configuration. It is important to remark that the system response is greatly influenced by the blade-pitch control strategy employed, as previous work demonstrated (El Beshbichi et al., 2021a). As a result, designing a specific control logic, such as integrating platform yaw motion as a control target to be minimized, can lead to improved system performance.

7.5.3 Tower Base Bending Moment

Figure 7.11 shows the tower base bending moment mean values, STDs, and maxima for the load cases considered. Values associated with the 2WT employed onshore are also included in the figure (considering 77.6 m tower). A similar trend of the mean values to the one already discussed can be observed, showing the highest mean values in the case of the spar configuration and the lowest in the case of the TLP configuration. Mean tower base bending moment is associated with the magnitude of the external aerodynamic loading and the gravitational loading of the upper structure acting on the main tower. The latter assumes significant values with increasing platform pitch angles. The mean tower base bending moment for the TLP configuration is very similar to the value associated with the tower-fixed deployment, clearly due to the high pitch stiffness. The TLP mean tower base bending moment is also about 65% of the value associated with the spar configuration, and it holds constant for all the load cases considered. This is clearly due to the linear relationship between external loading and associated platform pitch angle, and the relatively small mean platform pitch angles involved (so that $sin\phi_5 \approx \phi_5$).

The tower base bending moments STD tend to increase with the severity of the environmental condition, mainly due to higher hydrodynamic loadings. The tower base bending moment STD for the tower-fixed configuration gives an indication of the relative significance of wind turbulence intensity, contributing to about 30-40% of the load variability at the rated wind speed.

Figure 7.12 shows the tower base bending moment power spectral density (PSD) computed at the rated wind speed (LC2). Wave loading energy is clearly
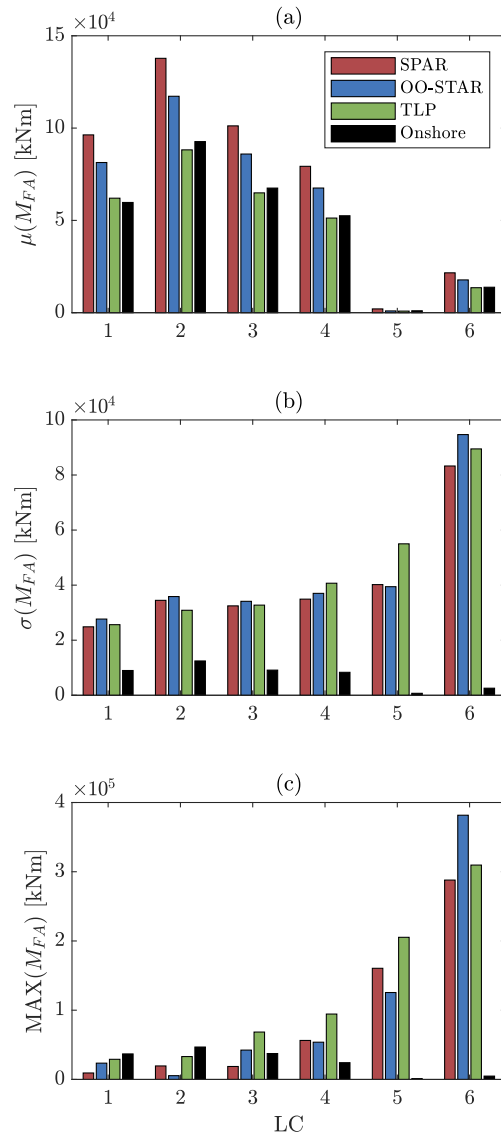
Figure 7.11: Tower base bending moment a) mean value, b) standard deviation, and c) maximum value. Onshore tower base bending moment is also included (77.6 m tower).
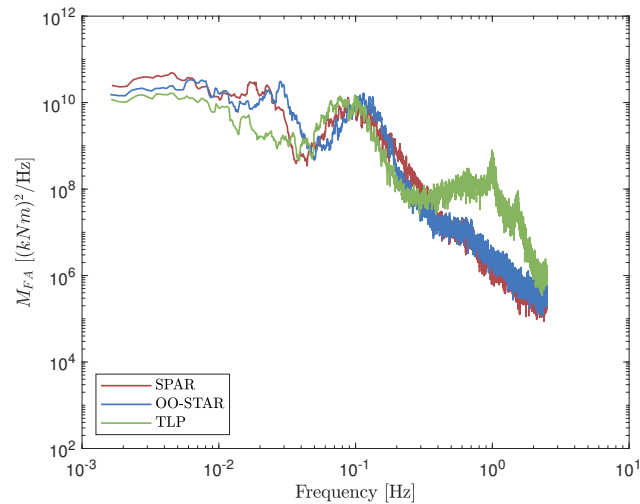
Figure 7.12: Tower base bending moment PSD (LC2 - U_W=11.4 m/s, H_S=3.1 m, T_P=10.1 s). Tower and blades are assumed rigid.

visible around the characteristic wave period (10.1 s - 0.09 Hz) and is similarly distributed for the configurations considered. Turbulent wind energy is also similarly distributed in the low-frequency region.

An increase in the bending moment power density is associated with the excitation given by the platform rigid motion in the pitch and heave directions, as clearly visible in the peaks at 1 and 1.5 Hz ca. for the TLP configuration and the peaks in the region 0.3-0.5 Hz for the spar and OO-Star configurations. For the TLP configuration, it is known that viscous drag loads acting on the platform can induce springing and increase pitch and heave motions (Shen et al., 2016). The high-frequency energy of the tower base bending moment may contribute to wind turbine component fatigue. Moreover, platform pitch motion may experience coupling effects with elastic modes of the structure. These effects are not considered to date and should be investigated in future work.

7.5.4 Upstream Line Tension

The standard deviation of line tension should be sufficiently small to avoid slack conditions and increase fatigue life, and considerations are often made in terms of the ratio between the STD and the mean value (Bachynski and Moan, 2012;
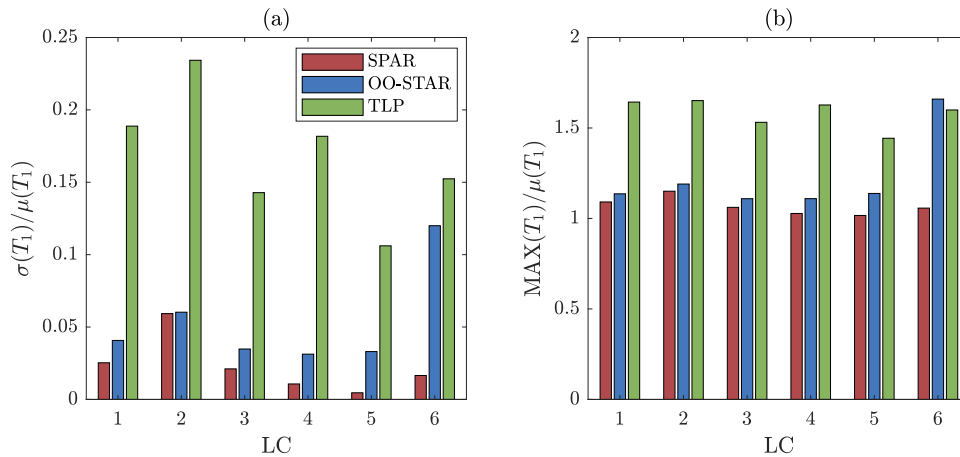
Figure 7.13: Line tensions. a) Ratio between STD and mean values. b) Ratio between maximum and mean value.

Cheng et al., 2017a). Figure 7.13a shows the ratio between line tension STD and the associated mean value. The largest ratio is obtained for the TLP configuration. It is clear from the figure that STD values are relatively significant if compared to the associated mean tension value (maximum 22% of the mean value for TLP configuration at 11.4 m/s). For the TLP configuration, tendon loads are greatly increased by viscous drag effects (Shen et al., 2016). Maximum line loads reach 60% of the associated mean value for the TLP configuration throughout the load cases considered and for the OO-Star configuration in the extreme storm condition. Large extreme line loads can pose limit state concerns. Figure 7.14 shows the upstream lines tension PSD computed at the rated wind speed (LC2). The energy content is clearly different for each configuration given the variation in line pre-tension. The energy content for the TLP configuration, for instance, is about four orders of magnitude higher than in the spar configuration at the wave frequency. In the TLP configuration, peaks are clearly visible at the platform heave and pitch natural frequencies.

7.6   Conclusions

This work presented a comparative dynamic performance analysis of a two-rotor wind turbine mounted on three different floating platforms, i.e., a spar-
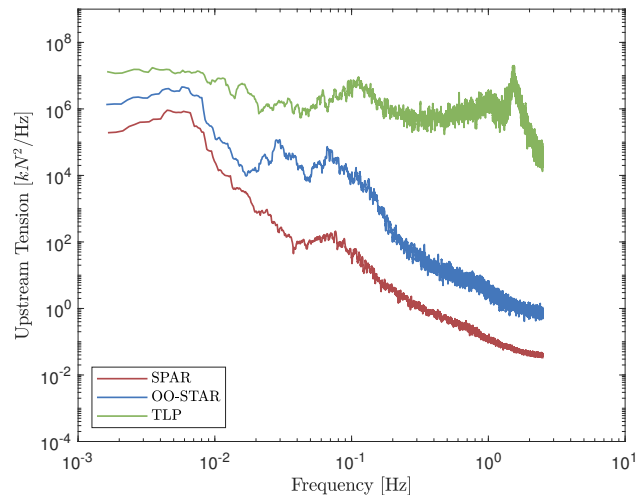
Figure 7.14: Upstream line tension PSD (LC2 - U_W=11.4 m/s, H_S=3.1 m, T_P=10.1 s). Tower and blades are assumed rigid.

type, a semi-submersible, and a tension-leg. The system employed 5-MW baseline wind turbines from NREL. The spar-type and tension-leg platform designs have been defined by means of simplified hydrostatic considerations applied to the two-rotor system. The well-known OO-Star platform design, originally defined for the DTU 10-MW baseline wind turbine, is instead considered as a reference semi-submersible platform. The OO-Star ballast mass is adjusted to compensate for the different overall system mass when employed with the two-rotor system to keep the original draft and water displacement. Fully-coupled dynamic simulations are performed by means of an in-house code developed in Modelica. The tool implements state-of-the-art simulation capabilities and integrates the well-established blade-element momentum code AeroDyn v15 from NREL to compute aerodynamic loads. Six load cases are used to assess the dynamic response of the concepts considered, composed of directionally congruent turbulent wind and irregular wave profiles.

Results indicate that platform yaw motion is a significant dynamic mode for each configuration. This result is in accordance with previous work employing simplified aerodynamics. The greatest yaw response is obtained for the spar configuration. Yaw motion can be directly correlated with the equivalent yaw stiffness of the system, which can be related to the stiffness of the station-

keeping lines and the fairlead distance to the platform centerline. The spar configuration employs the softest mooring lines and the shortest fairlead radius, thus resulting in amplified yaw response. Yaw response is shown to negatively contribute to the rotors' electric power output quality by increasing the associated standard deviation (about +100 kW if compared to TLP configuration). It is important to remark that the system response is greatly dependent on the blade-pitch control logic employed, as previous work on the subject demonstrated. The inclusion of platform yaw response mitigation as additional control objective can greatly improve the system response.

The mean response of the performance parameters is largely associated with wind loading. Mean platform pitch motion is greatest for the spar configuration, given the largest distance between thrust loads and center of buoyancy. Skewed conditions given by mean pitch motion can contribute to the reduction of the mean electric power output. The mean tower base bending moment obtained for the spar configuration is largest due to weight loads induced by the large mean platform pitch angle.

The tower base bending moment standard deviation is clearly much greater than in the case of the equivalent system deployed onshore. The dynamic variation is mainly associated with the hydrodynamic loads acting on the platform, as clearly visible in the fully-pitched load case (LC5). The periodic variation of tower base bending moment can lead to significant fatigue damage. The associated STD increases with increased sea state severity, and it is especially high in extreme storm conditions. Tower base bending moment power spectral density also showed significant energy content at the platform heave and pitch natural frequencies (about 1.5 and 1 Hz, respectively) for the TLP configuration. This high-frequency load variation may have a significant impact on tower fatigue life. Moreover, line tensions standard deviations and maxima normalized by the associated mean value are highest for the TLP configuration, reaching 22% and 60%, respectively. These high values may pose concerns regarding fatigue and limit state performance of the tendons.

Even though a candidate floating platform design is still to be selected, it is clear that the spar configuration is not ideal for two-rotor applications given the excessive platform yaw amplification and large mean pitch angle which reduce

the aerodynamic efficiency of the rotors. The TLP configuration rigidity entails improved dynamic response but may lead to excessive structural loading on the system components and fatigue damage of tower, blades, and tendons, especially for intense sea states. The semi-submersible configuration, even though associated with a platform design not optimized for the specific application and associated with large responses in extreme storm conditions, tended to the most balanced response in operational conditions. Results can be greatly improved by the utilization of a blade-pitch control strategy specifically designed for the two-rotor system. The present work is limited in scope, given the assumptions employed, the limited amount of load cases considered, and the short-term nature of the time realizations. The results presented may be nonetheless used as a basis for further detailed dynamic analysis.

Several assumptions have been used in this work. First, complex aerodynamic effects such as the aerodynamic interaction between the rotors are neglected. These effects may have important dynamic consequences and should later be investigated with higher fidelity tools. In the next future, a dedicated correction factor will be included in the code. Aerodynamic drag on the tower is not considered, as well as the aerodynamic effect of the tower on the local wind profile. Moreover, tower and blades have been assumed rigid. Aeroelastic effects are thus not visible in the present results. The analysis of the aforementioned issues will be covered in future work. Moreover, the present work can be further expanded by performing a comparative dynamic analysis of the two-rotor wind turbine against a single-rotor wind turbine with the same installed power capacity.

Acknowledgment

Chapter 8

Effect of Blade-Pitch Faults on the Loads of a Two-Rotor Floating Wind Turbine

Omar El Beshbichi [a], Yihan Xing [a], Muk Chen Ong [a]

[a] Department of Mechanical and Structural Engineering and Materials Science, University of Stavanger, Stavanger, Norway.

Abstract

Multi-rotor floating wind turbines are among the innovative technologies proposed in the last decade in the effort to reduce the cost of wind energy. These systems are able to offer advantages in terms of smaller blades deployed offshore, cheaper operations, fewer installations, and sharing of the floating platform. Current design standards typically define a set of load scenarios for which the floating wind turbine system must comply. As the blade-pitch actuation system is prone to failures, the assessment of the associated load scenarios is commonly required. Up until now, load assessment of blade-pitch fault scenarios has only been performed for single-rotor solutions. In this work, we address the effect of blade-pitch system faults and emergency shutdown on the dynamics and loads of a two-rotor floating wind turbine. The concept considered employs two NREL 5-MW baseline wind turbines and the OO-Star semi-submersible platform. The blade-pitch faults investigated are blade blockage and runaway, i.e., the seizure at a given pitch angle and the uncontrolled actuation of one of the blades, respectively. Blade-pitch faults lead to a significant increase in the dynamic loads acting on the system, especially for runaway conditions. Bending moments of the faulty blade are increased, as well as the main shaft bending moment. Torsional loads acting on the tower are significantly increased in blade-pitch runaway, manifesting large cyclic oscillations at the 1P frequency. Emergency shutdown significantly excites the platform pitch motion, the tower-bottom bending moment, and tower torsional loads, while suppressing the faulty blade flapwise bending moment after a short peak. Blade-pitch rate marginally increases the loads acting on the tower and main shaft, while the shutdown delay between rotors increases significantly the maxima of the torsional loads acting on the tower. Comparison of blade loads with data from single-rotor spar-type study show great similarity, highlighting that the faulty blade loads are not affected by 1) the type of platform used and 2) the multi-rotor deployment.

Keywords: Dynamic analysis, Pitch system fault, Floating offshore wind turbines, Multi-rotor, Semi-submersible platform.

8.1   Introduction

The need to attain renewable energy targets has thrust the development of the offshore wind resource in the last decade. Estimates from 2019 suggest that out of the total wind power capacity of about 600 GW, 30 GW are associated with offshore facilities (GWEC, 2019). Wind speeds are larger offshore than inland, so a wind turbine unit reaches higher capacity offshore (Cruz and Atcheson, 2016). Moreover, offshore development is appealing since it is associated with fewer interactions with populated areas and less variability on the market price (Ederer, 2015). Most of the innovative technologies proposed within the offshore wind industry have been aimed at the reduction of the cost of electricity produced. Considerable investments in floating offshore wind turbines (FOWTs) have been recently put forward, as the most economically attractive sites for wind energy extraction are located in deep waters, i.e., sites with a water depth larger than about 50 m. Examples of successfully commissioned FOWT projects are plenty. Hywind Scotland is the first FOWT farm composed of five 6-MW wind turbines mounted on spar-type floating platforms, commissioned by Equinor ASA and deployed in Scotland in 2017 (Equinor, 2015). In the first 4.7 years of activity, the farm has exceeded a life capacity factor of about 50% (Smith, 2022). Principle Power has also commissioned several FOWT farms (Principle Power, 2016). For instance, WindFloat Atlantic and Kincardine Offshore Windfarm were commissioned in 2017 and 2021, respectively. They are composed of three 8.4-MW and five 9.5-MW wind turbines mounted on semi-submersible floating platforms and deployed in Portugal and Scotland, respectively.

Multiple wind turbines installed on a single structure have also been proposed as an innovative solution for the reduction of offshore wind energy costs. The manufacturing, transportation, and installation procedures of large wind turbine blades are especially costly (Jamieson and Branney, 2012). An example is the multi-rotor wind turbine concept (4R-V29) installed at the Denmarks Tekniske Universitet (DTU) by Vestas A/S (van der Laan et al., 2019). Multi-rotor wind turbines mounted on floating platforms can lead to substantial advantages, such as cheaper offshore operations, fewer net installations, and shar-

ing of the floating platform and station-keeping systems. These advantages can significantly reduce the associated overall cost of energy. An example of multi-rotor FOWT system is TwinWay by Hexicon, a two-rotor wind turbine system mounted on a semi-submersible platform (Hexicon, 2021a). Hexicon is planning to deploy a full-scale demonstrator at the Metcentre's deep water area in Norway by the end of 2022 (Hexicon, 2021b).

Discontinuous dynamic loads should be carefully considered during the design process of wind turbine systems. Faults of various wind turbine subsystems can lead to abnormal dynamic conditions. For instance, common fault conditions included in International Electrotechnical Commission (IEC) standards are the failure of the blade-pitch system, emergency shutdown events, grid loss or failure of the power electronics, and fault of the control system (International Electrotechincal Commission, 2005). According to the results listed in the RELIAWIND report, failures of the blade-pitch system account for more than 20% of the total wind turbine failure rate and downtime (Gayo, 2011). These faults can be related to both actuation and sensor failures. For hydraulic actuation, the blockage of the hydraulic valves or pressure loss of the hydraulic oil can lead to the blockage of the actuation system, while sensor failures can bring about blade runaway. Research dealing with the effect of faulted conditions on the dynamic response of FOWTs is available but limited (Bachynski et al., 2013; Jiang et al., 2014; Etemaddar et al., 2016; Karimirad and Michailides, 2019; Jiawen et al., 2022). Analysis of the 5-MW NREL baseline wind turbine mounted on several floating platform types reported how blade-pitch faults, grid loss, and emergency shutdown lead to a significant increase in the structural loads and motions of the system. It was found that the load imbalance due to blade-pitch fault can lead to platform yaw instability. The emergency shutdown can also be associated with short peaks of the faulty blade flapwise bending moment and the excitation of the tower elastic response and platform pitch motion.

To date, in spite of the advances in the development of multi-rotor FOWT systems no substantial research addressing the system response due to blade-pitch faults has been published. In this work, the influence of blade-pitch system faults on the dynamic response and loads of a two-rotor wind turbine de-

ployed on a semi-submersible floating platform is analyzed. The study considered blade-pitch blockage, blade-pitch runaway, and the effect of emergency shutdown. The work employs an in-house tool for the fully-coupled dynamic analysis of two-rotor FOWTs (El Beshbichi et al., 2021b). The tool is developed in Modelica, a non-proprietary, declarative, object-oriented, equation-based language developed by the non-profit Modelica Association and used to model complex physical systems (Fritzson, 2014). The tool is coupled with the well-established open-source aerodynamic code NREL AeroDyn v15 based on the blade element momentum theory (BEMT) (Moriarty and Hansen, 2005). To date, the effect of complex aerodynamic interactions on the rotors' aerodynamic loads is not considered. The major aims of this work are 1) to analyze the effect of blade-pitch faults on the dynamic response of a two-rotor FOWT system and compare it with the response under normal operating conditions, 2) to compare the faulted response with and without the initiation of emergency shutdown, and 3) to analyze the effect of blade-pitch rate and shutdown delay between rotors during emergency shutdown.

8.2   Blade-Pitch System Faults

Variable-speed wind turbines exploit the variation of the blade-pitch angles to regulate the rotor speed when the wind speed exceeds rated values. Broadly speaking, the blade-pitch system is consisting of blade-pitch angle sensors, a controller, and blade-pitch actuators. Faults can occur at the actuation level as well as at the sensor level. Faults related to the blade-pitch angle sensor can, for instance, result in a fixed value or a gain factor on the measured value. Sensor faults are usually considered of low severity as physical redundancy is common (Odgaard et al., 2009). Blade-pitch actuation is driven either electrically or hydraulically (Cho et al., 2020). Electrical actuation is more precise but can lead to backlash and to fast component wear due to the presence of gears. Hydraulic actuation, on the other hand, is less precise but more suitable for dealing with sudden changes in load conditions. This study assumes hydraulic actuation given its broad deployment. Hydraulic actuation is broadly composed of a
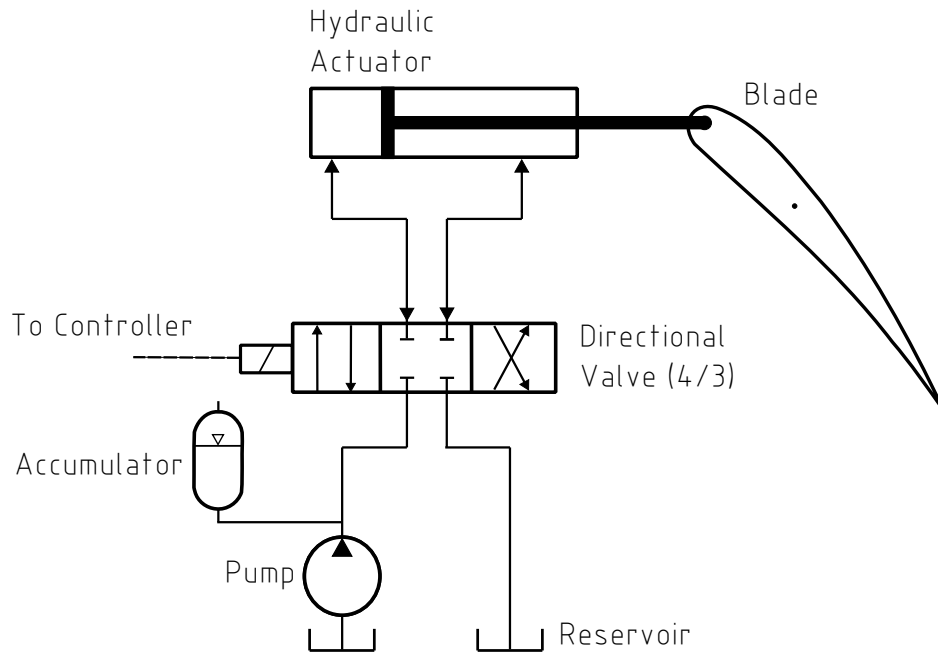
Figure 8.1: Schematization of hydraulic blade-pitch system.

pump, an accumulator, reservoirs, a 4/3 directional control valve actuated by
the controller, and a hydraulic piston for mechanical actuation of the blade (Luo
et al., 2014). Figure 8.1 shows a schematization of the hydraulic blade-pitch sys-
tem. Faults of the hydraulic actuation system can be associated, for instance,
with oil pressure drop, blockage of the directional valve, and hydraulic leakages
(Odgaard et al., 2009).

Detection of faults is commonly achieved by the control system by search-
ing for distinctive fault patterns in the sensors' data. A large amount of work
has been carried out to study fault detection methods. For instance, Cho et al.
(2016) presented a model-based fault detection method based on system state
estimation. The authors also presented fault isolation methods to classify the
fault type and fault-tolerant control methods where the classical blade-pitch
control strategy is reconfigured to minimize the impact of fault on the system
dynamics (Cho et al., 2018). Liu et al. (2021) presented a mixed model and
signal-based fault diagnosis architecture for detection and isolation of faults in
FOWTs. After detection of fault, the controller determines if the system can still
safely operate, or whether a preventive shutdown is necessary. Shutdown can
be executed either in a normal mode or in an emergency mode (Johnson and
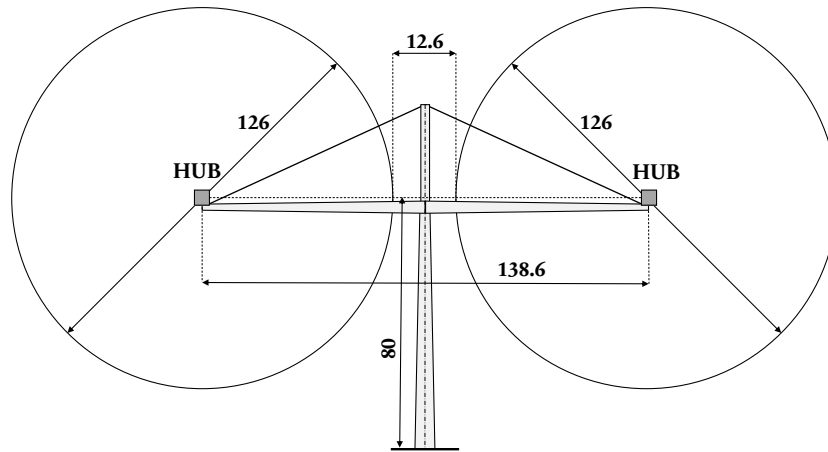
Figure 8.2: Two-rotor tower structure considered in the analysis (lengths in meters) (El Beshbichi et al., 2021a).

Fleming, 2011). The normal mode assumes minimal blade-pitch deceleration to avoid excessive dynamic disturbance (e.g., 1 rpm/s (Jiang et al., 2014)). On the other hand, the emergency mode assumes the maximum blade-pitch rate possible to stop the turbine in the shortest amount of time.

This paper focuses on the effect of several blade-pitch fault scenarios with and without the initiation of emergency shutdown.

8.3   Multi-Rotor Wind Turbine System (2WT)

The tower structure accommodating the wind turbines (2WT) is the preliminary design as proposed in El Beshbichi et al. (2021a), where limit state design was considered as design criterion. The structure is made up of a main vertical tapered tower, two horizontal tapered arms, and a supplementary vertical cylinder. Wires carrying the rotors' weight are also used. Figure 8.2 shows the 2WT tower structure considered in the analysis. Hub height is about 80 m from the tower base. The minimum distance between rotors is assumed to be 10% of the rotor radius, as in the Vestas four-rotor wind turbine prototype installed at DTU and recently decommissioned (Bastankhah and Abkar, 2019). The system employs standard 5-MW NREL baseline wind turbines. Table 8.1 lists major wind turbine parameters.

Table 8.1: NREL 5-MW Baseline Wind Turbine Specifications (Jonkman, 2007).

Rated Power	5 MW
Rotor Orientation, Configuration	Upwind, 3 Blades
Control	Variable Speed, Collective Pitch
Drivetrain	High Speed, Multiple-Stage Gearbox
Rotor, Hub Diameter	126 m, 3 m
Rated Tip Speed	80 m/s
Hub Height	90 m
Rotor Mass	110×10^3 kg
Nacelle Mass	240×10^3 kg
Cut-In, Rated, Cut-Out Wind Speed	3 m/s, 11.4 m/s, 25 m/s
Cut-In, Rated Rotor Speed	6.9 rpm, 12.1 rpm
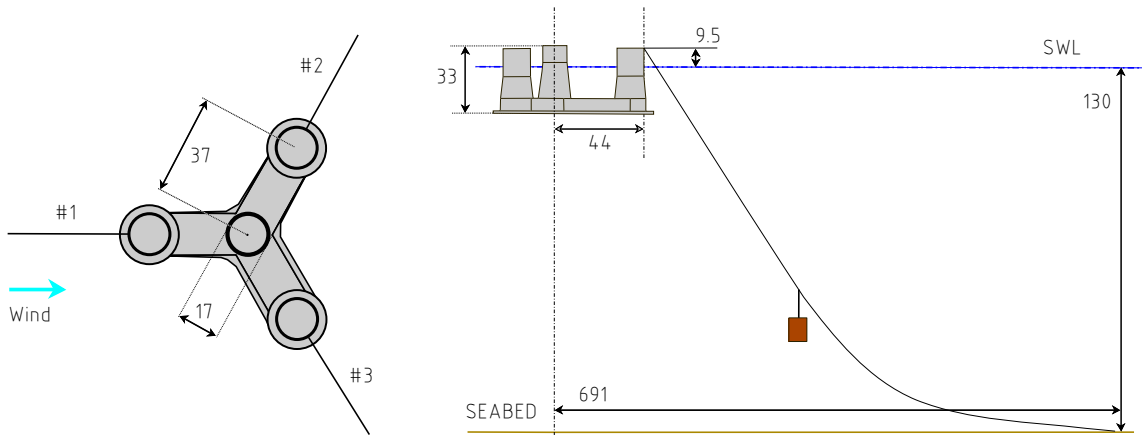
Figure 8.3: OO-Star platform major geometrical and mooring system specifications in the top view (left) and side view (right) (lengths in meters) (Berthelsen, 2015; Jiawen et al., 2022).

The floating platform considered in this study is the Olav Olsen OO-Star semi-submersible system. The Lifes50+ project has publicly released the system specifications (Berthelsen, 2015; Pegalajar-Jurado et al., 2018; LIFES50+, 2022). The platform is composed of a Y-shaped pontoon used to connect the central column with the three outer columns. The pontoon arms are geometrically displaced 120 degrees from each other, starting from the upwind direction. Figure 8.3 shows the platform configuration, together with the major geometrical and mooring system specifications. Table 8.2 lists the main geometrical platform parameters. The catenary mooring lines employed have a length of

Table 8.2: OO-Star platform major geometrical parameters (Berthelsen, 2015).

Draft	22 m
Pontoon length to axis	37 m
Pontoon height	6.5 m
Pontoon width	17 m
Outer column height (from pontoon)	24.5 m
Central column height (from pontoon)	26 m
Central column diameter (tapered)	16.2 (12.05) m
Outer column diameter (tapered)	15.8 (13.4) m
Fairlead radius	44 m
Fairlead distance from SWL	-9.5 m
Freeboard to tower base	11 m

Table 8.3: Damped natural periods of the 2WT floating wind turbine obtained from free decay tests.

	Natural period (s)	Natural frequency (rad/s)
Surge	147.5	0.042
Heave	18.5	0.339
Pitch	23.8	0.263
Yaw	108.6	0.057

703 m, a mass density of 375 kg/m, and a diameter of 0.137 m. The standard mooring configuration also employs clumped masses with an equivalent total mass in water of about 50 tonnes to achieve greater pretension per unit length. In this study, the clumped masses are disregarded, and dynamic equivalence is achieved by increasing the equivalent mass density of the mooring lines to match the original static fairlead tension. The final equivalent mass density used is about 650 kg/m. The OO-Star platform is originally designed in conjunction with the DTU 10-MW baseline wind turbine (Bak et al., 2013). As such, the ballast mass used in this work has been appropriately adjusted for employing the 2WT wind turbine concept without affecting platform draft and water displacement. The platform ballast has been thus increased by about 688 tonnes. The water depth considered is about 130 m. Table 8.3 lists the damped natural periods of the system as obtained from free decay tests.
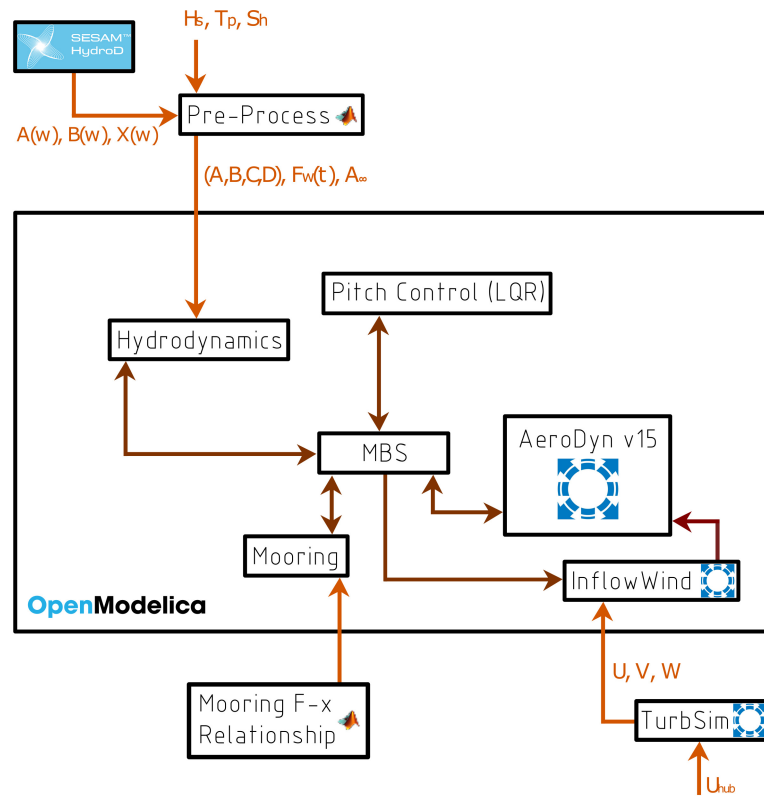
Figure 8.4: Modularized schematization of the simulation tool used in the analysis.

8.4   Methodology

The fully-coupled dynamic response of the 2WT system is obtained by means of an in-house code developed in the language Modelica (The Modelica Association, 2017). Figure 8.4 shows the schematization of the simulation tool used for analysis. Development is carried out by means of the open-source platform OpenModelica (OSMC, 2021). Rigid body dynamics and full structural flexibility of blades and tower are implemented by means of the multi-body environment within the Modelica Standard Library (MSL) (The Modelica Association, 2008). Previous work described the developmental approach in detail, in which a simplified aerodynamic modeling method based on steady-state coefficients was used (El Beshbichi et al., 2021b). More recently, full blade-element momentum (BEM) capabilities were achieved by integrating into the tool the well-known open-source codes AeroDyn v15 and InflowWind within FAST v8 by NREL (Jonkman and Buhl, 2005). InflowWind is used to compute at each time

step the wind velocity components at the location of the aerodynamic nodes. AeroDyn v15, on the other hand, carries out the BEM steady-state computation of the aerodynamic loads.

8.4.1   Hydrodynamic Modeling

Hydrodynamic loads acting on the FOWT system are computed assuming linear wave theory, i.e., Airy theory. Linear wave theory is commonly employed if the incident wave height is significantly smaller than the water depth (Faltinsen, 1993; DNV, 2010). Airy theory assumes the fluid to be irrotational and inviscid. The platform dynamics is assumed rigid. The platform equations of motion can be written as:

$$[M]\underline{\ddot{q}} + [C]\underline{q} + C_{0,3} = -[A]_{inf}\underline{\ddot{q}} - \int_0^t [K(t-\tau)]\underline{\dot{q}}d\tau + \underline{F}_{waves} + \underline{F}_g \qquad (1)$$

where $\underline{q}$ stands for the floater rigid degrees of freedom (DoFs), $[M]$ and $[C]$ are, respectively, the inertia and hydrostatic matrices, $C_{0,3}$ is the buoyancy load from Archimedes' principle, $[A]_{inf}$ is the added mass matrix at infinite incident wave frequency, $[K]$ is the wave-radiation-retardation kernel matrix, $\underline{F}_{waves}$ are the loads from incident waves, and $\underline{F}_g$ are the gravitational loads. The ij-th convolution term describing the radiative damping can be approximated in state-space as (Cummins, 1962):

$$\dot{\xi}_{ij} = [\alpha]_{ij}\xi_{ij} + [\lambda]_{ij}\dot{q}_j$$

$$\int_0^t K_{ij}(t-\tau)\dot{q}_j d\tau \simeq [\theta]_{ij}\xi_{ij} + [\gamma]_{ij}\dot{q}_j \qquad (2)$$

where $[\alpha]_{ij}, [\lambda]_{ij}, [\theta]_{ij}, [\gamma]_{ij}$ are the ij state-space matrices, and ξ_{ij} is the ij state vector. Previous work demonstrated how a small set of states resolve most of the impulse energy (El Beshbichi et al., 2021b). Consequently, a balanced model reduction is often employed to reduce the number of states considered. Two states are used in this work, which account for about 80% of the impulse energy. The frequency-domain hydrodynamic problem relative to the platform geometry presently considered is solved by employing HydroD within the DNV com-

mercial code SESAM-WADAM (see Figure 8.4) (DNV, 2017). An in-house pre-processor is used to compute model quantities from hydrodynamic input information, such as the matrices associated with the state-space approximation of the radiation damping and time-domain realizations from inverse Fourier transformations of the loads from incident waves.

8.4.2   Structural Dynamics

Structural flexibility of blades and tower elements are presently implemented by considering a multi-body-based approach. HAWC2, a fully-coupled tool developed by DTU Wind Energy, employs a similar formulation for the structural dynamics of slender elements (Larsen and Hansen, 2007). Small, linear, and elastic structural deformations are assumed. A series of flexible beam units are used to approximate the local structural properties of the slender structures. Each beam unit is composed of two rigid bodies connected by means of elastic joints. The flexibility about the main axes is considered, e.g., the flapwise and edgewise directions, while the torsional flexibility is disregarded. Distributed structural damping is assumed and defined by means of the stiffness proportional Rayleigh damping. The coefficients assumed are about 0.3% and 3% of the associated stiffness for the blades and tower, respectively. Previous work demonstrated the convergence of the inertial and elastic properties of the blades to reference values with the employment of about six beam units, i.e, twelve rigid bodies. The tower properties, on the other hand, converge with as little as two beam units given the structural regularity. Axial stiffness of the tower wires is also taken into account.

8.4.3   Aerodynamic Modeling

The blade-element momentum theory (BEMT), also called strip theory, is widely utilized to compute the aerodynamic state of wind turbines due to its simplicity, reasonable accuracy, and computational efficiency. AeroDyn v15 implements BEMT with the inclusion of Prandtl tip and hub losses, as well as Pitt-Peters skewed flow and Gaulert corrections (Moriarty and Hansen, 2005).
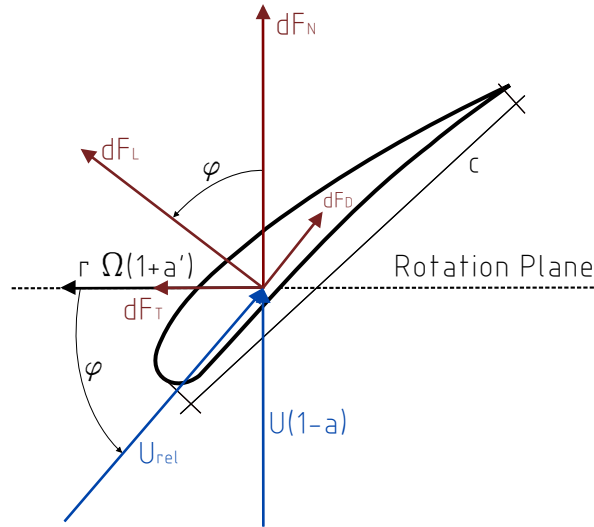
Figure 8.5: Relationship between local flow condition parameters and local aerodynamic loads of a single blade element.

In the blade element theory, the blades are discretized in finite independent elements. The relationship between local flow condition parameters and local aerodynamic loads of a blade element is typically depicted as in Figure 8.5, where Ω is the rotor angular speed, φ is the relative wind angle, U is the inflow wind speed, U_{rel} is the relative local wind speed, a is the local axial induction factor, a' is the local tangential induction factor, c is the blade element chord length, r is the distance of the blade element from the rotor center, dF_L and dF_D are, respectively, the differential local lift and drag forces, and dF_N and dF_T are, respectively, the differential normal and tangential forces referred to the rotation plane. The relationship between the total local aerodynamic loads and the local flow condition can be easily derived and expressed as:

$$dF_N = \frac{1}{2}b\rho U_{rel}^2(C_l cos\varphi + C_d sin\varphi)cdr \qquad (3)$$

$$dQ = \frac{1}{2}b\rho U_{rel}^2(C_l sin\varphi - C_d cos\varphi)crdr \qquad (4)$$

where dQ is the differential torque acting on the rotor, b is the number of blades, ρ is the air density, C_l is the airfoil lift coefficient, C_d is the airfoil drag coefficient, and dr is the radial differential thickness of the control volume. In this work, the tower influence on the wind field and the aerodynamic drag loads on

the tower are not included. Moreover, the present BEMT aerodynamic implementation, based on AeroDyn v15, is not able to consider aerodynamic interactions since each blade element is independent of other elements. The lack of aerodynamic interaction between rotors may have a significant impact on the fully-coupled response of the 2WT system presented in this study. Quantification of complex aerodynamic effects should later be investigated with higher-fidelity tools.

8.4.4   Station Keeping

The station-keeping loads associated with the catenary mooring lines employed in the OO-Star platform are computed by considering a non-linear quasi-static formulation. Consequently, inertial and damping effects of the catenary lines on the system dynamics are neglected and mooring loads are described as a function of the fairlead position only. The quasi-static approach is broadly used given its computational efficiency and accuracy for prototypal dynamics and loads analysis (Masciola et al., 2013).

8.4.5   Control System Modeling

Active control of variable-speed wind turbines is generally divided into two actuation mechanisms: 1) a generator-torque controller, optimizing the generator torque as a function of the generator speed, and 2) a blade-pitch controller, regulating the generator speed to the rated value at above-rated wind speeds (Jonkman, 2007). The standard control action proposed for the NREL 5-MW baseline wind turbine regulation divides the generator torque control into different regions. At below-rated conditions, the generator-torque control objective is the optimization of the mechanical power available at the shaft. On the other hand, at above-rated wind conditions, the generator-torque control objective is the regulation of either the generator torque or electric power output to rated values. The blade-pitch control generally assumes rotor-collective blade pitch angles, i.e., the blade-pitch angles are assumed to be the same. The blade-pitch control algorithm employed by the NREL 5-MW baseline wind turbine

is a gain-scheduled proportional-integral (PI) control regulating the generator speed to the rated value.

In this work, the standard generator-torque control employed by the NREL-5MW baseline wind turbine is considered, and a linear quadratic regulator (LQR) is used to design an optimal blade-pitch controller for the 2WT proto-type, as proposed in previous work. The LQR control objectives are: 1) the mitigation of platform yaw motion, which previous work found to be an important dynamic mode of two-rotor FOWTs employing conventional mooring systems, and 2) the regulation of the generators' speeds to rated values for above-rated wind conditions. Linear quadratic regulation employs the linearized representation of the system about a steady-state operational point. The global state vector used for linearization can be described as:

$$\tilde{\underline{x}}_T = [\beta_L, \beta_R, \dot{\beta}_L, \dot{\beta}_R, \Omega_L, \Omega_R, q_5, \dot{q}_5, q_6, \dot{q}_6, \Omega_{L,err}, \Omega_{R,err}] \tag{5}$$

where β_L and β_R are the rotor-collective blade-pitch angles, Ω is the rotor speed, Ω_{err} is the integral rotor speed error with respect to the rated value, q_5 is the platform pitch angle, and q_6 is the platform yaw angle. Subscripts L and R are referring to the left and right turbines, respectively. The input vector can be described as:

$$\tilde{\underline{u}} = [\beta_L, \beta_R] \tag{6}$$

The LQR algorithm minimizes a quadratic cost function describing state control and control input usage:

$$J = \int_{t_0}^{t_1} (\tilde{\underline{x}}_T^T [Q] \tilde{\underline{x}}_T + \tilde{\underline{u}}^T [R] \tilde{\underline{u}}) \, dt \tag{7}$$

where $[Q]$ and $[R]$ are weight matrices associated with the control objectives and whose definition is generally left to the control system designer. The control system is implemented as state feedback given by:

$$\tilde{\underline{u}} = -[K] \tilde{\underline{x}}_T \tag{8}$$

Table 8.4: Operating wind speeds associated with LQR controllers employed.

	U_{rel} (m/s)
Below-rated	3 - 10
Rated	11 - 12
Above-rated	13 - 25

Table 8.5: Steady-state operation points used for linearization.

	Below-rated	**Rated**	**Above-rated**
U_{rel} (m/s)	9	11.3	13
β (rad)	0.052	0.1	0.118

where $[K]$ is the control gain matrix obtained by solving the algebraic Riccati equation (ARE), yielding the gains minimizing the given cost function (Prasad et al., 2014). As the system dynamics is greatly non-linear, three gain schedules associated with below-rated, around-rated, and above-rated wind speeds are used. A dedicated linearization point is used for each control region. Table 8.4 lists the LQR control regions. Table 8.5 lists the operation points used for linearization. Table 8.6 lists the control weights used in this work. Table 8.7 lists the selected LQR gains.

8.4.6 Blade-Pitch Actuation Modeling

During normal operating conditions, blade-pitch dynamics is taken into account by means of a second-order transfer function from reference to actual

Table 8.6: LQR control weights.

	[Q]	**[R]**
Below-rated	*diag(0, 0, 0, 0, 0, 0, 0, 0, 500, 1, 0, 0)*	*diag(1000,1000)*
Rated	*diag(0,0,0,0,500,500,0,0,2500,2500,0.01,0.01)*	*diag(5000,5000)*
Above-rated	*diag(0, 0, 0, 0, 1, 1, 0, 0, 1000, 1000, 1, 1)*	*diag(1000,1000)*

Table 8.7: LQR control gain scheduling.

	[K]
Below-rated	$\begin{bmatrix} 0,0,0,0,-0.01,0.01,0,0,0.25,7.11,0,0 \\ 0,0,0,0,0.01,-0.01,0,0,-0.25,-7.11,0,0 \end{bmatrix}$
Rated	$\begin{bmatrix} 0,0,0,0,-0.42,0.12,0,0,0.63,-5.31,0.032,0 \\ 0,0,0,0,0.12,-0.42,0,0,-0.63,5.31,0,0.032 \end{bmatrix}$
Above-rated	$\begin{bmatrix} 0,0,0,0,-0.10,-0.02,0,0,0.30,6.62,0.001,0 \\ 0,0,0,0,-0.02,-0.10,0,0,-0.30,-6.62,0,0.001 \end{bmatrix}$

blade-pitch angle (natural frequency f_n= 5 Hz and damping ratio ζ = 2 % (Hansen et al., 2005; Hansen and Kallesøe, 2007)). Blade-pitch fault cases are introduced in the fully-coupled simulation at a particular user-specified time. Fault initiation effectively disengages the blade-pitch controller and forces fault-related conditions on the system.

8.4.7   Environmental Conditions

Three-dimensional turbulent wind profiles needed in InflowWind are computed in the NREL code TurbSim starting from the mean wind speed at the hub height (see Figure 8.4) (Jonkman, 2009a). The Kaimal spectrum for IEC Class B is used as turbulence model. The normal turbulence model (NTM) is used, as suggested by the DNV-OS-J101 guideline for load cases combining fault occurrences (LC 2.2) (DNV, 2010). A grid-point matrix of fifteen points is used. The grid is characterized by a height of 160 m and width of 300 m, and thus able to encompass the whole system. A time step of 0.05 s is used to realize the wind profile. Irregular waves are produced from the standard JOint North Sea WAve Project (JONSWAP) spectrum. Waves are assumed always aligned with the wind direction.

8.4.8   Numerical Simulation

The OpenModelica version 1.18.1 is used. All parameters are evaluated during the model translation. The solver employed is *cvode* and a tolerance of $1x10^{-4}$

Table 8.8: Load cases considered in the study (800 s simulations).

	U_W (m/s)	H_S (m)	T_P (s)	t_f (s)	t_d (s)	**Fault Type**
1A	8	2.5	9.9	-	-	
	11.5	3.2	10	-	-	
	14	3.6	10.3	-	-	
	22	4.2	10.5	-	-	
2A	8	2.5	9.9	600	-	Blockage
	11.5	3.2	10	600	-	
	14	3.6	10.3	600	-	
	22	4.2	10.5	600	-	
3A	8	2.5	9.9	600	-	Runaway
	11.5	3.2	10	600	-	
	14	3.6	10.3	600	-	
	22	4.2	10.5	600	-	
2B	8	2.5	9.9	600	0.1	Blockage
	11.5	3.2	10	600	0.1	&
	14	3.6	10.3	600	0.1	Shutdown
	22	4.2	10.5	600	0.1	
3B	8	2.5	9.9	600	0.1	Runaway
	11.5	3.2	10	600	0.1	&
	14	3.6	10.3	600	0.1	Shutdown
	22	4.2	10.5	600	0.1	

is used. Using cvode is found to be beneficial to reduce the number of Jacobian evaluations during simulation. The linear solver *totalpivot* and non-linear solver *kinsol* are used. Simulations of about 800 s are carried out, where the first 400 s are used to initialize the system. A time interval of 0.1 s is used to store the data, short enough to cover both rigid and structural dynamics.

8.5 Load Cases

Table 8.8 lists the load cases considered in this study, associated with both normal operating conditions and faulted conditions. The load cases are based on the work by Jiang et al. (2014). In the table, LC stands for the load case prefix, U_W is the mean wind speed at the hub height, H_S is the significant wave height, T_P is the wave period, t_f is the time at which the fault occurs, and t_d is the time delay from the occurrence of fault to the shutdown initiation. LC 1A

corresponds to the system undergoing normal operating conditions. In LC 2A, the second blade of the left turbine undergoes blockage, and its pitch-angle is fixed from t_f onwards. The blade-pitch angle under blockage conditions can be described as:

$$\beta_b(t) = \beta(t_f) \tag{9}$$

Blade blockage can ensue from faults in the hydraulic actuation system. The remaining working blades are still used by the controller to regulate the generator speed and minimize the platform yaw angle. In LC 3A, the same faulty blade is moving uncontrollably from its value at t_f to the minimum pitch angle setting (0 deg) at the normal pitch rate. The blade-pitch angle at runaway conditions can be described as:

$$\beta_r(t) = max\left\{\beta(t_f) - P_{r,n} * t, 0\right\} \tag{10}$$

where $P_{r,n}$ is the normal pitch rate (8 deg/s). Blade runaway can be considered as a sensor fault of high severity, where the measured value is effectively multiplied by a gain factor. This condition is generally a rare fault event, as physical redundancy of sensors is usually common practice. It is nonetheless important to analyze its effect on the system dynamics and loads, as recommended in certification guidelines (Germanischer Lloyd Industrial Services, 2010; International Electrotechincal Commission, 2010). A gain factor of zero is considered to account for the most unfavorable runaway condition. In LC 2B and LC 3B, the system undergoes the same fault conditions of LC 2A and LC 3A, respectively, but shutdown is executed after a short time delay t_d. During shutdown, the operative blades are fully feathered (that is, pitched at 90 deg) at the standard pitch rate as described in the following equation:

$$\beta_s(t) = min\left\{\beta(t_f + t_d) + P_r * t, \frac{\pi}{2}\right\} \tag{11}$$
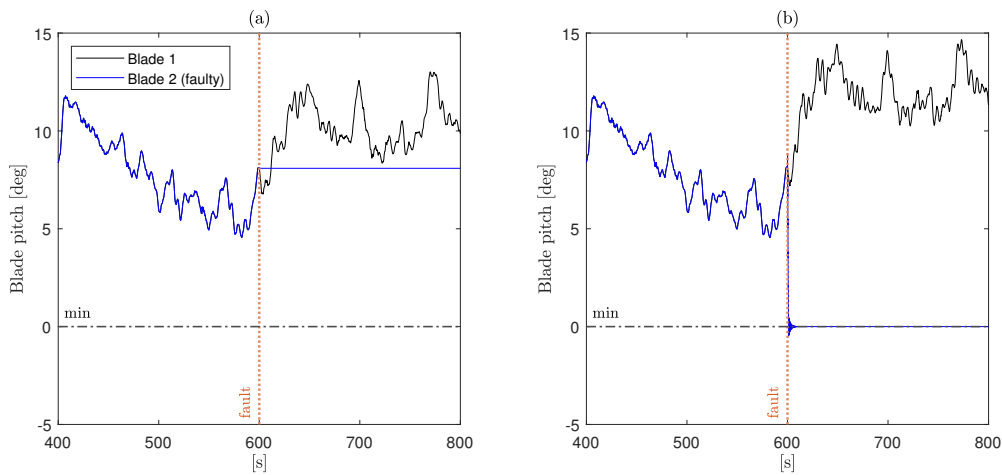
Figure 8.6: Time histories of the blade pitch angles for the faulty and one of the functioning blades in the case of a) blade blockage and b) blade runaway. LC 2A/3A, U_W = 14 m/s, H_S = 3.6 m, T_P = 10.3 s, t_f = 600 s, P_r = 8 deg/s.

8.6 Results and Discussion

8.6.1 Blade-Pitch Faults Without Initiation of Emergency Shutdown

In this section, the responses of the 2WT system undergoing blade-pitch faults are presented in both the time and the frequency domains (LC 2A/3A). Emergency shutdown is not initiated. Figure 8.6 shows the time histories of the blade pitch angles for the faulty and one of the functioning blades in the case of a) blade blockage and b) blade runaway (LC 2A/3A). The fault occurs at 600 s, after which the pitch angle of the faulty blade is either maintained constant or rapidly decreases to the minimum pitch setting. The rapid oscillations of the faulty blade in runaway conditions are associated with the blade-pitch dynamics. It can be noted how the mean value of the remaining working blades during blade runaway (case b) is higher than in the blade blockage case (case a) (about 2.5 deg). The increase is clearly associated with the attempt of the controller to compensate for the increase of aerodynamic torque at the low-speed shaft given by the runaway blade.

Figure 8.7 shows the time histories of the main rigid degrees of freedom of
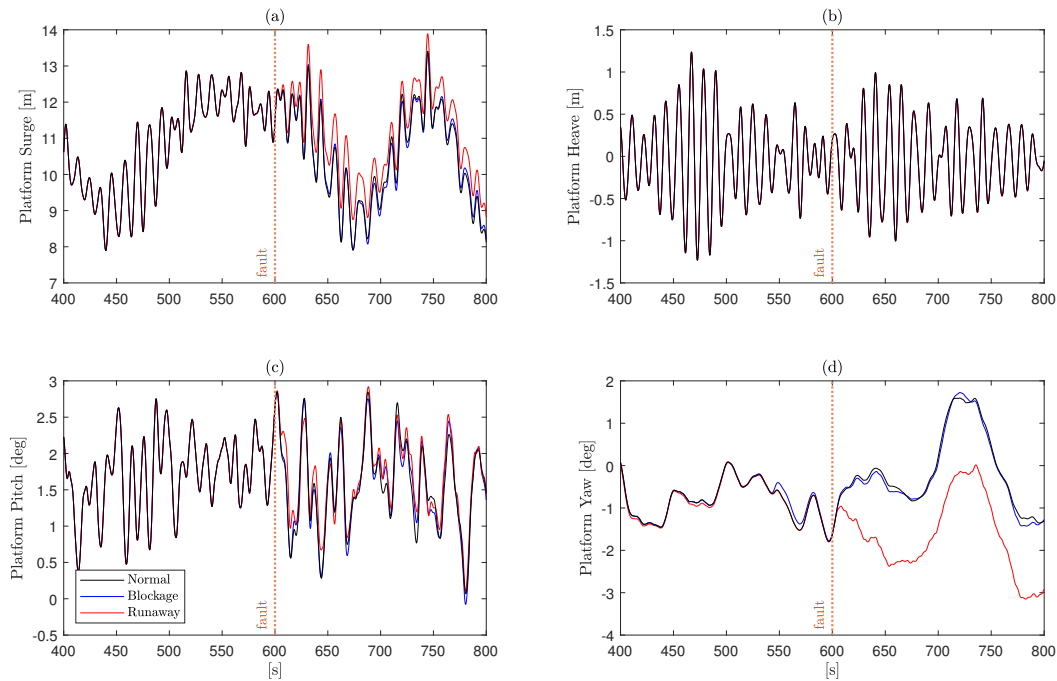
Figure 8.7: Time histories of a) platform surge motion, b) platform heave motion, c) platform pitch motion, and d) platform yaw motion in the case of normal operating conditions (black), blade blockage (blue), and blade runaway (red). LC 2A/3A, U_W = 14 m/s, H_S = 3.6 m, T_P = 10.3 s, t_f = 600 s, P_r = 8 deg/s.

the 2WT system under normal operating conditions, blade blockage, and blade runaway (LC 2A/3A). It is clear from the figure how the global system dynamics is not significantly affected by the blade fault. Only a marginal discrepancy of platform surge and yaw motions can be detected in the case blade runaway is considered, due to the increase of aerodynamic thrust impressed by the faulty turbine. However, the difference in dynamic response can be considered negligible.

The time histories of the flapwise and edgewise bending moments of the faulty blade (a-b), the tower bottom bending moment (c), and the main shaft (LSS) bending moment (d) (LSS associated with the left rotor) are shown in Figure 8.8 (LC 2A/3A). The equivalent bending moment acting on the LSS is calculated by considering the square root of the bending moments about the major shaft axes. The system is generally subjected to much higher loads when blade runaway occurs if compared to normal conditions and blade blockage condi-
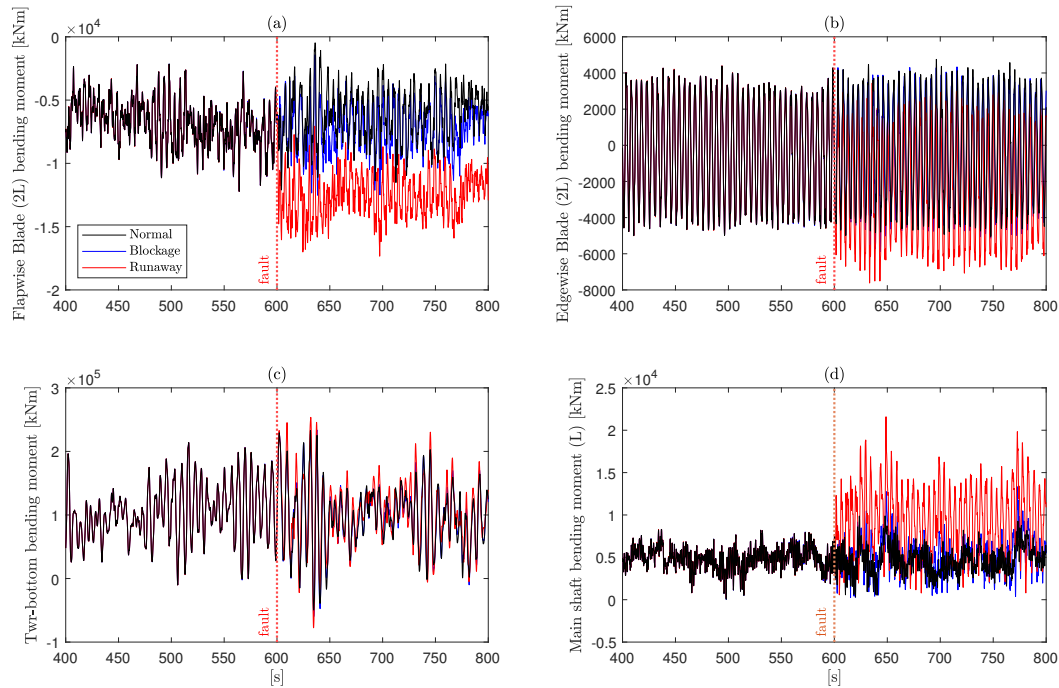
Figure 8.8: Time histories of a) the flapwise bending moment and b) edgewise bending moment of the faulty blade, c) the tower bottom bending moment, and d) the main shaft bending moment of the faulty rotor in the case of normal operating conditions (black), blade blockage (blue), and blade runaway (red). LC 2A/3A, U_W = 14 m/s, H_S = 3.6 m, T_P = 10.3 s, t_f = 600 s, P_r = 8 deg/s.

tions, due to the larger angle of attack of the faulty blade. The tower-base bending moment is only marginally affected. In blade-pitch runaway conditions, the peak values of the loads are much greater. Compared to normal conditions, the maximum flapwise bending moment is increased by about 45%, the maximum edgewise bending moment is increased by about 56%, and the maximum shaft bending moment is increased by about 120%. Note that these estimates may be higher, given the stochastic variability of wind and wave loads. Figure 8.9 shows the time series and power spectral densities of the torsion at the tower-bottom and tower arm root on the faulty side (LC 2A/3A). The torsional loads are greatly affected by blade runaway conditions. Compared to normal conditions, the tower-bottom torsion is about 1.6 times larger, while the tower arm root torsion is about four times larger. From power spectral analysis it is clear that the increase is associated with vibrations at the 1P rotor frequency. An ad-
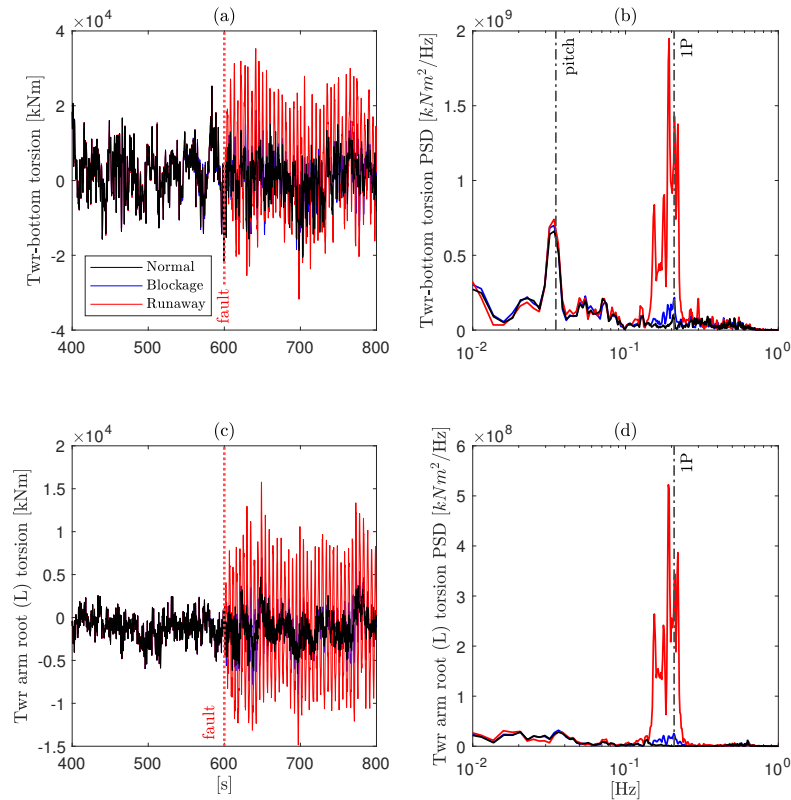
Figure 8.9: Time history (a) and power spectral density (b) of the tower bottom torsion. Time history (c) and power spectral density (d) of the tower arm root torsion on the faulty side. Normal operating conditions (black), blade blockage (blue), and blade runaway (red). LC 2A/3A, U_W = 14 m/s, H_S = 3.6 m, T_P = 10.3 s, t_f = 600 s, P_r = 8 deg/s.

ditional low-energy component at the platform pitch frequency is present for the tower-bottom torsion, which is present in all the cases considered. This component is associated with the pitch-yaw coupling given the gyroscopic inertia of the rotors and the large inertia of the semi-submersible platform in the yaw direction. The increase of aerodynamic thrust on the faulty blade due to the increased angle of attack generates a net torsional moment on the tower arm which varies orientation once per rotor revolution. The same is true for the main tower-bottom torsion, as the moment arm of the rotor thrust with respect to the main tower axis changes in length once per revolution. A large periodic variation of the torsional loads on the tower at a high frequency poses serious

concerns for the structural safety of the tower in terms of fatigue damage (1P frequency at above-rated wind speeds is about 0.2 Hz, thus inducing 300 high-amplitude periodic load cycles per minute on the structure). Therefore, the load imbalance given by blade-fault conditions on two-rotor wind turbine systems must be effectively considered during the structural design process of the tower to avoid excessive loading and fatigue damage.

Figure 8.10 shows the maximum of the major system responses occurring during blade-pitch fault as a function of the mean wind speed (LC 2A/3A). The maxima are normalized with respect to the maxima obtained under operating conditions (LC 1A). The general trend shows a negligible influence of the blade faults on the global system motions, greater loads on the structure under blade runaway conditions if compared to blade blockage conditions, and harsher loading for higher wind speeds. For blockage conditions, the normalized increment of blade flapwise bending moment, main shaft bending moment, and tower-bottom torsion (all about 20% larger than the operating maxima) is similar throughout the wind speeds considered. This can be related to the relative adjustment of the blade-pitch angle by the control system before failure. For runaway conditions, the normalized increment is greatly increasing with wind speed, as the angle of attack is forced to the minimum setting. The increase is especially large for the tower-bottom torsion and the main shaft bending moment, which reach values about 150% larger than the corresponding operating maxima. At below-rated wind speeds the blade-pitch controller is only used to mitigate platform yaw motion, which is a relatively small response if semi-submersible applications are considered. Consequently, the maxima at 8 m/s clearly indicate that the effect of blade faults on the system response at below-rated wind conditions is negligible.

8.6.2 Blade-Pitch Faults with Initiation of Emergency Shutdown

This section presents the responses of the 2WT system undergoing blade-pitch faults together with the initiation of emergency shutdown, as prescribed in LC 2B/3B (Table 8.8). Figure 8.11 shows the time histories relative to the blade
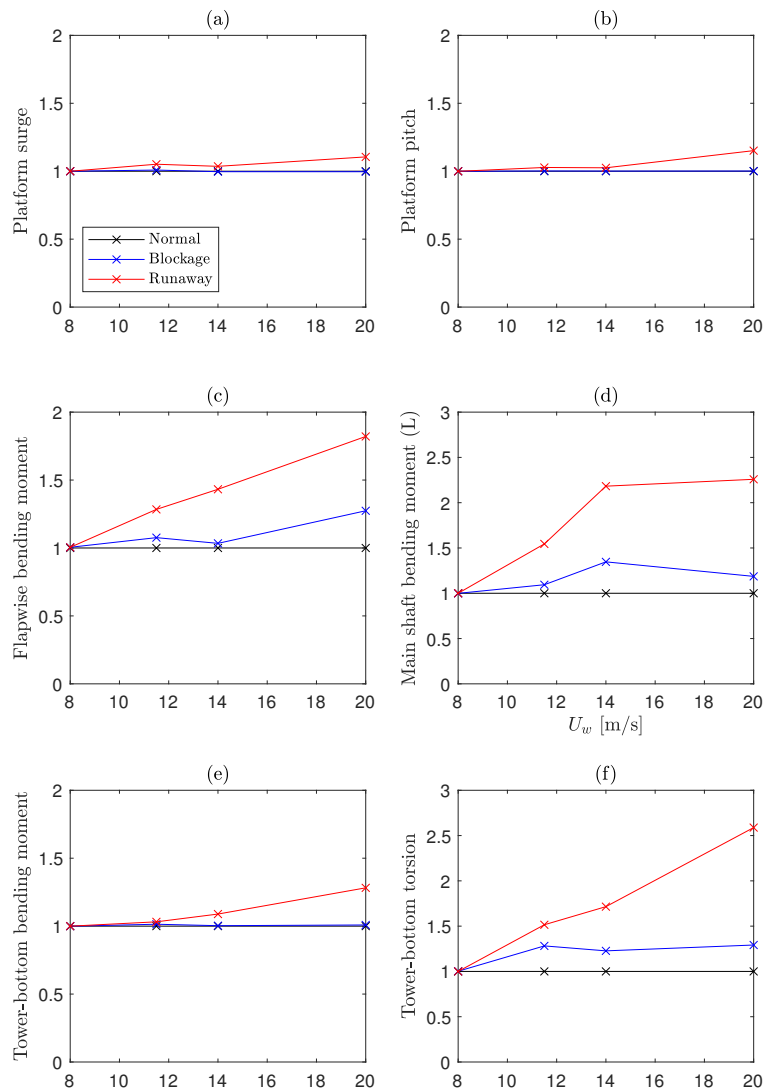
Figure 8.10: Maxima of global motions and structural responses normalized by the maximum in normal operating conditions as a function of the mean wind speed. Normal operating conditions (black), blade blockage (blue), and blade runaway (red).
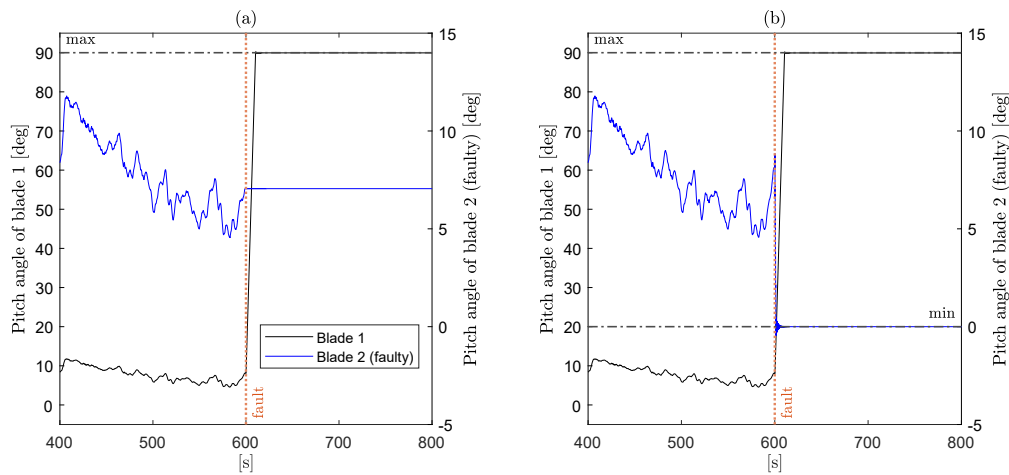
Figure 8.11: Time histories of the blade pitch angles for the faulty and one of the functioning blades in the case of a) blade blockage and b) blade runaway. System shutdown initiated. LC 2B/3B, U_W = 14 m/s, H_S = 3.6 m, T_P = 10.3 s, t_f = 600 s, t_d = 0.1 s, P_r = 8 deg/s.

pitch angles for the faulty blade and for one of the functioning blades in the two fault cases considered (LC 2B/3B). After the occurrence of fault at 600 s, the functioning blades are rapidly pitched to feather at the prescribed pitch rate. The load discontinuity given by the shutdown process affects the system global response, as the time histories of platform pitch and yaw motion depicted in Figure 8.12 indicate. After emergency shutdown initiation, the sudden drop of aerodynamic thrust on the rotors induces pitch motion excitation at the pitch natural frequency. Platform yaw motion is not significant if compared to the platform pitch motion. The large radiative damping in the yaw direction also effectively dissipates yaw oscillations after shutdown.

Figure 8.13 shows the time histories and power spectral densities of the thrust-induced bending moments at the tower-bottom and tower arm root on the faulty side (LC 2B/3B). The emergency shutdown triggers large oscillations in the tower bending moments and contributes to larger negative maxima (about 17% larger than in operating conditions). The overall response obtained in the two structural points considered is similar. Blockage and runaway fault conditions are also leading to a similar response, indicating that the dynamic amplification is mainly associated with the initiation of emergency shutdown.
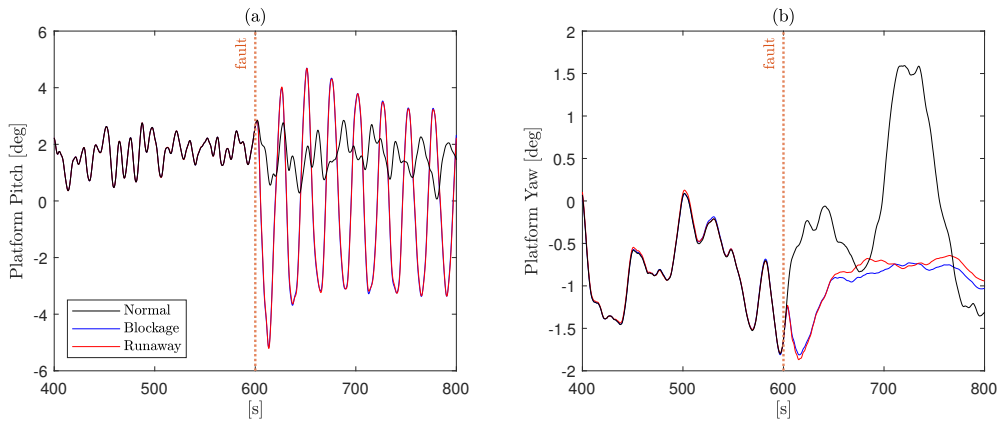
Figure 8.12: Time histories of a) platform pitch motion and b) platform yaw motion in the case of normal operating conditions (black), blade blockage (blue), and blade runaway (red). System shutdown initiated. LC 2B/3B, U_W = 14 m/s, H_S = 3.6 m, T_P = 10.3 s, t_f = 600 s, t_d = 0.1 s, P_r = 8 deg/s.

The power spectra indicate that the energy of the faulty load cases is mainly concentrated at the platform pitch natural frequency. Smaller energy contents around the wave frequency and for the fore-aft elastic response of the tower are also visible. While the wave energy is present for all load cases, the elastic response is related to the faulty cases only. At any rate, the elastic contribution is small if compared to the major energy component at the platform pitch frequency.

Figure 8.14 shows the time history of the flapwise bending moment of the faulty blade. The emergency shutdown initiation effectively reduces the load increase associated with the faulted conditions. In runaway conditions, immediately after the fault occurrence and before the load suppression due to shutdown, the bending moment is still able to rise to a high value for a short period of time (about 20% larger than in operating conditions). This increase can be detrimental to the structural integrity of the blade. This behavior is in accordance with previous work on single-rotor FOWT systems undergoing similar fault conditions (Jiang et al., 2014).

Figure 8.15 shows the time history and power spectral density of the tower-bottom torsion (LC 2B/3B). The shutdown initiation at 600 s coupled with the runaway fault induces large oscillations of the torsional load on the tower. Peak values are about three times the operating maxima in runaway conditions, and
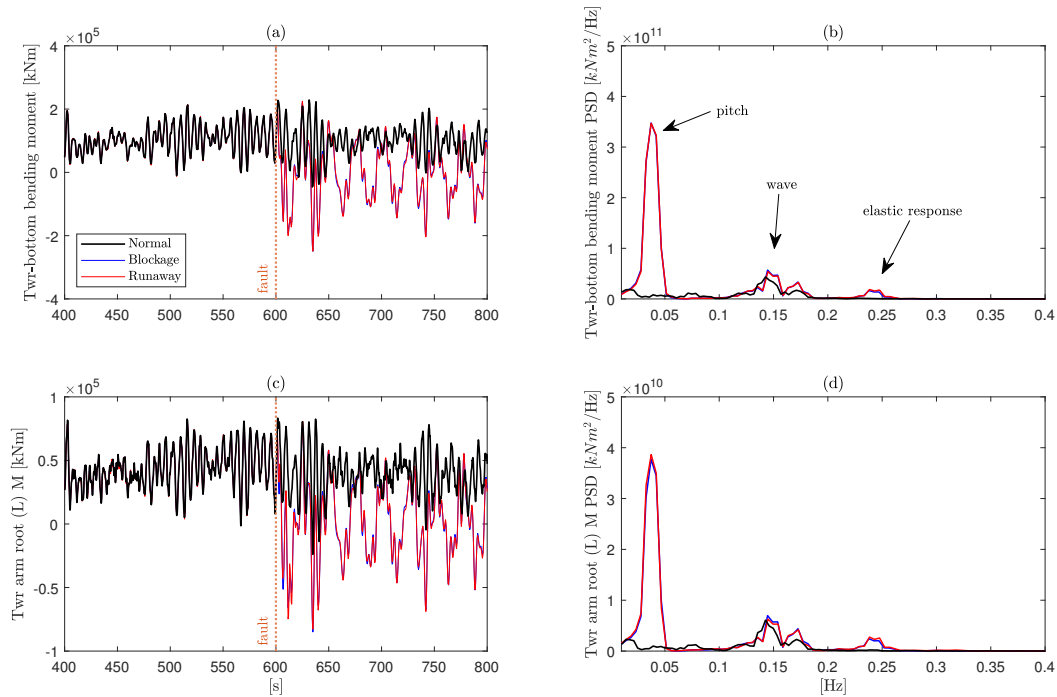
Figure 8.13: Time history (a) and power spectral density (b) of the tower bottom bending moment. Time history (c) and power spectral density (d) of the tower arm root bending moment on the faulty side. Normal operating conditions (black), blade blockage (blue), and blade runaway (red). System shutdown initiated. LC 2B/3B, U_W = 14 m/s, H_S = 3.6 m, T_P = 10.3 s, t_f = 600 s, t_d = 0.1 s, P_r = 8 deg/s.

about twice in blockage conditions. The oscillation frequency is about 0.31 Hz, associated with the fore-aft flexibility of the tower arms. The oscillation frequency is clearly detected in the power spectral density. Note that in this work the torsional flexibility of the slender elements is disregarded (see Section 8.4.2). The oscillations can be associated with the different rates of change of the aerodynamic thrusts acting on the rotor hubs. The torsion increase may pose concerns about the structural integrity of the tower.

Figure 8.16 shows the normalized maxima of the major system responses occurring during blade-pitch fault and emergency shutdown as a function of the mean wind speed (LC 2B/3B). As in the case without shutdown initiation (see Figure 8.10) the global motions of the system are only marginally affected by the wind speed. Throughout the wind speed range considered, platform surge
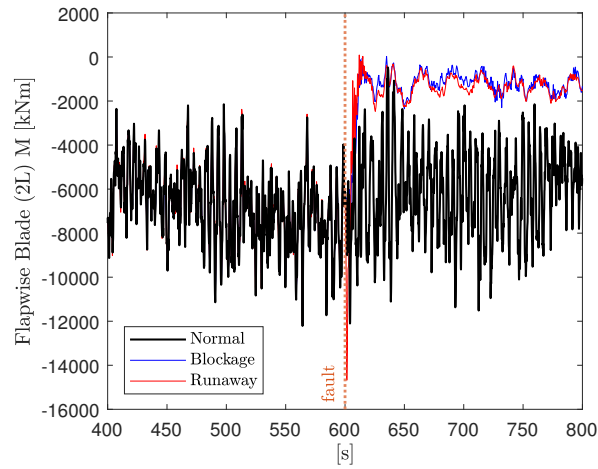
Figure 8.14: Time history of the flapwise bending moment of the faulty blade. Normal operating conditions (black), blade blockage (blue), and blade runaway (red). System shutdown initiated. LC 2B/3B, U_W = 14 m/s, H_S = 3.6 m, T_P = 10.3 s, t_f = 600 s, t_d = 0.1 s, P_r = 8 deg/s.
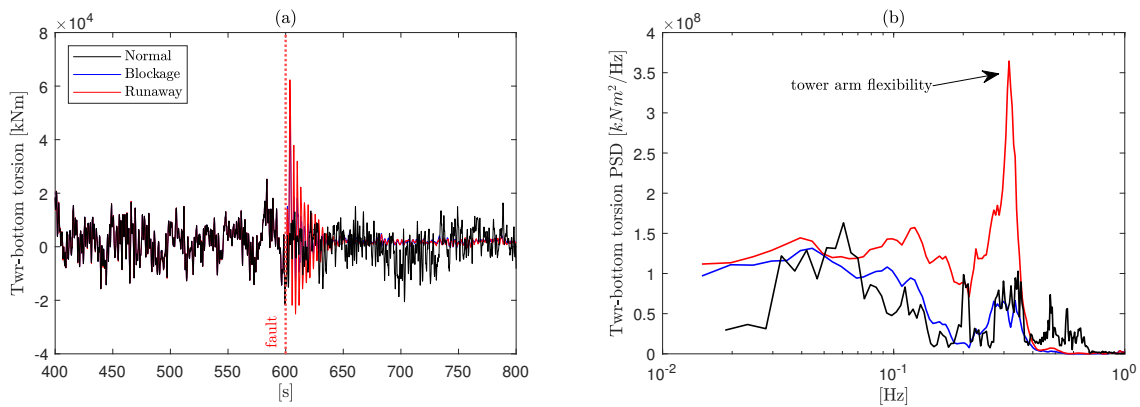
Figure 8.15: Time history (a) and power spectral density (b) of tower-bottom torsion. Normal operating conditions (black), blade blockage (blue), and blade runaway (red). System shutdown initiated. LC 2B/3B, U_W = 14 m/s, H_S = 3.6 m, T_P = 10.3 s, t_f = 600 s, t_d = 0.1 s, P_r = 8 deg/s.
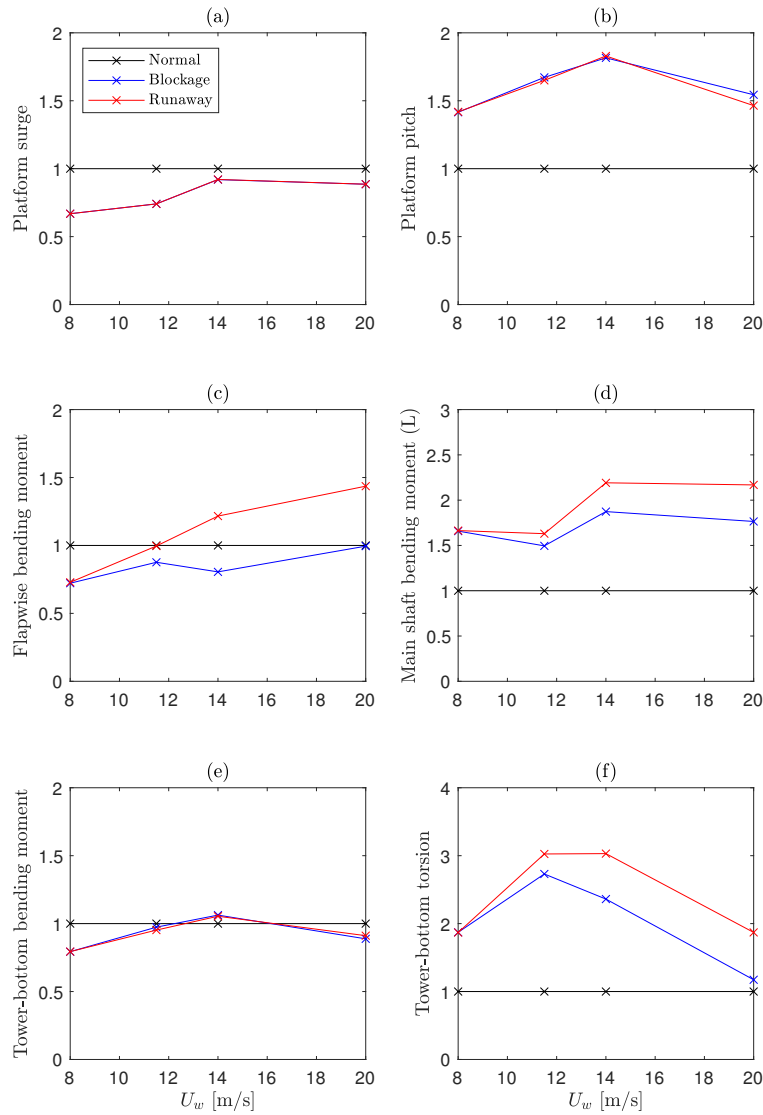
Figure 8.16: Maxima of global motions and structural responses normalized by the maximum in normal operating conditions as a function of the mean wind speed. Normal operating conditions (black), blade blockage (blue), and blade runaway (red). System shutdown initiated (LC 2B/3B).
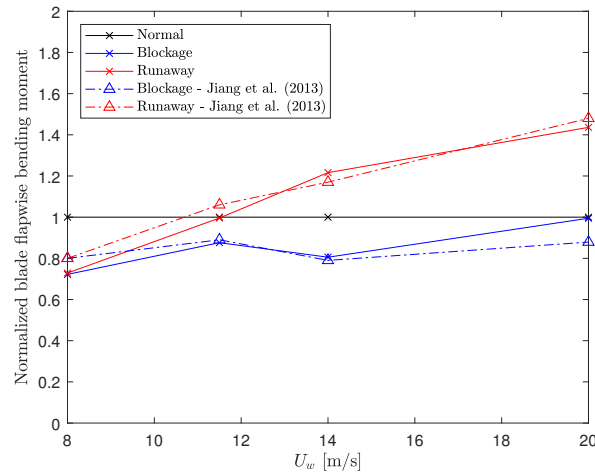
Figure 8.17: Comparison of normalized maxima of flapwise bending moment of the faulty blade as a function of the mean wind speed against values obtained for single-rotor spar-type FOWT by Jiang et al. (2014). System shutdown initiated (LC 2B/3B).

motion assumes lower levels than in operating conditions due to reduction of thrust, while the platform pitch motion is steadily about 50% larger than the operating maxima. The tower-bottom bending moment is also only marginally affected by the fault occurrence, and in most environmental conditions a response lower than the operating maxima is obtained. For the flapwise bending moment of the faulty blade, the runaway case can be up to 40% larger than the operating maxima. However, the maxima are generally reduced by about 20% if compared to those associated with the case without initiation of shutdown (see Figure 8.10c). This reduction is dominant throughout the environmental conditions considered (vertical shift of the response curve). The main shaft bending moment maxima are increased from 50% to 100% than in operating conditions. The decrease at rated conditions can be related to the larger shaft bending moment in operating conditions due to the discontinuous controller activation. No clear trend of the shaft moment variation as a function of wind speed can be detected. The largest values of the tower torsion maxima are close to the rated wind speed. The torsion decreases with higher wind speeds, as the blades are already pitched and the overall aerodynamic thrust is reduced.

Figure 8.17 reproduces the normalized maxima of flapwise bending moment

of the faulty blade as presented in Figure 8.16c, and compared against values obtained by Jiang et al. (2014) for the same 5-MW NREL baseline wind turbine mounted on a spar-type floating platform. The responses are relative to similar wind turbine system parameters. The trend is almost identical, highlighting that 1) the platform type and 2) the two-rotor configuration are generally not influential on the blade loads during blade-pitch faults. That is, maximum blade loads during faults are only influenced by the local system dynamics, which is much faster than the overall global dynamics.

8.6.3 Parameter Analysis

Effect of Blade-Pitch Rate during Emergency Shutdown

Blade-pitch rate can have a significant effect on the system dynamics and loads during fault and shutdown initiation (Jiang et al., 2014; Jiawen et al., 2022). Consequently, it is worth analyzing its parametric effect in more detail. The blade flapwise bending moment is not affected significantly as compared to the operating conditions. Figure 8.18 shows the normalized maxima of major response parameters as a function of the blade-pitch rate. The global motion maxima are reduced by increasing the pitch rate, as can be seen for the platform pitch motion. This behavior can be related to the filtering of high-frequency excitation loads by the large system inertia. The main shaft bending moment maxima are increased by about 45% and 20% the operating maxima from 6 deg/s to 12 deg/s in the runaway case and blockage case, respectively. The tower-bottom bending moment maxima are increased by about 20% from 6 deg/s to 12 deg/s for both fault cases. Tower-bottom torsion maxima are largest around 8 deg/s and rapidly decrease for higher blade-pitch rates. This can be associated with a less pronounced excitation of the torsional flexibility of the system by the unbalanced loads due to fault when the shutdown process is achieved rapidly.
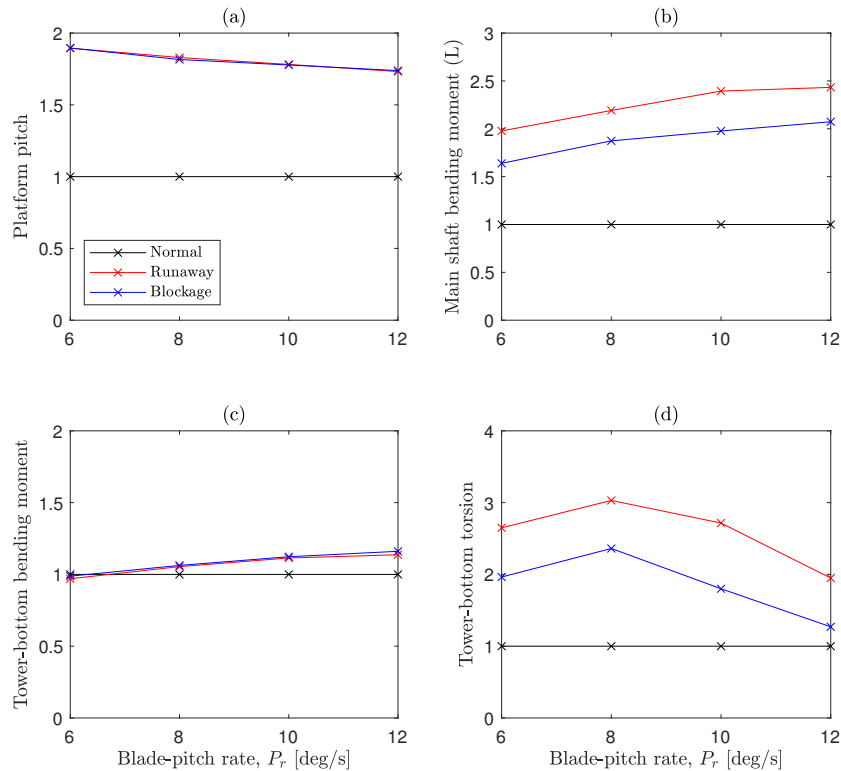
Figure 8.18: Normalized maxima of platform global motions and structural responses as a function of the blade-pitch rate. Normal operating conditions (black), blade blockage (blue), and blade runaway (red). System shutdown initiated. U_W = 14 m/s, H_S = 3.6 m, T_P = 10.3 s, t_f = 600 s, t_d = 0.1 s.

Effect of Shutdown Delay Between Rotors during Emergency Shutdown

In two-rotor designs, the rotors can have a certain degree of independence regarding the control system deployment and actuation of the associated pitch mechanisms. Consequently, during emergency shutdown initiation a short time delay between rotors may occur. Figure 8.19 shows the normalized maxima of the tower loads as a function of the shutdown delay between rotors. It is assumed that the shutdown is always initiated first on the rotor experiencing fault conditions. The global system dynamics and blade loads are not affected by the shutdown delay. The tower-bottom bending moment tends to decrease by increasing the delay (about -5% for a delay of 0.5 s). Moreover, the tower-bottom
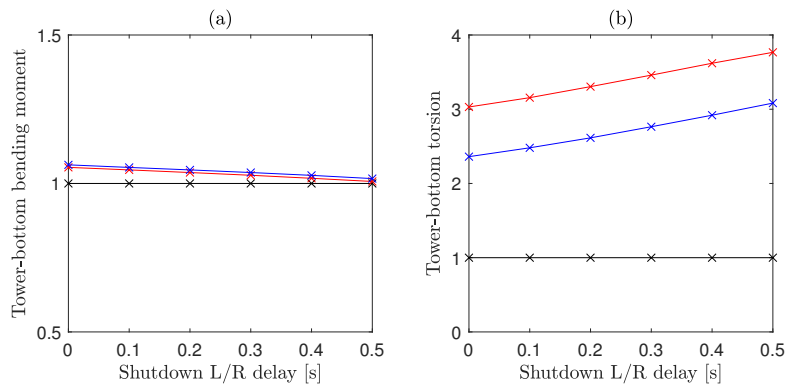
Figure 8.19: Normalized maxima of the tower loads as a function of the shutdown delay between rotors (shutdown is initiated first on the faulty rotor). U_W = 14 m/s, H_S = 3.6 m, T_P = 10.3 s, t_f = 600 s, t_d = 0.1 s.

torsion is greatly affected by the delay, exhibiting a linear increase of the associated maxima for longer delay times. The torsion increase with respect to the nominal value is about +30% with a delay of about 0.5 s, reaching values as high as +280% the maxima obtained during operating conditions.

8.7 Conclusions

This work presented the dynamic response of a two-rotor floating wind turbine undergoing several blade-pitch fault scenarios. Two blade-pitch scenarios are considered, i.e, blade blockage and blade runaway. The effect of these faults on the system dynamics is investigated with and without initiation of emergency shutdown.

The dynamic analysis is performed by means of an in-house code developed in Modelica. The tool takes into account the structural flexibility of blades and tower and assumes a rigid floating platform. Quasi-static mooring loads are assumed. Linear hydrodynamic loads are considered by coupling the code with the external commercial tool HydroD within DNV Sesam. The system is controlled by means of a linear quadratic regulator, aiming at regulation of the rotors' speeds above rated conditions and the mitigation of platform yaw motion. Moreover, the aerodynamic loads are computed by coupling the open-source code AeroDyn v15 within NREL FAST. To date, no complex aerodynamic inter-

action between the rotors is considered. This assumption may have a significant impact on the fully-coupled response of the system and should be later investigated in more detail.

If no emergency shutdown is initiated, blade-pitch faults lead to significant variations of the dynamic loads acting on the system. The global motion of the floater, on the other hand, is left mostly unaffected. Loads are increased close to the faulty blade, especially the flapwise and edgewise bending moments of the faulty blade and the associated main shaft bending moment. Bending moments are much larger in the runaway fault than in the blockage fault due to the large angle of attack. Tower-bottom torsion and tower arm root torsion are found to be significantly affected by the runaway fault due to uneven excitation loads. The response is characterized by a cyclic oscillation at the 1P frequency. High amplitude cyclic torsional loads can be critical to the structural integrity and fatigue life of the tower.

The initiation of emergency shutdown induces significant dynamic effects on the system. A large platform pitch resonant motion is excited due to the drop of aerodynamic thrusts. The tower-bottom bending moment is also increased; its energy content is mainly concentrated at the platform pitch natural frequency, wave frequency, and to a lesser extent at the fore-aft elastic mode of the main tower. The flapwise bending moment of the faulty blade is effectively suppressed, aside from a large increase shortly after shutdown. The tower-bottom torsion is also significantly excited by the emergency shutdown for the runaway fault. Large damped oscillations are detected at the tower arm fore-aft elastic frequency.

Comparison with literature data of a similar analysis focusing on a single-rotor wind turbine mounted on a spar-type floating platform showed very similar results regarding blade loads, highlighting that the loads on the faulty blade are not affected by 1) the platform type used and 2) the two-rotor deployment.

The effect of blade-pitch rate during shutdown as well as the shutdown delay between rotors were also investigated. Higher blad-pitch rate leads to smaller global motions. Some responses are marginally increased, as the tower-bottom bending moment and the main shaft bending moment. Longer shutdown delay between rotors leads to significantly larger maxima of the tower-bottom torsion

due to the unbalanced loads on the hubs.

Subjects for future work include the study of the effect of complex aerodynamic interactions between the rotors during fault occurrence, the study of fault-tolerant control strategies for two-rotor floating wind applications, and the inclusion of torsional flexibility of the tower elements and the associated impact on the torsional loads. The design of an optimal tower design that is fault-compliant may also be performed by including the considerations discussed in this work. Moreover, the effect of grid loss of either one or both turbines on the system's response should be investigated.

Acknowledgment

Chapter 9

Conclusion

9.1   Summary

This thesis focused on the development and benchmark of a novel computational tool for the dynamic analysis of two-rotor floating offshore wind turbines. The tool was then employed to examine the global dynamics of two-rotor floating wind turbine concepts. The primary aim was to gather useful information and inform researchers, designers, and standards organizations about the performance of such systems. All the research objectives formulated in this thesis (Section 1.3) are investigated and answered. The main conclusions are summarized as follows:

Research objective (1):

To establish and benchmark a comprehensive fully-coupled tool for the dynamic analysis of two-rotor floating offshore wind turbines. The tool should enable industry-standard fidelity levels and should be able to easily accommodate arbitrary platform and tower geometries and number of wind turbines used.

This thesis presented a novel object-oriented tool to model the fully-coupled dynamic response of two-rotor floating offshore wind turbines. The tool is developed in Modelica by means of the open-source platform OpenModelica.

The first development stage defined the general tool structure and implemented the external environmental loads and wind turbine servo systems. Major assumptions considered at this stage were 1) single rigid body dynamics, 2) simplified rotor dynamics, and 3) concentrated aerodynamic loads. This approach resulted useful to extract early results and perform analysis where a simplified approach was convenient. The second development stage defined the complete multi-body system dynamics, the structural dynamics of blades and tower, and localized aerodynamic loads based on the blade-element momentum approach. The MB-approach was employed to model the system structural dynamics, resulting in a flexible and accurate representation of the vibration modes of the system. Full blade-element momentum capabilities were achieved by integrating into Modelica the aerodynamic module AeroDyn v15 within NREL FAST. A dedicated aerodynamic subroutine was developed in Fortran 90 and imported as dynamic link library by means of a dedicated C buffer. Benchmark work against FAST demonstrated the tool accuracy. Some general conclusions regarding the development stage can be listed as follows:

- The tool structure entails easy implementation of models of arbitrary platform geometry and platform/rotor configuration.

- The object-oriented nature of the Modelica language offers a flexible modeling environment, resulting in easy model setup, code modification, and further development.

- The tool offers good numerical performance and industry-standard fidelity.

- Thorough single-rotor benchmark exercises against code FAST by NREL resulted in almost identical responses.

Research objective (2):

To analyze the global dynamic response of a two-rotor floating offshore wind turbine concept undergoing operational environmental conditions. The major dynamic aspects of the system should

be highlighted.

The present research investigated the dynamic analysis of a two-rotor wind turbine concept mounted on a spar-type platform. The global dynamics was first evaluated in the time domain by means of the fully-coupled simplified tool related to the first development stage of this thesis. The two-rotor wind turbine concept employs NREL 5 MW baseline wind turbines, while the tower is defined by performing a simplified ultimate limit state design. The spar-type platform employed is dimensioned through hydrostatic considerations, such as hydrostatic equilibrium, a limit on the maximum static platform pitch angle, a limit on the platform pitch and heave periods, and a limit on the system mass. A mass saving of about 26% may be achieved by employing the two-rotor configuration in place of an equivalent single-rotor configuration.

The system response was evaluated in operational environmental conditions and compared against the baseline OC3 Phase IV single-rotor system. Results showed a significantly large platform yaw response of the two-rotor system, of about 6 deg standard deviation at the rated wind speed. The platform yaw response is directly induced by the wind turbulence intensity at the hub and the transversal distribution of thrust loads on the structure. Mean platform surge motion is about twice than in the single-rotor system due to the increased thrust and the equivalent mooring system employed. Mean platform pitch motion is also about 1 deg lower than in the single-rotor system. A rotor-collective blade-pitch control strategy superimposing to the baseline control a proportional contribution to the platform yaw angle was proposed for platform yaw response mitigation. Results showed a reduction of the platform yaw response of about 60% at the cost of a reduction of the mean electric power output at below-rated wind speed of about 100 kW. The system response was also evaluated by means of the complete tool incorporating blade-element momentum aerodynamics and structural dynamics. Associated results were very similar to those obtained by means of the simplified method, thus highlighting the validity of the latter for global dynamic analysis.

Research objective (3):

To design and test a blade-pitch control algorithm suitable for two-rotor applications.

This thesis presented the design and performance analysis of an optimal rotor-collective blade-pitch control strategy for a two-rotor wind turbine concept mounted on a spar-type floating platform. The baseline non-linear generator torque control was employed, while the optimal blade-pitch control strategy considered is a linear quadratic regulator reducing platform yaw motion while regulating the generators' speed at above-rated wind speeds. The fully-coupled simplified tool related to the first development stage of this thesis resulted suitable for the linear state-space extraction and the dynamic assessment of the control system performance. Three gain schedules corresponding to below-rated, near-rated, and above-rated wind regions were considered to better accommodate system nonlinearities.

The performance of the controller was evaluated against the baseline OC3 proportional-integral control and the coupled control mitigating platform yaw response previously presented by the authors. Results showed that the linear quadratic controller performs significantly better than both reference controllers. The advantage is significant, especially at above-rated wind speeds. Platform yaw and pitch motions standard deviation is reduced considerably, about -58% and -40% than the coupled control at 12 m/s. This indicates better dynamic performance and stability. Electric output standard deviation is also reduced, about -17% than the coupled control at 17 m/s, indicating higher power quality. Performance is paid in terms of a higher blade-pitch rate root-mean-square, which can be correlated with actuation usage. However, peak values are well within the actuation saturation limits.

Research objective (4):

To investigate the long-term extreme response of a two-rotor

FOWT concept. Simplified methods, such as the environmental contour method and the modified environmental contour method, should be assessed to test their feasibility in two-rotor applications.

This work presented the evaluation of the 50-year extreme response of a two-rotor wind turbine concept mounted on a spar-type floating platform by means of a complete full long-term analysis (FLTA) and by means of simplified contour methods able to drastically reduce the amount of short-term simulation needed. The contour methods considered in the work are the standard environmental contour method (ECM) and the modified environmental contour method (MECM). The ECM is used to reduce the computational effort of the FLTA by only considering environmental conditions associated with a given return period. However, the ECM performs poorly if the loads acting on the system are not monotonically increasing with the environmental state. The MECM, on the other hand, is a modification of the ECM where additional contours are included to account for dynamic nonlinearities of the system. In this work, an additional contour considering the system cut-off initiation was included in the MECM. The fully-coupled simplified tool related to the first development stage of this thesis resulted suitable for the present analysis given its computational efficiency and the number of simulations needed.

As expected, the ECM leads to large underpredictions of responses governed by wind loads compared to the FLTA, as it is not capable of taking into account the system cut-off condition. Underestimation of platform yaw motion is about 50%, while underestimation of platform surge motion is about 30%. It was found that the MECM significantly improves the accuracy of wind-dominated results while predicting the same accuracy of the ECM for wave-dominated results. Most responses obtained by means of the MECM are within 15% difference with respect to FLTA results. Results gathered in this study suggest that the MECM may be assumed suited for the quick analysis of two-rotor floating wind turbines without the risk of underestimating long-term extreme responses.

Research objective (5):

To compare the dynamic response of a two-rotor wind turbine mounted on different floating platform types. Elements aimed at the definition of an optimal platform type for two-rotor applications should be highlighted.

This work presented a comparative dynamic analysis of a two-rotor wind turbine concept mounted on three different floating platforms, i.e., a spar-type, a semi-submersible, and a tension-leg. The spar-type and tension-leg platforms have been defined by means of simplified hydrostatic considerations applied to the two-rotor system. The OO-Star platform design was instead considered as reference semi-submersible platform. Fully-coupled dynamic simulations have been carried out by means of the complete tool related to the second development stage of this thesis. Complete multi-body dynamics of the system was thus considered, as well as blade-element momentum aerodynamic loads. The structure was assumed rigid.

Major results can be summarized as follow:

- Platform yaw motion is a significant dynamic mode for each configuration. The greatest response is obtained for the spar-type configuration. Platform yaw motion can be directly correlated with the equivalent platform yaw stiffness of the system, which can be associated with the stiffness of the station-keeping lines and the fairlead distance to the platform centerline. The spar configuration employs the softest mooring lines and the shortest fairlead radius, thus resulting in amplified platform yaw response. Platform yaw response is shown to negatively impact the electric power output quality by increasing the associated standard deviation.

- Mean motion responses, largely associated with wind loading, are largest for the spar-type configuration given the low station-keeping stiffness and the large distance from thrust loads and center of buoyancy.

- The tower base bending moment standard deviation is much greater than

onshore conditions given large hydrodynamic loads. The standard deviation is especially high in extreme storm conditions. Periodic variation of the tower bending moment can lead to significant fatigue damage. Tower base bending moment power spectral density shows high-frequency content for the tension-leg platform, indicating higher sensitivity to fatigue damage.

- For tension-leg platforms, large tendon loads can pose concerns in terms of fatigue and limit state performance.

- The semi-submersible configuration is associated with the largest response standard deviation in extreme storm conditions given its sensitivity to hydrodynamic loading.

Even though a candidate floating platform design is still to be selected, it is clear that spar-type configurations are not ideal for two-rotor applications given the excessive platform yaw amplification and large mean platform pitch response reducing the operational efficiency of the rotors. Tension-leg rigidity entails improved dynamic response but may lead to excessive structural loading on the system components and fatigue damage of tower, blades, and tendons, especially for intense sea states. The semi-submersible configuration, although associated with the largest response standard deviation in extreme storm conditions, tended to the most balanced response in operational conditions. Results can be greatly influenced by proper design of the control system. The latter should be thus considered integral to the platform design process.

Research objective (6):

To analyze the dynamic response and loads of a two-rotor floating offshore wind turbine concept undergoing blade-pitch actuation faults.

The last work of this thesis presented the dynamic response of a two-rotor wind turbine concept mounted on the OO-Star semi-submersible platform

undergoing several blade-pitch scenarios. The blade-pitch faults investigated are blade blockage and runaway, i.e., the seizure at a given pitch angle and the uncontrolled actuation of one of the blades, respectively. The effect of these faults on the system dynamics was investigated with and without initiation of emergency shutdown. Fully-coupled simulations considered complete multi-body dynamics, structural dynamics of tower and blades, and aerodynamic loads based on the blade-element momentum approach.

Blade-pitch faults lead to significant variations of the dynamic loads acting on the system, while the global motion is left almost unaffected. Loads are increased close to the faulty blade, especially the flapwise and edgewise bending moments of the faulty blade and the associated main shaft bending moment. Bending moments are much larger in the runaway fault than in the blockage fault due to the large angle of attack. Tower-bottom torsion and tower arm root torsion are found to be significantly affected by the runaway fault due to uneven excitation loads. The associated response is characterized by a cyclic oscillation at the 1P frequency. These torsional oscillations can be critical to the structural integrity and fatigue life of the tower.

The initiation of emergency shutdown induces significant dynamic effects on the system. Large platform pitch resonant motions are excited due to the drop of aerodynamic thrusts. Tower-bottom bending moment is increased, and its energy is concentrated at the platform pitch natural frequency, wave frequency, and the frequency associated with the fore-aft elastic mode of the tower. The flapwise blade bending moment is effectively suppressed. The tower-bottom torsion is greatly excited shortly after shutdown for the runaway fault, with oscillations at the tower arm fore-aft elastic frequency.

Literature data focusing on a single-rotor wind turbine mounted on a spar-type floating platform showed very similar results regarding the faulty blade loads, highlighting that blade loads during fault are not affected by 1) the platform type used and 2) the two-rotor application. Higher blade-pitch rate resulted in smaller global motions, while the tower-bottom bending moment

and main shaft bending moment are marginally increased. Longer shutdown delay between rotors leads to significantly larger maxima of the tower-bottom torsion due to the unbalanced loads on the hubs.

9.2 Recommendations for Future Research

The results of presented study assume that the proximity between rotors has no influence on the wind velocity profile. That is, the aerodynamic loads on blades are computed by considering the undisturbed turbulent wind profile and the blade local velocity induction factors only. The current modeling assumption resulted adequate to extract useful information about the global dynamics of two-rotor floating wind turbine systems. Nonetheless, the effect of the aerodynamic interaction between rotors on the system response should be later investigated in detail by means of high-fidelity tools and findings should be integrated into the code.

References

Aerodyn Engineering (2021). Official website (accessed: July 2022).

Alvarez, E. and Ning, A. (2017). Modeling multirotor aerodynamic interactions through the vortex particle method. *AIAA 2019-2827*.

Azcona, J., Palacio, D., Munduate, X., González, L., and Nygaard, T. (2017). Impact of mooring lines dynamics on the fatigue and ultimate loads of three offshore floating wind turbines computed with IEC 61400-3 guideline. *Wind Energy*, 20(5):797–813.

Bachynski, E., Etemaddar, M., Kvittem, M., Luan, C., and Moan, T. (2013). Dynamic analysis of floating wind turbines during pitch actuator fault, grid loss, and shutdown. *Energy Procedia*, 35:210–222.

Bachynski, E. E. and Eliassen, L. (2019). The effects of coherent structures on the global response of floating offshore wind turbines. *Wind Energy*, 22(2):219–238.

Bachynski, E. E. and Moan, T. (2012). Design considerations for tension leg platform wind turbines. *Marine Structures*, 29(1):89–114.

Bak, C., Zahle, F., Bitsche, R., Kim, T., Tde, A., Henriksen, L. C., Hansen, M. H., Blasques, J. P. A. A., Gaunaa, M., and Natarajan, A. (2013). The DTU 10-MW reference wind turbine.

Barltrop, N. (1993). Multiple unit floating offshore wind farm (MUFOW). *Wind Engineering*, 17(4):183–188.

Bastankhah, M. and Abkar, M. (2019). Multirotor wind turbine wakes. *Physics of Fluids*, 31(8):085106.

Berthelsen, A. P. (2015). Qualification of innovative floating substructures for 10 MW wind turbines and water depths greater than 50 m.

Bitner-Gregersen, E. M. (2011). Joint long term models of met-ocean parameters. *Marine Technology and Engineering*, 1:19–34.

Bossanyi, E. A. (2000). The design of closed loop controllers for wind turbines. *Wind Energy*, 3(3):149–163.

Box, G. E. P. and Muller, M. E. (1958). A note on the generation of random normal deviates. *The Institute of Mathematical Statistics*, 29(2):610–611.

Brommundt, M., Muskulus, M., Strach-Sonsalla, M., Strobel, M., and Vorpahl, F. (2012). Experiences with object-oriented and equation based modeling of a floating support structure for wind turbines in modelica. *Proceedings - Winter Simulation Conference*, pages 1–12.

Cheng, Z., Madsen, H. A., Gao, Z., and Moan, T. (2017a). Effect of the number of blades on the dynamics of floating straight-bladed vertical axis wind turbines. *Renewable Energy*, 101:1285–1298.

Cheng, Z., Wang, K., Gao, Z., and Moan, T. (2017b). A comparative study on dynamic responses of spar-type floating horizontal and vertical axis wind turbines. *Wind Energy*, 20:305–323.

Cho, S., Bachynski, E., Nejad, A., Gao, Z., and Moan, T. (2020). Numerical modeling of the hydraulic blade pitch actuator in a spar-type floating wind turbine considering fault conditions and their effects on global dynamic responses. *Wind Energy*, 23:370–390.

Cho, S., Gao, Z., and Moan, T. (2016). Model-based fault detection of blade pitch system in floating wind turbines. *Journal of Physics: Conference Series*, 753:092012.

Cho, S., Gao, Z., and Moan, T. (2018). Model-based fault detection, fault isolation and fault-tolerant control of a blade pitch system in floating wind turbines. *Renewable Energy*, 120:306–321.

Christiansen, S., Knudsen, T., and Bak, T. (2011). Optimal control of a ballast-stabilized floating wind turbine. In *2011 IEEE International Symposium on Computer-Aided Control System Design (CACSD)*, pages 1214–1219.

Christiansen, S., Knudsen, T., and Bak, T. (2014). Extended onshore control of a floating wind turbine with wave disturbance reduction. *Journal of Physics: Conference Series (Online)*, 555(1):1–10.

Clifton, A. and Wagner, R. (2014). Accounting for the effect of turbulence on wind turbine power curves. *Journal of Physics: Conference Series*, 524:012109.

Cordle, A. and Jonkman, J. (2011). State of the art in floating wind turbine design tools.

Cruz, J. and Atcheson, M. (2016). Floating offshore wind energy - the next generation of wind energy. *Springer*.

Cummins, W. E. (1962). The impulse response function and ship motions. *United States Department of the Navy, David Taylor Model Basin.*

DNV (2010). Offshore standard DNV-OS-J101 - design of offshore wind turbine structures.

DNV (2017). Wadam - wave analysis by diffraction and morison theory. sesam user manual.

DNV (2021). BLADED - engineering feature summary.

DNV-GL (2019). DNVGL-RP-0286 - Coupled analysis of floating wind turbines.

Du Kim, J. and Jang, B. S. (2016). Application of multi-objective optimization for TLP considering hull-form and tendon system. *Ocean Engineering*, 116:142–156.

Duarte, T., Sarmento, A., Alves, M., and Jonkman, J. M. (2013). State-space realization of the wave-radiation force within fast. *NREL.*

Dunne, F. and Pao, L. Y. (2016). Optimal blade pitch control with realistic preview wind measurements. *Wind Energy*, 19(12):2153–2169.

Ederer, N. (2015). The market value and impact of offshore wind on the electricity spot market: Evidence from Germany. *Applied Energy*, 154:805–814.

El Beshbichi, O., Xing, Y., and Ong, M. C. (2021a). Dynamic analysis of two-rotor wind turbine on spar-type floating platform. *Ocean Engineering*, 236:109441.

El Beshbichi, O., Xing, Y., and Ong, M. C. (2021b). An object-oriented method for fully coupled analysis of floating offshore wind turbines through mapping of aerodynamic coefficients. *Marine Structures*, 78:102979.

Elmqvist, H. (2014). Modelica evolution – from my perspective. *Proceedings of the 10th International Modelica Conference*.

EnBW (2021a). Floating wind turbine: Nezzy2 - official website (accessed: July 2022).

EnBW (2021b). Official website (accessed: July 2022).

Equinor (2015). Hywind scotland pilot park - environmental statement, non technical summary.

Equinor (2020a). Hywind demo official website (accessed: July 2022).

Equinor (2020b). Hywind scotland official website (accessed: July 2022).

Etemaddar, M., Blanke, M., Gao, Z., and Moan, T. (2016). Response analysis and comparison of a spar-type floating offshore wind turbine and an onshore wind turbine under blade pitch controller faults. *Wind Energy*, 19:35–50.

European Standard (2006). Eurocode 3 - design of steel structures, part 1-11: Design of structures with tension components (EN 1993-1-11).

EWEA (2013). Deep water - the next step for offshore wind energy.

Faltinsen, M. O. (1993). Sea loads on ships and offshore structures. *Cambridge Ocean Technology Series*.

Felippa, C. A., Park, K. C., and Farhat, C. (2001). Partitioned analysis of coupled mechanical systems. *Computer Methods in Applied Mechanics and Engineering*, (24):3247–3270.

Feng, Z., Zhu, J., and Allen, R. (2007). Design of continuous and discrete lqi control systems with stable inner loops. *Journal of Shanghai Jiaotong University (Science)*, 12(6):787–792.

Ferretti, G., Schiavo, F., and Vigano, L. (2005). Object-oriented modelling and simulation of flexible multibody thin beams in Modelica with the finite element method.

Ferri, F. et al. (2018). The MARINA project: Promoting responsible research and innovation to meet marine challenges. pages 71–81.

Flex2Power (2022). Official website (accessed: July 2022).

Fritzson, P. (2014). Principles of object-oriented modeling and simulation with modelica 3.3: A cyber-physical approach. *John Wiley & Sons LTD*.

Gasmi, A., Sprague, M. A., Jonkman, J., and Jones, W. B. (2013). Numerical stability and accuracy of temporally coupled multi-physics modules in wind-turbine CAE tools.

Gayo, J. (2011). Reliability-focused research on optimizing wind energy system design, operation and maintenance: tools, proof of concepts, guidelines & methodologies for a new generation, final publishable summary of results of project reliawind.

Germanischer Lloyd Industrial Services (2010). Guideline for the certification of wind turbines.

Gontier, H., Schaffarczyk, A. P., Kleinhans, D., and Friedrich, R. (2007). A comparison of fatigue loads of wind turbine resulting from a non-gaussian

turbulence model vs. standard ones. *Journal of Physics: Conference Series*, 75:012070.

GWEC (2019). Global wind report.

Hansen, M., Anca, D., Larsen, T., Stig, O., Sorensen, P., and Fuglsang, P. (2005). Control design for a pitch-regulated, variable speed wind turbine. *Risø-R-1500(EN)*.

Hansen, M. and Kallesøe, B. (2007). Servo-elastic dynamics of a hydraulic actuator pitching a blade with large deflections. *Journal of Physics: Conference Series*, 75:012077.

Haver, S. and Winterstein, S. R. (2008). Environmental contour lines: A method for estimating long term extremes by a short term analysis. *Transactions - Society of Naval Architects and Marine Engineers*, 116.

Heronemus, W. E. (1972). Pollution-free energy from the offshore winds. *Marine Technology Society*.

Hexicon (2021a). Operations update q2 2021.

Hexicon (2021b). Press release - hexicon to develop twinway project for floating wind in norway.

Hindmarsh, A. C., Brown, P. N., Grant, K. E., Lee, S. L., Serban, R., Shumaker, D. E., and Woodward, C. S. (2005). SUNDIALS: Suite of nonlinear and differential/algebraic equation solvers. *Association for Computing Machinery*, page 363–396.

INNWIND (2015). EU Deliverable 1.33. Innovative turbine concepts - multirotor system.

International Electrotechincal Commission (2005). Wind turbines: part 1: design requirements. tech. rep. IEC61400-1:2005(E).

International Electrotechincal Commission (2009). Wind turbines - part 3: Design requirements for offshore wind turbines (IEC 61400-3-1:2009).

International Electrotechincal Commission (2010). Wind turbines: Conformity testing and certification. tech. rep. iec61400-22:2010.

Jamieson, P. and Branney, M. (2012). Multi-rotors; a solution to 20 MW and beyond? *Energy Procedia*, 24:52–59.

Jena, D. and Rajendran, S. (2015). A review of estimation of effective wind speed based control of wind turbines. *Renewable and Sustainable Energy Reviews*, 43:1046–1062.

Jiang, S. and Duan, S. (2011). A four-rigid-body element model and computer simulation for flexible components of wind turbines. *ASME International Mechanical Engineering Congress and Exposition*, 7:935–941.

Jiang, S. and Duan, S. (2016). A multibody dynamics approach for vibration analysis of horizontal axis wind turbine blades. *ASME International Mechanical Engineering Congress and Exposition*, 4B.

Jiang, Z., Karimirad, M., and Moan, T. (2014). Dynamic response analysis of wind turbines under blade pitch system fault, grid loss, and shutdown events. *Wind Energy*, 17:1385–1409.

Jiawen, L., Jingyu, B., Zhenju, C., Yichen, J., and Shudong, L. (2022). Impact of pitch actuator fault on 10-mw semi-submersible floating wind turbine. *Ocean Engineering*, 254:111375.

Johnson, K. and Fleming, P. (2011). Development, implementation, and testing of fault detection strategies on the national wind technology center's controls advanced research turbines. *Mechatronics*, 21:728–736.

Johnson, K. E. (2004). Adaptive torque control of variable speed wind turbines.

Johnson, K. E., Fingersh, L. J., Balas, M. J., and Pao, L. Y. (2004). Methods for Increasing Region 2 Power Capture on a Variable-Speed Wind Turbine. *Journal of Solar Energy Engineering*, 126(4):1092–1100.

Johnson, N., Jonkman, J., Wright, A. D., Hayman, G., and Robertson, A. N. (2019). Verification of floating offshore wind linearization functionality in OpenFAST. *Journal of Physics. Conference Series*.

Jonkman, B. (2009a). Turbsim user's guide: version 1.50.

Jonkman, J. (2003). Modeling of the UAE wind turbine for refinement of FAS-TAD.

Jonkman, J. (2007). Dynamics modeling and loads analysis of an offshore floating wind turbine.

Jonkman, J. (2009b). Dynamics of offshore floating wind turbines-model development and verification. *Wind Energy*, 12(5):459–492.

Jonkman, J. (2010). Definition of the floating system for phase IV of OC3.

Jonkman, J. (2013). The new modularization framework for the FAST wind turbine CAE tool. *51st AIAA Aerospace Sciences Meeting including the New Horizons Forum and Aerospace Exposition*.

Jonkman, J. and Buhl, B. (2005). Fast user's guide.

Jonkman, J., Butterfield, S., Musial, W., and Scott, G. (2009). Definition of a 5MW reference wind turbine for offshore system development.

Jonkman, J., Larsen, T., Hansen, A., Nygaard, T., Maus, K., Karimirad, M., Gao, Z., Moan, T., Fylling, I., Nichols, J., Kohlmeier, M., Vergara, J., Merino, D., Shi, W., and Park, H. (2010). Offshore code comparison collaboration within iea wind task 23: Phase iv results regarding floating wind turbine modeling. *European Wind Energy Conference (EWEC)*.

Karimirad, M. and Michailides, C. (2019). Fault condition effects on the dynamic response of v-shaped offshore wind turbine. *J Mar Sci Technol*, 24:34–45.

Karimirad, M. and Moan, T. (2012a). A simplified method for coupled analysis of floating offshore wind turbines. *Marine Structures*, 27(1):45–63.

Karimirad, M. and Moan, T. (2012b). A simplified method for coupled analysis of floating offshore wind turbines. *Marine Structures*, 27(1):45–63.

Kenney, C. and Hewer, G. (1987). ecessary and sufficient conditions for balancing unstable systems. *Automatic Control, IEEE Transactions*, 32:157–160.

Kirchner-Bossi, N. and Porté-Agel, F. (2020). Multi-rotor wind farm layout optimization. *Journal of Physics: Conference Series*, 1618.

Kristiansen, E. and Egeland, O. (2003). Frequency-dependent added mass in models for controller design for wave motion damping. *IFAC Proceedings Volumes*, 36(21):67–73.

Kumar, A. and Stol, K. A. (2009). Simulating feedback linearization control of wind turbines using high☐order models. *Wind Energy*, 13:419–432.

Kung, S. Y. (1978). A new identification and model reduction algorithm via singular value decomposition. *Proc. Twelfth Asimolar Conf. on Circuits, Systems ans Computers.*, pages 705–710.

Larsen, T. and Hansen, A. (2007). How 2 hawc2, the user's manual.

Larsen, T. J. and Hanson, T. D. (2007). A method to avoid negative damped low frequent tower vibrations for a floating, pitch controlled wind turbine. *Journal of Physics: Conference Series*, 75:012073.

Leimeister, M., Kolios, A., and Collu, M. (2020). Development and verification of an aero-hydro-servo-elastic coupled model of dynamics for fowt, based on the mowit library. *Energies*, 13(8).

Leimeister, M. and Thomas, P. (2017). The onewind modelica library for floating offshore wind turbine simulations with flexible structures. *Proceedings of the 12th International Modelica Conference*, pages 633–642.

Li, L., Gao, Z., and Moan, T. (2013). Joint environmental data at five european offshore sites for design of combined wind and wave energy devices. *Journal of Offshore Mechanics and Arctic Engineering*, 137.

Li, L., Liu, Y., and Gao, Y. (2019). Dynamic and structural performances of offshore floating wind turbines in turbulent wind flow. *Ocean Engineering*, 179:92–103.

Li, Q., Gao, Z., and Moan, T. (2016). Modified environmental contour method for predicting long-term extreme responses of bottom-fixed offshore wind turbines. *Marine Structures*, 48:15–32.

Li, Q., Gao, Z., and Moan, T. (2017). Modified environmental contour method to determine the long-term extreme responses of a semi-submersible wind turbine. *Ocean Engineering*, 142:563–576.

Li, Q., Ren, N., Gao, Z., and Moan, T. (2018). Efficient determination of the long-term extreme responses by the modified environmental contour method for a combined wind turbine and wave energy converter system. *Journal of Ocean Engineering and Marine Energy*, 4.

LIFES50+ (2022). Official website (accessed: September 2022).

Lin, Y. H., Kao, S. H., and Yang, C. H. (2019). Investigation of hydrodynamic forces for floating offshore wind turbines on spar buoys and tension leg platforms with the mooring systems in waves. *Applied Sciences*, 9(3).

Lindeberg, E., Svendsen, H. G., and Uhlen, K. (2012). Smooth transition between controllers for floating wind turbines. *Energy Procedia*, 24:83–98.

Lindenburg, C. (2002). Aeroelastic modeling of the LMH64-5 blade.

Liu, G. R. and Quek, S. S. (2014). The finite element method (second edition). pages 43–79.

Liu, Y., Ferrari, R., Wu, P., Jiang, X., Li, S., and van Wingerden, J. (2021). Fault diagnosis of the 10 MW floating offshore wind turbine benchmark: A mixed model and signal-based approach. *Renewable Energy*, 164:391–406.

Luo, N., Vidal, Y., and Acho, L. (2014). Wind turbine control and monitoring. *Springer Cham*, 1.

Lupton, R. C. and Langley, R. S. (2017). Scaling of slow-drift motion with platform size and its importance for floating wind turbines. *Renewable Energy*, 101:1013–1020.

Machowski, J., Bialek, J. W., and Bumby, J. R. (2012). Power system dynamics. stability and control. *John Wiley and Sons*, pages 705–710.

Madsen, H. O. (1988). Omission sensitivity factors. *Structural Safety*, 5(1):35–45.

Mahdi, S. and Cenac, M. (2012). Estimating parameters of gumbel distribution using the methods of moments, probability weighted moments and maximum likelihood. *Revista de Matemática: Teoría y Aplicaciones*, 12:151.

Manolas, D. I., Riziotis, V. A., Papadakis, G. P., and Voutsinas, S. G. (2020). Hydro-servo-aero-elastic analysis of floating offshore wind turbines. *Fluids*, 5(4):200.

Masciola, M., Jonkman, J., and Robertson, A. (2013). Implementation of a multisegmented, quasi-static cable model.

Matha, D. (2010). Model development and loads analysis of an offshore wind turbine on a tension leg platform with a comparison to other floating turbine concepts.

Miller, S., Soares, T., Van Weddingen, Y., and Wendlandt, J. (2017). Modeling flexible bodies with Simscape multibody software - an overview of two methods for capturing the effects of small elastic deformations. *MathWorks*.

Mirzaei, M., Tibaldi, C., and Hansen, M. H. (2016). Pi controller design of a wind turbine: evaluation of the pole-placement method and tuning using constrained optimization. *Journal of Physics: Conference Series*, 753:052026.

Miyamoto, K., She, J., Sato, D., and Yasuo, N. (2018). Automatic determination of lqr weighting matrices for active structural control. *Engineering Structures*, 174:308–321.

Mo, W., Li, D., Wang, X., and Zhong, C. (2015). Aeroelastic coupling analysis of the flexible blade of a wind turbine. *Energy*, 89:1001–1009.

Moriarty, P. J. and Hansen, A. C. (2005). Aerodyn theory manual.

Murua, X., Martinez, F., Pujana, A., and Basurko, J. (2006). 3D flexible multi-body thin beam simulation in Modelica with the finite element method.

Newman, J. N. (1977). Marine hydrodynamics. *MIT Press Cambridge*.

Nielsen, F. G., Hanson, T. D., and Skaare, B. (2008). Integrated dynamic analysis of floating offshore wind turbines. *International Conference on Offshore Mechanics and Arctic Engineering*, 1:671–679.

NREL (2020). OpenFAST documentation - Release v2.3.0.

Odgaard, P., Stoustrup, J., and Kinnaert, M. (2009). Fault tolerant control of wind turbines – a benchmark model. *IFAC Proceedings Volumes*, 42:155–160.

OSMC (2021). Openmodelica user's guide. release v1.19.0.

Pegalajar-Jurado, A., Bredmose, H., Borg, M., Straume, G. J., Landb/o, T., Andersen, S. H., Yu, W., Müller, K., and Lemmer, F. (2018). State-of-the-art model for the LIFES50+ OO-Star wind floater semi 10 MW floating wind turbine. *Journal of Physics: Conference Series*, 1104:012024.

Perez, T. and Fossen, T. I. (2008). Time vs. frequency-domain identification of parametric radiation force models for marine structures at zero speed. *Modeling, Identification and Control*, 29.

Petzold, L. R. (1982). A description of DASSL: A differential/algebraic system solver.

Pham, T. D. and Shin, H. (2019). A new conceptual design and dynamic analysis of a spar-type offshore wind turbine combined with a moonpool. *Energies*, 12(19):3737.

Pham, T. K., Nam, Y., Kim, H., and Son, J. (2012). Lqr control for a multi-mw wind turbine. *International Journal of Mechanical and Mechatronics Engineering*, 6(2):507 – 512.

Prasad, L. B., Tyagi, B., and Gupta, H. O. (2014). Optimal control of nonlinear inverted pendulum system using pid controller and lqr: Performance analysis without and with disturbance input. *International Journal of Automation and Computing*, 11:661–670.

Principle Power (2016). The windfloat: Enabling a paradigm shift in offshore wind.

Ramachandran, G. K. V., Robertson, A., Jonkman, J. M., and Masciola, M. D. (2013). Investigation of response amplitude operators for floating offshore wind turbines. *NREL CP-5000-58098*.

Ramos-García, N., Kontos, S., Pegalajar-Jurado, A., González Horcas, S., and Bredmose, H. (2022). Investigation of the floating IEA wind 15 MW RWT using vortex methods part I: Flow regimes and wake recovery. *Wind Energy*, 25(3):468–504.

Robertson, A., Jonkman, J., Masciola, M., Song, H., Goupee, A., Coulling, A., and Luan, C. (2014a). Definition of the Semisubmersible Floating System for Phase II of OC4.

Robertson, A., Jonkman, J., Vorpahl, F., Popko, W., Qvist, J., Froyd, L., Chen, X., Azcona, J., Uzungoglu, E., Guedes Soares, C., Luan, C., Yutong, H., Pengcheng, F., Yde, A., Larsen, T., Nichols, J., Buils, R., Lei, L., Anders Nygard, T., and et al. (2014b). Offshore code comparison collaboration, continuation within IEA wind task 30: Phase II results regarding a floating semisubmersible wind system: Preprint.

Rosenblatt, M. (1952). Remarks on a multivariate transformation. *The Annals of Mathematical Statistics*, 23(3):470–472.

Saranyasoontorn, K. and Manuel, L. (2004). Efficient models for wind turbine extreme loads using inverse reliability. *Journal of Wind Engineering and Industrial Aerodynamics*, 92(10):789–804.

Sarkar, S., Fitzgerald, B., and Basu, B. (2021). Individual blade pitch control of floating offshore wind turbines for load mitigation and power regulation. *IEEE Transactions on Control Systems Technology*, 29(1):305–315.

SeaFEM (2018). Analysis of the response amplitude operator (RAO) of a spar buoy wind turbine.

Shen, M., Hu, Z., and Liu, G. (2016). Dynamic response and viscous effect analysis of a TLP-type floating wind turbine using a coupled aero-hydro-mooring dynamic code. *Renewable Energy*, 99:800–812.

Smith, Z. (2022). Uk offshore wind capacity factors. *ORCID 0000-0002-8215-4526*.

Stol, K. A. and Fingersh, L. J. (2004). Wind turbine field testing of state-space control designs: August 25, 2003–november 30, 2003.

Strobel, M., Vorpahl, F., Hillmann, C., Gu, X., Zuga, A., and Wihlfahrt, U. (2011). The onwind modelica library for offshore wind turbines - implementation and first results. *Proceedings of the 12th International Modelica Conference*, pages 633–642.

Taylor, A. G. and Hindmarsh, A. C. (1998). User documentation for KINSOL, a nonlinear solver for sequential and parallel computers.

The Modelica Association (2008). Modelica standard library. tutorial and reference. version 3.0.

The Modelica Association (2017). *Modelica® - A Unified Object-Oriented Language for Systems Modeling. Language Specification, Version 3.4.*

The Modelica Association (2020). Modelica official website - modelica language (accessed: July 2022).

Tibaldi, C., Hansen, M. H., and Henriksen, L. C. (2012). Optimal tuning for a classical wind turbine controller. *Journal of Physics: Conference Series*, 555:012099.

van der Laan, M. P., García, N., Angelou, N., Pirrung, G., Ott, S., Sørensen, K., Xavier, J., Neto, V., Larsen, G., Mikkelsen, T., Kelly, M., Sjöholm, M., and Andersen, S. (2019). Power curve and wake analyses of the Vestas multi-rotor demonstrator. *Wind Energy Science*, 4:251–271.

Wind Catching Systems (2022). Official website (accessed: September 2022).

WindEurope (2019). Our energy, our future. How offshore wind will help Europe go carbon-neutral.

Winterstein, S. R., Ude, T. C., Cornell, C. A., Bjerager, P., and Haver, S. (1993). Environmental parameters for extreme response: Inverse FORM with omission factors. *Proceedings, ICOSSAR-93*.

Wright, A. D. and Fingersh, L. J. (2008). Advanced control design for wind turbines; part i: Control design, implementation, and initial tests.

Xu, J., Zhang, L., Li, X., Li, S., and Yang, K. (2020). A study of dynamic response of a wind turbine blade based on the multi-body dynamics method. *Renewable Energy*, 155:358–368.

Zambrano, T., MacCready, T., Kiceniuk, T., Roddier, D. G., and Cermelli, C. A. (2006). Dynamic modeling of deepwater offshore wind turbine structures in gulf of mexico storm conditions. *Offshore Wind Energy; Ocean Research Technology*, 1:629–634.

Zhang, L., Shi, W., Karimirad, M., Michailides, C., and Jiang, Z. (2020). Second-order hydrodynamic effects on the response of three semisubmersible floating offshore wind turbines. *Ocean Engineering*, 207:107371.

Zhao, X., Maißer, P., and Wu, J. (2007). A new multibody modelling methodology for wind turbine structures using a cardanic joint beam element. *Renewable Energy*, 32(3):532–546.

Zheng, Z., Chen, J., Liang, H., Zhao, Y., and Shao, Y. (2020a). Hydrodynamic responses of a 6 mw spar-type floating offshore wind turbine in regular waves and uniform current. *Fluids*, 5:4–187.

Zheng, Z., Chen, J., Liang, H., Zhao, Y., and Shao, Y. (2020b). Hydrodynamic responses of a 6 MW spar-type floating offshore wind turbine in regular waves and uniform current. *Fluids*, 5(4).

Zhou, W., Ning, Z., Li, H., and Hu, H. (2017). An experimental investigation on rotor-to-rotor interactions of small uav. *AIAA 2017-3744*.

Ziegler, J. G. and Nichols, N. B. (1993). Optimum settings for automatic controllers. *Journal of Dynamic Systems, Measurement, and Control*, 115(2B):220–222.